UNIVERSITY OF LONDON THESIS

Degree PhD Year 2007 Name of Author ALAN RICHARD TODD

Department of Mechanical Engineering

University College London

Optical studies in a firing stratified-charge G-DI engine

Ph.D. thesis

Alan Richard Todd

February 2007

Submitted in partial fulfilment of the requirements for the degree of
Doctor of Philosophy

ProQuest LLC
789 East Eisenhower Parkway
P.O. Box 1346
Ann Arbor, MI 48106-1346

DECLARATION

I hereby declare that this thesis is my own work except where otherwise indicated. I have identified my sources of information and in particular have cited origins of any passages that have been quoted word for word.

Signed Date 13th February 2007

[ALAN TODD]

Abstract

This thesis describes investigations into fuel spray interactions within the cylinder of a prototype, direct injection, spark ignition engine.

The literature review discussed the future of the automobile and its possible prime movers. It concluded that gasoline direct injection (G-DI) engines have the potential to meet increasingly stringent emissions regulations except for their excessive unburnt hydrocarbon emissions. Further studies are necessary to understand the causes and to investigate possible methods of reduction.

A prototype cylinder head was supplied by Jaguar Cars Ltd. and a cylinder block and piston were designed and manufactured to provide optical access to study the fuel spray interactions. The design featured a piston with a deep bowl, three versions of which were made. One was non-optical (for benchmark testing), the second had a thin quartz slice to allow sheet illumination, while the third had a quartz disc set in the base of the bowl.

The most suitable optical methods for the investigation were assessed. Mie scattering and Laser Induced Fluorescence (LIF) were chosen for their ability to show fuel in liquid and vapour form and their compatibility with an existing laser unit. The Mie tests were performed using pump gasoline with the engine firing. The main variables were injection timing, engine temperature and optical access through the piston.

The LIF tests used the firing engine, but a three-component hydrocarbon fuel replaced gasoline. The fuel components were chosen to represent the evaporative behaviour of gasoline, but not to fluoresce. A dopant in known concentration was added to provide the fluorescence. Images were recorded using a charge-coupled device camera. Extensive image post-processing was performed to correct for background illumination, window fouling and light-sheet intensity variation.

Finally, a comparison was made between the Mie and the LIF images, also taking into account corresponding ambient air fuel spray images.

Acknowledgements

This research was carried out during a period of great change in the Department. A constant and reassuring presence through it all was that of Dr. Chris Nightingale, whose expertise, enthusiasm and wisdom were invaluable. Many have benefited from his supervision.

Enormous gratitude is also due:
to Jaguar Cars for financial backing and especially Dr. X-D. Chen for technical assistance.

to the Institution of Mechanical Engineers (IMechE), not only for the Clayton award but for their superb library service.

to the Engineering and Physical Sciences Research Council (EPSRC) for funding.

to UCL Graduate School for funding and in particular Anne MacDonald for her interest and encouragement.

to the UCL Department of Mechanical Engineering, especially Dr. M. Davy (for giving me the opportunity), Dr. P. Williams (for exceptional guidance) and Dr. R. Balachandran (for devoting many hours to addressing the problems of LIF) and the Technical Staff (especially Phil Jeavons, Richard Winn and Dave Hurley for expert technical skills).

to past and present members of the I.C.Engines Group, even though they hardly ever arrived in time for morning team-tea.

to my friends, for keeping my feet firmly on the ground and continually pointing out other ways in which tax-payers' money might be spent.

to S.A.C.M and I.A.E.R.X.

but most of all, to R and J.

TABLE OF CONTENTS

DECLARATION **2**

ABSTRACT **3**

ACKNOWLEDGEMENTS **4**

TABLE OF CONTENTS **5**

LIST OF FIGURES **10**

LIST OF TABLES **16**

NOMENCLATURE **17**

CHAPTER 1

THE PRESENT AND FUTURE OF THE AUTOMOBILE **19**

1.1 INTRODUCTION 19

1.2 FACTS AND FIGURES: THE PRESENT STATE OF THE AUTOMOBILE 19

1.3 OVERVIEW OF THE GLOBAL AUTOMOBILE INDUSTRY 19

1.4 FACTORS REDUCING AUTOMOBILE USE 20

1.5 UNPREDICTABLE FACTORS 21

1.6 FACTORS INCREASING AUTOMOBILE USE 23

1.7 SUMMARY 24

CHAPTER 2

FUTURE AUTOMOTIVE PRIME MOVERS **27**

2.1 INTRODUCTION 27

2.2 EMISSIONS 27

2.2.1 Background 27

2.2.2 Legislation 27

2.2.3 Stoichiometry and air fuel ratio 29

2.2.4 Formation of regulated emissions species 30

2.3 CONTROL OF EMISSIONS 33

2.3.1 History 33

2.3.2 Engine design 34

2.3.3 Engine control strategies 35

2.3.4 Diluents and Exhaust Gas Recirculation (EGR) 35

2.3.5 Catalytic treatment 36

2.3.6 Emission control in compression ignition engines 40

2.4 IC ENGINES, SPARK IGNITION 41

2.4.1 Carburettor 41

2.4.2 Fuel injection 41

2.4.3 Gasoline direct injection (G-DI) 42

2.4.4 Variable valve actuation (VVA) 43
2.4.5 Rotary engine 44
2.5 IC ENGINES, COMPRESSION IGNITION AND ALTERNATIVE FUEL 45
2.5.1 High-speed direct injection (HSDI) 45
2.5.2 Homogeneous charge compression ignition (HCCI) 46
2.5.3 Hydrogen 47
2.5.4 Natural gas and petroleum gas 48
2.5.5 Alcohols 49
2.5.6 Bio-diesels 50
2.6 ALTERNATIVES TO IC ENGINES 51
2.6.1 Electric drive: battery power 51
2.6.2 Electric drive: photo-voltaic cells 51
2.6.3 Electric drive: fuel cell 52
2.6.4 Flywheel energy storage 54
2.6.5 External combustion engines: steam engines 55
2.6.6 Stirling engine 55
2.6.7 Gas turbines 57
2.6.8 Hybrid drives 57
2.7 SUMMARY 59

CHAPTER 3

GASOLINE DIRECT INJECTION ENGINES 61
3.1 INTRODUCTION 61
3.2 FUEL SPRAYS AND AIR-FUEL MIXING 61
3.3 THE INFLUENCE OF OPERATING CONDITIONS 65
3.3.1 Injector deposits 70
3.3.2 Injector and spark plug location 71
3.4 MODES OF OPERATION – HOMOGENEOUS CHARGE (HC) AND STRATIFIED CHARGE (SC) 72
3.4.1 Introduction 72
3.4.2 Homogeneous charge mode 73
3.4.3 Stratified charge mode 74
3.4.4 Transition 77
3.5 SUMMARY 78

CHAPTER 4

OPTICAL METHODS 81
4.1 INTRODUCTION 81
4.2 SPECTROSCOPIC TECHNIQUES: SRS (SPONTANEOUS RAMAN SCATTERING), LRS (LASER RAYLEIGH SCATTERING), LIF (LASER INDUCED FLUORESCENCE) ... 81
4.3 IN-CYLINDER FLOW FIELD MEASUREMENT: LDA (LASER DOPPLER ANEMOMETRY), PIV (PARTICLE IMAGE VELOCIMETRY), PTV (PARTICLE TRACKING VELOCIMETRY) 84
4.3.1 Laser Doppler Anemometry 84
4.3.2 Particle Image Velocimetry 85

4.4 IN-CYLINDER LIQUID FUEL MEASUREMENT TECHNIQUES 87
4.4.1 Fraunhofer 87
4.4.2 Phase Doppler Anemometry (PDA) 87
4.4.3 Mie scattering 89
4.4.4 Laser Induced Exciplex Fluorescence (LIEF) 89
4.4.5 Laser extinction/absorption (LEA) 91
4.5 VISUALISATION OF IN-CYLINDER EVENTS 91
4.6 SCHLIEREN AND SHADOWGRAPH PHOTOGRAPHY 94
4.7 MULTI IONISATION PROBES (MIPS) 96
4.8 MULTIPLE OPTICAL FIBRES (MOFS) 97
4.9 ENDOSCOPES 98
4.10 CONCLUSION 98

CHAPTER 5

DESIGN OF TEST RIG 103
5.1 INTRODUCTION 103
5.2 REVIEW OF UCL OPTICAL ENGINE WORK 103
5.3 SPECIFICATION 107
5.4 DESIGN PHILOSOPHY 107
5.5 DESIGN CHALLENGES 108
5.6 MATERIAL SELECTION 109
5.6.1 Introduction 109
5.6.2 Critical joints 109
5.6.3 Precautions 110
5.6.4 Materials selected: connecting rod 110
5.6.5 Materials selected: piston 110
5.6.6 Materials selected: block 110
5.6.7 Materials selected: windows 111
5.6.8 Materials selected: mirror 111
5.6.9 Materials selected: PEEK (Poly ether ether ketone) 111
5.7 MODIFICATIONS TO LISTER ENGINE 112
5.8 CONNECTING ROD DESIGN 113
5.9 PISTON DESIGN 115
5.10 DESIGN OF CYLINDER BLOCK 119
5.11 DESIGN OF OPTICAL BLOCK 121
5.12 DESIGN TASKS ON THE CYLINDER HEAD 122
5.13 FUEL, OIL AND WATER SYSTEMS 124
5.14 SUMMARY 125

CHAPTER 6

TEST BED, INSTRUMENTATION, COMMISSIONING AND BENCHMARK TESTS 128
6.1 INTRODUCTION 128
6.2 TEST BED 128

6.3 INSTRUMENTATION 132
6.4 BENCHMARK TESTS 134
6.5 DATA ANALYSIS 135
6.6 DISCUSSION OF BENCHMARK TEST RESULTS. 136
6.7 SUMMARY 138

CHAPTER 7

A MIE STUDY 140
7.1 INTRODUCTION 140
7.2 AIMS AND SCOPE OF TESTING 140
7.3 EQUIPMENT 141
7.3.1 Laser 141
7.3.2 Elements on optics rail 142
7.3.3 Camera 143
7.4 METHOD OF IMAGE CAPTURE 143
7.5 CONVERSION OF METAL ENGINE TO OPTICAL MODE 143
7.6 CONTROL OF ENGINE AND INSTRUMENTATION 146
7.6.1 Laser 147
7.6.2 Computer 147
7.6.3 Camera Gating 148
7.6.4 Injector 148
7.7 EXPERIMENTAL METHODS 149
7.8 MIE TESTS 150
7.9 RESULTS 150
7.10 DISCUSSION 158
7.10.1 Introduction 158
7.10.2 Observations 158
7.10.3 Features 165
7.10.4 Comparisons 168
7.11 CONCLUSIONS 169

CHAPTER 8

A LIF STUDY AND FURTHER ANALYSES 172
8.1 INTRODUCTION 172
8.2 AIMS 172
8.3 THEORY: SPRAYS IN G-DI ENGINES 172
8.4 LIF STUDY 173
8.4.1 Selection of dopant and base fuel 173
8.4.2 Laser 175
8.4.3 Optical elements 175
8.4.4 Camera 177
8.4.5 Filters 177
8.4.6 Control of equipment 178
8.4.7 Method of image capture 178

8.4.8 Post-processing 181
8.4.9 Refining the LIF procedure 186
8.4.10 Finalised procedure 189
8.4.11 LIF tests 189
8.4.12 Results 191
8.4.13 Discussion of LIF results 203
8.5 INTENSITY ANALYSIS 226
8.5.1 Theory 226
8.5.2 Analysis of mean intensities for Mie scattered images 227
8.5.3 Discussion of maxima 227
8.5.4 Discussion of kink 229
8.5.5 Discussion of recovery after maximum 230
8.5.6 Analysis of mean intensities for the ambient air images 230
8.5.7 Analysis of mean intensities for LIF images 231
8.6 VELOCITY ANALYSIS 232
8.6.1 Method 233
8.6.2 Discussion of piston velocity results 233
8.6.3 Discussion of fuel velocity results 233
8.6.4 Discussion of air velocity results 235
8.7 LIF IMAGES POST-PROCESSED USING A NOVEL SUBTRACTION METHOD 238
8.7.1 Method 238
8.7.2 Results 239
8.7.3 Discussion 239
8.8 CONCLUSIONS 244

CHAPTER 9

SUMMARY AND CONCLUSIONS, CLAIMS OF ORIGINALITY, RECOMMENDATIONS FOR FUTURE WORK 247
9.1 INTRODUCTION 247
9.2 SUMMARY AND CONCLUSIONS 247
9.3 CLAIMS OF ORIGINALITY 250
9.4 RECOMMENDATIONS FOR FUTURE WORK 251

APPENDIX A – Equipment lists and calibration 254

APPENDIX B – Engine commissioining 259

APPENDIX C – Ambient air injection images 261

APPENDIX D – Optical correction 275

APPENDIX E – Current and future European emissions standards 282

REFERENCES 283

LIST OF FIGURES

CHAPTER 1

Figure 1-1 The success of the car [The Economist, 2000c] 20

Figure 1-2 Real change in the cost of transport [The Economist, 2000d] 22

Figure 1-3 Estimated and predicted growth of world population [United Nations, 2001] 24

CHAPTER 2

Figure 2-1 European passenger car petrol engine exhaust emissions standards, 1971-2005, UHC and NO_x maximum limits [Richardson, 1997] 28

Figure 2-2 Detail from Figure 2-1 28

Figure 2-3 Typical conversion efficiencies at different temperatures for thermal oxidation of UHC and CO [Milton, 1998] 37

Figure 2-4 Typical conversion efficiencies at different temperatures for catalytic oxidation of UHC and CO [Milton, 1998] 37

Figure 2-5 Window for three-way operation of catalytic converter [Milton, 1998] ... 39

Figure 2-6 NO_x conversion efficiency for diesel catalyst with 2:2 molar UHC/NO_x ratio by fuel addition ahead of catalyst [Charlton, 1998] 41

Figure 2-7 Valve lift characteristics with cam phasing [Lumley, 1999] 44

Figure 2-8 Predicted NO_X emissions versus engine load for typical HCCI and DI diesel combustion [Stanglmaier and Roberts 1999] 47

Figure 2-9 The operation of a hydrogen-oxygen fuel cell [Cengel and Boles, 1994]. 53

Figure 2-10 Toyota fuel cell stack [Garrett et al., 2001] 54

Figure 2-11 Schematic diagram of rhombic-drive, beta-type, Stirling engine [Urieli et al., 1884] 56

Figure 2-12 Brayton cycle, applicable to gas turbines [Cengel and Boles, 1994] 58

Figure 2-13 Hybrid drive taxi [Fenton, 1998] 58

CHAPTER 3

Figure 3-1 Basic internals of multi-hole (left) and pressure swirl (right) injectors [Pruessner et al., 1998] 62

Figure 3-2 Air entrainment during second stage of atomisation [Van der Wege and Hochgreb, 2000a] 64

Figure 3-3 Limit of penetration distance as fuel pressure is increased [Pruessner et al., 1998] 66

Figure 3-4 Variation in developed spray cone angle for pre-production injector, ref A [Williams et al., 2001] 68

Figure 3-5 Variation in developed spray cone angle for pre-production injector, ref B [Williams et al., 2001] 68

Figure 3-6 Slit nozzle injector [Takeda et al., 2000] 70

Figure 3-7 Mixing strategies for stratified charge mode, squish (left), swirl (centre) and tumble (right) [Guerrier, 1999] 74

Figure 3-8 Direct injection combustion systems [Cathcart and Xavier, 2000] 75

CHAPTER 4

Figure 4-1 Schematic energy level diagram showing Rayleigh scattering, vibrational Raman scattering and LIF [Zhao and Ladommatos, 2001] 83
Figure 4-2 Optical engine with setups for simultaneous measurements of 2-d LIF (items marked *) and 1-d Raman spectroscopy [Ipp et al., 2001] 83
Figure 4-3 Coaxial LIF system for fuel liquid visualization [Kakuhou et al., 1999] .. 84
Figure 4-4 Injection rig to measure instantaneous flow rates in high pressure pipeline of G-DI engine [Ismailov, 1973] 85
Figure 4-5 Two CCD cameras recording PIV data from injector in pressurised chamber [Kubo et al., 2001] 86
Figure 4-6 Experimental setup for Fraunhofer diffraction technique [Zhao and Ladommatos, 2001] 88
Figure 4-7 Schematic for PDA tests [Williams et al, 2001] 88
Figure 4-8 Experimental setup for 2-d Mie scattering experiment [Ipp et al., 1999] . 90
Figure 4-9 Schematic of setup for linear LIF (with exciplex tracer) using a pressure chamber [Befrui et al., 2002] 90
Figure 4-10 LEA imaging system [Suzuki et al., 1993] 92
Figure 4-11 High-speed rotating drum camera [Zhao and Ladommatos, 2001] 93
Figure 4-12 High-speed rotating prism camera [Zhao and Ladommatos, 2001] 93
Figure 4-13 Experimental configuration for back-lighting method [Georjon et al., 2000] 95
Figure 4-14 Experimental configuration for schlieren method [Georjon et al., 2000] 95
Figure 4-15 Head gasket consisting of instrumented probes on a printed circuit board [Zhao and Ladommatos, 2001] 97
Figure 4-16 Spark plug probe containing seven optical fibres [Witze et al., 1988] 98
Figure 4-17 Optical device main body (left) and components (right) [Shepheard et al., 2002] 99

CHAPTER 5

Figure 5-1 Optical path into the combustion chamber [Queenan, 1998] 105
Figure 5-2 Schematic diagram of flood illumination applied to optical engine [Davy, 2000] 106
Figure 5-3 Schematic of Jaguar 4-valve pent roof G-DI cylinder head 108
Figure 5-4 Principal parts of UCL/Jaguar optical engine 109
Figure 5-5 CADD model showing modifications to Lister crankshaft 113
Figure 5-6 CADD model of special connecting rod 114
Figure 5-7 Modules used to form piston 116
Figure 5-8 CADD model of the "disc" crown 116
Figure 5-9 CADD model of the optical piston, main body 118
Figure 5-10 CADD model of left hand/right hand connector 118
Figure 5-11 Details of cylinder block 120
Figure 5-12 Details of optical block 122
Figure 5-13 Section through Jaguar/UCL optical engine showing path of laser light into combustion chamber 126

CHAPTER 6

Figure 6-1 Plan showing positions of main items on test bed 129
Figure 6-2 Underside of Jaguar head showing swirl valve location 131
Figure 6-3 Section through intake port illustrating orientation of swirl control valve 131
Figure 6-4 Engine control circuit used for benchmark tests 132
Figure 6-5 Location of instrumentation on optical engine, shown in side elevation 133
Figure 6-6 Valve opening times, where 720 CAD is TDC firing 136

CHAPTER 7

Figure 7-1 Layout of main equipment used for Mie study 142
Figure 7-2 Layout of optical elements used to create light sheet in the optical engine cross-bore. 143
Figure 7-3 Relationship of light sheet to mirror, piston and injector 145
Figure 7-4 Equipment for control of instrumentation 147
Figure 7-5 Timing of events using SRSs (Stanford Research Systems signal generators) 148
Figure 7-6 Thumbnails of Mie scattering images in firing engine, SOI 639, 654 and 675 CAD, alongside ambient air images. 151
Figure 7-7 Mie scattering images in firing engine, SOI 639 CAD. 152
Figure 7-8 Mie scattering images in firing engine, SOI 654 CAD. 153
Figure 7-9 Mie scattering images in firing engine, SOI 675 CAD. 154
Figure 7-10 Mie scattering images in firing engine, delta 05, 06, 07, 08 and 09 CAD 155
Figure 7-11 Mie scattering images in firing engine, delta 10, 11, 15, 20 and 25 CAD. 156
Figure 7-12 Mie scattering images in firing engine, delta 30, 45 and 63 CAD. 157
Figure 7-13 Layout of quartz windows and camera 159
Figure 7-14 Field of view superimposed on combustion chamber 159
Figure 7-15 Establishing shots of scales in combustion chamber illustrate distortion caused by quartz. Left image taken through main window. 160
Figure 7-16 Schematic showing typical form of spray cone from pressure swirl injector. Letters A to D refer to cases in Figure 7–17 161
Figure 7-17 Intensity of reflected light according to position in spray cone 161
Figure 7-18 Images and pressure traces from repeated runs to investigate cyclic variability 163
Figure 7-19 Cycle to cycle variation of penetration distance, during firing 164
Figure 7-20 Cycle to cycle variation of peak pressure during firing 165
Figure 7-21 Typical pre-spray and main spray 166
Figure 7-22 Fresh air images, delta 30 CAD, intensity more uniform in absence of quartz piston crown 167
Figure 7-23 Normalised intensities for band across delta 30 CAD images 168
Figure 7-24 Layout of camera and engine to show offset between axes 168

CHAPTER 8

Figure 8-1 Measured values of the biacetyl absorption cross-section [Lozano, 1992 176
Figure 8-2 Biacetyl fluorescence emission spectrum. Ordinates in arbitrary units [Lozano, 1992] 176
Figure 8-3 Percentage transmittance of UG-5 bandpass filter [Comar Instruments, 2004] 178
Figure 8-4 Percentage transmittance of gelatine filter Wratten number 2E [Comar Instruments, 2004] 179
Figure 8-5 Plan showing main elements used to introduce 355 nm laser light into optical engine. 179
Figure 8-6 Light sheet correction image (corresponding to SOI 543 CAD) showing influence of quartz slot in piston crown on transmitted light. 184
Figure 8-7 Flowchart showing use of Matlab programs for post-processing LIF images 187
Figure 8-8 Timing of camera gating used to maximise the amount of fluorescence captured by camera 188
Figure 8-9 Thumbnails of LIF tests I, III, V, for SOI 639, 654 and 675 CAD 193
Figure 8-10 Post processed images for LIF test I, SOI 639 CAD 194
Figure 8-11 Post-processed images for LIF test I, SOI 654 CAD 195
Figure 8-12 Post-processed images for LIF test I, SOI 675 CAD 196
Figure 8-13 Post-processed images for LIF test III, SOI 639 CAD 197
Figure 8-14 Post-processed images for LIF test III, SOI 654 CAD 198
Figure 8-15 Post-processed images for LIF test III, SOI 675 CAD 199
Figure 8-16 Post-processed images for LIF test V, SOI 639 CAD 200
Figure 8-17 Post-processed images for LIF test V, SOI 654 CAD 201
Figure 8-18 Post-processed images for LIF test V, SOI 675 CAD 202
Figure 8-19 Mean intensity for a band of pixels across the sheet correction images, using the disc crown and the slot crown 204
Figure 8-20 Dark region caused by quartz refracting the light sheet 204
Figure 8-21 Grouped results, LIF, Mie, ambient air, for SOI 639 CAD, TFA (A) .. 205
Figure 8-22 Grouped results, LIF, Mie, ambient air, for SOI 639 CAD, TFA (B) ... 206
Figure 8-23 Grouped results, LIF, Mie, ambient air, for SOI 639 CAD, TFA (C) ... 207
Figure 8-24 Grouped results, LIF, Mie, ambient air, for SOI 639 CAD, TFA (D) .. 208
Figure 8-25 Grouped results, LIF, Mie, ambient air, for SOI 639 CAD, TFA (E) ... 209
Figure 8-26 Grouped results, LIF, Mie, ambient air, for SOI 639 CAD, TFA (F) ... 210
Figure 8-27 Grouped results, LIF, Mie, ambient air, for SOI 639 CAD, TFA (G) .. 211
Figure 8-28 Grouped results, LIF, Mie, ambient air, for SOI 654 CAD, TFA (A) .. 212
Figure 8-29 Grouped results, LIF, Mie, ambient air, for SOI 654 CAD, TFA (B) ... 213
Figure 8-30 Grouped results, LIF, Mie, ambient air, for SOI 654 CAD, TFA (C) ... 214
Figure 8-31 Grouped results, LIF, Mie, ambient air, for SOI 654 CAD, TFA (D) .. 215
Figure 8-32 Grouped results, LIF, Mie, ambient air, for SOI 654 CAD, TFA (E) ... 216
Figure 8-33 Grouped results, LIF, Mie, ambient air, for SOI 654 CAD, TFA (F) ... 217
Figure 8-34 Grouped results, LIF, Mie, ambient air, for SOI 654 CAD, TFA (G) .. 218

Figure 8-35 Grouped results, LIF, Mie, ambient air, for SOI 675 CAD, TFA (A) ..219
Figure 8-36 Grouped results, LIF, Mie, ambient air, for SOI 675 CAD, TFA (B)...220
Figure 8-37 Grouped results, LIF, Mie, ambient air, for SOI 675 CAD, TFA (C)...221
Figure 8-38 Grouped results, LIF, Mie, ambient air, for SOI 675 CAD, TFA (D) ..222
Figure 8-39 Grouped results, LIF, Mie, ambient air, for SOI 675 CAD, TFA (E)...223
Figure 8-40 Grouped results, LIF, Mie, ambient air, for SOI 675 CAD, TFA (F)...224
Figure 8-41 Grouped results, LIF, Mie, ambient air, for SOI 675 CAD, TFA (G) ..225
Figure 8-42 Mean intensity of Mie images plotted against time after SOI.....228
Figure 8-43 Proposed mechanism for mean intensity to rise after EOI.....229
Figure 8-44 Mean intensity of ambient air images plotted against time after SOI...231
Figure 8-45 Mean intensity of LIF images plotted against time after SOI.....232
Figure 8-46 Calculated velocity of piston for one crankshaft revolution (1500 rev/min).....234
Figure 8-47 Velocity of pre-spray, Mie and ambient air images.....234
Figure 8-48 Velocity of main spray, Mie and ambient air images.....234
Figure 8-49 Elevations of fuel spray (red dots) and CFD predictions (arrows) of air flow (cm/sec) versus crank angle [Chen, 2005].....236
Figure 8-50 Plan view on fuel spray predictions versus CAD [Chen, 2005].....236
Figure 8-51 LIF "subtraction" images, SOI 639 delta 6-5 to 11-10 CAD.....240
Figure 8-52 LIF "subtraction" images, SOI 639 delta 15-11 to 53-45 CAD.....241
Figure 8-53 LIF "subtraction" images, SOI 654 delta 6-5 to 11-10 CAD.....242
Figure 8-54 LIF "subtraction" images, SOI 654 delta 15-11 to 53-45 CAD.....243

APPENDIX A

Figure A-1 Calibration graph for UEGO air fuel ratio sensor.....255
Figure A-2 Calibration graph for Ford hot wire anemometer.....255
Figure A-3 Arrangement of equipment for injector calibration.....256
Figure A-4 Calibration of Bosch inwardly opening pressure swirl injector.....257

APPENDIX C

Figure C-1 Ambient air images, delta 05 CAD.....262
Figure C-2 Ambient air images, delta 06 CAD.....263
Figure C-3 Ambient air images, delta 07 CAD.....264
Figure C-4 Ambient air images, delta 08 CAD.....265
Figure C-5 Ambient air images, delta 09 CAD.....266
Figure C-6 Ambient air images, delta 10 CAD.....267
Figure C-7 Ambient air images, delta 11 CAD.....268
Figure C-8 Ambient air images, delta 15 CAD.....269
Figure C-9 Ambient air images, delta 20 CAD.....270
Figure C-10 Ambient air images, delta 25 CAD.....271
Figure C-11 Ambient air images, delta 30 CAD.....272
Figure C-12 Ambient air images, delta 45 CAD.....273
Figure C-13 Ambient air images, delta 63 CAD.....274

APPENDIX D

Figure D-1 Set up of optical elements 276
Figure D-2 Plan on optical system using OSLO software, fan of light rays..... 278
Figure D-3 Plan on optical system using OSLO software, parallel rays of light..... 278
Figure D-4 Relationship between area of interest and pixels in vertical case..... 279
Figure D-5 Relationship between area of interest and pixels in horizontal case 279
Figure D-6 Plan on elements illustrating correction factors for horizontal intervals on IPP images..... 281

LIST OF TABLES

CHAPTER 2

Table 2-1 Passenger vehicle emissions standards (including particulate matter, PM), EU [European Parliament, 2003] 29

Table 2-2 Passenger vehicle emissions standards, Japan [Japanese Ministry of the Environment, 2003] 29

Table 2-3 Passenger vehicle emissions standards, USA [United States Environmental Protection Agency, 2003] 29

CHAPTER 6

Table 6-1 Specification of Jaguar cylinder head 130

Table 6-2 Results of Jaguar (denoted "Jag" or "Jg") and UCL benchmark tests) 137

CHAPTER 8

Table 8-1 Conditions used for studies using LIF technique 190

APPENDIX A

Table A-1 Hardware used in tests 254

APPENDIX D

Table D-1 Conversion factors for horizontal intervals on IPP images 281

APPENDIX E

Table E-1 Passenger vehicle emissions standards, Euro 4 [European Parliament, 2007] 282

Table E-2 Passenger vehicle emissions standards, Euro 5 [European Parliament, 2007] 282

NOMENCLATURE

Acronym	Definition
AAA	air assisted atomiser
AAFV	air-assisted fuel vaporiser
AFR	air fuel ratio
AOI	area of interest
ATDC	after top dead centre
BMEP	brake mean effective pressure
BTDC	before top dead centre
CAD	crank angle degrees
CADD	computer-aided drawing and design
CCD	charge coupled device
CFD	computational fluid dynamics
CI	compression ignition
CNC	computer numerically controlled
CNG	compressed natural gas
CRO	cathode ray oscilloscope
DI	direct injection
DOC	diesel oxidation catalyst
DOHC	dual overhead camshaft
EGR	exhaust gas recirculation
EOI	end of injection
f	aperture
FL	full
G-DI	gasoline direct injection
h	Planck's constant
HC	homogeneous charge
HCCI	homogeneous charge compression ignition
HSDI	high-speed direct injection
HWA	hot wire anemometer
IC	internal combustion
IDI	indirect injection
Ii	individual intensity
Im	maximum intensity
IPP	Image Pro Plus
IMEP	indicated mean effective pressure
IVC	inlet valve closing
jpeg	joint photographic experts group
LDA	laser Doppler anemometry
LEA	laser extinction/absorption
LH/RH	left hand/right hand
LIEF	laser induced exciplex fluorescence
LIF	laser induced fluorescence
LNG	liquified natural gas
LPG	liquified petroleum gas
LRS	laser Rayleigh scattering
MIP	multi-ionisation probe
MOF	multiple optical fibre
MOP	mid opening point
MPFI	multi-point fuel injection
NO	nitric oxide
NO_x	oxides of nitrogen
NR	near

OPEC	Oil Producing and Exporting Countries
P0	disc crown
P1	slotted crown
PC	personal computer
PCV	positive crankcase ventilation
PDA	phase Doppler anemometry
PEEK	poly ether ether ketone
PEM	proton exchange membrane
PFI	port fuel injected
PIV	particle image velocimetry
PLIEF	planar laser induced exciplex fluorescence
PM	particulate matter
ppm	parts per million
PPT	phosphorescent particle tracking
PTFE	poly tetra fluoro ethylene
PTV	particle tracking velocimetry
RTV	room temperature vulcanising
SC	stratified charge
SCV	swirl control valve
SI	spark ignition
SOF	soluble organic fraction
s/n	serial number
SOI	start of injection
SRs	spontaneous Raman scattering
SRS	Stanford Research Systems
T40	40 degrees Celsius
T80	80 degrees Celsius
TDC	top dead centre
TFA	time from arrival (of fuel)
TIFF	tagged image file format
TTL	transistor transistor logic
TWC	three-way catalyst
UEGO	unheated exhaust gas oxygen (sensor)
UHC	unburnt hydrocarbons
ULEV	ultra low emissions vehicle
UV	ultra violet
VCM	variable charge motion
VVA	variable valve actuation
VVT	variable valve timing
WWMP	world wide mapping point
ΔE	energy change between different states
λ	inverse of equivalence ratio
υ	frequency of radiation
ϕ	equivalence ratio

Chapter 1

The present and future of the automobile

1.1 Introduction

The majority of internal combustion engines produced are used to power automobiles. Gasoline Direct Injection (G-DI) engines are a relatively recent development and are the subject of research worldwide since they promise reduced exhaust emissions and improved fuel economy for automobiles. This literature survey begins by looking at the current state of the automobile and making some predictions as to its future.

1.2 Facts and figures: the present state of the automobile

According to Stiglitz [1997]: "Of all the inventions that have shaped the world during the past century, perhaps none has had so profound an effect as the automobile". Statistics for 1998-99 show that 24 million cars were registered in the UK and 72% of UK households had use of a car [National Statistics, 2001a]. Figure 1-1 illustrates the dominance of the car. In 1999, 93% of the 728 billion total passenger kilometres travelled were by road [Department of the Environment, Transport and the Regions, 2001a]. The UK motor industry contributes 5.5% of Gross Domestic Product by turning over £40 billion; approximately 330,000 people work in vehicle and component production and manufacturing activities; taxes paid by the motor industry and the road transport industry make up about 11% of the UK Government's entire revenue from taxation [The Society of Motor Manufacturers and Traders Ltd., 2001].

1.3 Overview of the global automobile industry

Over-capacity exists in some areas of the industry, but there are also many areas of growth. According to The Economist [2000a], automobile companies require more than 80% utilisation of worldwide plants to make money. This figure was achieved in 1990, but in 2000 it stood at 68%. Consolidation is the most effective means of reducing over-capacity. An article in The Economist [1999a] claimed that "the car industry is in a fever of consolidation". Both the new and former chief executives of Ford Motor Company have stated that

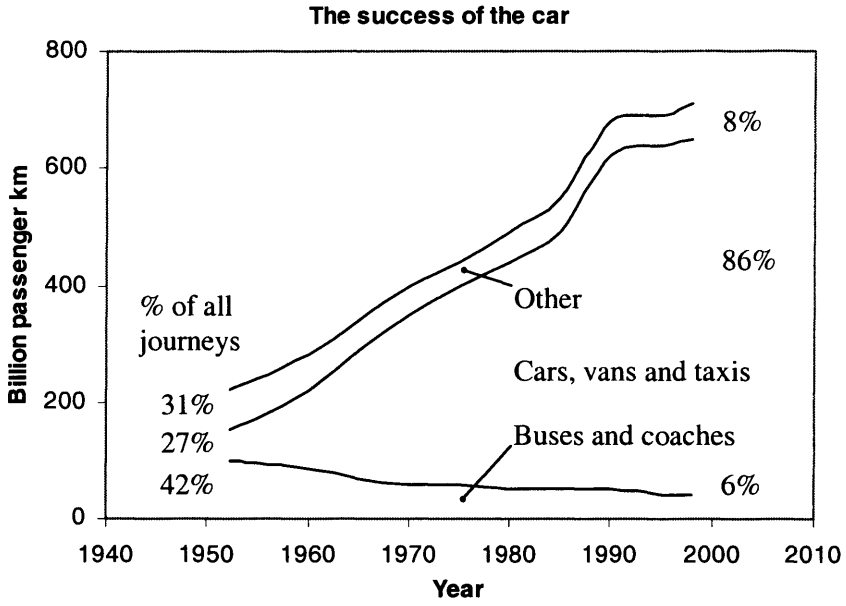

Figure 1-1 The success of the car [The Economist, 2000c]

"there would soon be only six makers of volume cars in the world: two in America, two in Europe and two in Japan" [The Economist, 1999a].

Although growth was expected to taper off in Europe and North America in 2000 [Financial Times, 2000a], a dramatic rise in car- and house-ownership was evident across the ex-communist world [The Economist, 1999b]. After the Asian financial crisis in 1998, resulting in a contraction of the market by 30%, growth of 20% was achieved in 1999, and industry analysts were predicting growth of 8-10% in 2000, [Financial Times, 2000a]. Moreover, despite being heavily populated, India and China have only modest car-use [Financial Times, 2000a], so the growth potential for this part of the world is huge. To take advantage of this obvious potential, alliances such as Daimler-Chrysler with Mitsubishi, General Motors with Suzuki, and Renault with Samsung have taken place. Other manufacturers, such as Volkswagen, are producing VW and Audi models in local plants.

1.4 Factors reducing automobile use

There are factors in the UK likely to reduce automobile use and these could be considered as indicators of the future global situation. The number of people receiving a state pension is increasing while the population as a whole remains

fairly constant [National Statistics, 2001a]. This suggests a reduction in the number of people of working age. The vast majority of car journeys are for commuting to work, so as the average age of the population rises, car use reduces. In many urban areas, travel by car has become inconvenient and average journey times have increased. For example, congestion and absence of parking spaces may prompt many to switch to alternative forms of transport. In both rural and urban areas, a belief that using other forms of transport does less harm to the environment may also reduce car use. Some may cycle or walk to improve personal health, particularly if the journey is short. Radical changes in lifestyle and town planning are foreseen by many [Financial Times, 1998]. They predict mixed use of buildings (for work and living) which will minimise the need for travel within cities. This is difficult to achieve for existing cities, though.

1.5 Unpredictable factors

Some factors will have an unpredictable effect on the amount people use their cars. Emissions regulations and traffic congestion are putting governments under pressure to reduce car use, therefore governments' transport policies typically provide disincentives to use cars and incentives to use other forms of transport.

It is possible to levy taxes on fuel, parking spaces, road use and the price of cars themselves. However, in the case of company cars (with 80% of new cars being sold to company car fleets) [The Economist, 1998], the companies involved seem willing to meet larger bills for fuel and cars. Fuel price rises also seem to have little effect on car use. The Organisation of Petroleum Exporting Countries (OPEC) often adjusts production of oil to bolster profits. Although The Economist [2000b, 2000e] argues that it is dangerous to ignore this on a national level, individuals seem prepared to pay more and more to continue filling their car with fuel. Moves to tax company car parks and charge road tolls meet with the same response [Financial Times, 1999c]. Even though the rise in petrol and car taxes exceeded the rate of inflation in 1998 [Financial Times, 1999b], the number of private car users seems unaffected. Figure 1-2 shows the real change in the cost of transport, which helps explain

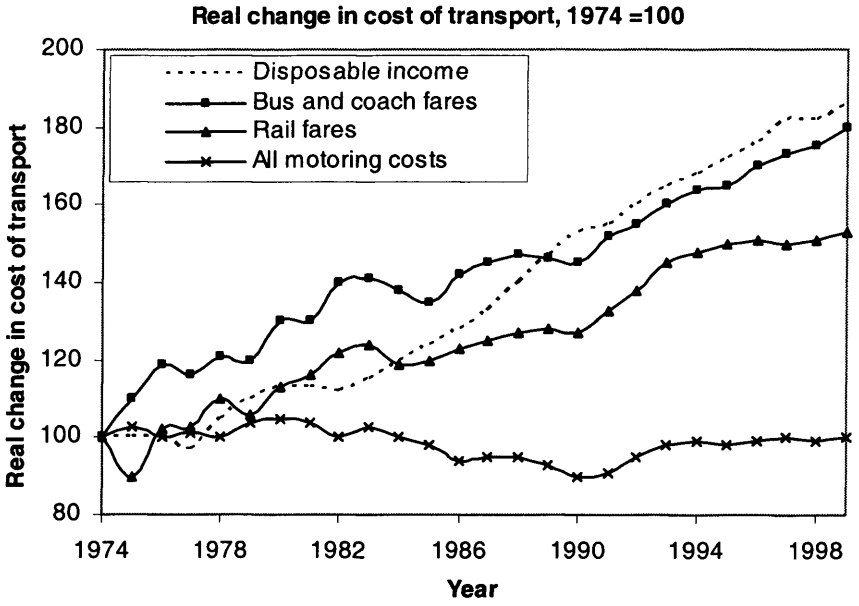

Figure 1-2 Real change in the cost of transport [The Economist, 2000d]

why many would still prefer to travel by car. Arguments used against public transport are that it is expensive and lacks efficiency. Improvements to the public transport system could be funded by tax revenues from the above sources and an efficient system could then be available for commuters. However, the indications are that the preference of many would be to continue using their car, even if part of the improvement to the public transport system added to road congestion (by establishing bus lanes, for example).

The European Union has agreed a draft directive, 2000/53/EC, to apply recycling laws to automobiles, with expired vehicles returned to their manufacturer instead of scrapping [Financial Times, 1999d]. Other than increasing the selling price, it is difficult to forecast how this will affect car use. Even in Germany, where the environmental Green Party is represented in Government, car sharing seems to be unpopular [Financial Times, 1999a] and may even increase congestion [Financial Times, 1999f]. Voluntary car free days take place in many cities, but in some, this has actually increased the numbers of car journeys on those days [Financial Times, 2000b].

Parents driving their children to school cause localised congestion. They are unlikely to be persuaded to do otherwise since they act for reasons of safety. On the other hand, it might be thought that fear of accidents may lead commuters to stop using their cars. Figures from the Department of the Environment, Transport and the Regions [2001b] though, show that the numbers of car drivers and passengers killed fell each year from 1989 to 1999. Moves to introduce safer cycle lanes, separated by kerbs from vehicle traffic, may overcome the fear of many to travel by bicycle. The risk of car theft may dissuade some from owning a car, but this may be balanced by those who travel by car out of fear of personal attack and street crime.

The World Wide Web allows cars to be bought more easily, enables the buyer to obtain a competitive price and thus leads to higher volumes of sales. On the other hand, the Web makes working from home easier, reducing the amount of commuting to work. Shopping via the Web also produces contradictory effects: goods are ordered without needing to leave home, but more journeys are required to deliver the items. The balance between hours worked and leisure hours is changing [National Statistics, 2001b]. Since people still travel to work and leisure activities often involve travel, this factor is also hard to predict.

1.6 Factors increasing automobile use

The population of the world continues to rise, Figure 1-3. Africa, South America and Asia account for most of the increase. The standard of living in these areas is rising too, which is promoting more car ownership. As an example, the Malaysian economy has grown by roughly 8% each year between 1987 and 1997, the figure for Indonesia is similar and the economic growth in Thailand reached double figures between 1988 and 1990. Given that their populations are 20 million (Malaysia), 60 million (Thailand) and 200 million (Indonesia), the regional head for General Motors in the United States was justified in saying: "It is clear the future growth potential in the world auto industry is going to be in the Asia-Pacific region" [Financial Times,

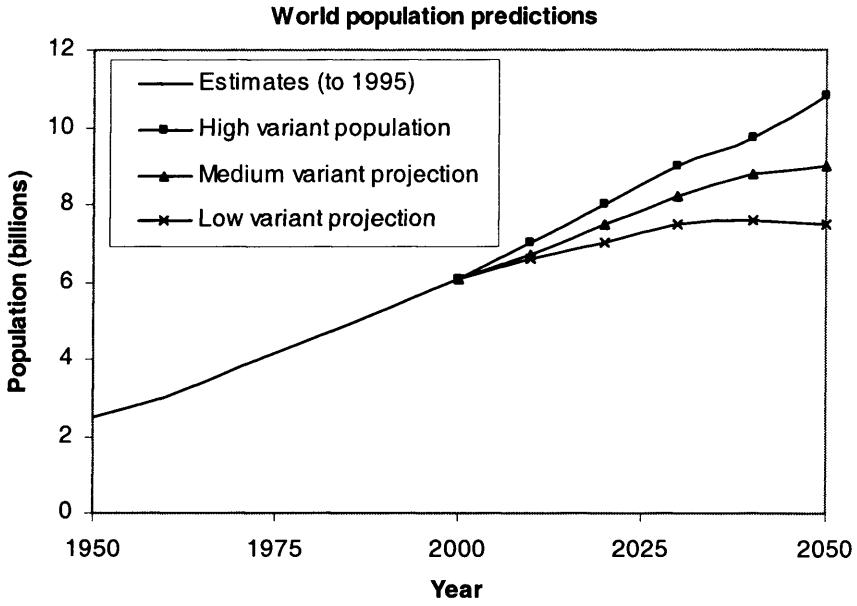

Figure 1-3 Estimated and predicted growth of world population [United Nations, 2001]

1997]. At a more local level, the demographics of the UK are changing, with an increasing number of people moving to the cities or to within commuting distance of the cities. It is planned to build almost a million new homes in the South East region to accommodate this influx. It is unlikely that a corresponding number of jobs will be available locally, hence resulting in many more passenger kilometres of car journeys.

The European Parliament implemented regulation 1400/2002 in 2002 to remove disparities in car prices in the European Union [Financial Times, 1999d]. This measure is likely to make cars more affordable in the UK. The strength of sterling, especially on conversion to euros, inflates UK car prices [Financial Times, 1999d]. It seems likely that acceptance of the unified monetary system in the UK would therefore reduce car prices and increase their usage.

1.7 Summary

The greatest change in car use will be in the developing world, where more and more people are able to afford cars. The Society of Motor Manufacturers and Traders [2001] expects the UK car parc (number of cars on the road) to

reach 31 - 32 million by 2020. If car use remains unchanged or even reduces in the developed world, a huge market will still exist to replace vehicles as they wear out.

The arguments presented have shown that the automobile will continue to be a significant means of transport, throughout the world. In Chapter 2, the most likely power sources for future automobiles will be considered.

Chapter 2

Future automotive prime movers

2.1 Introduction

It was established in Chapter 1 that the automobile will continue to be a significant means of transport throughout the world. In Chapter 2, the prime movers that are most likely to power these cars will be identified. It is beneficial for prime movers to be cheap, lightweight, require low maintenance and offer high performance. Importance is attached to ease of re-cycling at end of use and it is essential for them to be safe and reliable, but increasing emphasis is placed on the economical use of fuel and limiting exhaust emissions to manageable levels. Since internal combustion (IC) engines are the dominant automobile prime mover and vehicle emissions legislation is specifically applicable to them, the first part of Chapter 2 deals with emissions. A survey of possible future prime movers concludes the chapter, beginning with IC engines, then alternatives to IC engines and finally hybrid drives.

2.2 Emissions

This section considers IC engine emissions, current legislation, the importance of stoichiometry and air fuel ratio (AFR), the formation mechanisms of legislated emission species and finally control of emissions.

2.2.1 Background

Dense smog, which irritated lungs and eyes, became common in California, USA, from the 1940s. In 1952 Hagen-Smit (California Institute of Technology) demonstrated the culpability of cars by re-creating the smog in the laboratory using automobile exhaust in the presence of sunlight [Borman and Ragland, 1998]. In 1968, public demand led to federal emission controls being introduced for vehicles produced from 1972. The first European directive was implemented in 1970 [Owen and Coley, 1995]. Since then, emission controls have become increasingly stringent (see Figure 2-1 and Figure 2-2).

2.2.2 Legislation

The species of emissions produced by an IC engine include oxides of nitrogen

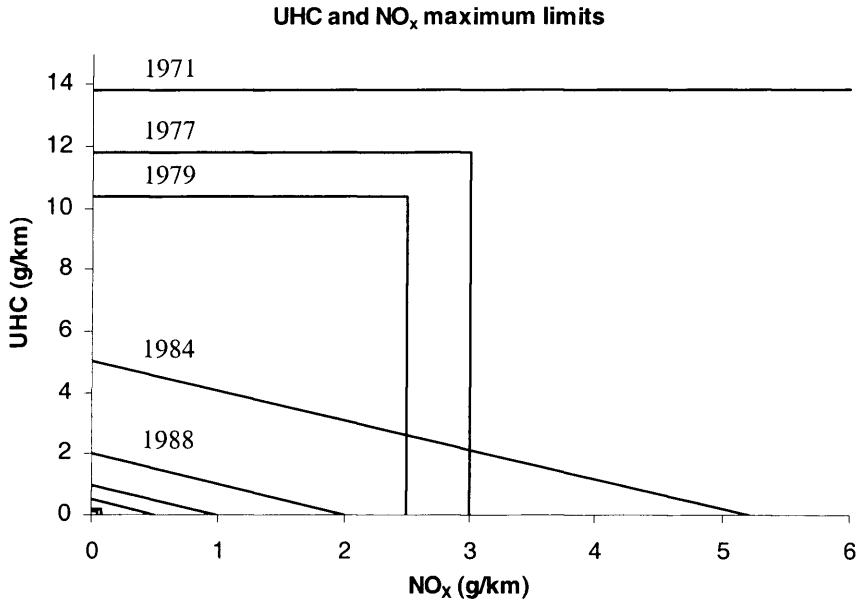

Figure 2-1 European passenger car petrol engine exhaust emissions standards, 1971-2005, UHC and NO_x maximum limits [Richardson, 1997]

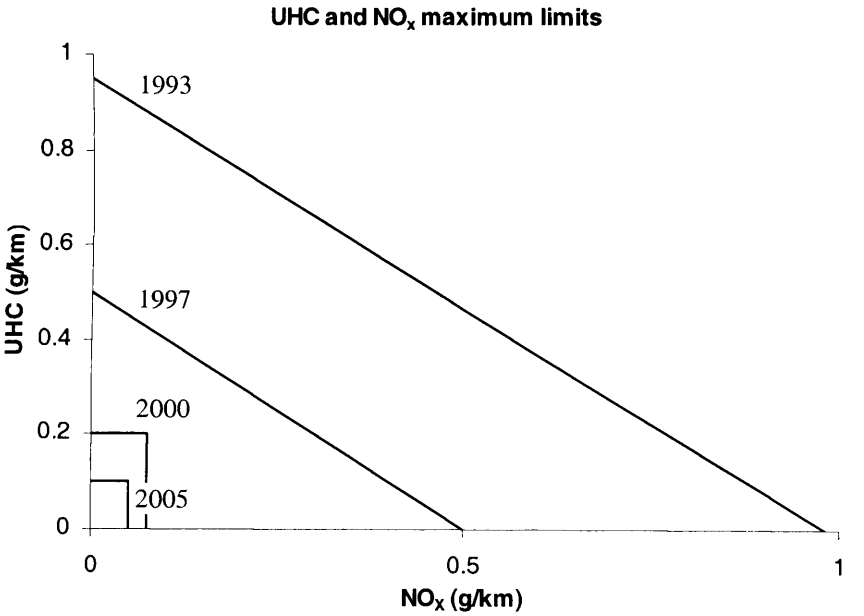

Figure 2-2 Detail from Figure 2-1

(under the generic label NO_X), unburnt hydrocarbons (UHC), carbon monoxide (CO), carbon dioxide (CO_2), polyaromatics, soots, aldehydes and nitro-olefins. Some of these are produced in as little as tens of parts per million (ppm), but exhaust gas typically contains 12% by volume of CO_2 [Degler, 1938] and it contributes to climate change while NO_X, UHC and CO

are known to be significant pollutants [Garrett et al., 2001]. Although the remaining emissions are currently believed to be insignificant polluters, Garrett points out that this may not always be the case. The major trading blocks, the EU, Japan and the USA each have their own emissions regulations, which are either adopted directly by other countries or form the basis of their legislation. The regulations change often, but a typical set of values, up to date at the time of writing, is presented in tables 2-1 to 2-3.

	Test: Euro 3, 2000.01	
	Diesel engine (g/km)	Gasoline engine (g/km)
CO	0.64	2.30
UHC	-	0.20
UHC+NO_x	0.56	-
NO_x	0.50	0.15
PM	0.05	-

Table 2-1 Passenger vehicle emissions standards (including particulate matter, PM), EU [European Parliament, 2003]

	Test:10.5 Mode			
	Diesel engine		Gasoline engine	
	Mean (g/km)	Max (g/km)	Mean (g/km)	Max (g/km)
CO	2.10	2.70	2.10	2.70
UHC	0.40	0.62	0.25	0.39
NO_x	0.50	0.72	0.25	0.48
PM	0.20	0.34	-	-

Table 2-2 Passenger vehicle emissions standards, Japan [Japanese Ministry of the Environment, 2003]

Test:	Federal test procedure (FTP), Tier 1		FTP, ultra-low emissions vehicle (ULEV)	
Vehicle life	50,000 miles	100,000 miles	50,000 miles	100,000 miles
	g/mile	g/mile	g/mile	g/mile
CO	3.40	4.20	1.70	2.10
UHC	0.41	-	0.41	-
NO_x	0.40	0.60	0.20	0.30
PM	0.08	0.10	0.08	0.04

Table 2-3 Passenger vehicle emissions standards, USA [United States Environmental Protection Agency, 2003]

2.2.3 Stoichiometry and air fuel ratio

The chemistry of hydrocarbon combustion must be discussed before addressing the formation of the significant pollutants. The combustion of a hydrocarbon fuel in air is a heat-releasing oxidation reaction: the hydrogen is

oxidised to water (H_2O), the carbon is oxidised to carbon dioxide (CO_2). In equation (2.1), $C_\alpha H_\beta$ denotes a typical hydrocarbon fuel. Atmospheric air is represented by the term (O_2 + $3.76N_2$) and is taken to be 21% oxygen and 79% nitrogen by volume, with the nitrogen assumed to be inert.

$$C_\alpha H_\beta + \left(\alpha + \frac{\beta}{4}\right)(O_2 + 3.76N_2) = \alpha CO_2 + \frac{\beta}{2} H_2O + 3.76\left(\alpha + \frac{\beta}{4}\right)N_2 \qquad (2.1)$$

A stoichiometric chemical reaction is one in which exactly the right quantities of reactants are present for them to turn fully into products. One mole of fuel would yield the number of moles shown of CO_2, H_2O and N_2 in equation (2.1) and this ratio of fuel to air is known as the stoichiometric ratio. It is convenient to define an equivalence ratio, ϕ, where

$$\phi = \frac{\left(\frac{Fuel}{Air}\right)_{actual}}{\left(\frac{Fuel}{Air}\right)_{stoichiometric}} \qquad (2.2)$$

such that ϕ indicates how close to stoichiometric an actual mixture is. Another useful indicator is λ, where λ is the inverse of ϕ, ie

$$\lambda = \frac{1}{\phi} = \frac{\left(\frac{Air}{Fuel}\right)_{actual}}{\left(\frac{Air}{Fuel}\right)_{stoichiometric}} \qquad (2.3)$$

Thus $\phi < 1, \lambda > 1$ for fuel-lean mixtures

$\phi = \lambda = 1$ for stoichiometric mixtures

$\phi > 1, \lambda < 1$ for fuel-rich mixtures

2.2.4 Formation of regulated emissions species

The products of an ideal reaction involving a stoichiometric mixture of air and fuel are carbon dioxide, water and nitrogen. More complicated mechanisms produce the pollutant species CO, NO_X, UHC and PM. Although CO_2 is not a

legislated species, it is known to be a greenhouse gas and thus is responsible for contributing to climate change. However, since the production of CO_2 is the natural consequence of burning hydrocarbon fuel, only the use of fuel with a lower carbon content or reduced fuel consumption will lessen the amount of CO_2 emitted [Hawley et al., 1998].

Compression ignition (CI) engines always operate on the lean side of stoichiometric, making CO emissions low enough to be unimportant [Heywood, 1998a]. For spark ignition (SI) engines, Hochgreb [1998] describes CO formation in terms of an incomplete multi-stage process. Fuel is converted to smaller, intermediate hydrocarbons, then oxidised to aldehydes and ketones. Next the ketones and aldehydes are oxidised to CO which is, in turn, oxidised to CO_2. The final oxidation to CO_2 is notably slower than the previous stages. Incomplete conversion of CO to CO_2 results in CO emissions, with fast expansion of the burned gases freezing the final oxidation reaction and a lack of oxygen when the mixture is fuel-rich being the two main causes of CO production [Hochgreb, 1998].

The combustion of hydrocarbons can lead to nitric oxide (NO) and nitrogen dioxide (NO_2) formation by two mechanisms: firstly, at high temperatures, molecular oxygen (O_2) and nitrogen (N_2) present in the combustion air can become thermally fixed, secondly, atmospheric oxygen can react with nitrogen-containing compounds in the fuel [Hawley et al., 1998]. Hence the main factors influencing production of NO_X are temperature, local oxygen concentration and residence time (amount of time in the combustion cycle spent at high temperature). The governing reactions are those defined by Zeldovich [Heywood, 1998a] :

$$O + N_2 \leftrightarrow NO + N \tag{2.4}$$

$$N + O_2 \leftrightarrow NO + O \tag{2.5}$$

$$N + OH \leftrightarrow NO + H \tag{2.6}$$

Since the breakdown of the products takes longer than their formation and the process is too rapid for equilibrium to be reached, the concentration of NO_X

exceeds that predicted by equilibrium thermodynamics. Although NO_2 can be present in substantial amounts in CI engines, this is not the case for SI engines and for these only NO is of relevance [Hochgreb, 1998].

Heywood [1998a] identifies several sources of hydrocarbon emissions including overmixing, undermixing, over-penetration, bulk quenching and fuel leaking. Since these mechanisms are similar for CI and SI engines, they will be discussed at the same time. Overmixing is a possible problem with CI engines and stratified charge SI engines and is caused by the mixture becoming too lean, the problem being most significant at idling and light loads. Undermixing occurs when insufficient air is present in the mixture, resulting in some of the fuel not burning fully. In direct injection engines, the fuel spray may be over-penetrating, wetting the cylinder walls which can allow unburnt fuel to pass out with other exhaust products. Expansion of the mixture can lead to bulk quenching of the reaction, but this is restricted to very specific operating conditions. For diesel and direct injection gasoline engines, if fuel remains in the nozzle sac after injection, it may enter the combustion chamber late in the cycle and only be partially burned.

Particulates emanating from diesel engines have been identified as possible carcinogens and hence a cause for concern. According to Hawley et al. [1998], particulate matter from the combustion of diesel fuel can comprise: sulphates and water, unburned fuel, unburned oil, carbon and unknowns. Oxidation of sulphur in the fuel forms sulphur dioxide, SO_2 and sulphates, the latter binding with water on the carbon nuclei. The majority of the carbonaceous particulates are soot and unburned hydrocarbons and, if lubricating oil enters the combustion chamber, it may be only partially burned also representing a major source of particulates [Hawley et al., 1998]. For SI engines, the particulates emitted are sulphates, lead and organic particulates (including soot). Sulphur is mainly oxidised in the engine to form SO_2. The catalyst then converts this to SO_3, sulphur trioxide, and this can form an aerosol of sulphuric acid by combining at ambient temperature with water. The catalyst used, the level of sulphur in the fuel and the operating conditions of the engine are all factors in the quantities of sulphate particulates emitted.

However, European Union gasoline and diesel specifications ensure that sulphur levels continue to fall from the 1993 level of 500 ppm max (EN228, Euro II), to 150 ppm max (directive 98/80, 2000, Euro III) and are projected to be 50 ppm max in 2005 (directive p98/70 Euro IV) [Dixson-Decleve, 2002]. Particles are either emitted directly or agglomerate, becoming emitted during acceleration when the mass flow rate suddenly increases. Whereas particulates are likely to be included in future SI engine emissions legislation, they are already a regulated pollutant for diesel engines.

2.3 Control of emissions

2.3.1 History

Early attempts to control emissions were unsophisticated once CO and UHC were identified as harmful. The approaches were either to oxidise them or curtail their production. Thermal reactors (or afterburners) were used to oxidise CO and UHC in the exhaust system to CO_2 and H_2O. A rich mixture is required to achieve high enough temperatures and since additional oxygen must be pumped in (adding to cost, bulk and complexity) and thermal efficiency is reduced, thermal reactors were phased out at a relatively early stage in the history of emissions control [Milton, 1998].

Gas inevitably leaks past the piston rings leading to a build-up of pressure in the crankcase, making crankcase ventilation essential. Nowadays, these gases are not vented to the atmosphere as they are high in unburned gases (a source of UHC), particularly so since the crevice near the piston rings is remote from the initiation of the flame front. The sub-atmospheric pressure in the inlet manifold can be used to re-introduce these gases into the intake flow to combust normally [Milton, 1998]. Known as positive crankcase ventilation (PCV) this helps to eliminate a significant source of UHC and CO. After it became clear that in combination, engine emissions were damaging the ozone layer and producing photochemical smog, more complicated control methods were introduced. These methods included:

modification of engine design parameters
targeted engine strategies

diluents and exhaust gas recirculation
catalysts

The following sub-sections, §2.3.2, §2.3.3, §2.3.4 and §2.3.5 focus on each of the above strategies in turn. For completeness, emission control in compression ignition engines will be addressed also (§2.3.6).

2.3.2 Engine design

Design features which can be adopted to help curtail emissions [Milton, 1998] include:

electronic ignition and engine management systems
positive crankcase ventilation
ensuring the fuel tank and supply is vented through an evaporative emission system
a compact combustion chamber which will lessen wall effects, reduce UHC emissions and keep efficiency high.

As regards this last point, quench zones on the combustion chamber walls lead to the presence of UHC as demonstrated by Saito et al. [1978]. The proportion of these zones to combustion zones decreases if clearance volume is increased relative to swept volume. However, a more dominant effect of reducing the compression ratio [Min et al., 1994], is that the CO and UHC oxidise better in the tailpipe with the exhaust gases at higher temperatures due to the lower expansion ratio. In addition, the end of compression temperature is lower, which lowers peak temperatures reached in subsequent combustion, thereby reducing NO_X. A serious consequence is reduced engine efficiency leading to increased fuel use, which in turn increases CO_2 output. Quench zones and crevice volumes can be reduced by using larger cylinders, which have smaller surface area to volume ratios. This reduces UHC but increases NO_X since a higher proportion of burning occurs in higher temperature gases distant from the walls [Trinker et al., 1993]. A pentroof can closely approximate the spherical roof (which has the optimum surface area to volume ratio) and is good for the positioning and sizing of valves.

2.3.3 Engine control strategies

A large proportion of engine emissions are linked to cold running, either at start or before the engine is fully warmed up. Thermostatic control and mixing the exhaust manifold-heated air with cold intake air are possible design measures to help reach operating temperature rapidly. The latter is easier to achieve with port injection engines.

Engine control strategies have to reconcile that rich AFRs are needed to provide power while lean AFRs promote good fuel economy. Increasingly lean mixtures give increasing economy, as long as combustion remains stable. For $\phi = 0.95$ or 0.9, CO and UHC are low, but NO_X emissions are near their peak and separate control is needed, (see §2.3.4 and §2.3.5). New types of NO_X reducing catalysts in combination with oxidizing catalysts to clean up remaining UHC emissions could be used at an even leaner ϕ of 0.7, since NO_X is substantially reduced and UHC only slightly raised. At this AFR, combustion irregularity, ignition failure, partial burn and cycle to cycle variations are potential problems [Milton, 1998]. Effective emissions control by running lean has proved a challenging goal and this has led many manufacturers to adopt the alternative approach of using the effective three-way catalyst (TWC) which requires the mixture to be held very close to stoichiometric (see §2.3.5 below) [Taylor, 1985] .

Where spark timing is used to reduce knock, there is a benefit for emissions too. CO and UHC are oxidised more thoroughly in the exhaust system as a result of increased exhaust temperatures if the spark timing is retarded. The peak engine pressure is lower, reducing the peak temperature which leads to reduced amounts of NO_X [Milton, 1998] albeit at the cost of reduced efficiency.

2.3.4 Diluents and Exhaust Gas Recirculation (EGR)

Diluents are another means of lessening NO_X production via a reduced peak combustion temperature. Possible diluents (which must not increase the production of other emissions) include CO_2, argon, exhaust gas and water. Based on availability, the choice is between exhaust gas and water. Dryer

[1976] found that the addition of water cooling the end-gas (inhibiting end-gas auto-ignition), lowered the combustion temperature and substantially reduced NO_X emissions. However, the disadvantages were a rise in UHC emissions, increased engine corrosion and the need for a storage tank for the water. If exhaust gas is the chosen diluent, the process is known as EGR (exhaust gas recirculation). EGR tends to reduce the rate at which burning takes place which has a detrimental effect on cycle efficiency. Further disadvantages of EGR are that it demands a continuous but variable supply of exhaust gas and combustion irregularity can occur if too much EGR is used [Milton, 1998]. EGR can be deactivated altogether at idle since significant quantities of residuals are present in the combustion chamber through deficiencies in the gas exchange process. EGR is harder to achieve in diesel engines and unthrottled SI engines. The engine is run unthrottled, hence the required pressure differential between inlet manifold and combustion chamber is absent [Stone, 1999]. Introducing a pump to force the gas into the chamber would overcome the problem, but at the cost of reducing efficiency.

2.3.5 Catalytic treatment

Chemical reactions (such as the oxidation of CO to CO_2 and UHC to H_2O and CO_2) initiate at lower temperatures when a catalyst is used (Figure 2-3 and Figure 2-4) [Milton, 1998]. The presence of a catalyst permits lower exhaust temperatures and the spark timing and compression ratio can remain at their optimised levels, maintaining the engine at the best efficiency for the AFR used. Noble metals such as platinum, plated onto honeycomb ceramic or a metal matrix, make suitable catalysts for automobile use. 90% oxidation of CO is achieved at 300^0C and for UHC 90% oxidation occurs at 350^0C to 370^0C. For these oxidation reactions, lean AFRs are best since sufficient oxygen is available in the exhaust gas, whereas at other ratios, additional air must be pumped in. Oxidation rates of 90% (UHC) and 95% (CO) are possible at stoichiometric or lean conditions. The same noble metals can also decrease the amount of NO_X entering the atmosphere, by a reduction reaction (removal of oxygen) reducing NO_X to N_2 and O_2. The majority of oxygen is removed by CO, although any H_2 along with UHC (as a source of CO) also contribute. Therefore, this reaction occurs much more efficiently when there

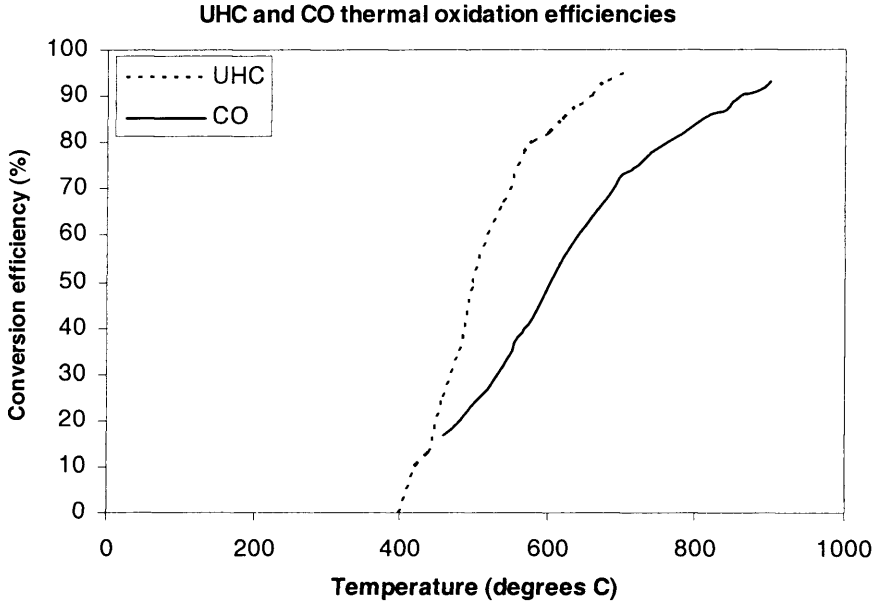

Figure 2-3 Typical conversion efficiencies at different temperatures for thermal oxidation of UHC and CO [Milton, 1998]

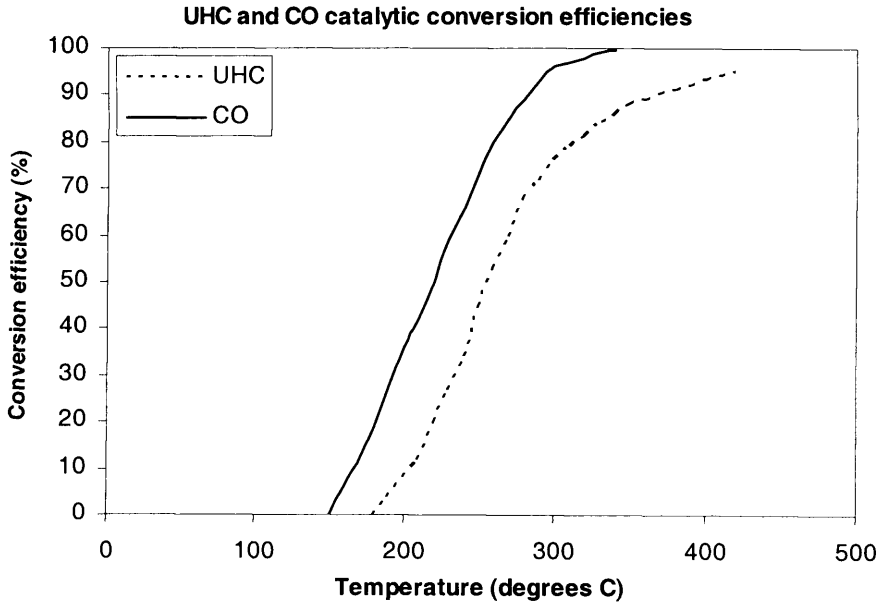

Figure 2-4 Typical conversion efficiencies at different temperatures for catalytic oxidation of UHC and CO [Milton, 1998]

is no O_2 in the exhaust gases, ie during rich operation. If ϕ is maintained between 0.995 and 1.008 a removal efficiency of around 90% is achievable for all three of CO, UHC and NO_X [Department for Transport, 2002]. However, enriching above this value leads to a small lowering of the NO_X reduction reaction efficiency and for leaner mixtures, efficiency falls off rapidly (only

20% conversion efficiency at 1.5% lean of stoichiometric). Careful control of lean-burn combustion is clearly needed for NO_X catalytic converters, although zeolite based catalysts have some ability to reduce NO_X under lean operation [Milton, 1998]. The simultaneous oxidation of CO and HC and reduction of NO_X gives rise to the term three-way catalyst, TWC. Close control of the AFR in the combustion chamber is essential for TWC operation and transients (either long-term at warm-up or short-term during acceleration) produce problems. Light-off temperature is defined as the temperature at which an efficiency of 50% is achieved and to meet Ultra-Low Emissions Vehicle (ULEV) standards, it must be attained within 20 to 30 seconds of engine start.

Since catalytic reactors must rapidly reach operating temperature, especially as large deviations in AFR are most likely at cold-start, they must have low thermal inertia, ie high thermal conductivity and low specific heat. Warming the engine prior to start, or very rapidly at start, may help to reduce pre-light off emissions, although this is costly and, if attempted electrically, burdens the battery at the worst time. Other methods such as the Saab intelligent system proposed by Jost [1995], storage and timed release of UHC [White, 1996], fuel vaporiser [Jackson, 1997] and free engine rotation [Milton, 1998] appear ingenious but expensive and difficult to realise. Maintaining AFR within the window required for effective operation of the TWC (Figure 2-5) requires a feedback system, which is based on an exhaust oxygen sensor. The oxygen partial pressure is measured and a relatively sudden change in the signal produced by the sensor occurs if the mixture switches from lean to rich or vice versa. Delays in gas transport make it impractical to use the oxygen sensor for feedback control during fast transients so a calculation is performed to achieve stoichiometric AFR based on air flow measurement.

More recently, developments have led to production of catalysts capable of reducing NO_X in the presence of excess oxygen (ie lean running conditions such as would be encountered on stratified charge engines). The catalyst is

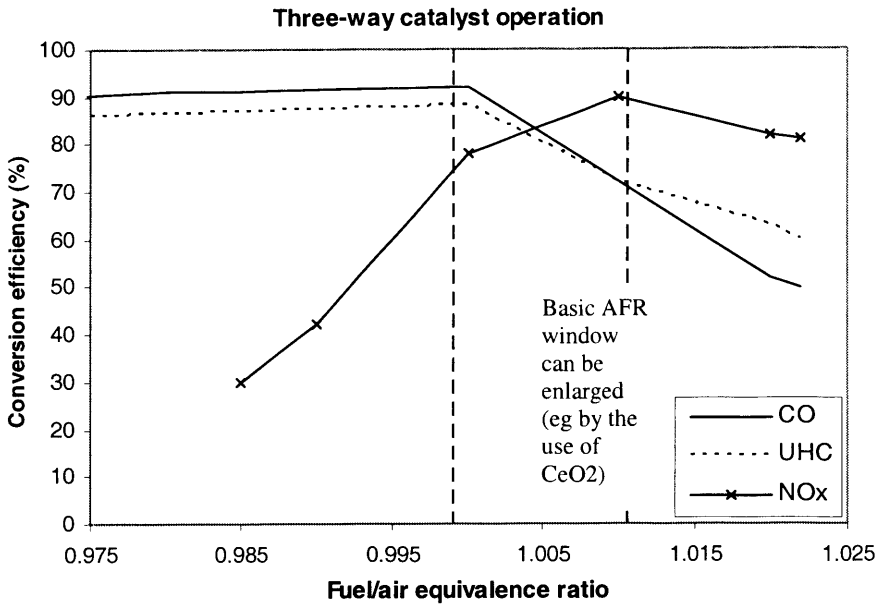

Figure 2-5 Window for three-way operation of catalytic converter [Milton, 1998]

able to store the NO_X during lean operation, and once full, the engine management system arranges a rich spike which is capable of carrying out the necessary NO_X reduction. Among the causes of catalysts becoming damaged or performing poorly are malfunction of the engine so that fuel passes through the exhaust or simple engine overheating which may destroy the catalyst. Lead (when it was used as a fuel additive) harmed catalyst performance by coating the catalyst surface and preventing contact with the exhaust gas [McTague, 1990]. Sulphur, naturally occurring in crude oil, is the precursor of sulphur dioxide, which converts to hydrogen sulphide and is the cause of acidity in the atmosphere, unpleasant odour and degradation of lean catalysts. This is particularly so nowadays following the removal of nickel oxide from catalysts on health grounds. Thus the fuel supplied by the refinery is required to have minimal levels of sulphur.

A further important consideration for both SI and CI catalysts (see §2.3.6), is to avoid back-pressure being applied to the engine by a restricted flow of gas through the catalyst, since this increases fuel consumption.

2.3.6 Emission control in compression ignition engines

The three-way catalyst is aimed at gasoline engines, since the oxidising and reducing reactions are only able to proceed simultaneously close to stoichiometric AFRs, whereas diesel engines operate with λ between 1.25 and 5.0:1. Soot filters (also known as particulate traps) have been adopted on automotive diesel engines and diesel catalysts are also used, sometimes as two-part devices, with a primary catalyst close to the turbocharger turbine outlet and a secondary one in the tailpipe [Charlton, 1998]. Early diesel catalysts were only able to lessen NO_X by relatively small amounts, see Figure 2-6. Their main application, though, was to control UHC, CO and the SOF (soluble organic fraction) of particulates. The typical diesel oxidation catalyst (DOC) is a passive device which is nevertheless required to be selective by suppressing undesired reactions and promoting desired ones [Smedler et al., 1995].

Desired reactions:

$$C_nH_m + \left(n + \frac{m}{4}\right)O_2 = nCO_2 + \frac{m}{2}H_2O \qquad \text{HC oxidation} \qquad (2.7)$$

$$CO + \frac{1}{2}O_2 = CO_2 \qquad \text{CO oxidation} \qquad (2.8)$$

Undesired reactions:

$$SO_2 + \frac{1}{2}O_2 = SO_3 \qquad \text{Sulphur trioxide formation} \qquad (2.9)$$

$$SO_3 + MO = MSO_4 \qquad \text{Sulphate storage} \qquad (2.10)$$

An approach that has been used particularly in large industrial and marine diesel engines is to introduce a reducing agent upstream of a catalyst. This leads to the selective catalytic reduction of NO_X [Charlton, 1998]. Urea is the agent most used and it converts to ammonia which is a strong reducing agent. Careful control is necessary to ensure that excess ammonia is not produced. A more common approach for automotive diesel engines is to use the lean NO_X reduction catalyst described in the previous section for use with stratified charge SI engines. Having detailed the causes of emissions and strategies for their control, the remainder of Chapter 2 surveys possible prime movers

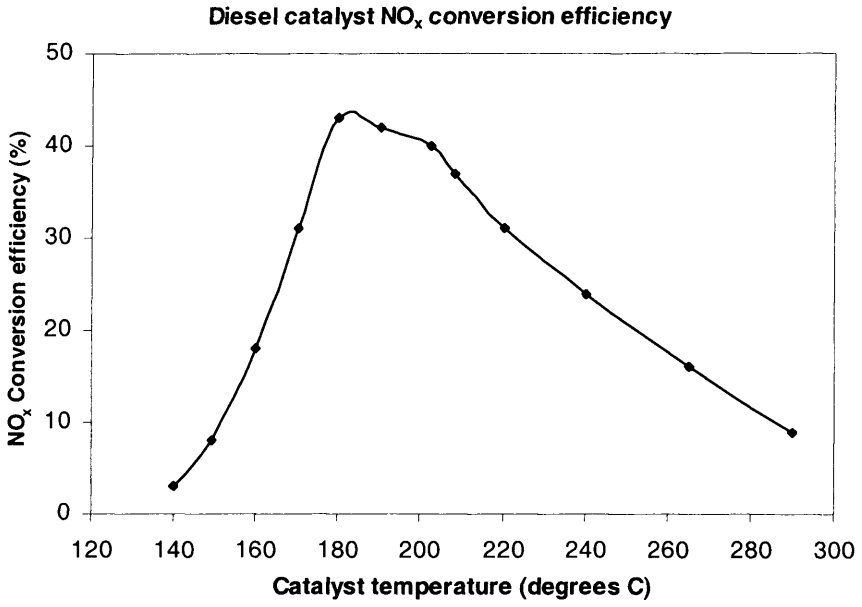

Figure 2-6 NO_x conversion efficiency for diesel catalyst with 2:2 molar UHC/NO_x ratio by fuel addition ahead of catalyst [Charlton, 1998]

beginning with IC engines, then alternatives to IC engines and finally hybrid drives.

2.4 IC engines, spark ignition

2.4.1 Carburettor

The carburettor became a very complicated piece of equipment towards the end of its life. It incorporated solutions to the problems of controlling droplet size, encouraging the droplets to form a vapour and mixing the vapour uniformly with air [Lumley, 1999]. However, the transient response with carburettors was poor, as a consequence of the distance between the fuel delivery point and the cylinder. Even using electronics, AFR control was less than perfect and crucially, the AFR could not be kept within the limits required by catalysts. Hence carburettors are obsolete in almost all markets.

2.4.2 Fuel injection

With single-point fuel injection, the venturi restriction of a carburettor is avoided [Heisler, 1995]. Instead, a single injector sprays fuel into the inlet port (hence port fuel injection, PFI) upstream of the throttle valve. Fuel can be discharged at relatively low pressure. Since no precise injection timing is

required and the injector is not exposed to combustion, the system is relatively uncomplicated [Heisler, 1995]. PFI is superior to carburettors because it is possible to employ electronic control in a far more direct manner. Mixture transport and distribution occur within the manifold, though, so that the manifold design is crucial. It is especially difficult to achieve uniform mixture distribution under all operating conditions [Bosch, 1996] and AFR control is marginal for use with a three-way catalyst [Heisler, 1995].

In multi-point fuel injection (MPFI) the inlet manifold of each cylinder has one or more injectors [Heisler, 1995], pure air flows through most of the tract and fuel is injected close to the intake valve. The injectors are normally positioned to spray fuel directly on the backs of the hot intake valves for quick evaporation to provide excellent conditions for homogeneous mixture within the cylinder [Bosch, 1996] and the short distance travelled before entering the cylinder permits a reasonably close degree of control. Since the induction manifolds only pass induced air, these can be enlarged and extended to maximise the ram effect of the incoming air [Heisler, 1995]. Despite the improved metering and AFR control offered by MPFI, wall-wetting of the port is a design feature, often leading to undesirable emissions of UHC under cold-start or transient conditions. It seems likely that these inevitable emissions will ultimately lead to the demise of this type of fuel system.

2.4.3 Gasoline direct injection (G-DI)

It might have been expected that, given the shortcomings of the carburettor, the next logical step would be to try injecting fuel directly into the cylinder. This was attempted by Hesselman around 1925 [Lumley, 1999]. The methods of control at the time, though, were inadequate to support such a system. Also it proved difficult to achieve longevity due to degradation of the fuel within the injector. As control technology became more powerful, work on direct injection engines resumed.

With G-DI engines, rapid starting is possible, transient response is good and charge cooling leads to high volumetric efficiency. There can be problems, though, with high emissions of UHC and particulates. NO_X emissions are a

problem if lean burn (ie stratified charge G-DI) combustion is adopted, since the conventional TWC cannot be used. However, the development of lean NO_X storage catalysts (referred to in §2.3.5) offers a possible way forward.

It is complex to optimise performance of a G-DI engine. Its parameters, including nozzles, in-cylinder flow, types of fuel, event timing and combustion chamber geometry allow much scope for improving operation to meet more and more stringent emissions standards and, most significantly, to improve fuel usage and efficiency, thereby reducing CO_2 production.

2.4.4 Variable valve actuation (VVA)

If the inlet and exhaust valves are directly driven from the crankshaft, the timing of their opening is always at the same relative time during the cycle. Compromises must be made, therefore, at the engine design stage, since this timing cannot be optimal for all conditions, Figure 2-7. For example, a much reduced quantity of air is required at low speed. The pumping loss associated with these compromises can be reduced if the amount of valve lift, duration and sequence of opening could be continuously adjusted. Furthermore, EGR can be controlled internally, helping to limit emissions. This concept is known as variable valve actuation, VVA. A simpler approach is to vary the phasing of the camshafts alone, without attempting to alter lift or duration. This approach is known as variable valve timing (VVT) and has become quite widely adopted on current production engines.

An early VVT system [Hatano et al., 1993] had three operating modes selected by the engine control unit depending on the engine operating conditions. The system developed by Moriya et al. [1996] used an engine control unit to monitor the engine operating condition. The pulley driven by the valvetrain belt was then adjusted by changes in oil pressure dictated by the engine control unit. A more advanced system by Vogel et al. [1997] added a second valve in series with the conventional intake valve. Not having to withstand the high temperatures and pressures of combustion allowed this valve to be of lightweight design, which in turn made adjusting its timing easier.

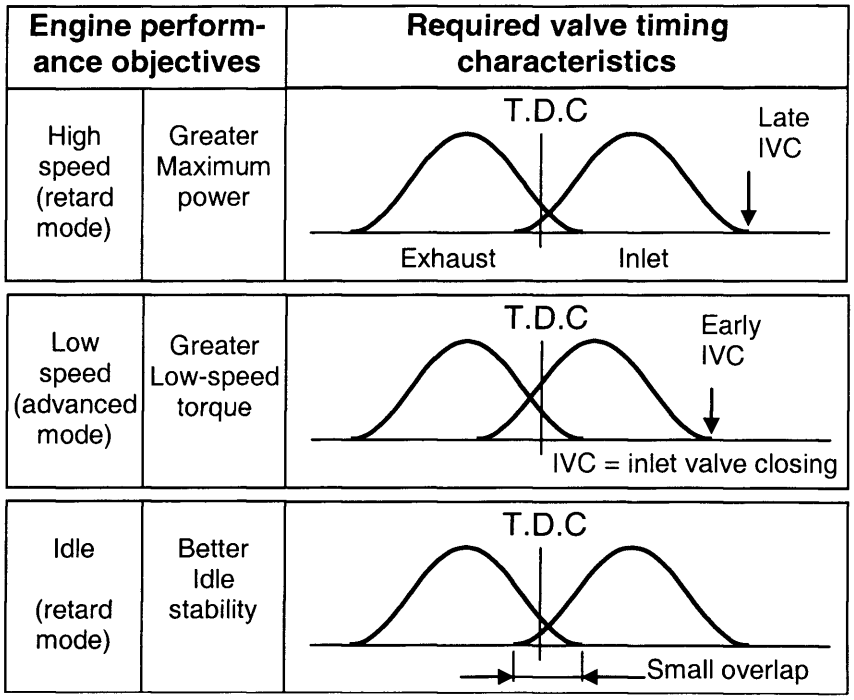

Figure 2-7 Valve lift characteristics with cam phasing [Lumley, 1999]

If each valve could be controlled individually, this would provide the greatest control. Such a development is described by Flierl and Klüting [2000] where control of each valve is via a high efficiency actuator mounted on the crankshaft. This approach is highly complex, though, and engines using it are heavy and expensive. Despite this, the development of more versatile VVA systems will be achieved to meet future needs and should be considered as an engine technology for the future.

2.4.5 Rotary engine

The Wankel rotary engine appeared to be a highly promising development in IC engines, being highly compact and producing a favourable torsional force curve [Bosch, 1996]. Mass balancing was easy, it required no valvetrain assembly and was relatively simple compared to most modern IC engines. Despite this simplicity, manufacturing costs were high and compression ratios low which limited efficiency [Institution of Mechanical Engineers, 2002]. Furthermore, the combustion chamber shape created long flame paths [Bosch, 1996] which led to high emissions of UHC and high heat loses. By the mid-1990s, only snowmobiles and some Mazda sports cars still used the Wankel engine [The Economist, 1997].

Seal reliability problems were overcome though and a two-rotor version allows all three exhaust ports to be completely closed when the intake port is open thus reducing UHC emissions. Inefficient burns associated with earlier versions were countered by carrying hydrocarbons over into the next cycle [Institution of Mechanical Engineers, 2002]. Mazda claims the current rotary engine meets Euro-4 and ULEV-II emissions standards, but it may be difficult for them to meet future, more stringent standards.

2.5 IC engines, compression ignition and alternative fuel

A diesel engine has an advantage over an equivalent spark ignition engine because load is controlled by controlling fuel, thus pumping losses associated with throttle control in spark ignition engines do not occur and fuel economy is consequently better. General reliability is similar to spark ignition engines but since diesel engines must operate with excess air at full throttle, specific outputs are lower. In-cylinder pressures are higher, dictating a greater engine mass per horsepower [Bosch, 1996] in order to deal with the higher induced stresses.

2.5.1 High-speed direct injection (HSDI)

Direct injection, DI, for diesel engines, has several advantages over indirect injection (IDI): pre-conditions are better for boosting, there is improved ability to start from cold and lubrication oil suffers less degradation [Horrocks, 1992]. With DI, the absence of a swirl chamber and connecting passages prevents some heat transfer losses. In addition there are no pumping losses associated with the chamber. In a typical IDI combustion system, late combustion as the rich swirl chamber mixture expands into the main chamber leads to thermodynamic losses. These losses are not incurred with DI systems. The fuel economy of DI is thus superior to that of IDI [Challen and Baransecu, 1999]. DI diesel engines used to be better suited for use in trucks and buses than cars, since cars required too large a range of engine speeds. Once the problem of tuning the mixture formation and combustion parameters for a wider range of engine speed was solved, the high-speed direct injection engine (HSDI) was established [Challen and Baranescu, 1999].

A significant advance for HSDI engines was the introduction of the 4-valve cylinder head reducing pumping losses and improving volumetric efficiency and more recently, common rail fuel injection has allowed multiple injections as well as high injection pressures at low speeds. Work by Kakoi et al. [1998] established that a high pressure fuel injection system would help reduce smoke. An oxidation catalyst adapted to work at low temperatures would be needed to reduce UHC emission and PM. However, significant advances have been made in recent years [Hotta et al., 2002], [Nitu et al., 2002] and the HSDI diesel continues to be the subject of considerable research interest. The author believes that developing concepts (such as HSDI diesel engines) will compete with other prime movers to power a wider range of cars of the future.

2.5.2 Homogeneous charge compression ignition (HCCI)

The severity of pending legislation to reduce NO_X emissions for diesel engines is prompting interest in the Homogeneous Charge Compression Ignition (HCCI) concept. This has been described as the third type of combustion [Christensen et al., 1997], since a homogeneous charge is used (as for SI combustion) but the charge is compressed sufficiently to auto-ignite (as in diesel engines). A mixture of fuel, air and recycled combustion products is compressed until it auto-ignites, causing heat releasing reactions to be initiated simultaneously at many sites [Stanglmaier and Roberts, 1999]. HCCI differs from the diffusion-controlled diesel combustion because the mixing rate at the fuel jet/oxidiser interface does not necessarily limit the reactions. HCCI differs from SI combustion because there is no discernible flame front and no localised high-temperature reaction region [Stanglmaier and Roberts, 1999]. In fact, HCCI combustion is characterised by distributed, low-temperature reactions occurring relatively fast.

HCCI engines have demonstrated high thermal efficiency at part load and very low emissions of NO_X and PM (see Figure 2-8), but full-time HCCI engines are currently unable to produce power comparable to conventional diesel or stoichiometric engines [Stanglmaier and Roberts, 1999]. In addition, tests of limited scope by Ryan and Callahan [1996] reported problems of misfire and knock.

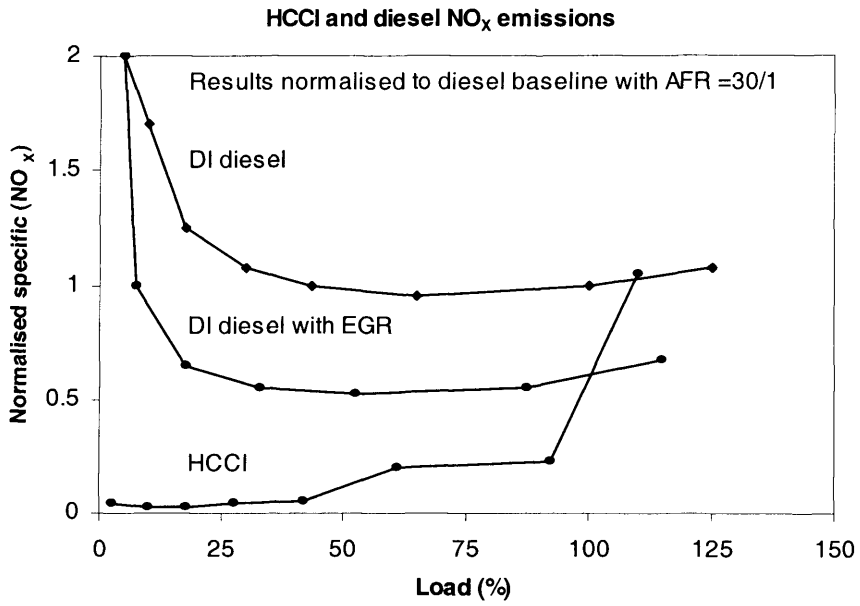

Figure 2-8 Predicted NO_X emissions versus engine load for typical HCCI and DI diesel combustion [Stanglmaier and Roberts 1999]

Dual-mode operation is suggested by Thring [1989] where the HCCI mode is used at idle and light loads, with switching to either spark-ignition or conventional diesel combustion at full load. Another way to realise engines operating full-time in the HCCI mode could be to develop HCCI-specific fuels or additives [Stanglmaier and Roberts, 1999].

2.5.3 Hydrogen

Hydrogen would be a suitable fuel for SI engines – its ignitability range is wide, permitting extremely lean AFRs and lean running would result in low levels of NO_X emissions and no UHC or CO emitted. Use of hydrogen as a fuel may eventually realise the ultimate goal of emitting only H_2O from the exhaust [Owen and Coley, 1995].

A possible source of hydrogen is natural gas, but production methods should take into account emissions resulting from manufacture. This is particularly true in the case of hydrogen production by the electrolysis of water, as much depends on how the electricity is generated. Problems arise with storage and safety: the most obvious means of storage would be in liquid or compressed gas form, requiring a bulky tank. This would add to the size of the cars,

adversely affecting performance. The highly explosive nature of hydrogen mixed with air would require careful design to avoid safety problems.

Hydrogen adsorbed by hydrides and reclaimed with heat (using the thermal energy in the exhaust gases) could overcome the safety problems by limiting the quantity of free-flowing gas. In addition, it is a simple, low energy, reversible process to bind hydrogen with a metal alloy [Greig and Boyes, 2002]. However, filling would be slow, the system would be bulky and the cost would be prohibitively high.

A solution could lie in the development of carbon nano-fibres and other materials which might be able to combine high hydrogen packing densities, rapid binding and easy discharge, low self density and require storing pressures close to atmospheric [Greig and Boyes, 2002]. However, much work needs to be done before these goals are reached. Hydrogen on its own is not considered to be a practical automotive fuel for the short- to medium-term but could feature as a feedstock for fuel cells (§2.6.3).

2.5.4 Natural gas and petroleum gas

Natural gas is available as liquefied natural gas (LNG) or compressed natural gas (CNG) whereas petroleum gas is available as LPG (liquefied petroleum gas). Although it is more costly to produce LNG than CNG [Owen and Coley, 1995], both these forms of natural gas and petroleum gas have the advantage of being cheaper than gasoline or diesel, although much depends on the tax regime applied by governments. Natural gas has excellent anti-knock properties, allowing higher compression ratios than for gasoline-powered engines and thereby increasing efficiency. If supercharged, higher boost pressures than gasoline engines are possible, giving brake mean effective pressure (BMEP) levels comparable to heavy-duty diesels [Owen and Coley, 1995].

LPG is a mixture of several hydrocarbons, its sources include natural gas processing and petroleum refining. For LPG, propane has good anti-knock properties, but the knock resistance of LPG is actually determined by the

constituent most likely to detonate spontaneously and this may significantly worsen its performance. For SI engines, both natural gas and LPG are mainly used in stoichiometric proportions so that a three-way catalyst can be fitted resulting in emission levels similar to gasoline engines [Bunting, 1998].

For CI engines, natural gas can be used in dual-fuel mode, where some diesel fuel is injected to ignite the whole charge. This is impractical for LPG given its greater tendency to knock. Emissions for natural gas dual-fuel systems are mixed: very low NO_X, high UHC and CO and poor light load efficiency [Owen and Coley, 1995].

A major disadvantage of LNG, CNG and LPG is the poor energy density in their various forms of storage [Bunting, 1998]: all three require bulky tanks, with CNG stored in high-pressure cylinders, LNG as a cryogenic liquid and LPG as a liquid under pressure.

2.5.5 Alcohols

Of the alcohols, ethanol and methanol are suitable for use as automotive fuels [Bunting, 1998]. These have the advantage over hydrocarbon fuels of being from renewable sources in the case of ethanol (from fermentation of agricultural products) or in the case of methanol, from a more plentiful source if synthesised from coal (it can also be synthesised from natural gas).

For use in SI engines, methanol and ethanol burn cleanly, have good anti-knock properties (permitting the use of high compression ratios) and reasonably suitable boiling points. Their low energy content (compared to gasoline) can be partly offset by thermal efficiency improvements, but the volumetric fuel consumption is higher, requiring the vehicle to have a larger tank. Turbo- or super-chargers can improve fuel economy by reducing engine weight for the same power output. The relatively high boiling points of ethanol and methanol cause poor cold weather starting. This problem can be overcome by mixing the alcohol with a small percentage of gasoline (eg E85 is a fuel which is 85% ethanol and 15% gasoline). NO_X emissions are generally a little lower with alcohol fuels due to their relatively high latent

heat of vaporisation reducing the peak combustion temperature. Three-way catalysts can be used but the low exhaust temperature tends to lower their efficiency. A lower photochemical reactivity than gasoline reduces the potential for smog formation [Owen and Coley, 1995]. Alcohols are unsuitable for use alone in CI engines, as a result of their property of resistance to autoignition. Special blending with diesel fuel, though, can help produce a practical fuel with the potential for low exhaust emissions.

2.5.6 Bio-diesels

Since vegetable oils are an alternative source of diesel fuel, they are often known as bio-diesels. They can be 100% vegetable oil or blended with conventional diesel fuel or blends of different vegetable oils, methyl esters of vegetable oils or even water/oil emulsions.

Soya beans and peanuts are possible sources of vegetable oils, but rape-seed has received most attention. Tests on rape-seed methyl ester showed levels of UHC and CO to be lower than diesel, but NO_X levels higher. Alfuso et al. [1993] found more smoke and particulates emitted by the rape-seed methyl ester than for diesel and high levels of smoke occurred during transient cycling.

The smell of exhaust emissions has been criticised but more problematic are build-ups of carbon on injector tips and gummy deposits in the combustion chamber. This implies that more frequent servicing is necessary, or the fuel must be dosed with a suitable additive such as an anti-oxidant.

Murayama et al. [2000] experimented with waste vegetable oils, finding that several harmful substances appeared in the exhaust gases. In addition to methanol, formaldehyde and acrolein, a large number of particulates were emitted. Bio-diesel is currently more expensive to produce than conventional diesel fuel and its future popularity is likely to be sensitive to the price of oil.

2.6 Alternatives to IC engines

2.6.1 Electric drive: battery power

Electric vehicles which draw their electricity from batteries are a relatively simple technology, but they either have a very limited range before recharging is necessary or are excessively heavy with a consequent loss of efficiency. Lailler et al. [2001] tested aqueous electrolyte batteries (lead-acid, nickel-metal hydride, nickel-cadmium) and organic electrolyte batteries. They concluded that the lead-acid battery would be dominant for long-range electric vehicles, as a result of a cost-efficiency far superior to its rivals. However, performance of battery-powered vehicles is poor in comparison to internal combustion engines, with Bunting [1998] reporting a range of 245 km achievable at 30 km/h, 170 km at 70 km/h and 120 km at 90 km/h.

Webster [1999] looked at whether the national electricity grid would be able to cope if there was a wholesale switch to electric vehicles. She concluded that care must be taken to ensure that vehicle owners benefit from collaborative efforts to set up a charging system. Interestingly, Kempton and Kubo [2000] believe that the cost of the running the vehicle could be reduced, if electricity remaining in the vehicle storage system after use were returned to the grid during peak hours, as long as it had been stored at off-peak hours.

Although the use of electric power is perceived as leading to zero emission vehicles, the concepts of total cost and overall emissions have been gaining importance. For example, if electric cars obtain their electricity from power stations, they will be as inefficient and unclean as the power stations. Cleaner electricity could be derived from renewable sources such as wind, wave and sun, although this would be more expensive.

2.6.2 Electric drive: photo-voltaic cells

It is possible to produce electricity on board the vehicle itself. Photo-voltaic panels have become very efficient, helping to boost electricity supply to domestic dwellings. However, in the UK, Europe and many other regions the intermittent occurrence of direct sunlight would seriously limit their use. A constant level of supply would be needed, so that even if storage for inclement

conditions was highly efficient, the author concludes that photo-voltaic panels are impractical for car use.

2.6.3 Electric drive: fuel cell

The fuel cell was invented in 1839, but only now is becoming the subject of intense research as a possible successor to the internal combustion engine. The fuel-cell powered Mercedes Necar prototype, for example, was reported to have a 400 km operating range and a top speed of 120 km/h [Bunting, 1998]. The chemical energy is stored outside the cell, in the fuel and oxidant. These are continuously fed to the cell (Figure 2-9), where the fuel is oxidised at the anode, oxygen is reduced at the cathode and electrons flow from anode to cathode [Cengel and Boles, 1994]. The most attractive feature of fuel cells is that when powering an automobile, the only significant roadside emission is water vapour [Lave et al., 2000]. The alkaline fuel cell was the first to be developed, but its size and use of liquid electrolyte make it unsuitable for most modern applications. High temperature fuel cells, such as the solid oxide fuel cell which operates between 700^0C and 1000^0C, are unsuitable for transport applications. Fuel cell research for automotive applications is directed at the proton exchange membrane (PEM) cell which operates at temperatures of around 80^0C. As well as the safety issues associated with the flammability of hydrogen, supplying it to the cell presents additional thermal problems. It may be supplied direct or reformed from methanol, gasoline or other sources [Ashley, 2001]. However, methanol is not a favoured source, since reforming it requires a temperature of 300^0C, it is also toxic and the cost of new infrastructure would be prohibitive. Although the infrastructure already exists to supply gasoline, a temperature of 850-1000^0C is needed for reformation, the sulphur released will poison the fuel cell and the hydrogen yielded is of inferior purity [Ashley, 2001]. Pollutants may be released in the reformation of other hydrocarbons and new infrastructure would again be needed. Supplying hydrogen directly to the cell shows much the most promise as it avoids the need for complex on-board reforming plant. The various methods of on-board storage of hydrogen have already been discussed in §2.5.3.

As previously noted, careful consideration must be given to the energy

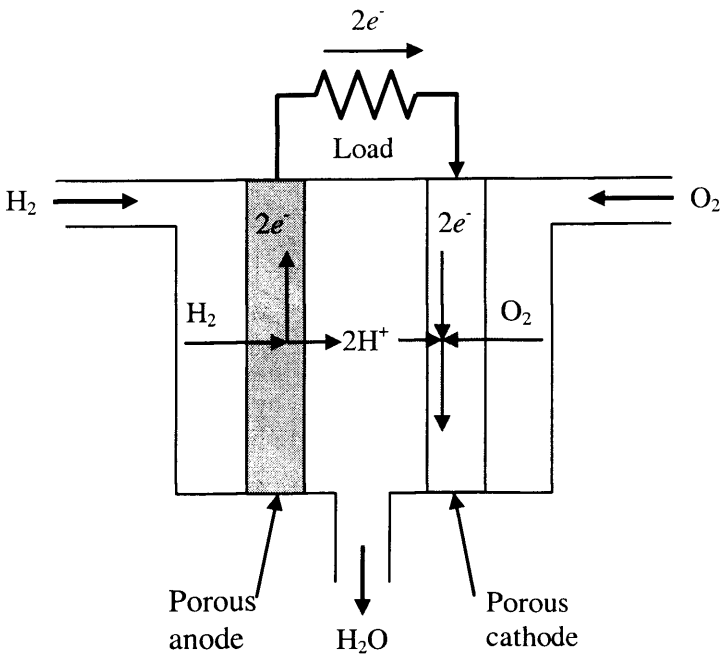

Figure 2-9 The operation of a hydrogen-oxygen fuel cell [Cengel and Boles, 1994]

expended in order to produce, distribute and store the fuel, ie the total cost must include this energy. Ashley [2001] notes that the electricity for electrolysis (of water into hydrogen and oxygen) usually involves powerplants that burn hydrocarbon fuel, leading to emissions of CO_2. Any emissions associated with the reactants must also be taken into account.

The commitment of many automotive manufacturers to fuel cell development is evident with a research alliance between BMW, Renault and Delphi Automotive Systems [Ashley, 2001], Ford Motor Company obtaining stakes in Ballard Power Systems (a front-runner in fuel cell production), Toyota developing their own fuel cell stack (see Figure 2-10) and Daimler–Benz manufacturing small numbers of fuel-cell powered cars and buses to gain operational experience [Bunting, 1998]. The view of Christensen [1997] is that customers' demands for performance would eventually be exceeded by the actual performance of the vehicles. The amount of effort being put into fuel cell research suggests fuel cells may eventually replace IC engines, but, this will not happen in the short- to mid-term. The most promising use of fuel

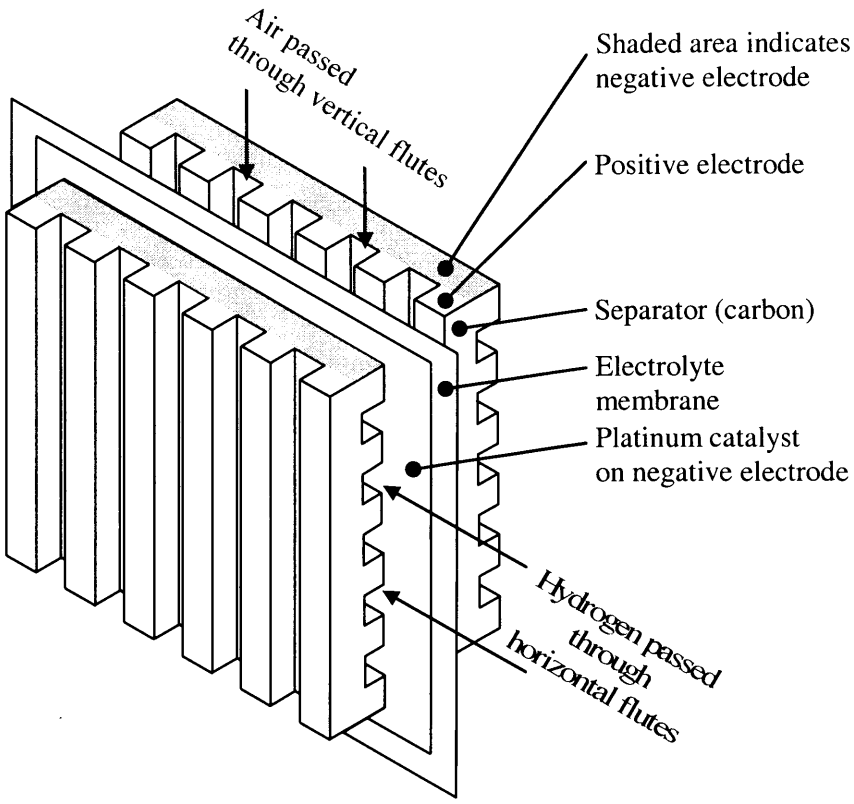

Figure 2-10 Toyota fuel cell stack [Garrett et al., 2001]

cells, now or in the future, could be to pair them with another powerplant in a hybrid vehicle as discussed in §2.6.8.

2.6.4 Flywheel energy storage

Electricity can indirectly power vehicles if a flywheel is used. Before the journey begins, the flywheel is given enough rotational kinetic energy to power the vehicle to its next charging point and it moves on in the same way by stages. Roadside emissions are non-existent and the vehicle creates little noise.

Although flywheels will never be capable of storing energy over a long period of time, modern flywheel energy storage systems are capable of efficient short term storage. This type of operation is best suited to passenger buses with electric power transmission between the flywheel unit and the wheels. An overall fuel chain efficiency has been estimated at approximately 19% [Bucknall et al., 1998] with the use of regenerative braking. The cost of

installing the infrastructure of the re-charging points would be considerable. Inertia flywheels could not be a future power plant for passenger cars.

2.6.5 External combustion engines: steam engines

Cars powered by steam engines have often been proposed, the steam engine being classified as an external combustion engine. Amann [1999a] reports on an experimental car driven by steam, noting that, in their favour, steam engines can produce torque for zero output-shaft speeds and are insensitive to fuel specifications. Problems arise with their size and mass, as well as the need for a very large radiator. It is also a disadvantage to have to set aside warm-up time. Amann [1999a] reports that the fuel economy of the steam car was poor, with little chance of significant improvement. This means that the steam engine is not viable as a future automotive powerplant.

2.6.6 Stirling engine

The Stirling engine, Figure 2-11, is another example of an external combustion engine and it is also the name given to its thermodynamic cycle. In one of the more common configurations, a power piston and a displacer piston are attached to concentric rods, all housed in a single cylinder. Out of phase reciprocating motion of the pistons is achieved by a rhombic drive, which includes the output shaft. Rapid heat transfer to and from the working fluid (usually hydrogen) is critical if a reasonable amount of power is to be obtained and all variants include a heater and a cooler, which heat or cool the working gas at appropriate times during the cycle. The thermal energy applied to the heat transfer system is changed to provide work delivery to the output shaft [Amann, 1999a].

The potential advantages of Stirling engines are: low pollution (since combustion is continuous), silent and relatively vibration-free operation, multi-fuel capacity and the potential for high thermal efficiency. In addition, reversible operation makes regenerative braking a possibility and the torque characteristics are favourable, which would allow the use of a relatively simple transmission system [Bosch, 1996]. According to Bosch [1996] fuel consumption is potentially similar to that of a direct-injection diesel engine at comparable speeds. Disadvantages are a relatively poor specific power output

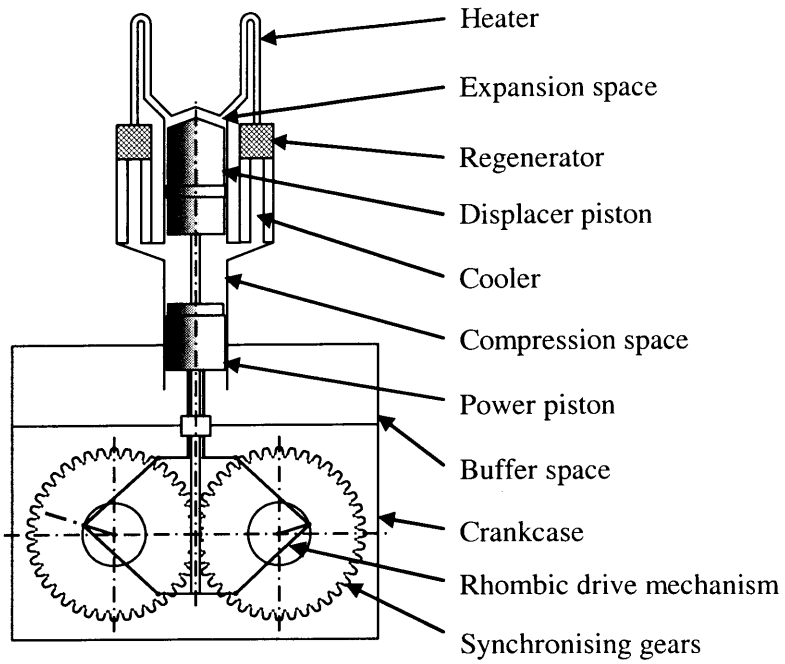

Figure 2-11 Schematic diagram of rhombic-drive, beta-type, Stirling engine [Urieli et al., 1884]

and the need to overcome the challenges of having to contain hydrogen at high temperature and pressure.

Several configurations of Stirling engine exist with a version of the alpha type using linked cylinders of a swash-plate mechanism being one of the most promising for automotive applications. A collaboration between the Ford Motor Company and Philips to develop a passenger vehicle powered by an alpha-Stirling engine is reported by Postma et al. [1973]. The car showed some promise compared to a conventional machine of the same period. However, a Stirling-engine powered car jointly developed by the United States Department of Energy and General Motors Research Laboratories in 1984 produced poor performance and failed to meet emissions criteria [Amann, 1999a].

Stirling engines are costly due to their sophisticated design and the need to adopt expensive materials. Despite their multi-fuel capability, they lack power for their weight and volume and will not become a significant engine for the future.

2.6.7 Gas turbines

Gas turbines are sometimes put forward as potential automotive prime movers. There is no engine vibration, the power delivery is free of impulses and they are tolerant to a wide range of fuels, able to provide positive torque at zero output-shaft speed and require little maintenance [Amann, 1999b]. A car jointly developed by the Rover car company and the Owen organisation [Spear and Penny, 1964] powered by gas turbine, successfully completed the Le Mans 24-hour race in 1963. The reliability of the car for the period of the race is clear, but the paper lacks scientific analysis and machines of this type seem likely to be applied in automotive applications only for their novelty.

Gas turbines can be described by the Brayton thermodynamic cycle, Figure 2-12. An analysis of this cycle reveals the dependency of the overall efficiency on the individual efficiencies of its main components (compressor/s, turbine/s). Small compressors and turbines tend to be less efficient than their larger counterparts. Units of a size suitable for car use are thus inherently inefficient. This inefficiency of smaller gas turbines and their high manufacturing costs make them unsuitable for automotive use. They will not be considered further.

2.6.8 Hybrid drives

Concern over pollution levels in urban areas, the poor efficiency of SI engines at part load and advances in computer control have begun to make hybrid drives look increasingly attractive. These drives usually contain two different powerplants: often one is electric and the other an IC engine. Automatic switching between the two takes place depending on prevailing conditions. Several practical examples of hybrid drives exist, often on public transport vehicles and taxis, Figure 2-13. A CNG – electric hybrid system currently used for smaller buses [Fenton, 1998], is compact enough to suggest it may be suitable for passenger vehicles in the future.

Lumley [1999] described the configuration of a possible passenger vehicle hybrid drive, comprising a relatively small combustion engine, an alternator, batteries and electric motors. The batteries are charged by the engine, which

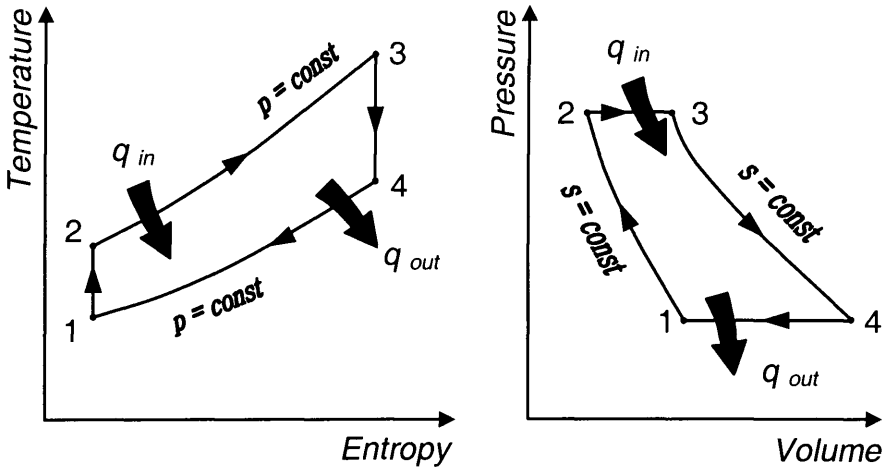

Figure 2-12 Brayton cycle, applicable to gas turbines [Cengel and Boles, 1994]

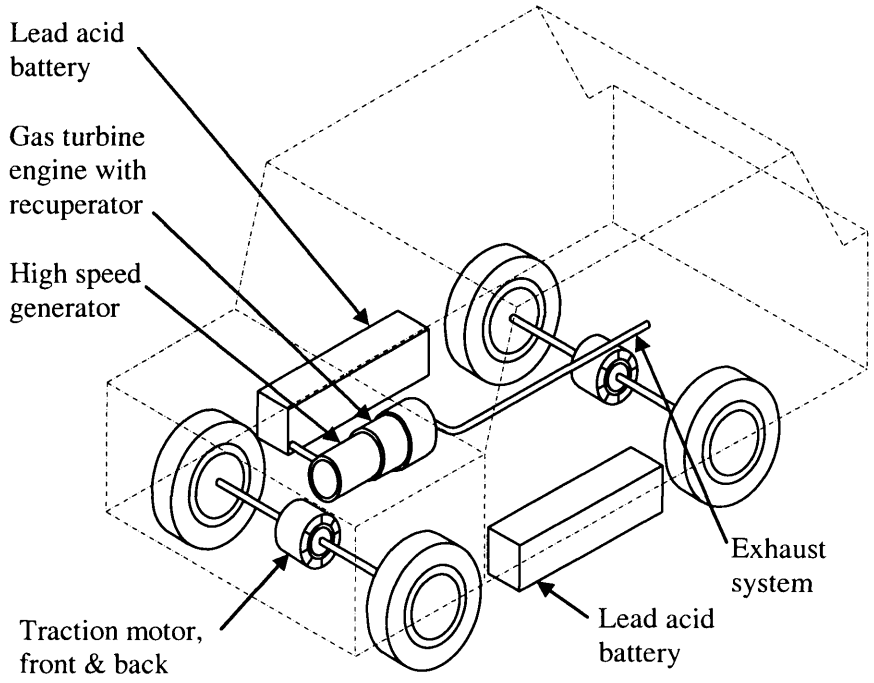

Figure 2-13 Hybrid drive taxi [Fenton, 1998]

runs continuously at its operating condition of maximum efficiency to limit fuel consumption and emissions. The batteries drive the car through the motors and regenerative braking is used to avoid wasting kinetic energy. In regions of high pollution, the engine can be shut down. Overall efficiency is limited by the individual efficiencies of the energy conversions and hybrid drives often carry a weight penalty.

The Toyota Prius was the first mass-produced hybrid electric vehicle, going on sale in 1998. Its main elements are a VVT gasoline engine, an electric motor, an electric generator and a regenerative braking system [Duoba et al., 2001]. A power split device distributed varying proportions of the engine's output to the generator and the drivetrain according to driving conditions. Each system component was monitored and controlled to maximise fuel efficiency and minimise emissions. Performance figures of 0-60 mph in approximately 25 seconds were claimed, based on the US06 acceleration test. One shortcoming, however, was that response depended on generator speed, engine speed and vehicle speed and it was also inconsistent from test to test. An electronically controlled continuously variable transmission was added to later vehicles to improve this response.

2.7 Summary

The aim of this section was to highlight propulsion units capable of continuing to meet emissions criteria while delivering ever-improving fuel economy.

Fuel cells show most promise amongst the non-internal combustion engines and are a promising long-term proposition.

For IC engines using traditional fuel: VVT, G-DI (gasoline) and HSDI (diesel) will dominate. HCCI could become widely adopted if all the considerable development problems are overcome.

Where IC engines are run on non-traditional fuel, bio-diesel shows promise.

Hybrid vehicles are currently realising some efficiency benefits, but they are unlikely to become dominant because of the high cost and weight penalty.

The author believes that G-DI engines, many using VVT, will dominate car propulsion in the short and medium terms. Accordingly, the next section, Chapter 3, reviews recent progress in G-DI engine development.

Chapter 3

Gasoline direct injection engines

3.1 Introduction

Chapters 1 and 2 have shown that the automobile will continue to be a significant means of transport throughout the world and that G-DI engines are amongst those expected to continue meeting emissions regulations. Now Chapter 3 reviews G-DI engines.

3.2 Fuel sprays and air-fuel mixing

G-DI makes widely differing demands of injectors. For the early injection mode of operation, a well-dispersed fuel spray is needed to ensure a homogeneous charge. For light-load, stratified-charge operation, a stable and compact spray geometry is essential for efficient combustion of the stratified mixture and the injector must deliver the required amount of fuel using a short fuel pulse. In all cases, a well-atomised spray is needed and there must be good spray symmetry over the entire range of a particular mode of operation. Fuel metering must be accurate and the pulse-to-pulse variation in fuel quantity and spray characteristics must be minimal.

The two most important injector types for G-DI are pressure-swirl atomisers and multi-hole injectors (Figure 3-1). For swirl atomisers, liquid emerges to form an initially hollow-cone spray, the exact details of which depend on injector design factors such as nozzle geometry, opening characteristics and supply pressure. For multi-hole injectors, such as those recently developed for G-DI applications by Robert Bosch GmbH [Ortmann et al., 2001], the spray dispersion is largely dependent on the number and positioning of the nozzle holes. Regardless of the specific injector type employed, the injection system must be matched to the in-cylinder flow field to provide a mixture distribution to suit the entire operating range of the engine. The spray must atomise and distribute the fuel to the required locations within the cylinder, which may vary according to load. On many G-DI versions, with the engine running at part-load, the stratified charge mode is used and a compact spray is needed for efficient combustion. The fuel is injected late and the pressure in the

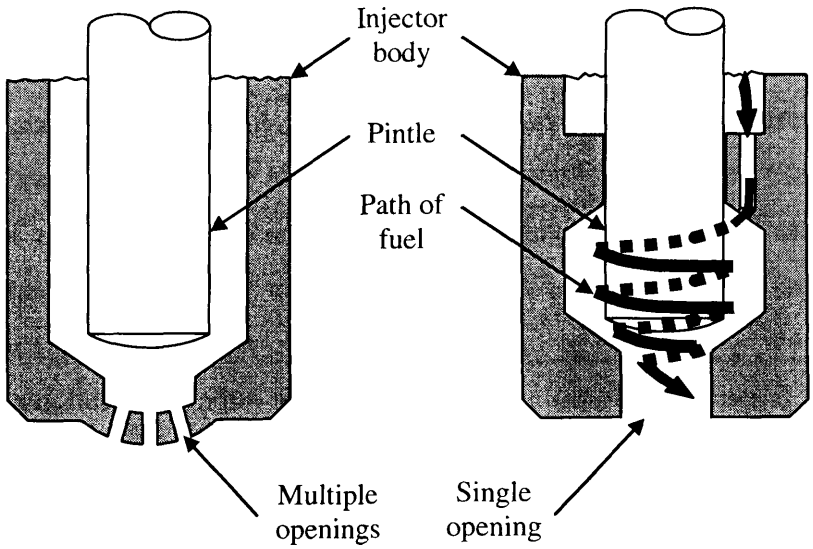

Figure 3-1 Basic internals of multi-hole (left) and pressure swirl (right) injectors [Pruessner et al., 1998]

combustion chamber at that point in the cycle can be as high as 2 MPa. The fuel quantity required is less than that for homogeneous mode, but a high rate is needed to deliver it in the short time available. The fuel pressure needed to achieve such a delivery rate in these conditions, produces a highly atomised spray, but one which may be over-penetrating.

With the engine running at full-load, all versions of G-DI engines will require a homogeneous mixture and a well-dispersed spray is needed to ensure full mixing of the fuel and air. The pressure in the cylinder at the time of injection is less than for a stratified version running at part load. In addition, the piston is lower in its stroke than for stratified charge mode so that the longer spray path enhances fuel vaporisation. However, impingement of the fuel on the piston surface or cylinder walls, leading to liquid fuel film, must be avoided. One cause of this is an excessive fuel delivery pressure.

In general, finer atomisation of the fuel helps reduce UHC emissions as long as pockets of very lean mixture are avoided. Such pockets may be too lean to burn and thus pass unburnt out of the exhaust and can even result in increased emissions of particulates due to pyrolysis. Strong levels of turbulence can reduce this tendency by improving mixing.

With a pressure swirl atomiser, optimising the spray cone angle and injector position can minimise wall wetting at full load. Fuel sprays from high-pressure swirl nozzles have axial momentum as well as rotational momentum (some of the energy associated with a fluid under pressure is effectively transformed into rotational momentum). The liquid emerges as an annular sheet which forms a hollow-cone spray by spreading out radially, atomisation is enhanced, but penetration limited. The distribution of drop sizes is typically narrower than for a non-swirl nozzle and the wide spray angles and high delivery pressures that are typical of production G-DI fuel injectors promote excellent fuel atomisation.

For a high-pressure swirl injector, atomisation occurs in two main stages [Van der Wege et al., 2000a]. The first is at or near the exit and the second during spray penetration. The second stage is dominated by fuel droplets interacting with the surrounding air flow field (Figure 3-2). Four regions are identifiable in the subsequent cone formation. 1) The largest droplets, whose axial velocity is high, arise from the beginning of the injection pulse and form a leading edge. 2) The fuel velocity is steady once the needle is fully open, resulting in a conical region of droplets. 3) A trailing edge is formed as the needle closes. 4) Small droplets carried away from the spray by circulating air form a vortex region. Typically, air is entrained to the extent that the vortex ring generated near the injector tip becomes a large-scale toroidal vortex towards the end of the injection event.

Although research is often focused upon the detail of the fuel spray, consideration must also be given to the way the spray influences the in-cylinder gas flow. Large-scale in-cylinder flows can be affected, with mean velocities of gases in the spray region increased. For early injection, some of the momentum of the droplets in the injected spray transfers to the surrounding gases so that the kinetic energy of the charge is increased [Zhao et al., 1997], although this increased kinetic energy dissipates as the piston completes the compression stroke. In the homogeneous, early-injection mode, the turbulence at TDC (top dead centre) compression is more intense the later

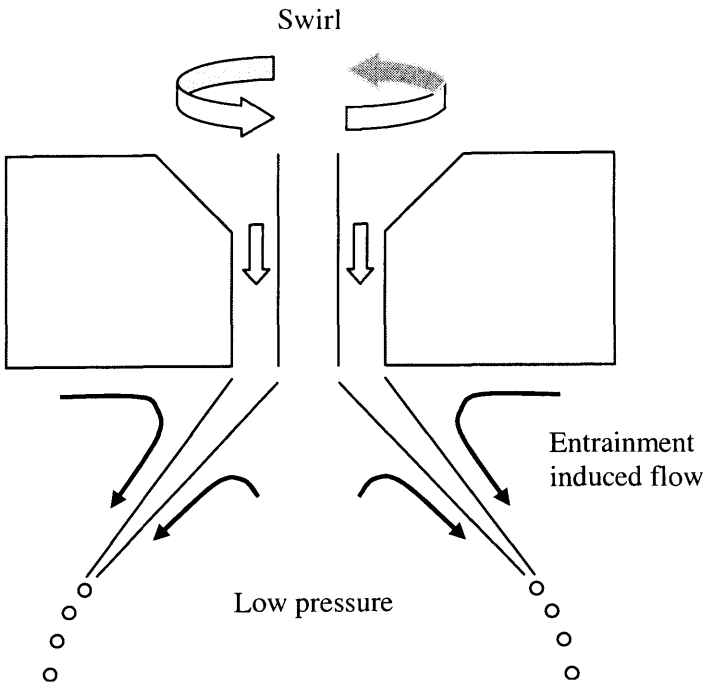

Figure 3-2 Air entrainment during second stage of atomisation [Van der Wege and Hochgreb, 2000a]

the injection. If the spray itself generates turbulence during the intake stroke, this can last into the compression stroke thus aiding the subsequent combustion event [Han et al., 1996] by promoting mixing and increasing flame velocity.

As regards the requirements of air-fuel mixing within the cylinder, the results of Davy et al. [2000] suggest that the preparation of a homogeneous charge in a G-DI engine requires adequate droplet dispersion in the initial phases of fuel injection. Interestingly, Davy et al. [2000] also point out that the hollow-cone swirl injectors typically employed in G-DI engines can, under some conditions, produce dense, filled spray structures which might be regarded as ideal for stratified charge operation but may be unable to produce a fully homogeneous charge at medium or full-load operating conditions. Choi et al. [1999] suggested that spray dispersion from pressure-swirl atomisers was increased by the formation of a ring vortex from entrained air. Spray under high ambient pressure was reported to have a strong ring vortex structure, which was said to be good for atomisation and mixing. However, in common with the results of Davy et al. [2000], the basic spray shape was compact. Note that for all fuel compositions and injection timings tested by Davy et al.

[2000] (including early induction-stroke injection), the mixing of the airborne droplet/vapour cloud and the surrounding charge was shown to be incomplete.

3.3 The influence of operating conditions

The spray characteristics of conventional G-DI pressure-swirl atomisers are known to be sensitive to changes in their operating conditions [Williams et al., 2001]. At higher fuel supply pressures, atomisation characteristics are improved, resulting in a smaller mean droplet size, greater homogeneity [Ipp et al., 1999], [Kubo et al., 2001], [Miyajima et al., 2000] and the sprays also become more penetrating, although Pruessner et al. [1998] found this penetration reached a limit (Figure 3-3).

Swirl atomiser efficiency and spray structure are also affected by changes in the cylinder pressure and charge density. As ambient pressure is increased (thus increasing charge density and therefore viscous drag on the droplets), spray penetration reduces and sprays became more compact [Kubo et al., 2001], [Miyajima et al., 2000], [Ipp et al., 1999]. A similar effect is seen if air density is increased by a reduction in its temperature. On the other hand, an increase in ambient temperature may cause an increase in spray tip penetration due to the decrease in gas density and hence a decrease in the viscous forces which decelerate the fuel droplets [Ipp et al., 1999], [Park et al., 1999], [Van der Wege and Hochgreb, 2000a]. Note however, that Ipp et al., [1999] found little change in the degree of penetration of the spray tip above 370 K, since the reduction in the viscous forces was compensated for by enhanced evaporation.

Fuel temperature and composition may also affect the spray structures from pressure-swirl atomisers [Williams et al., 2001]. Davy et al. [2000] and Van der Wege and Hochgreb [2000a] have demonstrated the effects of flash boiling on pressure-swirl atomiser spray formation. In the extreme, the typical hollow-cone structure of the spray was replaced by a highly atomised narrow columnar spray. A similar phenomenon was reported in an optical investigation by Ipp et al. [1999]. As the injector body and fuel temperatures were increased, a more compact distribution of liquid and vapour fuel

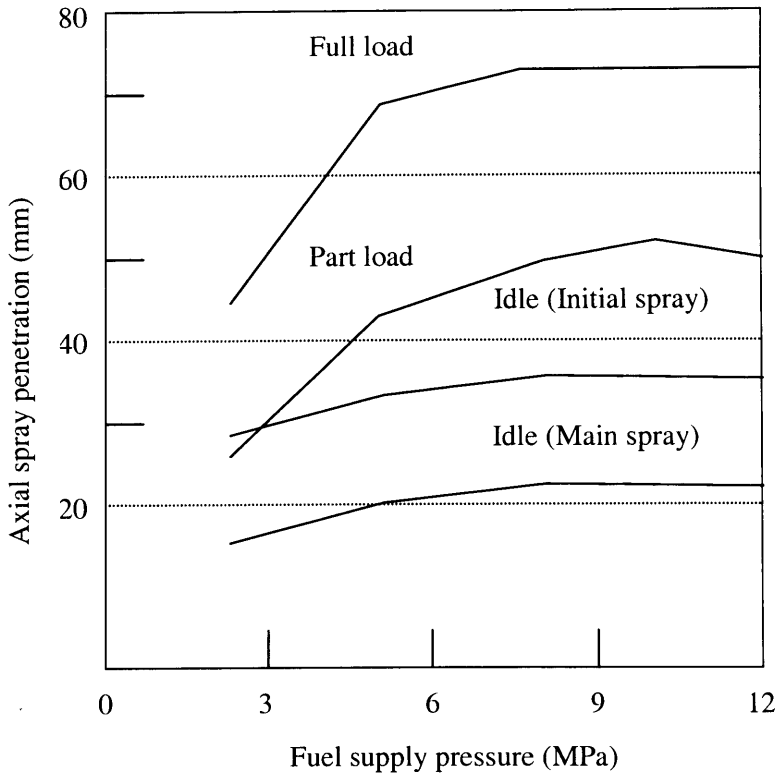

Fluid	Premium unleaded gasoline
Spray angle	90^0
Chamber pressure	0.56 MPa
Temperature	23^0 C

Figure 3-3 Limit of penetration distance as fuel pressure is increased [Pruessner et al., 1998]

was seen accompanied by a reduction in the number of large drops.

By considering sprays in isolation, Van der Wege and Hochgreb [2000a] defined three fuel dependent regimes:

slow evaporation (for conditions not exceeding the fuel mixture's boiling point);

non-disruptive evaporation (where the more volatile components migrated towards the axis of the spray);

disruptive evaporation or flash boiling (lighter fuel components vaporised, affecting the initial spray behaviour and narrowing the spray as smaller droplets became drawn towards the centre).

It will be noted that the behaviour described above is not only sensitive to fuel composition and temperature but also to ambient (in-cylinder) pressure. Thus, the spray behaviour may be affected by changes in injection timing as demonstrated by Van der Wege and Hochgreb [2000a]. Davy et al. [1998] looked in detail at how injection timing affects the spatial and temporal development of injected fuel sprays. The state of the intake-generated gas flows at start of injection (SOI) was shown to control the location of the injected sprays during the induction stroke and the early part of the compression stroke. The cylinder pressure at SOI was seen to dominate the temporal and spatial development of the injected sprays during the late compression stroke. As a result, the formation of liquid films in the cylinder was seen to be affected by injection timing.

It is important to acknowledge the balance between temperature and viscous effects. Sprays may change from a "full" to a "collapsed" form, where the conditions causing the changeover vary with injector design; for example, a larger nominal cone angle implies a higher radial component of velocity and more resistance to collapse [Williams et al., 2001]. Collapse is likelier at higher cylinder pressures due to increased aerodynamic drag and greater pressure differences across the spray wall. Spray momentum may be expected to increase as fuel pressure increases, since initial sheet velocity and mass flow rate increases. However, the momentum of an individual droplet can decrease with rising fuel pressure, since initial momentum is the product of initial velocity and mass and the higher delivery pressure will have led to smaller droplet sizes. A summary of the effects of the parameters which influence developed cone angles is shown in Figure 3-4 and Figure 3-5 for two different types of pre-production injectors.

Flash boiling is a phenomenon that occurs when the fuel is injected under conditions where its vapour pressure exceeds the pressure within the cylinder.

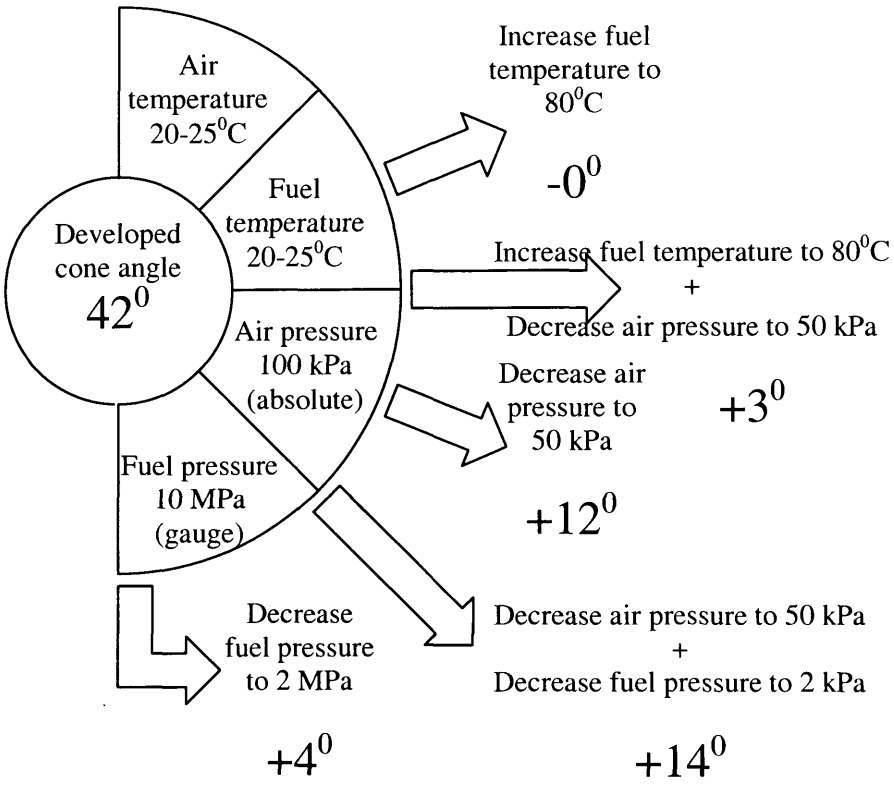

Figure 3-4 Variation in developed spray cone angle for pre-production injector, ref A [Williams et al., 2001]

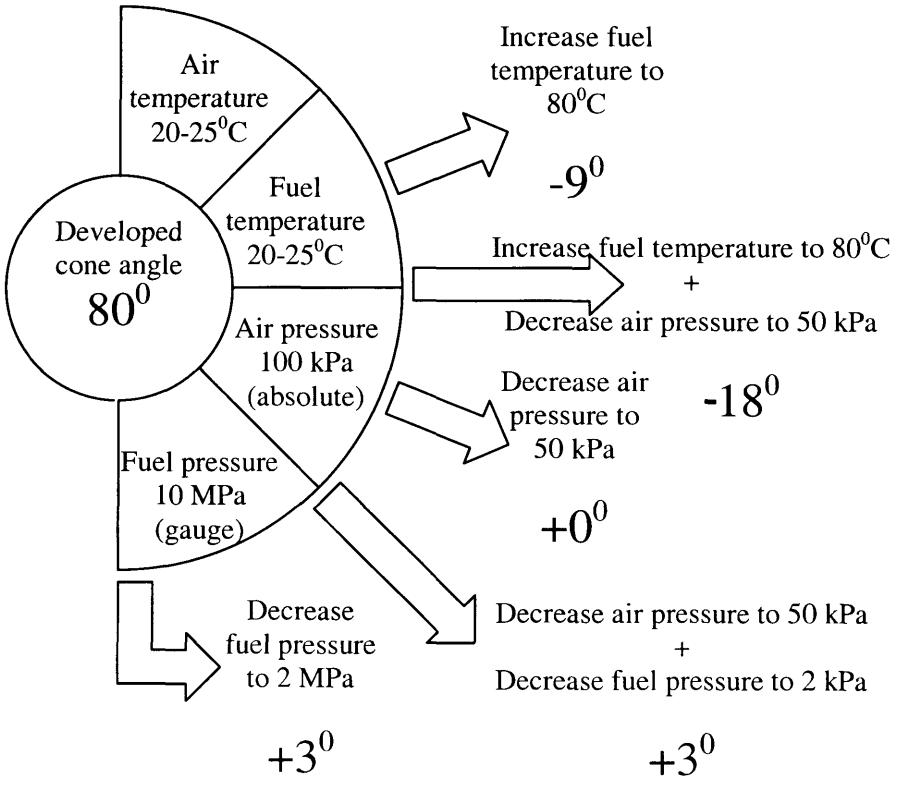

Figure 3-5 Variation in developed spray cone angle for pre-production injector, ref B [Williams et al., 2001]

Flash boiling is a disruptive effect, increasing the number of small droplets and reducing the number of large ones in a spray [Davy et al., 2000]. Small droplets of low-momentum appear to be drawn towards the spray core, which is a low-pressure region. The result is a filled cone appearance and a reduction of spray angle. The mechanisms responsible for the collapse of an otherwise open spray cone are not necessarily additive. Williams et al. [2001] note that once collapse has occurred, the evidence shows the cone becomes relatively stable and less vulnerable to further change (Figure 3-4 and Figure 3-5).

The previous paragraphs in this section refer specifically to the sensitivities shown by conventional pressure-swirl atomisers to changes in their ambient operating conditions. As regards the multi-hole type of injector mentioned in the introduction to this section, it should be noted that one of its claimed advantages is relative insensitivity to changes in ambient conditions. A study by Zhao et al. [2002] though, has demonstrated that the cone angle from multi-hole injectors is sensitive to increasing ambient pressure with the cone collapsing at reduced back pressures in hot conditions. However, it is worth noting that other injector concepts are being developed to address the issue of spray stability under the wide range of ambient conditions that are found during normal G-DI engine operation. Toyota have reported on a G-DI injector featuring a slit nozzle (Figure 3-6). The injector, which produces a thin fan-shaped spray, is said to exhibit wide spray dispersion, moderate spray penetration and fine atomisation characteristics [Takeda et al., 2000] and is intended to improve spray stability under varying ambient conditions.

Miyajima et al. [2000] adopted a different approach to improve spray stability, producing modified versions of the conventional pressure-swirl atomiser. Two newly-designed nozzles, an L-type and a taper-type nozzle, were tested under varying ambient conditions. As ambient pressure increased, the L-type's spray pattern changed little, but that of the taper-type became more compact; the penetration of both decreased. As fuel pressure increased, neither spray pattern changed greatly. The penetration of the L-type was unchanged with increasing fuel pressure but the taper-type produced a more penetrating spray.

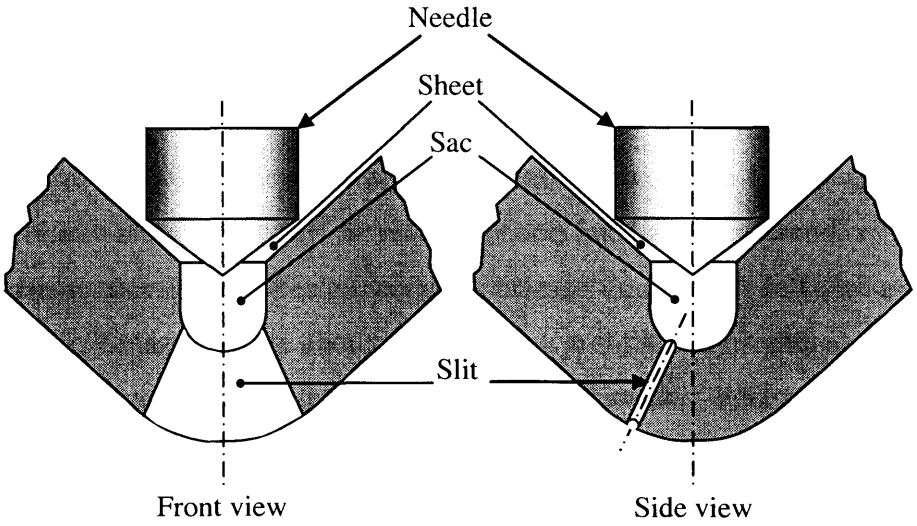

Figure 3-6 Slit nozzle injector [Takeda et al., 2000]

3.3.1 Injector deposits

It has been found that the fuel flow rate through an injector nozzle can be changed due to the formation of chemical deposits, which may alter spray characteristics and harm performance [Kinoshita et al., 1999]. Swirl nozzles are sensitive to small amounts of deposits, with the early stages of deposition affecting skew angle [Zhao et al., 1997].

Deposits can form internally or externally or both. Internal deposits (near the metering area of the flow path) reduce fuel flow rates, whereas external deposits degrade sprays. Aradi et al. [1999] found external injector deposits were wholly due to crankcase lubricant elements (cadmium, zinc, magnesium, potassium and sulphur) whereas internal deposits were solely fuel-derived. The mechanics of deposition are thought to be temperature dependent. Kinoshita et al. [1999] found that deposit accumulation occurred and reduced fuel flow rates if the nozzle temperature exceeded 150^0C. Deposit precursors in the fuel were washed away by fuel injections because the residual fuel, being liquid, dispersed these precursors. At higher temperatures, the precursors cohered to each other and adhered to the walls, making it harder for

the fuel to disperse them. They concluded that keeping the residual fuel in the liquid state would restrain deposit formation. However, Zhao et al. [1997] contended that typical G-DI fuel pressures of the time (4 to 7 MPa) were insufficient to prevent deposition under continuous engine operation.

Guthrie [2001] surveyed deposit mechanisms for whole G-DI engine systems. To help prevent deposits he recommended limiting the presence of depositing chemistries in the area of concern or else continuous self-cleaning should occur. Smart designs should be used to promote environments which limit deposit formation by thermal or mechanical means. Fuel composition or oil additives could be used to reduce or prevent deposit formation - for example, the test matrix of fuels used by Aradi et al. [1999] showed that sulphur had a positive effect on the reduction of injector deposition, but that increased olefin levels had an adverse effect. In addition, designs should be robust enough to tolerate some deposit formation, leaving function unaffected. Since tip temperature appears to be crucial, injector positioning and the inclusion of a conductive path from the injector mounting boss to coolant passages would be beneficial. Finally, methods should be found for the periodic removal of deposits by thermal, mechanical or chemical means, for example, by incorporating hot-soak intervals into operating cycles [Zhao et al., 1997].

3.3.2 Injector and spark plug location

The fixed location of the ignition source in SI engines produces a challenge for designers when it comes to arranging for stratified charge operation at part load. Compromises are necessary in locating the spark plug and injector, since no single set of positions is optimal for all speed/load combinations. The six most influential parameters in finally selecting the spark plug and injector locations are: 1) the injector spray characteristics, 2) the structure and strength of the in-cylinder flow field, 3) the geometry of the injector body and tip, 4) the spark plug design and extent of electrode protrusion, 5) the combustion chamber geometry and 6) the piston crown geometry [Zhao et al., 1997]. An injector position and optimised spray cone angle which minimises wall wetting at full load is preferred since wall wetting is widely known as a source of UHC emissions.

The detrimental effects of injector fouling (deposits) were discussed in the previous section. Since there is evidence that injector fouling depends on tip temperature, the injector should not be located on the exhaust side of chamber, where tip temperatures of 285^0C are possible [Zhao et al., 1997]. Pontopiddan et al. [2000] noted that positioning a fuel injector in a central location in the pentroof meant that, for approximately 35 CAD (crank angle degrees), the injector tip was surrounded by high temperature post combustion products, which increased the risk of injector clogging. In comparison, [Zhao et al., 1997] have shown that locating the injector under the intake port reduces the thermal loading on the injector and provides additional tip cooling from the intake air.

Injector position, though, should not be considered in isolation. The position of the injector relative to the spark plug must also be taken into account. Positioning a single spark plug in a near-central location in a modern pentroof combustion system helps minimise flame travel distance and provides low heat losses during combustion for open-chamber designs. However, if the injector and spark plug are very close, the valve sizes may be restricted. If the fuel spray fouls the electrodes, this can lead to ignition problems and injector tip deposits can occur if the tip is too close to the ignition source. The lack of proven and effective G-DI anti-deposit additives in fuel make it highly important to find the optimal design to resist coking and make it desirable to carry out more research into operating cycles.

3.4 Modes of operation – homogeneous charge (HC) and stratified charge (SC)

3.4.1 Introduction

The full potential of the G-DI concept can be realised by using both modes at various times and managing the transitions between them [Zhao et al., 1997]. Homogeneous charge mode (§3.4.2) is used for high load operation and charge stratification (§3.4.3) is employed for low-load requirements. With the stratified charge mode, there is the possibility of improving operational efficiency, since the engine can potentially be run unthrottled. This avoids losses in efficiency associated with pumping work.

In the homogeneous mode, fuel is injected in the induction stroke which allows thorough mixing of the air and fuel spray prior to ignition. In the stratified charge mode, fuel injection occurs later, during the compression stroke, less fuel is injected with the aim of maintaining a distinct and compact vapour cloud adjacent to the ignition source. The main charge motion strategies available for mixing and stratifying are swirl, tumble, reverse tumble and squish (Figure 3-7) and these are employed alone, or in combinations. They also help manage the transition between the two modes (§3.4.4).

3.4.2 Homogeneous charge mode

In the homogeneous mode, intake-generated flows affect the direction and penetration of the spray. The spray-induced gas flows influence the large-scale flow structure, enhancing the turbulence intensity but the initial development of the spray is largely unaffected. The later the start of injection, the higher the turbulence intensity at TDC on compression [Zhao et al., 1997].

If fuel is injected during the induction stroke, a widely-dispersed fuel spray is needed to form a homogeneous mixture. With optimised induction stroke injection timing, a higher compression ratio is possible (due to charge cooling), this improves fuel economy, reduces transient and cold-start emissions and helps overcome the problem of smoke.

Only a moderate window exists, however, for the injection event [Suh and Rutland, 1999]. When fuel is injected as the piston moves away on the induction stroke, spray impaction is reduced and volumetric efficiency improves, due to charge cooling. However, if the injection event only just precedes intake valve closure, the fuel droplets have too little time to evaporate before the valve closes. There is charge cooling, but volumetric efficiency is not improved since the valve is shut. Moreover, if injection occurs too late in the induction stroke, the time for air-fuel mixing, may be insufficient to ensure full evaporation and a homogeneous charge. When injection occurs at the beginning of the intake stroke, the piston is close to the

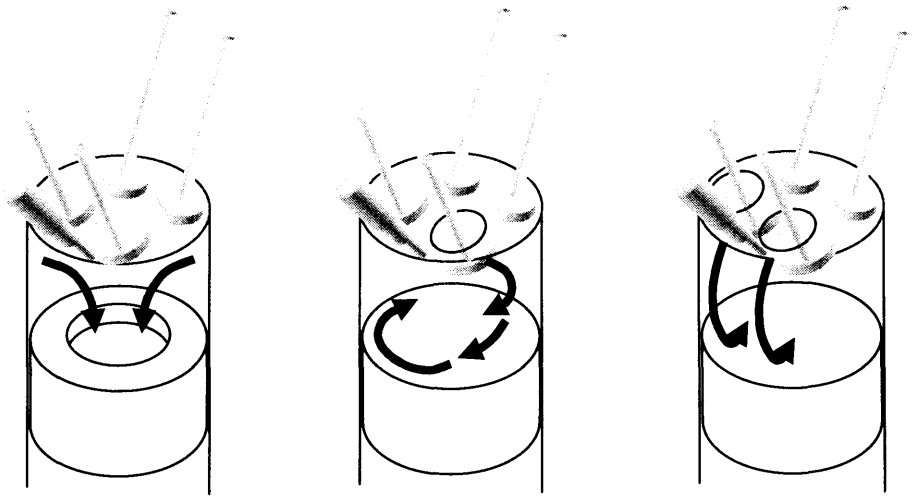

Figure 3-7 Mixing strategies for stratified charge mode, squish (left), swirl (centre) and tumble (right) [Guerrier, 1999]

injector and has low velocity. The fuel impinges on the piston crown, reducing the amount of energy that can be transferred from the induction air to vaporise the fuel [Stanglmaier et al., 1999]. Since engine speed and injection timing affect impingement of fuel on the walls, spray over-penetration and wall-wetting can be minimised by optimising these timings [Stevens and Steeper, 2001]. This is especially important since another result of wall wetting can be increased wear as fuel washes oil from the bore. In general, the best injector timing for homogeneous charge ensures that the leading edge of the spray tip chases the receding piston.

3.4.3 Stratified charge mode

Charge stratification can be achieved by: air-guiding, spray-guiding or wall-guiding the fuel cloud (Figure 3-8). With air-guiding (also known as charge motion mode), the air motion (swirl or tumble) set up in the induction stroke is designed to keep the cloud of vapour near the spark plug. Spray-guiding (also known as jet-guiding or short spacing) relies on the injector parameters and the proximity of spark plug and injector to achieve stratification [Ortmann et al., 2001]. The wall-guided mode uses a specially shaped piston to direct the spray to the spark plug electrodes.

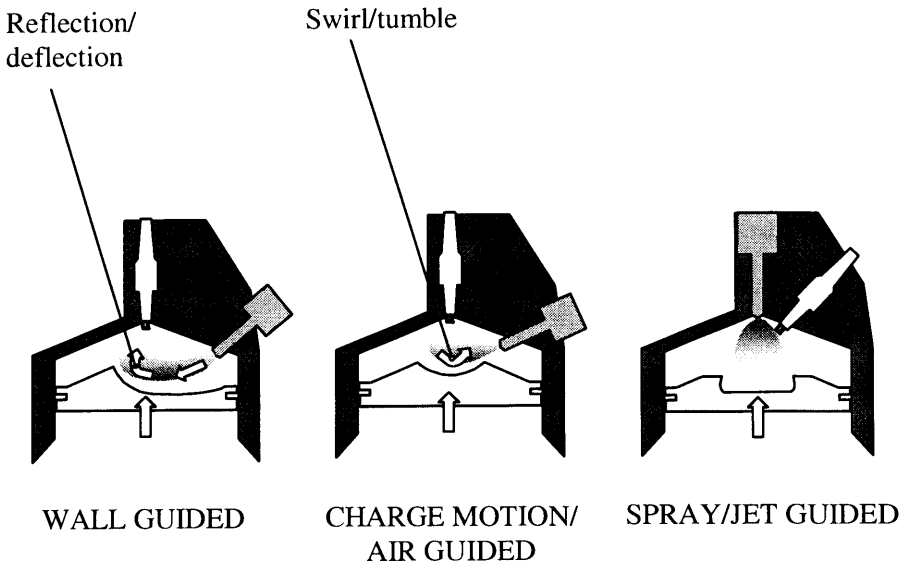

Figure 3-8 Direct injection combustion systems [Cathcart and Xavier, 2000]

For a successful stratified charge system, a combustible mixture must be concentrated at the spark plug over a wide operating range. A controlled charge motion matched to the fuel guiding method is essential. Mitsubishi and PSA Peugeot Citroën use reverse tumble, whereas Toyota (first generation), Nissan, Ford and Opel employ swirl and VW and Toyota (second generation) use forward tumble. Some systems use a variable charge motion (VCM) strategy [Baumgarten et al., 2001], employing a horizontal partition in the inlet duct. Partial deactivation of the duct leads to high tumble intensity at part load which supports the charge stratification. The distance required for mixture formation is considerably shorter for air-guided systems than for wall-guided ones, which in theory helps avoid over lean sectors in the combustion chamber. When air-guided engines are compared to wall-guided ones, raw emissions can be lower, EGR tolerance can be higher and NO_X production can be lower [Geiger et al., 1999]. Fuel economy can be good and the compact combustion chamber with centrally-positioned injector can lead to thermodynamically optimal and knock-free combustion [Geiger et al., 1999]. However, if mixture formation and charge stratification are not optimised, engine to engine deviations and cycle to cycle variations can lead to stochastically occurring misfiring cycles. Hence, air-guiding would be a

viable system as long as it can be made tolerant to the cycle to cycle variations resulting from inconsistencies in the air motion.

Spray-guided systems require the ignitable mixture to be sprayed directly into the spark gap location, and with as little as 20 mm between injector and plug, spray-guiding is also known as short spacing. Spray-guiding is characterised by a short mixture formation time before ignition and thus less time for overmixing to occur [Cathcart and Xavier, 2000]. Georjon et al. [2000] found that the best ignition conditions were obtained in the spray tail and that the mixture preparation could be affected by the spray dynamics themselves. High demands are placed on injector design since fine atomisation and perfect axi-symmetry are essential. Air-assist injectors are well suited to spray-guided systems producing diffuse sprays of very small droplets, the sprays having low penetration rates. The air-assist injector developed by Orbital [Cathcart and Xavier, 2000] produced a highly stratified spray at very lean AFRs, using a relatively low fuel pressure, 0.65 MPa. With significant pumping losses at low loads, fuel consumption can be reduced by increasing dilution ratios. However, lower exhaust temperatures accompany this increase, adversely affecting catalyst conversion efficiency. A possible problem with both multi-hole and air-assisted injectors in spray-guided engines is spark plug fouling, leading to the possibility of misfires.

For wall-guided systems, timing of fuel injection, design of the specially-formed piston bowl and geometry of the combustion chamber are all crucial [Baumgarten et al., 2001] since a balance is needed between fuel trapping by the piston bowl and fuel film formation on the piston crown [Kakuhou et al., 1999]. With injection timing set too early: the fuel eludes the piston bowl and the redirecting effect is lost. Fuel reaches the exhaust side of the chamber, preventing stratification and causing large fluctuations of mixture concentration in the vicinity of the spark plug. This is termed overmixing, where the spray becomes too diffused and unstable combustion results. Castagné et al. [2000] confirmed this by comparing their model results from the wall-guided Mitsubishi 1.8 litre G-DI engine. With injection timing set too late, the air is relatively motionless, so the injected fuel impinges directly

on the piston crown [Kakuhou et al., 1999]. This has the advantage that fuel may bounce off the piston, promoting vaporisation, but the disadvantage that a fuel film will tend to remain on the piston. This is termed undermixing, where rich areas are left in the middle of the mixture cloud, particularly in the vicinity of the spark plug. However, there is an increase of liquid film in the bottom of the piston bowl, resulting in poor combustion efficiency and high levels of UHC emissions [Zhao et al., 1997]. For injection late in the compression stroke, Castagné et al. [2000] noted that ignition was reliable, but combustion occurred with difficulty due to the high AFR.

Wall-guided systems have inherent difficulties in reducing emissions since liquid film formation on the piston bowl appears to promote soot and UHC emissions. For an engine that had no readily measurable soot emissions in homogeneous mode, during stratified operation soot formed in zones where the mixture was very lean, ie where undermixing had taken place [Sandquist et al., 1998].

In the absence of wall films, overmixing (quenching) at the boundaries of the air/fuel mixture cloud and undermixing both in the spray centre and on the surface of the piston bowl are the dominating mechanisms for UHC emissions. The amount of overmixing and undermixing varies with change of injection timing. As mixture preparation time (the interval between SOI and ignition) decreases, the effects of undermixing and liquid fuel/wall interactions become more important. To avoid overmixing, the time interval between SOI and ignition must be kept short, ie narrow spacing of injector and spark plug. If the mixture preparation time is reduced too much, though, undermixing increases and CO and soot emissions rise [Sandquist et al., 1998]. Sandquist et al. [2000] found a fuel dependent optimum injection timing that minimised UHC emissions from overmixing and undermixing.

3.4.4 Transition

For a successful G-DI concept, not only must the homogeneous and stratified modes be optimized, but every transition between the two must work well. An overall lean mixture can occur in the transition between low-load stratified

charge and high-load homogeneous charge operation and this is to be avoided since the result may be partial burning or misfires.

The benefits of stratified charge mode are clear to see since the engine can be run unthrottled. However, if emissions are excessive, or if its use otherwise compromises homogeneous charge mode or if transitions between the modes are too difficult to execute, stratified charge may be a redundant mode.

If using stratified charge mode causes problems, it is useful to discover how often this mode is used. Gäfvert et al. [2000] found that during a complete run through the European emission test drive cycle, the simulated engine spent about equal time in each mode. Furthermore, the fuelling strategy they adopted resulted in the engine reverting to stratified charge mode (however briefly) for every gear change. It is thus a high priority to solve the problems associated with the stratified charge mode.

3.5 Summary

This chapter has reviewed G-DI engines by looking at injectors, fuel sprays, operating conditions, modes of operation and the main fuel-guiding strategies available.

Wall-guided engines are in production and remain viable for the future, as a result of their robustness compared to both spray- and air-guided systems. Even so, problems exist with G-DI engines, especially in the area of fuel spray interactions.

Fuel spray/wall collisions are unavoidable in air- and spray-guided systems and it is a deliberate strategy to allow fuel sprays to hit the piston crown in wall-guided engines. Impaction is of critical importance in the stratified charge mode where there is little time for liquid fuel evaporation, so optimisation of G-DI engines requires greater knowledge of groups of droplets/sprays impinging on the piston crown.

It is vital to improve understanding of all fuel spray interactions and the experimental work proposed here will have relevance for other experimenters and modellers, who are attempting to explain the effects witnessed. This Ph.D. aims to increase knowledge of fuel spray/piston crown interactions, concentrating on the stratified charge mode. Chapter 4 describes the optical methods and Chapter 5 the optical engine used to study these events.

Chapter 4
Optical methods

4.1 Introduction

Optical engine studies can be qualitative or quantitative. Different optical techniques are available including flow field imaging of both liquid and vapour phases to reveal spray structures and the path of the combustion flame. They can also provide approximate mass flux measurements and estimate droplet sizes and species concentrations. Some of the techniques are restricted to static testing but others can be used with motored or firing engines. Still images and sequences (both real time and "false movies") are possible. In addition there are several pseudo-imaging techniques.

The physics behind the techniques is well established, but the number of adaptations and variations continues to increase. Furthermore, advances in cameras, lasers, computer software and in the fields of materials (windows, glues, sealants) and chemistry (dopants, seeding particles) help suggest new techniques and improve the quality of existing ones. The following section discusses the main techniques currently available and evaluates which were the most appropriate for the planned tests.

4.2 Spectroscopic techniques: SRs (Spontaneous Raman Scattering), LRS (Laser Rayleigh Scattering), LIF (Laser Induced Fluorescence)

These techniques are laser-based, spectroscopic diagnostics producing two dimensional images of scattered laser light in IC engines [Zhao and Ladommatos, 2001]. If a beam of monochromatic light, say a laser beam, is shone at a transparent gas mixture, a small portion of the light will be scattered, the rest will pass through unaffected. Of this scattered light, the majority will be at the same frequency as the incident light, the remainder will be at frequencies above or below the incident light. The frequency of the scattered light depends on whether the collisions between the photons of light and gas molecules are elastic or inelastic. In the former case, both the photons and gas molecule are unchanged by the collision and no energy is exchanged between them. The light collected will be of an identical frequency to the incident light and this is known as Rayleigh scattering. However, in inelastic

collisions, energy will be exchanged and this is known as Raman scattering [Eckbreth, 1996].

Quantum theory states that the molecule will move to a different energy state, ΔE, away from its initial state where ΔE is the difference between the two allowed states. Either the gas molecule gains energy from the photon or vice versa and the frequency of the resulting radiation will be $\nu \pm \Delta E / h$ compared to ν for the incident beam (h is Planck's constant). If the scattered radiation has a lower frequency than the incident, it is termed Stokes radiation. If the frequency is higher, then it is anti-Stokes radiation. Note that for anti-Stokes radiation to occur, the gas molecules must already be in an excited state [Zhao and Ladommatos, 2001]. In general anti-Stokes radiation has less intensity than Stokes, and Rayleigh scattering has considerably more intensity than either of the Raman modes. Fluorescence is a useful means of highlighting the path or motion of a specific element in a fluid flow. Whereas Rayleigh and Raman scattering occur if the excitation is at the ultraviolet wavelength or any visible wavelength, to obtain fluorescence, a precise frequency is required. This is because molecules will only fluoresce if they move from one rovibronic level (ground state) to an equivalent rovibronic state of higher energy (excited state) [Zhao and Ladommatos, 2001]. Rovibronic excitation stands for rotational vibrational electronic excitation of a molecule [Graybeal, 1988]. A carefully chosen dopant and a laser wavelength to suit ensures that LIF produces images with high spatial resolution. The transitions between electron levels for SRs, LRS and LIF are summarised in Figure 4-1 and the uses of the Raman and LIF techniques are illustrated in Figure 4-2 and Figure 4-3. The ability of SRs, LRS and LIF to determine species temperature and concentrations makes them powerful techniques. In addition, fluorescence from the liquid and vapour phases of the dopant is possible since fluorescence is a volume effect. The ability to detect vapour is rare and this makes LIF particularly useful in engine studies. Other optical methods will now be discussed.

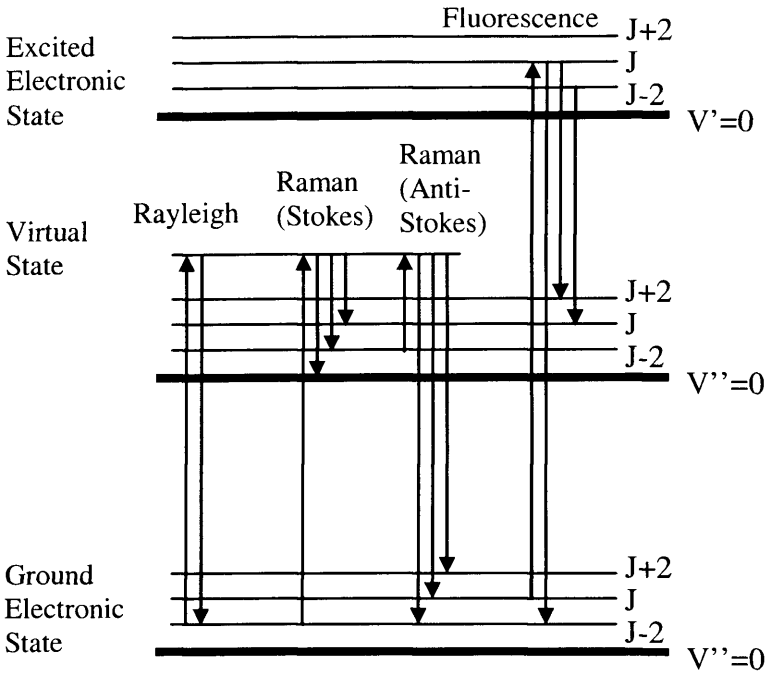

Figure 4-1 Schematic energy level diagram showing Rayleigh scattering, vibrational Raman scattering and LIF [Zhao and Ladommatos, 2001]

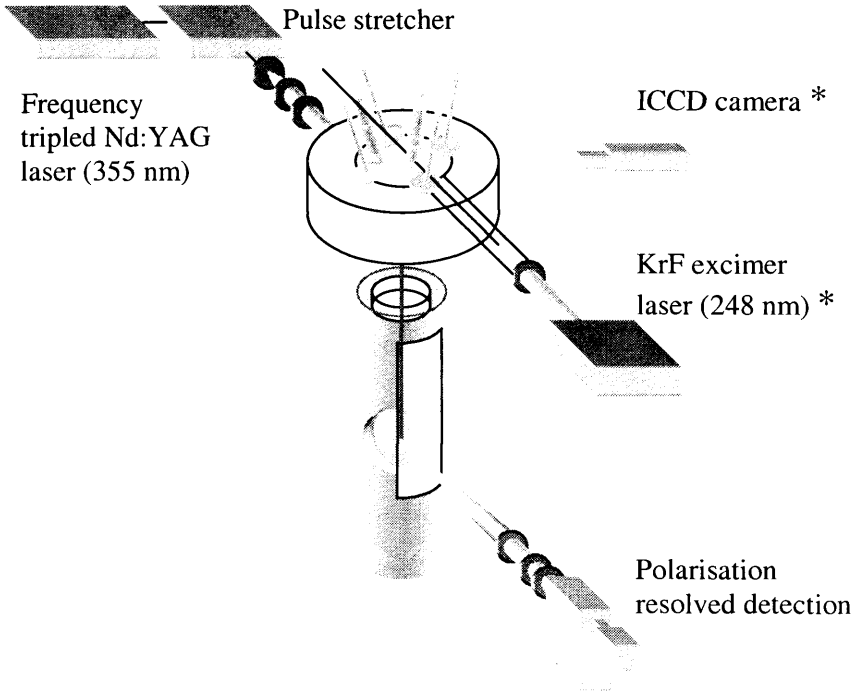

Figure 4-2 Optical engine with setups for simultaneous measurements of 2-d LIF (items marked *) and 1-d Raman spectroscopy [Ipp et al., 2001]

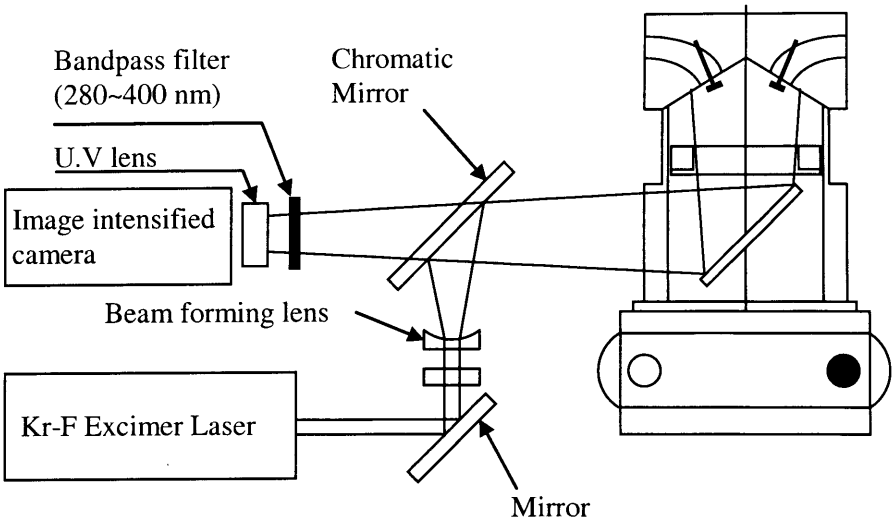

Figure 4-3 Coaxial LIF system for fuel liquid visualization [Kakuhou et al., 1999]

4.3 In-cylinder flow field measurement: LDA (Laser Doppler Anemometry), PIV (Particle Image Velocimetry), PTV (Particle Tracking Velocimetry)

These techniques provide high resolution measurements of flow velocity and turbulence in the cylinder by use of single point and whole field methods. Quantitative use of PTV and PIV can reveal details of complex unsteady flows [Zhao and Ladommatos, 2001].

4.3.1 Laser Doppler Anemometry

In a similar way to the Doppler shift in pitch of a moving sound source, there will be a Doppler shift in laser light when it is scattered by small particles in motion. Hence the flow of a fluid of interest can be monitored by seeding it with suitable particles and analysing the Doppler shift of laser light scattered by the particles. This is the physics underlying LDA. The process is complicated by the fact that the velocities involved are very much less than the speed of light so that the Doppler shift is difficult to measure in absolute terms [Zhao and Ladommatos, 2001]. However, very small Doppler shifts can be measured by applying a photodetector to the light-beating effect which occurs between the incident light and the (minutely) shifted scattered light [Ismailov, 1973]. A novel application of LDA is shown in Figure 4-4. Several options are

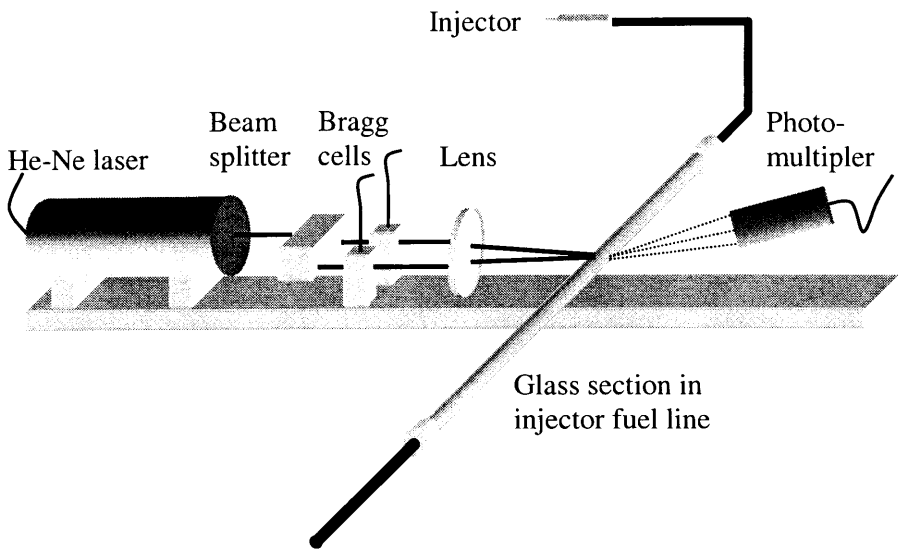

Figure 4-4 Injection rig to measure instantaneous flow rates in high pressure pipeline of G-DI engine [Ismailov, 1973]

available for analysis of the data, including ensemble averaging, use of low-pass/high-pass filtering and application of correction functions to the averaged velocity. The first is the most popular, even though the results cannot be cycle-resolved [Zhao and Ladommatos, 2001].

4.3.2 Particle Image Velocimetry

PIV is able to produce velocity vectors for the instantaneous motion of particles introduced into gas flows.

The camera is fixed on the area of interest and two still images are taken within a very short time interval. The velocity vector is found from the displacement of the particle and the known time interval [Zhao and Ladommatos, 2001].

A laser light sheet is formed with the camera set perpendicular to it. The laser is double-pulsed to provide the two images, stored as separate frames, or sometimes on the same frame. Kubo et al. [2001] used two charge-coupled device (CCD) cameras, capturing light through one lens, Figure 4-5. Electronic control was used to manage the gating period and delay of each camera.

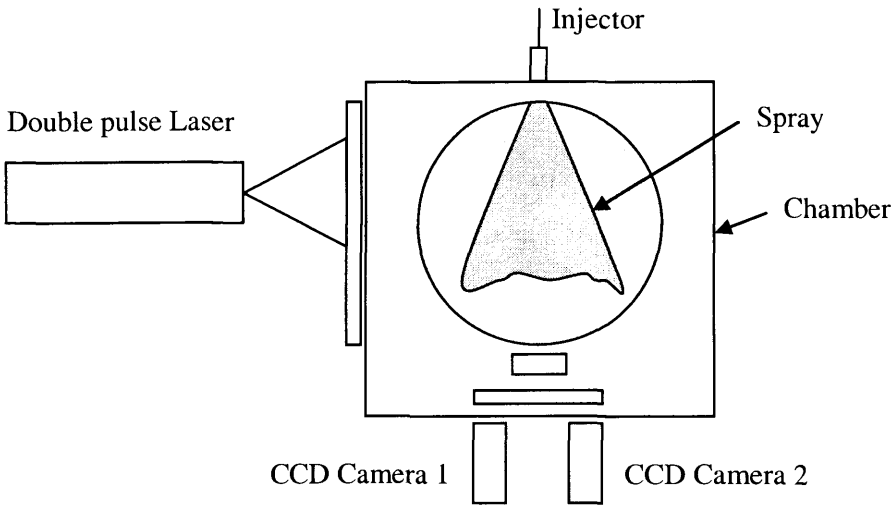

Figure 4-5 Two CCD cameras recording PIV data from injector in pressurised chamber [Kubo et al., 2001]

Once the two sets of data have been obtained, interrogation methods are applied to determine the displacement of the particles. With low populations of seeding, the interrogation could be completed manually, giving rise to the term Particle Tracking Velocimetry (PTV). The information gleaned from this approach would be relatively imprecise. Computer-based analysis methods became obligatory with dense seeding and the method becomes known as PIV.

Firstly the image is divided into a large number of square regions, based on a regular grid. For the first image: one matrix is established for position and another for intensity. This is repeated for the second image and the assumption is made that the displacement of all particles is constant. Vector manipulation of this information then reveals a separation vector for the correlation plane. A distinction can be made between uncorrelated pairs (this corresponds to background noise) and correlated pairs of particles, ie those of interest. The data can be presented in the form of arrows for the complete field. The direction of the arrow shows the path taken, and the length indicates the magnitude of velocity [Zhao and Ladommatos, 2001]. The most commonly used PIV method is two-frame cross-correlation which avoids directional ambiguity, at the expense of slightly inferior spatial resolution.

4.4 In-cylinder liquid fuel measurement techniques

The most used and simplest techniques for characterising fuel sprays are direct imaging methods recorded using single frame film cameras and CCD cameras, possibly applied in a way that would allow holographic images to be constructed. Droplet size distributions can be found by use of light-scattering techniques or direct-imaging. The former divides into integral and particle counting. Fraunhofer lends his name to the main integral method and the principal particle method (droplet method in the context of fuel sprays) is PDA (Phase Doppler Anemometry) [Zhao and Ladommatos, 2001].

4.4.1 Fraunhofer

The Fraunhofer method uses the distinctive pattern produced by particles diffracting light in order to determine the size of the droplets causing the diffraction [Eckbreth, 1996]. Monochromatic light in a parallel beam (usually from a laser source) is shone at the cloud of droplets (Figure 4-6). The pattern is captured by a lens with Fourier transfer properties and consists of dark and light rings, corresponding to maximum and zero intensities [Jenkins and White, 1981]. An array of photo-detectors measures the intensity of the distribution. Complex algorithms and a least-squares minimisation-of-errors technique are required to relate this information to the particle size. Software developed by Malvern Instruments Limited, but whose details are unknown, assists with this. Malvern droplet size analysers do not require calibration although it advisable to validate their results.

4.4.2 Phase Doppler Anemometry (PDA)

PDA provides droplet diameter information using the fact that rays of light interacting with a sphere undergo phase changes according to the nature of their interactions (Figure 4-7). The principal interactions are: rays which are reflected from the sphere front surface, rays that are transmitted or refracted by the sphere and rays which are internally reflected/refracted in a backward direction [Zhao and Ladommatos, 2001]. A theoretical ray emanating from the centre of the sphere is considered. Path length differences exist between each incident ray and the reflected/refracted rays. Once these differences are found, the phase difference can be computed. Thereafter the techniques described for LDA can be applied. A limitation of PDA is that the control

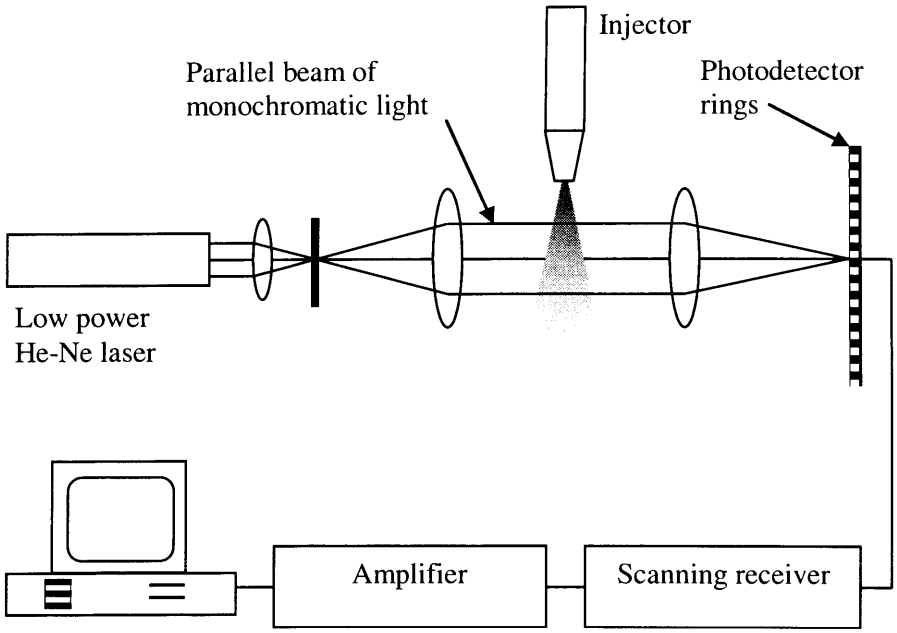

Figure 4-6 Experimental setup for Fraunhofer diffraction technique [Zhao and Ladommatos, 2001]

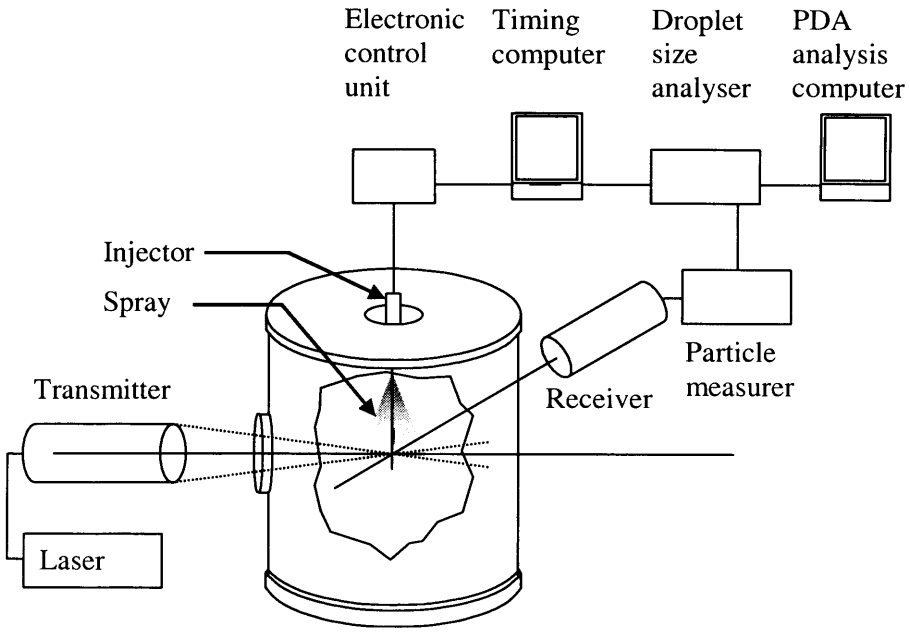

Figure 4-7 Schematic for PDA tests [Williams et al, 2001]

volume must contain only one particle. One disadvantage of this technique is that three different access points are required within a cylinder, one for the incident and two for the reflected/diffracted rays, set at different angles.

4.4.3 Mie scattering

The Mie theory of scattering was developed by the German physicist Gustav Mie in 1908 [Zhao and Ladommatos, 2001]. Use of the technique is straightforward since it is the droplets which cause the scattering, no dopant is required and a non-intensified CCD camera can be used (Figure 4-8). This is true as long as the droplets meet certain criteria, chiefly that the wavelength of the light used must be much smaller than the diameter of the droplets, ie diameter/wavelength >>1 [Eckbreth, 1996]. This corresponds to droplets larger than 0.5 μm if visible light is used. A Nd:YAG laser will produce suitable light and is especially effective if the light is formed into a sheet, using suitable optical elements. The sheet is arranged to pass through an area of interest at such an angle that light scattered from the droplets is collected in a plane perpendicular to the sheet. The Mie signal is strong enough so that a non-intensified CCD camera can be used [Ipp et al., 1999]. Alternatively, a high speed rotating drum camera would enable movies to be made, assuming the laser repetition rate is high enough. However, CCD cameras allow better manipulation of the images and are more frequently used.

4.4.4 Laser Induced Exciplex Fluorescence (LIEF)

LIEF is not a true optical technique although Zhao and Ladommatos [2001] believe it is since the results have a visual element. Melton and Verdieck [1984] coined the term exciplex from 'excited state complex'. Their work addressed the problem of distinguishing between fluorescence from vapour and liquid fuel. The absorption and fluorescence spectra from organic molecules dissolved in non-polar solvents are virtually identical whether in the vapour or liquid phase. Experimental work (Figure 4-9) is further hampered because the vapour fluorescence signal is considerably weaker than that from the liquid fuel [Ipp et al., 1999]. LIEF allows the vapour phase to be monitored even in the presence of liquid phase by weighting the proportion of exciplex species in the mixture. If a fluorescent molecule M* reacts with a dopant dopant molecule, G, while M* is in an excited state, the M* G species,

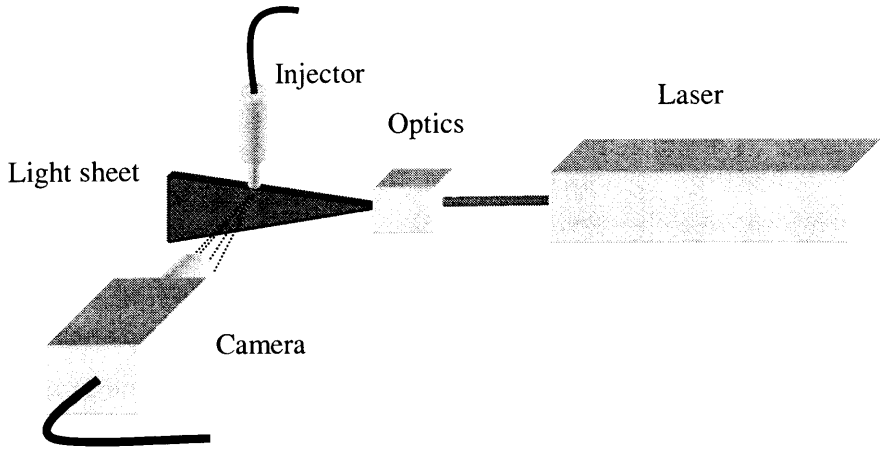

Figure 4-8 Experimental setup for 2-d Mie scattering experiment [Ipp et al., 1999]

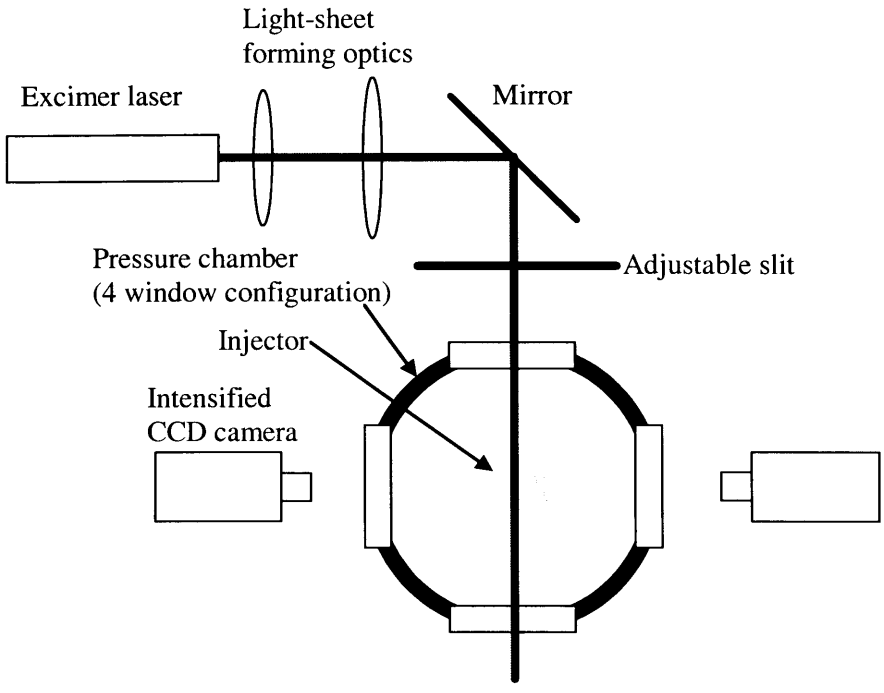

Figure 4-9 Schematic of setup for linear LIF (with exciplex tracer) using a pressure chamber [Befrui et al., 2002]

known as (M-G)*, will also be in the excited state [Eckbreth, 1996]. A red shift then exists between the fluorescent emissions from (M-G)* and M. M and G are chosen to have an adequate separation of emissions peaks. The

reaction of M and G is reversible which makes it possible to have (M*-G) as the dominant emitter in the liquid phase, leaving M* the dominant emitter in the vapour phase. The emissions from the markers can be filtered and measured to give qualitative information, ie a visual record of the mix of vapour and liquid [Zhao and Ladommatos, 2001]. PLIEF is a variant on LIEF, where a light sheet is used, thus interactions in a plane of choice can be studied.

4.4.5 Laser extinction/absorption (LEA)

Simultaneous measurement of fuel vapour concentration and liquid droplet concentration is possible using the LEA technique. A light beam incident on an evaporating spray will be attenuated by scattering (from the liquid drops) and absorption (by both the liquid and vapour fuel). Measurements of transmission are taken both at an absorbing wavelength and at a non-absorbing wavelength (Figure 4-10). The vapour concentration is found indirectly from the difference between these measurements [Zhao and Ladommatos, 2001]. Knowledge of the droplet size distribution is obtained using the Fraunhofer method (see § 4.4.1). Then the intensity, scattering and extinction efficiency functions have to be combined. This provides the raw data from which fuel vapour and liquid droplet concentrations can be derived.

4.5 Visualisation of in-cylinder events

Photographic film is mainly being superseded by photoelectric devices, the latter having the advantages of instantaneous referral and the ease by which software can be used to analyse the images. For both these media, two main strategies are available: firstly intermittent recordings at high shutter speed. This is known as high-speed single-shot, where, for instance, one image is taken per cycle, and assembled into a 'false' movie. By contrast, in the high-speed continuous approach, hundreds or even thousands of images per second are recorded in a continuous sequence from one cycle. In both methods, light is introduced into the volume of interest and some of the resulting interactions can be captured by a camera. Essential equipment includes a light source and high-speed enabled camera. Pulsed or continuous light sources, with adequate brightness, repetition rate and spectral distribution are suitable [Zhao and Ladommatos, 2001]. The very short duration of a pulsed source is preferable

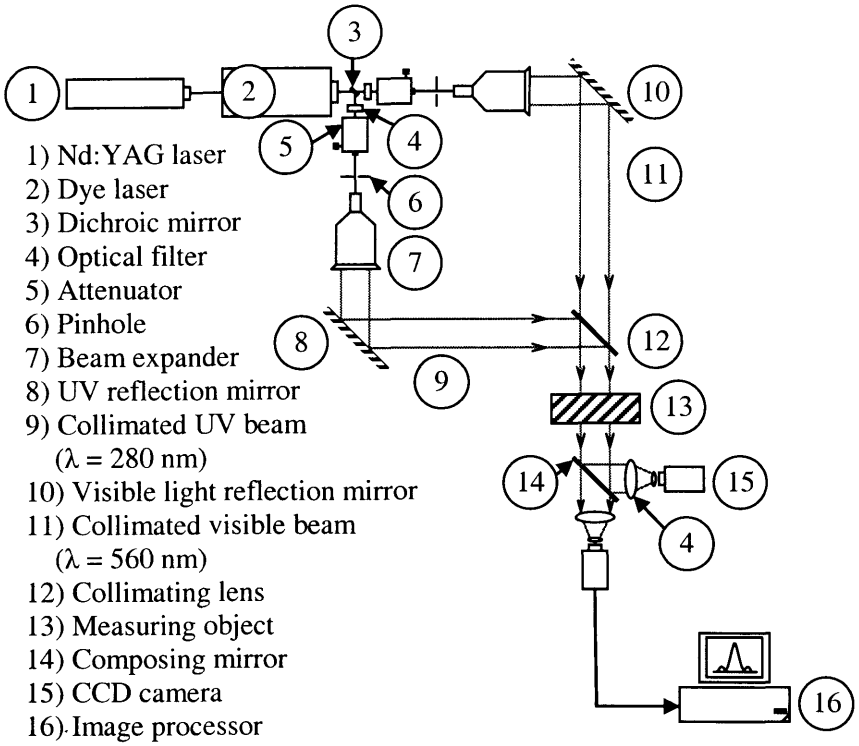

Figure 4-10 LEA imaging system [Suzuki et al., 1993]

for single-shot work, where the duration defines the resolution of the system. Lasers are generally used for high-speed continuous work, with certain Nd:YAG lasers able to deliver pulses of 30 ns duration or less, at repetition rates in the kHz range. The final element is the camera, with high-speed cine film, electronic imaging and high-speed video CCD cameras the main choices.

Cine cameras include rotating drum and rotating prism designs where both the film and the final element of the optical system move to produce combined speeds of up to 200,000 frames per second, see (Figure 4-11 and Figure 4-12). With the rotating prism design, a proportion of the film is usually wasted before the device reaches the correct speed, but high resolution images are still possible and other data can be projected onto the film as a reference track. The rotating drum camera uses a different principle which involves spinning a drum, internally lined with film, up to speed first and directing light on to it using a rotating optical element.

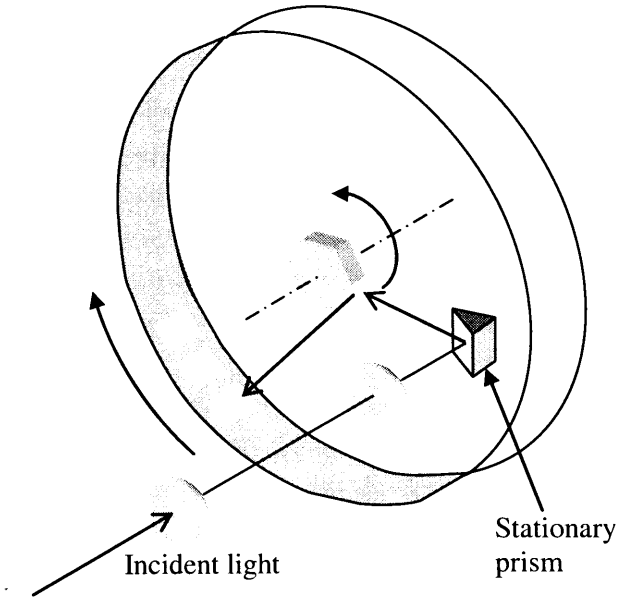

Figure 4-11 High-speed rotating drum camera [Zhao and Ladommatos, 2001]

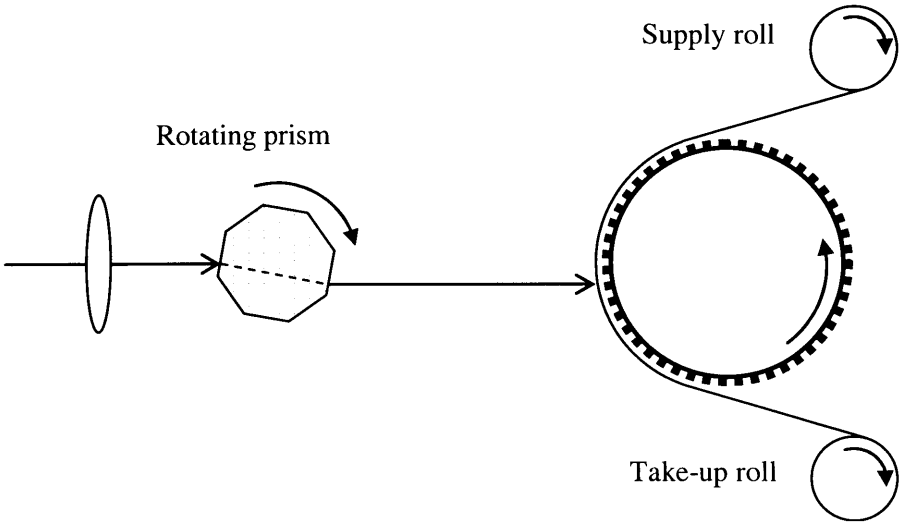

Figure 4-12 High-speed rotating prism camera [Zhao and Ladommatos, 2001]

Electronic imaging cameras use an image converter tube whereby photons develop arrays of electrons which represent the image [Befrui et al., 2002]. A re-conversion back to photons is used for storage (on film or CCD) but since the image manipulation is non-mechanical, frame rates of 10,000 to 20 million

per second are possible. These systems also have the advantage of great flexibility of timing and exposure duration [Zhao and Ladommatos, 2001].

High-speed video cameras typically have a maximum recording time of 30 seconds, during which 200 to 4,500 frames per second can be stored on videotape or in solid state memory. Although sharp images (ie the 'freezing' of events) are possible using an integral stroboscopic light, a high-repetition laser is essential for in-cylinder studies.

In general, film has the advantage of high resolution and high data acquisition rates, but the disadvantage of a non-linear response curve and long processing times [Zhao and Ladommatos, 2001]. With solid state cameras, instant feedback is possible, eliminating delay in adjusting equipment; it can be more sensitive than film and has a linear response. Furthermore, low-light studies are possible with the addition of an intensifier. The initial disadvantage of solid state devices is the frame capture rate which was limited to 50 Hz or lower, but considerable development has taken place in recent years such that rates of the order of 250 Hz [LaVision, 2004] and even 1000 Hz [Photonic Science, 2004] are claimed.

4.6 Schlieren and Shadowgraph photography

These techniques (Figure 4-13 and Figure 4-14) are very useful in auto-ignition and knock research since both are able to detect density changes and are thus well suited to studying non-luminous events [Georjon et al., 2000].

The physics underlying the schlieren technique also explains the shimmering seen above heated surfaces. Namely, the amount of refraction experienced by a ray of light is proportional to the refractive index of the medium in which it is travelling. If the refractive index is not constant in a fluid, light passing through the fluid will refract by varying amounts. A means of augmenting the effect is the placement of a knife-edge in front of the camera, blocking roughly half the light [Jenkins and White, 1981]. Turbulent flow has regions of varying densities and consequently varying refractive indices. Transmission through these regions will refract the light to a greater or lesser extent.

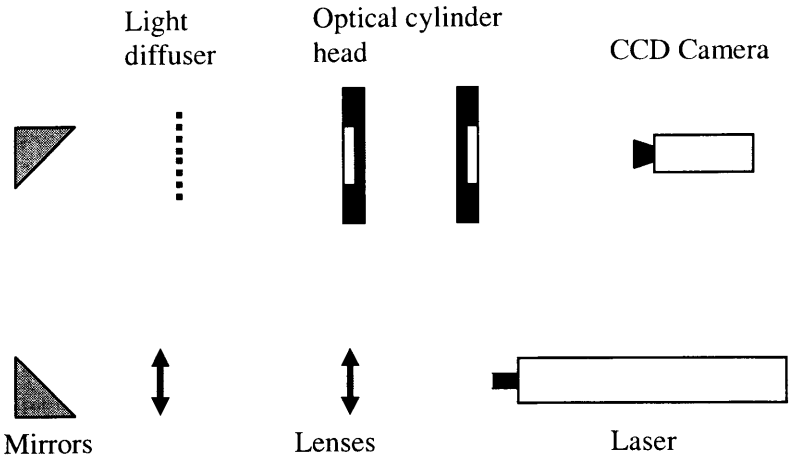

Figure 4-13 Experimental configuration for back-lighting method [Georjon et al., 2000]

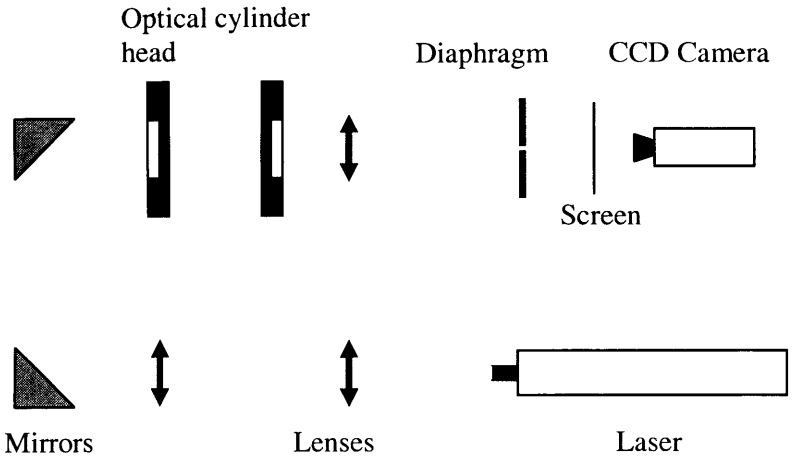

Figure 4-14 Experimental configuration for schlieren method [Georjon et al., 2000]

Hence, some rays that would have entered the camera will now strike the knife-edge and other rays that would have struck the knife-edge will enter the camera. This is evident as regions of light and dark. When the schlieren technique is applied to engines, the volume of interest, ie the combustion chamber, is positioned between a light source and a camera. Changes in density in the combustion chamber can thus be observed and recorded [Georjon et al., 2000]. The method used for shadowgraph photography is similar except that no knife edge is used. This results in schlieren being sensitive to the first derivative of density, whereas the shadowgraph method is

sensitive to the second derivative [Zhao and Ladommatos 2001]. The schlieren approach is often preferred for flow visualisation since greater contrast is achievable compared to the shadowgraph technique. However, for engine applications, steep enough density gradients are possible with shadowgraph. It can be cheaper to run a shadowgraph system since it tolerates lower quality optical components. Furthermore, the knife edge used in schlieren work means that even slight motion of any mirrored surface (ie a piston crown) disrupts the captured image.

4.7 Multi Ionisation Probes (MIPs)

The data from MIPs should be considered as being pseudo-optical. The technique works by measuring current flow through a series of ionisation probes. A voltage across the probe induces the current, the strength of which depends on the probe surface area, the magnitude of the voltage across it and the density of ions in the surrounding atmosphere. The surface area and voltage can be regarded as constants leaving ion density as the only variable [Zhao and Ladommatos, 2001]. Since burning gases are a strong source of ions, locating the probe in an engine combustion chamber will produce a sudden and marked increase in the signal corresponding to the arrival of the flame front. A grid of such probes, carefully located around the piston and combustion chamber will permit accurate mapping of the transit of the flame front (Figure 4-15).

One disadvantage of the technique is the difficulty in routing the probe wires back to the monitoring unit, particularly for piston-mounted devices. In addition, extensive machining of the head is often required. Witze and Bopp [1991] overcame these difficulties by producing a head gasket which incorporated the probes, although it was used only in a low compression ratio research engine. Some advances have been made by including the probes in printed circuit boards and judicious choice of materials has permitted a probe life of several hours in a production engine [Jackson et al., 1996].

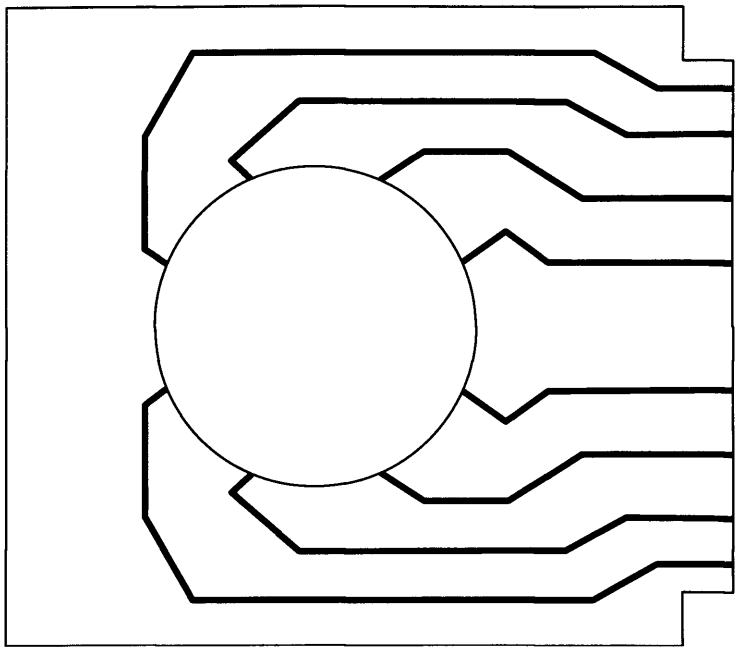

Figure 4-15 Head gasket consisting of instrumented probes on a printed circuit board [Zhao and Ladommatos, 2001]

4.8 Multiple Optical Fibres (MOFs)

The principal use of MOFs is for recording flame kernel development. An individual fibre optic is able to guide light along its length to be received by recording equipment. The assembled information from a number of such probes can accurately track the path of the flame. Each individual fibre optic consists of a core and cladding arrangement [Zhao and Ladommatos, 2001]. The materials are carefully chosen in respect of their relative refractive indices. This means that light entering the probe undergoes a series of total internal reflections such that it emerges at the far end of the fibre optic with relatively little attenuation. Although the use of MOFs precludes the need for large optical windows, disruption to the engine is inevitable. The set up used by Spicher and Velji [1984] required many drillings and tappings in the cylinder bore. The specially adapted spark plug (Figure 4-16) developed by Witze et al. [1988] contained eight fibres, was less invasive and tried to achieve a more comprehensive view - however, once the tips of each fibre optic were protected against the heat and pressure of combustion, the gathering angle led to a somewhat restricted view of the combustion chamber.

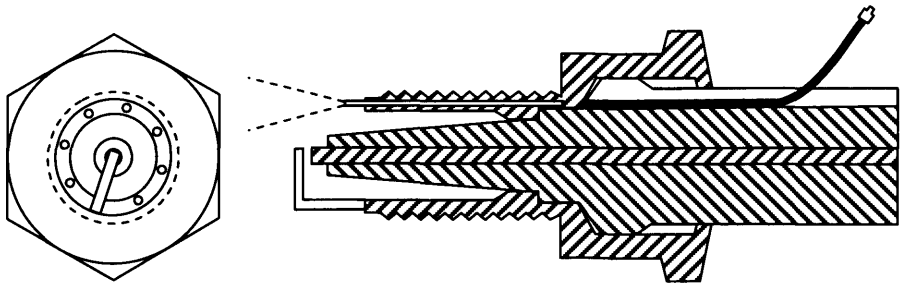

Figure 4-16 Spark plug probe containing seven optical fibres [Witze et al., 1988]

4.9 Endoscopes

Some endoscopes require a hole no larger than that for a pressure transducer. In a firing engine, however, tip cooling will be required since the maximum operating temperature of the probe is around 110^0C [Zhao and Ladommatos, 2001]. This can make the scope too bulky to fit through the transducer hole and limits probes of this size to non-firing work. A bulkier scope will fit through an engine valve hole (on 4-valve engines) but this will inevitably disrupt flow. A solution for the future may be the spark plug endoscope designed by Shepheard et al. [2002], Figure 4-17. This device has the advantage that the spark plug remains operative, allowing the engine to be fired as normal. Cooling is included, the endoscope has a machined end to widen the acceptance cone and the probe also includes a fibre optic to provide a light source.

4.10 Conclusion

Both SRs and LRS are unsuitable for the present work: LRS is best used for measuring air fuel ratios while the SRs technique requires special fuels and the engine may only be motored. The overriding concern, though, was that the signal from both SRs and LRS would be overwhelmed by any Mie signal present.

PIV and LIEF can both be termed "pseudo-optical" techniques since they do not produce true images of sprays. PIV is useful for measuring nozzle velocities and can provide velocity profiles, although a choice must be made

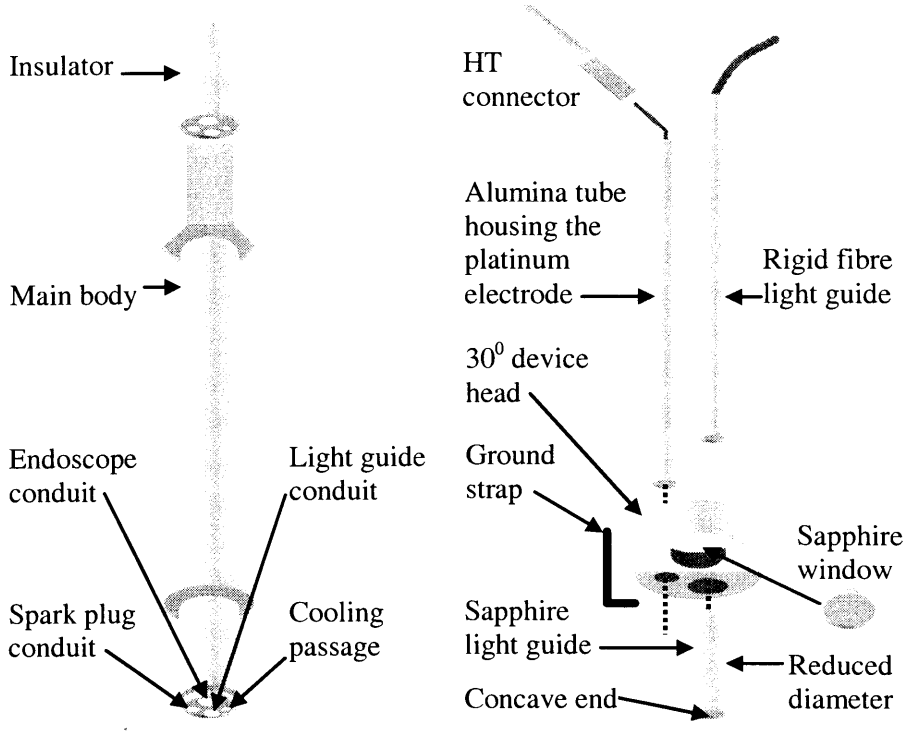

Figure 4-17 Optical device main body (left) and components (right) [Shepheard et al., 2002]

between directional ambiguity and spatial resolution. This detailed information would be useful in some contexts, but in this investigation, the main interests were how the fuel was distributed relative to the spark plug and information on its evaporation. LIEF is in theory capable of detecting liquid and vapour phases simultaneously. However, one tracer is required for each phase. Doubts about how the dopant evaporates compared to the carrier fuel are at least doubled and so this technique was not adopted.

The usual applications of the LEA, Fraunhofer and PDA techniques are in measuring droplet sizes and even though PDA can also determine axial and radial velocities of sprays as well, these were not crucial to the present work.

The LDA and LDV techniques are primarily used for measuring velocities. LDA can provide flow images, but it adopts a point-wise approach and so was inappropriate for this work which required a global picture of behaviour.

If the equipment for high-speed photography had been available, it may have been considered. Even so, the main drawbacks in its use are the prolonged set up time required (a whole film must be shot before any adjustments can be made) and the potential loss of quality in processing the images.

Among the capabilities of schlieren and shadowgraph techniques are the imaging of sprays and the measurement of cone angles and spray penetration distances. However, they are poor at visualising the interior of spray cones and a complex correction is necessary if the viewing windows have sufficient curvature to act like a lens. Such correction would be unnecessary if flat windows were used, but it was felt that these would be too disruptive to the in-cylinder flow. The strength of these techniques lies in auto-ignition and knock studies so they were not used here.

Whereas MIPs can only be used for detecting flame arrival and location of end-gas, MOFs, can be used to visualise fuel sprays. Their installation in the engine, though, can be so invasive as to render the engine unrepresentative of an equivalent non-optical engine. Therefore, neither MIPs nor MOFs were used in the testing.

Although endoscopes can directly visualise sprays, there are some (serious) reservations about their use. The fixed location restricts the choice of view and, though the fitting of a wide-angle lens helps, distortion is pronounced. In addition, their use may be restricted to the period of combustion to use the combustion flame as illumination since they transmit too little light on their own. For this work, the spray behaviour before spark was of vital importance. Endoscopes may be useful for verification, but were not used as the main imaging tool.

The main advantage of the Mie scattering technique is the strength of the signal available from the liquid fuel. In addition, it is relatively easy to set up, interpretation of images is straightforward and it has been successfully used in several previous UCL studies. It was therefore adopted as the technique to visualise liquid spray behaviour in these tests.

LIF is a powerful technique, able to distinguish between rich and lean areas of fuel and capable of visualising liquid and vapour phases simultaneously. It is also an established technique at UCL. However, the signal can suffer from quenching, experiments may be difficult to set up and great care must be taken in selecting dopants. Despite these reservations, it was selected as the imaging technique to visualise the vapour phase in the tests.

Having established that the Mie and LIF techniques were the most suitable for the studies, the next chapter describes the optical engine designed to allow their application.

Chapter 5
Design of test rig

5.1 Introduction
Previous chapters predicted that the G-DI engine will be able to meet increasingly stringent emissions legislation. However, when G-DI engines are run in stratified charge mode, excessive smoke emissions can occur. A discussion of the optical methods best suited to studying and subsequently improving combustion was presented in Chapter 4. The techniques of Mie scattering and LIF were chosen to investigate fuel spray interactions in the Jaguar G-DI engine in stratified mode. Chapter 5 now details the design of an optical version of the Jaguar engine suitable for carrying out these investigations. The chapter begins with a brief review of previous optical engine work at UCL, then sets out the specification of the optical engine required for the present study. The design philosophy is presented next, followed by a discussion of the design challenges faced and the materials selected. The chapter ends by detailing the specific design tasks.

5.2 Review of UCL optical engine work
Miller [1992] designed several rigs to compare carburettor and MPFI performance in the Ford V6 and Zeta engines. The study found that use of MPFI led to better cold starting, improved stability of combustion and reduced fuel consumption at idle. The part of Miller's work that was most applicable to the current study was the use of the Malvern droplet size analyser. However, since accurate sizing could only be achievable outside the engine, it was not considered for use here.

Work by Fry [1994] on a Jaguar ECP2 MPFI engine was divided between a steady flow rig and an optical engine. The study showed that a 'ski-jump' movable valve in the intake port created tumble, improving combustion performance. An air-assisted atomiser (AAA) produced very fine droplets, which increased the evaporation rate and reduced emissions of UHC. By contrast, pintle-type injectors were found to produce a jet rather than a spray, increasing levels of UHC. This optical engine proved very effective in observing the complex nature of induction processes. Useful results were

produced, despite the limitations of the optical techniques available at the time. Some of the designs on which present UCL optical work is based were developed by Fry, including a Bowditch piston riding past an angled mirror, quartz piston crowns and quartz windows in holders. The Bowditch piston and angled mirror concepts were adopted in the current study.

An air-assisted fuel vaporiser (AAFV) with a heating element was initially conceived by Fry [1994] and then developed by Jackson [1997]. It was proposed that vaporising the fuel during cold start could be an alternative to heating the catalyst. Testing used an engine with the optimised composite injector. The electrical energy needs of the AAFV were similar to those of a heated catalyst. The optical elements of Jackson's work were unsuitable for the current study.

A Ford Zetec MPFI engine was converted to stratified mode by Queenan [1998] as a means of reducing emissions. Several optical techniques were applied to the engine in MPFI mode to study the path of fuel using a variety of injectors (Figure 5-1). This led to the conversion to stratified mode and emissions testing showed this to be a fruitful endeavour. This was another example of the Bowditch piston, quartz crown and angled mirror approach that was adopted in the current study.

A new technique known as PPT (phosphorescent particle tracking) was developed by Guerrier [1999]. A different tracer material could be used for each of a number of flow streams. The potential of this approach was its ability to show how two incoming streams interacted in lean burn engines. The results from Guerrier's work were impressive. They suggested possible future work on the current project, but were not adopted as further development is necessary before its full potential is reached.

Davy [2000] developed an optical engine to study fuel sprays and combustion

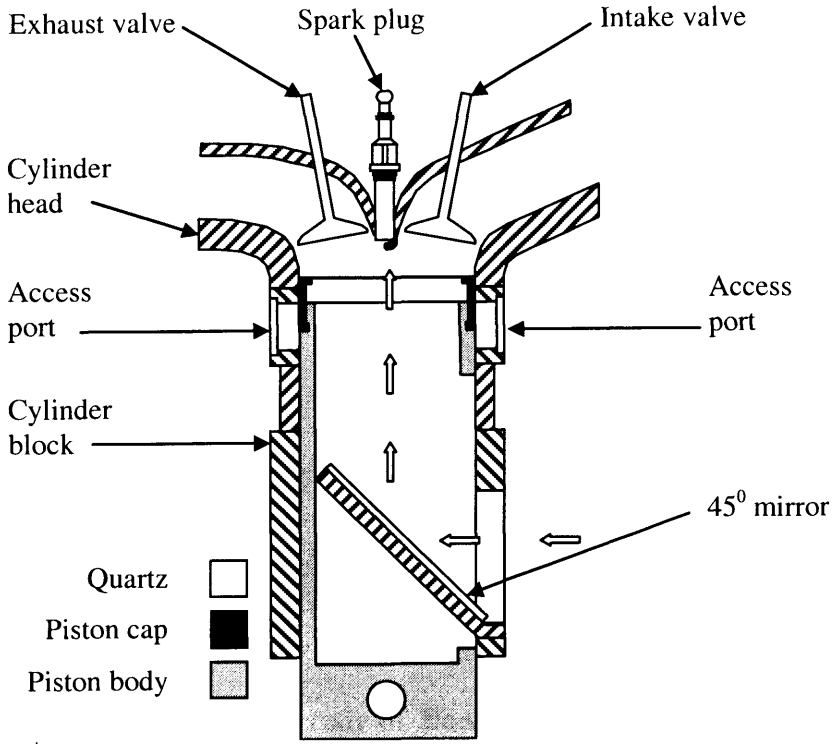

Figure 5-1 Optical path into the combustion chamber [Queenan, 1998]

in a G-DI cylinder head designed for homogeneous combustion. The work revealed the factors affecting liquid phase fuel behaviour. Flash boiling was found to be the major factor influencing the mixing of fuel and air. The present study began in Davy's test cell so that the general layout (Lister bottom end, electric motor and dynamometer combination) was the same. Davy's camera, laser and optics bench were also used for this work although a considerable number of changes were required, particularly when the engine had to be switched to a newly-constructed test cell. The Bowditch piston and mirror arrangement were based on Davy's work (Figure 5-2) and his choices of dopant and test fuel were adopted.

Work carried out on a homogeneous G-DI engine design by O'Donoghue [2002] established relationships between fuel spray structure, emissions and fuel economy. The 'design of experiments' work was non-optical except for the superimposition of images recorded on static test rigs onto schematics of the cylinder, combustion chamber and piston. O'Donoghue produced a very useful library of spray images, but his engine work was essentially non-optical.

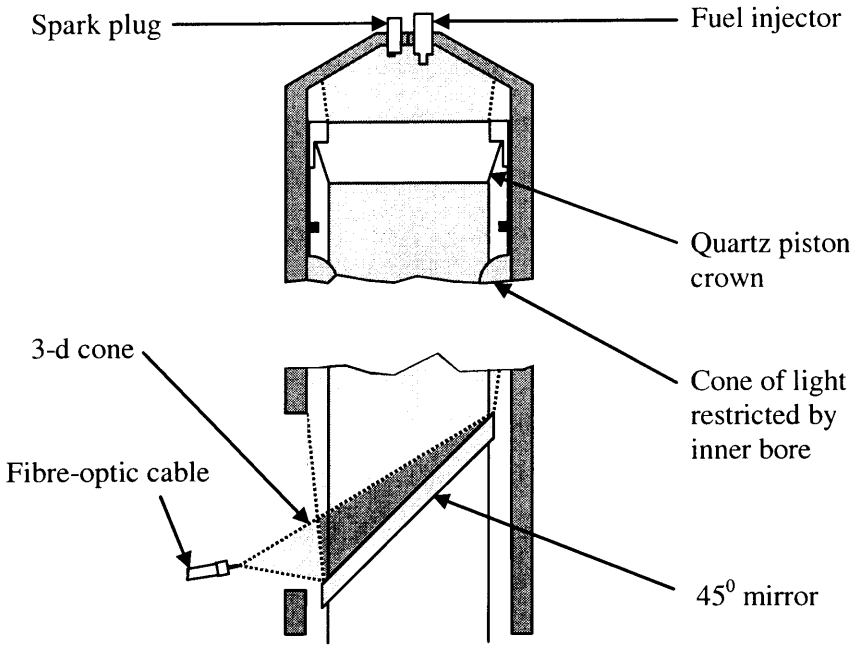

Figure 5-2 Schematic diagram of flood illumination applied to optical engine [Davy, 2000]

Shepheard [2002] developed an endoscope to view events in an engine operating at normal speeds and loads. The device acted as a working spark plug so modifications to the engine were not required and preliminary images showed much promise. Even when fully developed and tested, though, light levels would be too low for LIF work. Hence it was not selected for the current work.

Loustalan [2005] investigated the near nozzle behaviour of a pressure-swirl injector to explain the effects of fuel pressure, back pressure and impingement of air flows. The images from the study act as a good reference source, but since the tests were conducted on various designs of static rig they will not be carried forward into the present study.

The block, Bowditch piston and angled-mirror arrangements used by Fry, Queenan and Davy formed the basis of the optical engine in this study. The current design differed from the earlier work in that the block was designed to be split into two sections, the quartz windows were not in carriers and the piston crown had a complex computer numerically-controlled (CNC) machined profile as compared to the flat-top arrangements of the earlier work.

The flanged joint in the optical block allowed the cylinder head to be raised for window cleaning. This approach had the advantages of preserving the engine timing during cleaning and of allowing the head to be used for static testing. As a result, the simpler option of bonding the windows into the block could be used. The piston crown quartz windows were also bonded in position.

5.3 Specification

The principal parts of the Jaguar G-DI system were the cylinder head, the fuel injector and the contoured piston. The head was a 4-valve pent roof design, with a central spark plug and a pressure swirl, side-mounted, injector (see Figure 5-3). The bore of the engine was 89 mm and the stroke was 79 mm. Jaguar supplied the cylinder head together with a computer-aided drawing and design (CADD) file of the piston crown and the optical engine was built around these items. It had to fit into an existing test bed (see § 6.2), be suitable for benchmark testing and allow Mie scattering and LIF images of the fuel interactions to be recorded

The benchmark testing involved motoring the engine up to 1500 rev/min with a load applied to the crankshaft, initiating combustion and, after a brief period of allowing the engine to warm up, various readings were recorded to check on engine performance. For the Mie scattering and LIF studies, the engine was again motored but only fired in short bursts to avoid fouling of the windows. Optical access was provided by the cross-bore mirror and the quartz windows in the block and piston crown. The piston window matched the contours of the bowl, the side windows permitted access right up into pent roof and the cross-bore mirror allowed laser light into the combustion chamber. A choice of piston crowns and a rotatable section of the optical block built some flexibility into the design. The principal requirements of the optical engine were to be robust, simulate the real engine as closely as possible and maximise optical access.

5.4 Design philosophy

Careful consideration was given to safety, so each item and the assembled test rig were safe. The inlet/exhaust flow passages and the combustion chamber

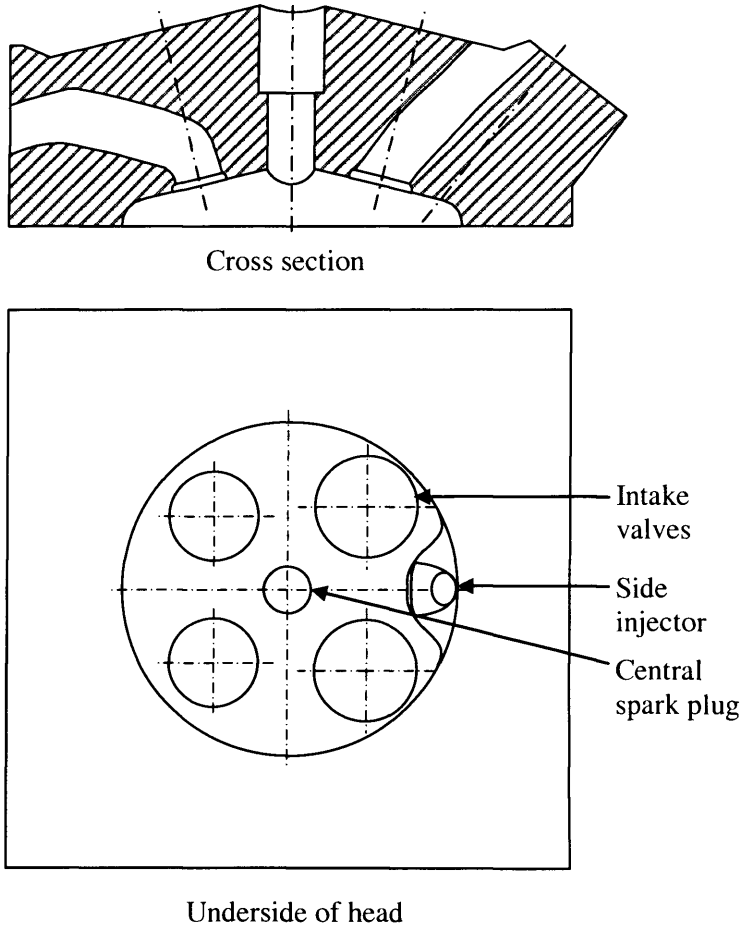

Figure 5-3 Schematic of Jaguar 4-valve pent roof G-DI cylinder head

formed between the cylinder head, cylinder and piston were designed to replicate the Jaguar G-DI design so far as was possible. Ease of operation was achieved through simplicity of design. Since meticulous cleaning of the mirror and quartz windows was crucial to obtaining the best possible images, the design ensured that frequent cleaning was convenient. Steps were taken to ensure that the exchange and cross-checking of ideas and data with computational fluid dynamics (CFD) researchers was optimised. Finally, where possible, the test rig was designed to accommodate future projects.

5.5 Design challenges

The greatest challenge was the design of the contoured pistons. The shape of the Jaguar G-DI piston was complex yet this had to be reproduced with the required optical access. A further challenge was to integrate the various materials used in the design, particularly given their range of coefficients of thermal expansion. Figure 5-4 shows the principal parts of the engine. The next section describes the selection of materials used.

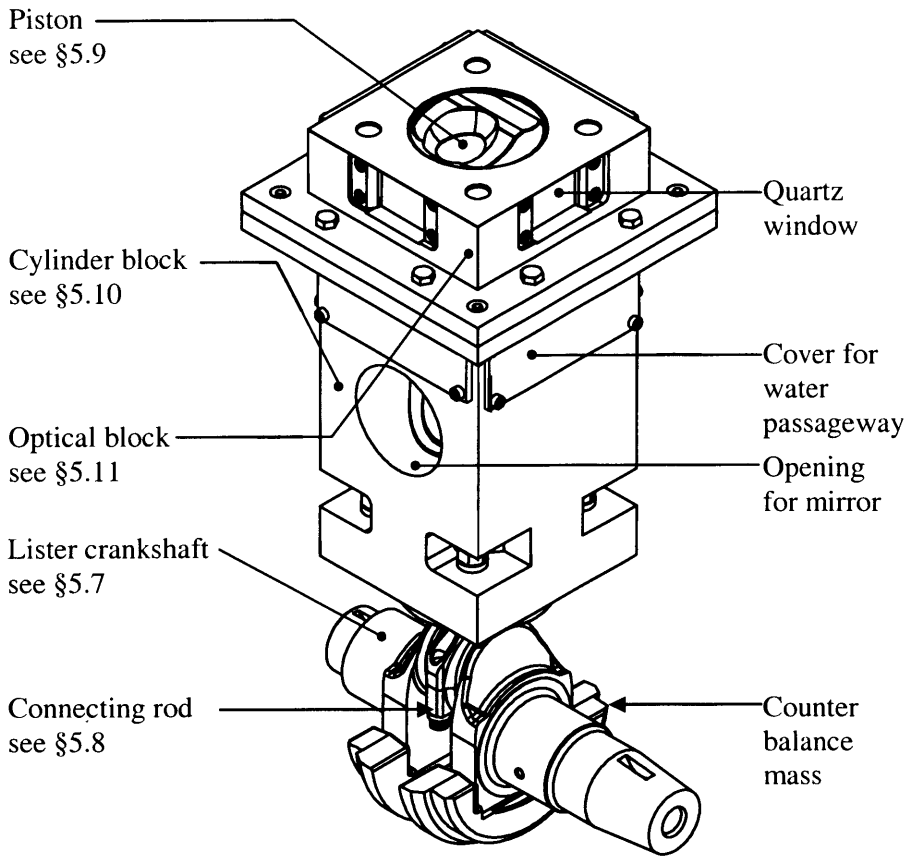

Figure 5-4 Principal parts of UCL/Jaguar optical engine

5.6 Material selection

5.6.1 Introduction

Corrosion and voltaic effects were unlikely to be a problem, but the combustion chamber surface temperatures of around 100^0C meant differential thermal expansion had to be taken into account. This section explains how the material choices were made.

5.6.2 Critical joints

There were several locations in the optical engine where different materials came into close contact. For example, the Jaguar head (aluminium) was bolted to the optical block (cast iron), via a copper gasket and next to a fused silica window. The piston contained two aluminium sections bolted to a steel retainer as well as a fused silica plug in an aluminium crown. A pyrex substrate, aluminium holder and the meehanite block were in close proximity at the mirror.

5.6.3 Precautions

The chance of damage by differential thermal expansion was lessened by careful design of the confluence points. Correctly torqued bolts prevented lateral movement between the aluminium head and the cast iron block. The copper gasket deformed without danger to take up longitudinal expansion. The aluminium piston was made undersize to accommodate its greater expansion compared to the cast iron block. Sealants were chosen to be flexible in the case of the quartz inserts and mirror. Operating precautions such as limiting the engine speed to 1500 rev/min and only firing for limited periods with windows in position reduced the time spent at elevated temperatures.

5.6.4 Materials selected: connecting rod

The connecting rod was made from EN24T steel as recommended by Arrow Precision Limited, specialist manufacturer of connecting rods.

5.6.5 Materials selected: piston

The crown and body of the piston were machined from 7075 T651 aluminium, which was a similar material to the Jaguar piston. The left-hand/right-hand (LH/RH) retainer was made from free machining steel. To maximise the amount of light reaching the combustion chamber, it was crucial to minimise encroachment into the hollow bore of the piston. Hence steel was chosen for the retainer, since it could be thinner than an equivalent aluminium design of equal strength. In addition, the tendency for threaded connections to bind if aluminium runs in aluminium was removed by employing a steel connector.

5.6.6 Materials selected: block

Meehanite cast iron was chosen ahead of steel and aluminium for the block, based on its oil-retaining properties. It had adequate strength and was more easily machined than steel. Its coefficient of thermal expansion is around $6.8 \times 10^{-6}/\ ^{0}C$, compared to free machining steel $12.6 \times 10^{-6}/\ ^{0}C$ and aluminium $13.0 \times 10^{-6}/\ ^{0}C$. The relatively low value for meehanite compared to aluminium meant that the quartz windows in the blocks would be put under less strain than if aluminium had been used.

5.6.7 Materials selected: windows

The choice of material for the optical inserts was between sapphire and quartz. Sapphire has the higher refractive index and would thus bend light more, producing a wider field of view than a quartz window of the same dimensions. It is also stronger than quartz. However, it is more difficult to machine, liable to chip very easily and is considerably more expensive. The coefficient of thermal expansion of sapphire is $8.40 \times 10^{-6}/\ ^{0}C$ compared to $0.54 \times 10^{-6}/\ ^{0}C$ for quartz. The relatively similar coefficients of expansion between meehanite and sapphire would be helpful if the sapphire was subjected to the same temperature rise as its surrounding metal components, but would be a potential problem area if the sapphire alone experienced the temperature rise. Finally sapphire could be more affected than quartz by optical distortion due to its greater coefficient of thermal expansion. Quartz was the chosen material.

5.6.8 Materials selected: mirror

The mirror chosen was reference NT32-137, supplied by Edmund Optics Ltd. and specifically intended for research work. It was a front-surface research quality, elliptical flat mirror. It consisted of a pyrex substrate coated on its front surface with an enhanced aluminium coating, to reduce stray reflections. Research quality denoted that the flatness of this surface was better than $\lambda/8$, where λ was the wavelength of the test light source, ie 546.1 nm. The enhanced aluminium coating was suitable for 250 to 650 nm wavelengths. The mirror selected had the maximum dimensions possible to fit the block bore and still allow the piston to ride past it, hence the elliptical shape. It was bonded to an aluminium holder and problems of differential expansion were not anticipated since the whole assembly was located in the relatively cool region towards the bottom of the optical engine.

5.6.9 Materials selected: PEEK (Poly ether ether ketone)

The presence of lubrication oil on the quartz windows would reduce image quality, hence the piston ring and pad material were required to run on the cast iron cylinder without lubrication. To achieve this at the temperature expected and with minimal damage to the quartz windows, the plastic, PEEK, was chosen. The most suitable grade was 450FC30, which was filled with carbon fibre, graphite and PTFE (poly-tetra-fluoro-ethylene) to improve its

mechanical and tribological properties.

5.7 Modifications to Lister engine

The Lister ST-1 diesel engine is known for being a robust and reliable diesel engine used for such applications as powering portable electric generators and pumping units. During previous studies at UCL, this type of engine had proved a suitable base engine for conversion for optical work, whether motored by an electric motor or self-driving. The engine chosen was secondhand, but in good condition. Modifications included adding a second oil pump to increase the flow of lubricant, using an extended optical piston in place of the Lister piston and replacing the Lister cylinder block by an optically accessed design whose bore matched the optical piston. The cylinder head was the Jaguar G-DI design which was to be investigated.

The composite piston (Bowditch main section, left-hand/right-hand connector and the interchangeable crowns) had a very similar mass to the Lister piston (see § 5.9). Thus, no modifications had to be made to the Lister crankshaft as a result of exchanging pistons. However, the crankshaft did require modification since the Jaguar G-DI engine stroke was 79 mm, compared to 88 mm for the Lister (see Figure 5-5). An ideal solution would have been to re-grind the Lister crankshaft to match the Jaguar engine stroke and at the same time adjust the crankshaft pin diameter to accept the Jaguar V6 connecting rod. A CADD model created in "I-DEAS" [Structural Dynamics Research Corporation, 2001] to test the feasibility of this showed that material could be removed from the Lister crankshaft pin to achieve the required stroke. However, oil passageways prevented the pin diameter being reduced to match the big end diameter of the Jaguar connecting rod. The conclusion was that the pin diameter should be reduced as much as possible and a special connecting rod would be needed. The centre of the pin would be moved to achieve the correct stroke. There was insufficient time to perform a finite element analysis on the modified crankshaft but there was considerable confidence in the modified crankshaft for two reasons:

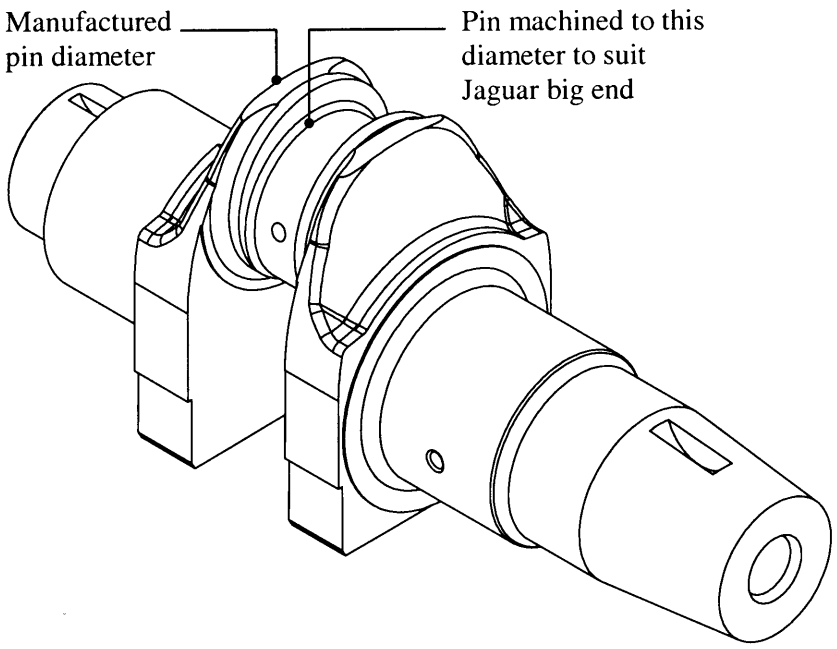

Figure 5-5 CADD model showing modifications to Lister crankshaft

1) the operating speed of the optical engine was to be limited to 1500 rev/min compared to 3000 rev/min of the standard Lister ST-1 engine.
2) similar crankshaft modifications had been carried out at UCL previously [Fry, 1994 and Queenan, 1998] without experiencing any problems.

Off-the-shelf shell bearings were chosen to match the design diameter of the new pin. A specialist automotive company re-ground the crankshaft to achieve the correct throw and match the pin diameter to the shell bearings. The connecting rod was designed to suit the outside diameter of the shell bearings.

5.8 Connecting rod design

The Lister crankshaft had been re-ground so that the pin to pin centres produced the same throw as the Jaguar engine. A special connecting rod was needed (Figure 5-6) because the Lister crankshaft pin diameter could not be ground to match the Jaguar V6 connecting rod.

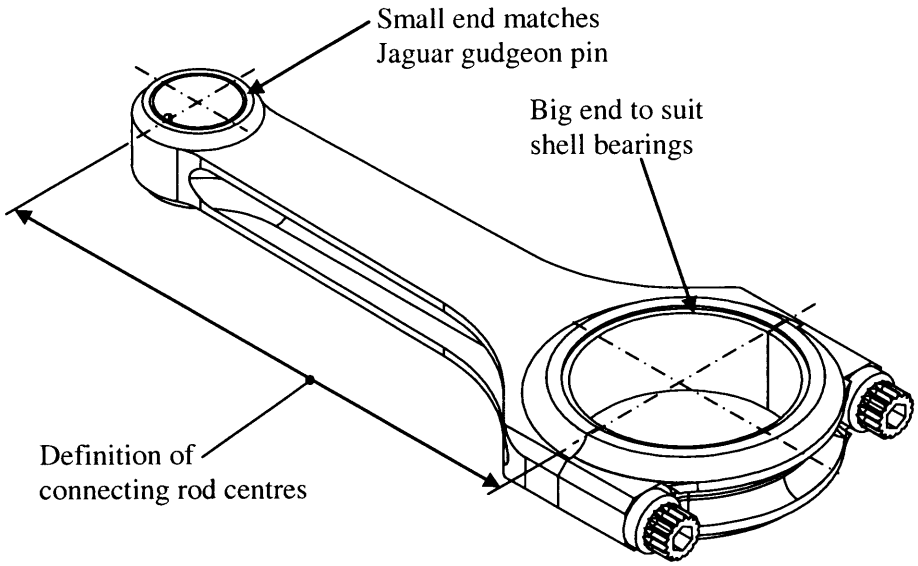

Figure 5-6 CADD model of special connecting rod

It should be noted that any increase in the effective length of the connecting rod would leave the stroke unaffected, but would alter the relationship between crankshaft angle and piston position.

Three options were available: option 1 would be to specify rod centre distance to achieve the same clearance as the standard Lister engine between the piston skirt and counter-balance mass found on the crankshaft. This would mean the connecting rod centres would be further apart than the Jaguar design. The skirt on the optical piston would be designed to match the Jaguar piston. Option 2 was the same as option 1, except the skirt would be designed to match the Lister piston. For option 3, the centre distance would be the Jaguar standard value, which would result in a clash between piston skirt and counter-weight, thus requiring modification of skirt or weight.

Option 2 was chosen since there was very little difference in the relationship between crankshaft angle and piston position for the 3 cases and arranging for the piston of the optically-accessed engine to have the same clearance and lower skirt length as the original Lister piston led to a consistent design.

Selection of the diameter of the small end bearing was governed by the gudgeon pin of the Jaguar G-DI piston. The big end diameter was selected to match the proprietary shell bearings chosen for the crankshaft. This data as well as piston mass and maximum rotational speed of the crankshaft were supplied to a specialist connecting rod manufacturing company. Their design was approved and the resulting connecting rod was supplied in EN24T alloy steel, rumbled and peened to produce a hardened surface layer.

5.9 Piston design

The optically-accessed piston was designed to have a modular construction whereby one of three interchangeable piston crowns could be attached to a common body via a screwed section (see Figure 5-7). The modular design simplified the changeover between set-ups for Mie scattering and LIF work, and it was simpler than making three complete pistons. The crowns were all machined from 7075 T651 aluminium, but two had quartz inserts, while the third was made entirely of aluminium. The all-aluminium crown was identical to that of the Jaguar design and was used for benchmark tests

The purpose of quartz windows in the other two crowns was to transmit laser light. One crown was "slotted" and had a sliver of quartz across almost the full width to allow a light sheet to pass up into the combustion chamber. The second optical crown ("disc") had a quartz plug over much of the base of the bowl to allow global illumination (see Figure 5-8).

The dimensions of the quartz inserts were chosen to maximise the spread of light transmitted. Calculations were then required to choose the critical dimension, the thickness. The calculations were based on a maximum cylinder pressure of 50 bar [Stone, 1999] and the resulting thickness values were rounded up. The maximum cylinder pressure for the low-load stratified tests was expected to be around 25 bar so that a safety factor of at least two was included.

A bolted ring retained the disc window and the slotted window was trapped between the piston halves, on the ledge formed by an undersized opening. It

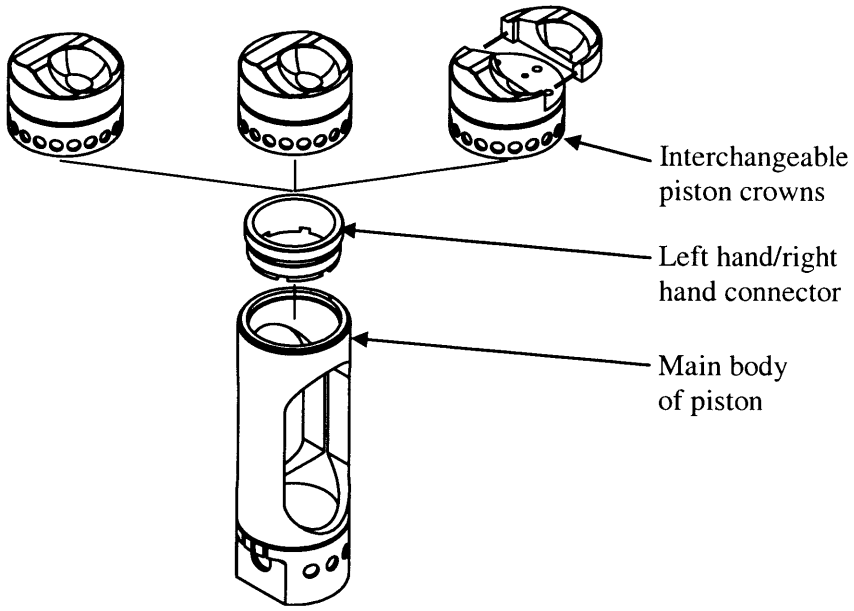

Figure 5-7 Modules used to form piston

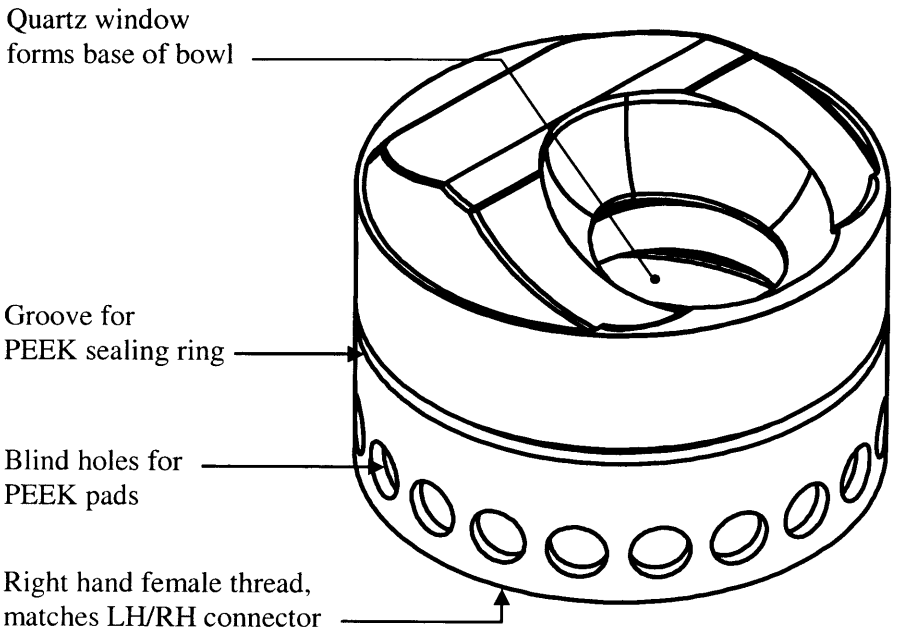

Figure 5-8 CADD model of the "disc" crown

was originally intended that the windows would be retained using bonding agent Permabond ISP110 which was selected to provide an airtight seal and accommodate the thermal expansion at the working temperature. A gap of 1 mm was left to accommodate the bonding agent. Later experience caused this retention method to be changed (see § 7.5). The piston common body, made of 7075 T651 aluminium, was an extended version of the Jaguar piston (see Figure 5-9). It had a slotted hole cut through it to enable it to ride over the cylinder block's fixed mirror. The height of the slotted hole was chosen so that the whole of the mirror was visible for the entire piston stroke.

The screwed section between the crowns and extended body had one left-hand threaded portion and one right-hand threaded portion. It was made of steel and was designed to draw together the piston crown and the common body, with a dowel pin for repeatable alignment (see Figure 5-10). The top of the composite piston was identical to the top of the Jaguar piston as regards bowl shape. The bottom was identical to the bottom of the Jaguar one in terms of gudgeon pin, circlip, oil passageways and grooves for rings. The bowl shapes of the three crowns were matched to the Jaguar design by using data from a CADD file supplied by Jaguar.

The overall diameter of the piston was chosen to suit the bore of the Jaguar engine which was smaller then the Lister bore and stepped correspondingly. The allowance for thermal expansion of 0.65 mm on diameter was based on Jaguar guidelines and previous optical work.

The wall thickness was also selected using knowledge of earlier optical engines and validated by stress calculation. The overall length of the piston was determined by the size of the slotted opening for the mirror and by the skirt design. The masses of the composite piston with each of the composite crowns was deemed close to that of the Lister design: Lister; 1.60 kg, Bowditch and metal crown: 1.67 kg, Bowditch and 'slot' crown: 1.68 kg, Bowditch and 'disc' crown: 1.67 kg.

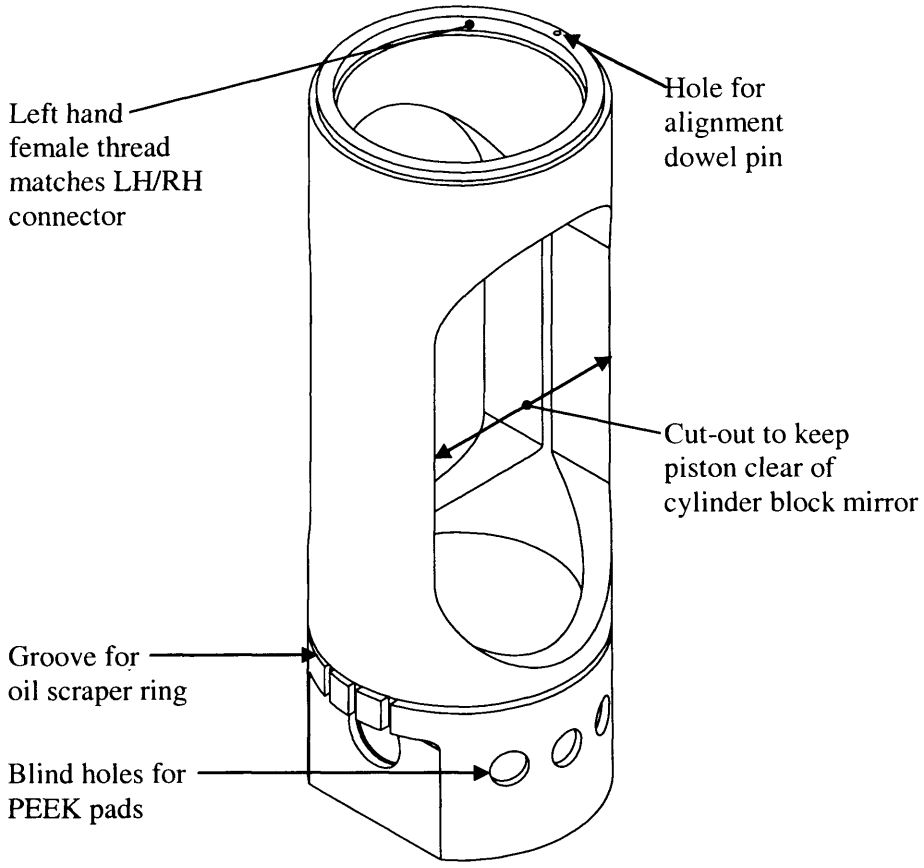

Figure 5-9 CADD model of the optical piston, main body

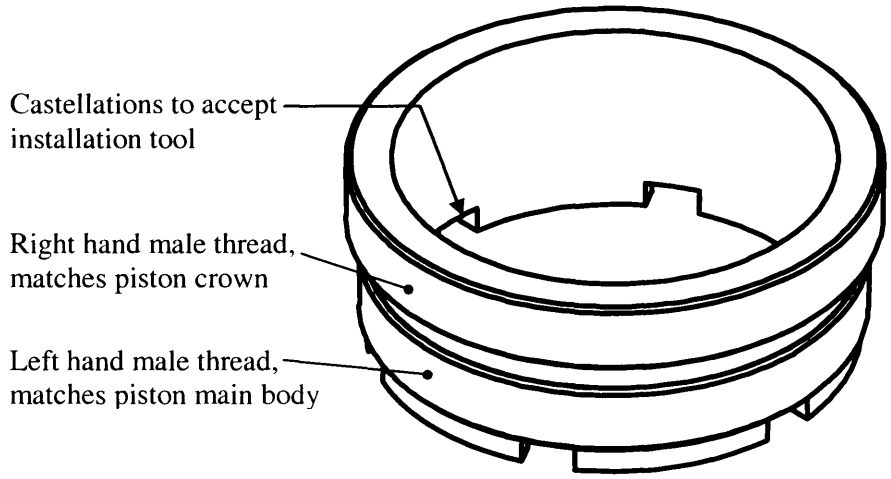

Figure 5-10 CADD model of left hand/right hand connector

After the piston was machined, all surfaces liable to be exposed to laser light were black anodised. The matt finish helped to minimise reflections and act as a safety measure, since even reflected laser light can be harmful. After anodising, the piston rings and pressure pads were fitted, the latter held in position using Loctite 4204. Both piston rings were sprung fit. The oil scraper ring was re-used from the Jaguar engine in the bottom position. For the top position, the Jaguar sealing ring could not be used since lubrication was not provided in the upper part of the cylinder. A ring was made from PEEK since this material has self-lubricating properties. It has good wear resistance but, due to its thermal resistance properties, had to be fitted further from the top of the piston (25 mm) than the Jaguar design (4 mm) where temperatures were slightly lower. The total volume of crevices in the optical engine was consequently slightly larger than for the Jaguar engine. The purpose of the pads, one set just below top ring, one set around the piston skirt, was to resist side loads. These pads were also made from PEEK and bonded in place. Attempts were made to manufacture the PEEK ring in such a way that it would push outward onto the bore of the cylinder. It was manufactured as a solid ring with an external diameter greater than that of the cylinder (89.5 mm for the ring compared to 89.0 mm for the cylinder). The solid ring was then slit such that the gap between the ends was 0.25 mm when it was positioned in the cylinder. Subsequent motoring and firing traces of cylinder pressure when the engine was assembled showed that adequate compression was achieved by the ring.

5.10 Design of cylinder block

The Lister crankshaft had been modified to connect to the optical piston via a special connecting rod. The standard Lister block was too short for the optical piston and its bore diameter (95 mm) exceeded that of the Jaguar engine bore (89 mm). A special block was made.

This block, including optical access and provision for cooling water, was divided into two sections, the special features of the upper block (denoted "optical block") are detailed in section § 5.11. The lower section is denoted the "cylinder block", see Figure 5-11. A raising mechanism was included

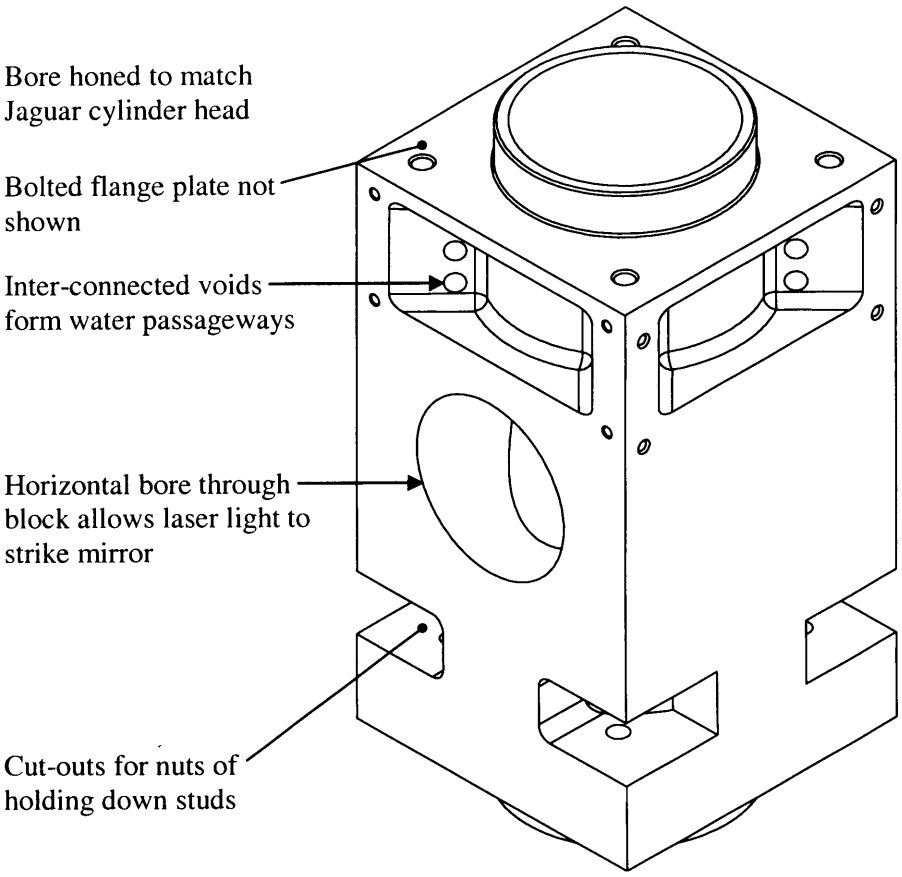

Figure 5-11 Details of cylinder block

between the two blocks to give access to the quartz windows for cleaning. Meehanite cast iron was selected as the material for the blocks. The blocks were designed using I-DEAS CADD software. The length of the optical piston determined their combined height. In order to limit the mass to be lifted by the raising mechanism, the joint between them had to be positioned as high as possible. This joint position was fixed once enough material had been specified in the optical block to house the window. The cylinder block was designed to bolt onto the casing of the Lister bottom end and included a downstand extending into the Lister casing. This added slightly to the cylinder block height, but provided support in transmitting the piston side load.

The cooling passages and other features of the cylinder block were added to the CADD model, so that the width and breadth of the block could be calculated to resist the burst pressure of 50 bar. It was straightforward to manufacture the block by CNC machine using its CADD file and all

operations were completed with the exception of the bore. This was deliberately left undersize by 0.05 mm. A specialist company then honed the bores of both blocks, bolted together, to achieve a surface finish to match a commercial engine.

Prior to honing, a circular hole was cut through the block, this time horizontally. The front opening admitted laser light while the rear accepted a mirror and holder. The mirror was fixed at 45^0 in ramp fashion, so light shone horizontally from the optics bench at the mirror was reflected vertically upwards, through the quartz piston insert, into the combustion chamber. The piston had a cut-out which allowed it to ride past this mirror.

The mirror was bonded to an aluminium holder and consideration was given to fitting goniometers between the mirror and holder for adjustment purposes. However, adjustment would have to be in situ, which would have been very difficult to achieve. The solution used was to have the block and optical table true and level and make all adjustments with the optical elements.

5.11 Design of optical block

The optical block contained passages for cooling water, as well as cut-outs for its quartz windows, Figure 5-12 . The Jaguar head bolted to it from above and it had a flanged connection to the cylinder block below. A raising mechanism based on the use of four pneumatic cylinders was included to lift the optical block and head off the cylinder block.

The quartz windows in the block were placed in adjacent sides to allow in-cylinder events to be viewed from two orthogonal directions. The range of injection timings to be investigated determined the range of piston travel over which fuel was expected to impact on the piston. This information was used to specify the height of the windows so that the fuel behaviour could be observed. The internal radius of the window matched the cylinder bore. The width was chosen so that the field of view was the entire diameter of the combustion chamber. The ray tracing software "OSLO" [Sinclair Optics Incorporated, 2001] was used for this. Stress calculations determined the

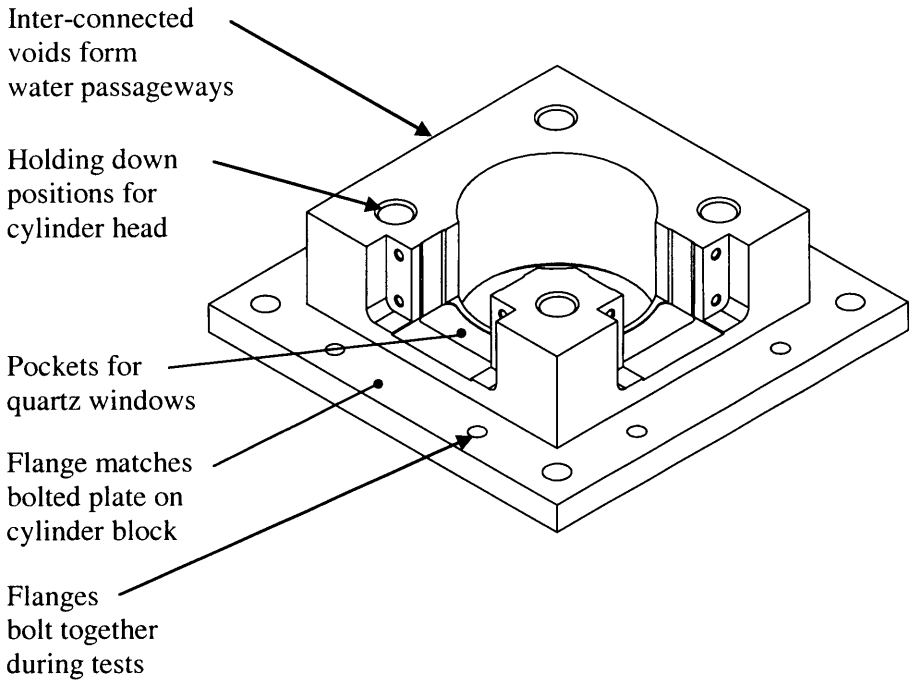

Figure 5-12 Details of optical block

minimum thickness to resist the forces resulting from the cylinder pressure. The windows were retained on their external surface with metal strips, and Permabond ESP-110 bonding agent provided a gas-tight seal. This method of retention was later changed (see § 7.5).

The raising mechanism elevated the optical block by 100 mm so that a hand could be inserted between the two blocks to clean each quartz window. Minimising the inconvenience of cleaning the windows in this way would help keep image quality high. Pneumatic cylinders were selected over hydraulic, because shop air was readily available at a suitable pressure. The cylinders chosen were the double-acting, cushioned variety, which made it simple to lower the head too. With the head lowered, the flanges were bolted together so that when the engine was firing, the bolts resisted the burst pressure rather than the pneumatic cylinders. In fact, this pneumatic raising of the head was not implemented in practice as it proved to be relatively simple to winch the head up and down using a block and tackle arrangement.

5.12 Design tasks on the cylinder head

With the block and optical piston designed, the combustion chamber was completed by fitting the modified cylinder head, a pre-production G-DI head. Jaguar Cars Limited supplied the head itself as well as its CADD file. The major modification needed on the Jaguar head was to insert a window to allow optical access into the pent-roof of the combustion chamber. This involved removing the section of the head which contained provision for a cylinder pressure transducer and meant that an alternative mounting point had to be established.

The late injection used in G-DI stratified mode, resulted in fuel impacting on the piston crown when the piston was close to TDC. A quartz window was therefore needed as high as possible in the pent-roof to observe these events. Since this window was directly above the window in the optical block, it was sensible to select the same material and try to match the widths as well. Inspection of the CADD file of the head showed what maximum height and width of window could be accommodated by the head's layout. The CADD file also revealed the complex shape of the pent-roof, which would have made it very difficult to correct for the optical distortion found if a quartz window were made to match this topography. A reasonable approximation to the combustion chamber shape was found by continuing the cylindrical bore up into the pent-roof. A quartz window made to that pattern would have changed the shape of the combustion chamber only marginally. With the radius selected, the minimum thickness of the window was calculated to withstand the specified burst pressure. Finally, the field of view was checked using OSLO ray-tracing software. The window was held in place with strips of steel screwed to the block and Permabond ISP110 provided a seal (later changed, see § 7.5).

The modified Jaguar head was designed to be bolted and dowelled onto the optical block. In order to increase the viewing options, the pattern of drillings in the optical block was chosen to permit two positions, rotated 90^0 from each other. Careful thought was given to the engine services, especially since flexible and extendible pipes and couplings were needed throughout. This was

to allow for frequent raising and lowering operations and to suit both orientations of the Jaguar head.

The cylinder head camshafts were driven by the Lister camshaft using two toothed belts. The lower belt transferred drive from the Lister camshaft to the upper belt system. The upper belt went around four pulleys, one driven by the lower belt, one each for the optical engine camshafts and one idler. The mount for the idler could be moved away from the driver pulley to take up slack in the upper belt system. To raise the engine head, the upper belt was slackened off by moving the idler toward the driver pulley, unlaced from the camshaft pulleys which were then freed. Valve timing was set according to the Jaguar engine map. Piston top dead centre was found by placing a dial gauge indicator onto the crown through the spark plug hole. The camshaft pulleys were rotated until protractors lined up with static markers, the toothed belt was placed around the pulleys and the idler pulley moved until the belt was taut.

5.13 Fuel, oil and water systems

Jaguar Cars Limited supplied the fuel injector and its electronic driver. The driver was a sealed unit, driven by TTL (transistor-transistor logic) pulses and running from a 12 v supply. The injector was a pressure swirl model (as discussed in §3.2) with zero offset angle, a cone angle of 70^0 and rated for 10 MPa fuel pressure. Jaguar also supplied the swirl control valve (SCV) for the air intake, but new manifolds had to be fabricated for the engine's air intake and exhaust systems. An existing air damping chamber and throttle arrangement were re-used. The fuel system also pre-existed this project, designed by Davy [2000]. The design was based on a hydraulic cylinder which pressurised the fuel system under the action of compressed air from a dedicated compressor. The multiplying effect of the cylinder was such that an air pressure of 0.5 MPa produced a fuel pressure of 10 MPa. The Mie and LIF testing of this project required the engine to run in short bursts (typically 10 to 40 seconds). Thus the limited capacity of the hydraulic cylinder, which could only contain sufficient fuel for approximately 10 minutes of continuous engine running at the world wide mapping point (WWMP) condition, was not a

problem for the optical testing. One advantage of the arrangement was the relatively steady fuel supply pressure as compared to that obtained from a high pressure mechanical pump.

A shaft encoder was connected to the camshaft to provide timing signals for the injection system.

A Volkswagen Beetle oil pump was used in addition to the Lister engine's integral oil pump. The latter provided lubrication only within the Lister engine whereas the Volkswagen pump was attached to a geared spigot on the Lister engine and distributed oil to the feeds in the cylinder head. The return oil was fed to a top-up tank which supplied both the pumps.

Water was supplied from an external circuit which included a pump, heater and heat exchanger. The flow of cold water to the heat exchanger could be adjusted to give some degree of control over the temperature of the water circulating around the engine. The water passageways machined into the optical and cylinder blocks were linked in series with the ducts in the Jaguar head. The copper head gasket blanked off the redundant passageways which would have been used to connect the Jaguar head to a Jaguar block.

5.14 Summary

This chapter has detailed the design tasks to complete the test rig. It addressed:

- the engine itself, (Lister bottom end, blocks, cylinder head)
- the piston and connecting rod
- provision for window cleaning
- fuel oil and water systems
- optical access

Figure 5-13 illustrates the path of laser light through the completed optical engine.

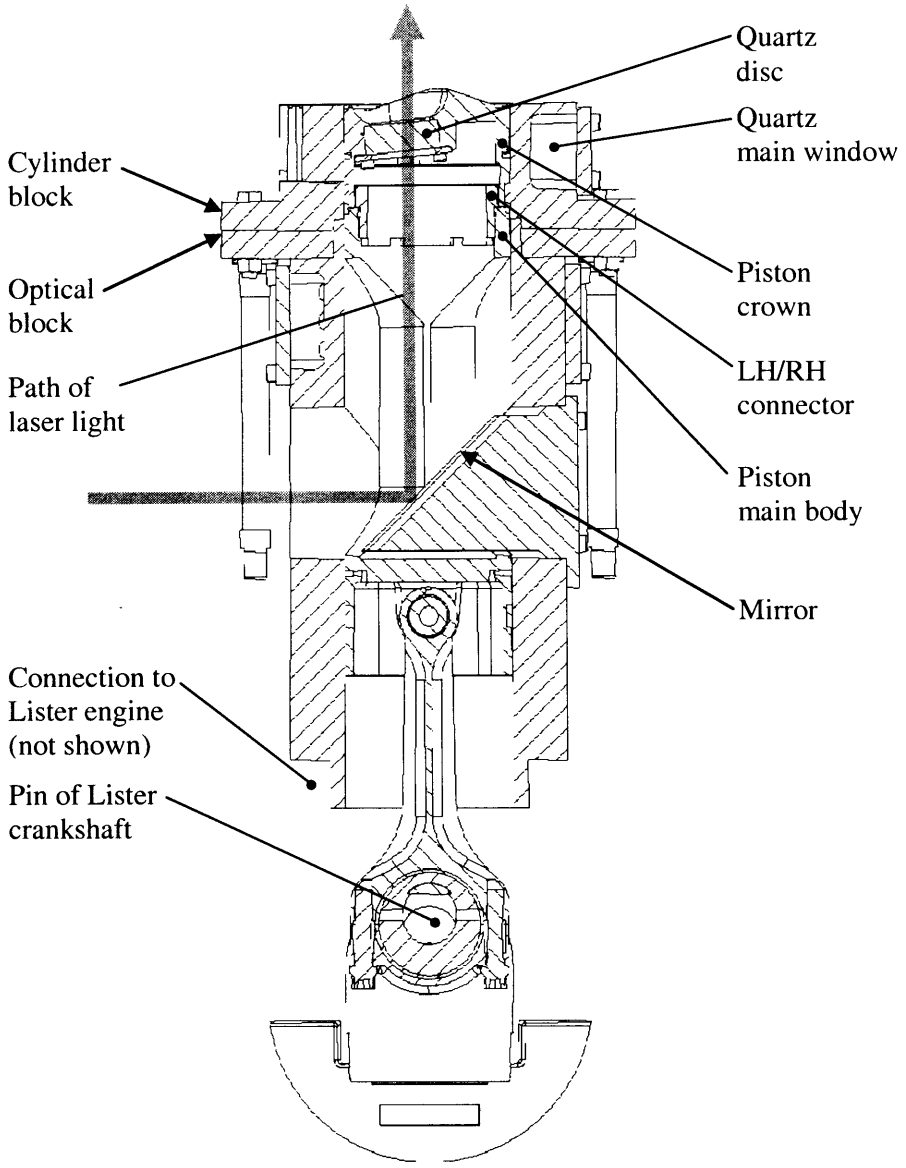

Figure 5-13 Section through Jaguar/UCL optical engine showing path of laser light into combustion chamber

Chapter 6 describes the engine's test bed, its commissioning and benchmark tests.

Chapter 6

Test bed, instrumentation, commissioning and benchmark tests

6.1 Introduction

The choice of optical methods for this study was discussed in Chapter 4 and the design of an optical engine to suit these investigations was described in Chapter 5. The current chapter begins with an outline of the test bed housing the engine and its instrumentation. The commissioning work is then described and the chapter concludes with a report on the benchmark tests. It should be noted that the quartz windows were removed and replaced by appropriate cast iron blanks (for the block) and aluminium blanks (for the cylinder head) for the benchmark testing described in this chapter.

6.2 Test bed

The optical engine was initially installed on an existing test bed, but the rescheduling of a laboratory modernisation programme required the test bed to be dismantled before commissioning was completed. There was a delay of around 9 months before the new laboratory was ready for occupation. The optical engine was installed in a new "state of the art" test bed. However, the process was quite protracted since all the test equipment and instrumentation had to be installed from scratch. Also, teething problems with some of the services added to the delay.

The test facility comprised an interconnected test cell and control room. The control room was used to house the majority of the electrical and electronic equipment, with cables reaching the test rig via under-floor conduits. The test cell housed a plinth to take the engine and its dynamometer and also contained a camera table, an optical bench, a fuel ram, an intake-air stilling chamber, an engine exhaust extract, a water circulation system and a small suction pump (see Figure 6-1). Further features of the test cell included: in-cell chilled water and compressed-air supplies, soundproof panelling, room ventilation, safety cut-outs, interlocks on the interconnecting door, a gas detection system for

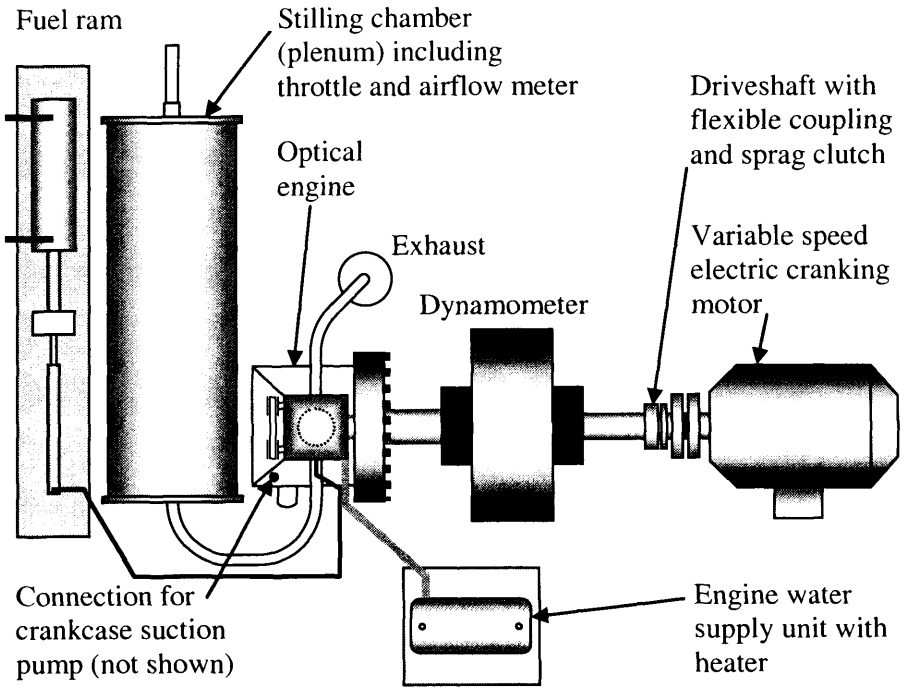

Figure 6-1 Plan showing positions of main items on test bed

hydrocarbon and carbon monoxide and a foam inlet.

The optical engine was connected to its dynamometer which in turn, was connected via a sprag clutch to a 10 kW electric motor with variable speed control. The electric motor allowed the engine to be run at its test speed while its instrumentation was set prior to firing tests. An adjustable load could be imposed on the engine crankshaft by the dynamometer so that real driving conditions could be simulated, including the WWMP of 1500 rev/min and 2.62 bar BMEP. The motor and dynamometer were controlled remotely from the control room.

The concrete plinth forming the test bed was bolted to the laboratory floor slab through an anti-vibration rubber mat, to isolate it from the remainder of the cell. A baseplate consisting of structural steel sections and designed to suit the motor, dynamometer and optical engine was bolted to the plinth.

A specification of the Jaguar cylinder head is included in Table 6-1. A bifurcated manifold incorporating a swirl valve was attached to the cylinder

Engine type	4-stroke, single cylinder, dual overhead camshaft (DOHC)
Combustion chamber	4-valve, pentroof
Piston shape	Bowl in crown
Bore/stroke (mm)	89/79
Displacement (cc)	498
Injector type	Bosch, 70^0 pressure swirl atomiser
Injector position	Side

Table 6-1 Specification of Jaguar cylinder head

head to provide air intake. The branches of the manifold lay side by side and a butterfly valve in one branch induced variable amounts of horizontal swirl as it was adjusted from fully open to fully closed (see Figure 6-2 and Figure 6-3). The manifold was fed by a plenum chamber via a 2 m long pipe. The plenum had a capacity of 100 litre and was designed to still the air entering the engine. A standard throttle and airflow meter were positioned at the inlet to the plenum chamber. The cylinder head was supplied with a Bosch inwardly opening pressure swirl injector, type 100 Wdgn, nominal cone angle 60^0 and a Bosch driver, ES-HDEV-1. Fuel was supplied by a pneumatic/hydraulic ram arrangement, capable of delivering fuel at up to 15 MPa.

A four-contact Bosch spark plug, type HGR 7 LQPE0, was supplied with the cylinder head. It was energised using a standard coil attached to a 12 v supply. Spark timing was controlled by a Lumenition Optronics PMA 50 optical switch and a cutter disc attached to the Lister crankshaft. The low part of the disc led to charging until the high part broke the light beam and the coil discharged across the plug terminals. Spark advance was set by rotating the cutter disc clamp bracket.

Each of the optical engine blocks and the cylinder head had their own water jacket, linked by flexible hoses, to avoid disassembly whilst the engine head was raised. A water unit containing both a heater and a heat exchanger was sited in the cell, with only the benchmark tests requiring the cooling option. Heating was used to maintain the engine block at the required temperature for the optical testing.

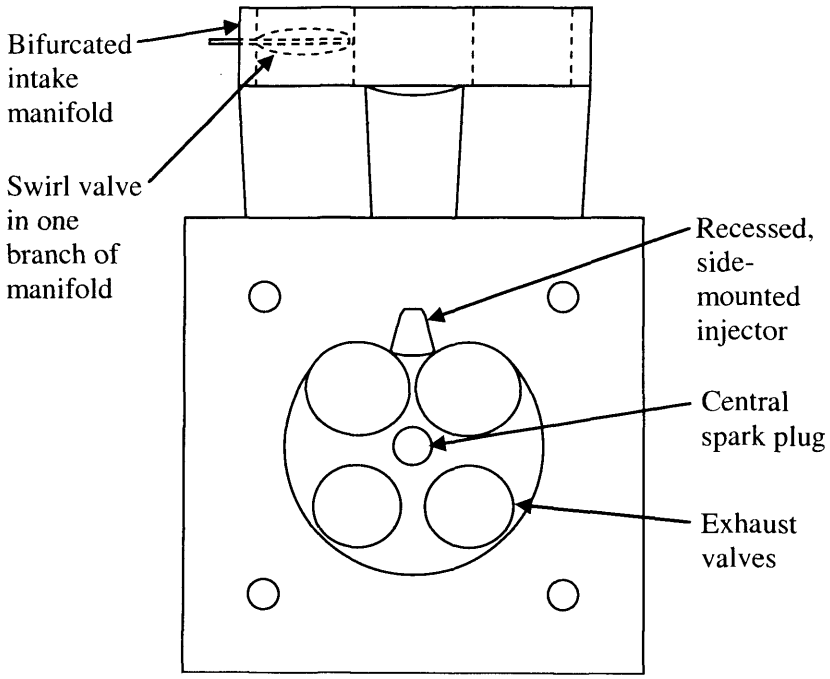

Figure 6-2 Underside of Jaguar head showing swirl valve location

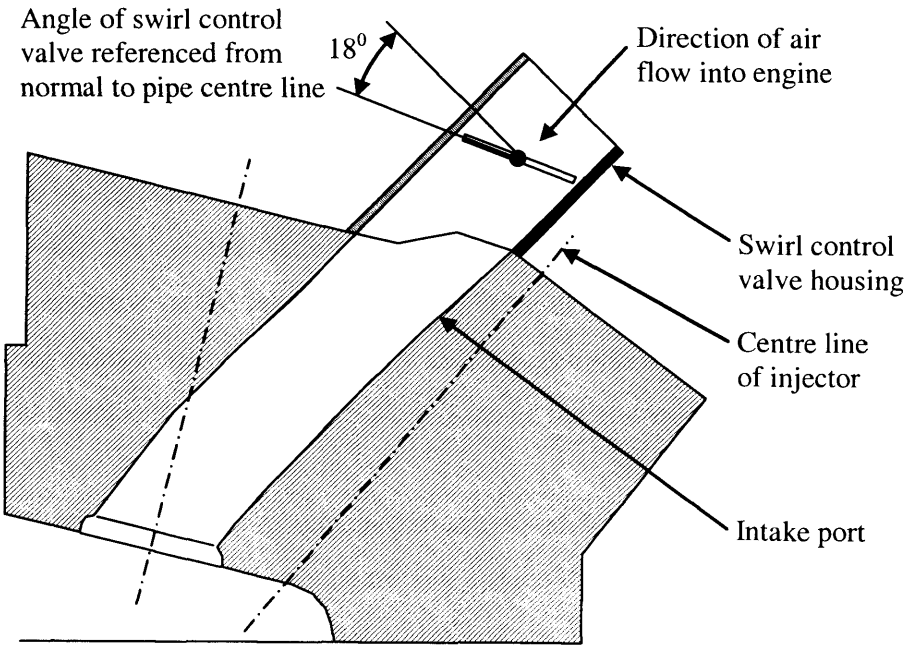

Figure 6-3 Section through intake port illustrating orientation of swirl control valve

Engine control was achieved by using a Hohner shaft encoder (fixed to the optical engine camshaft), a Stanford Research Systems signal generator unit (SRS), model DG535 and the Bosch injector driver (see Figure 6-4). The encoder fed a TTL signal to the SRS, acting as a trigger for it to send a TTL

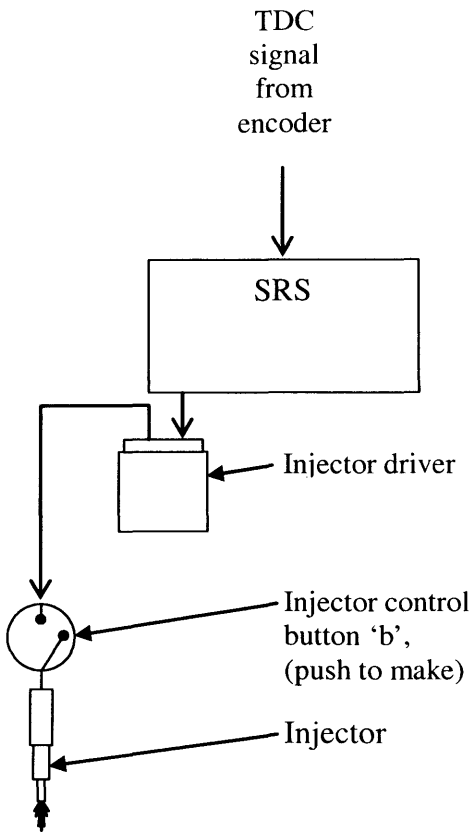

Figure 6-4 Engine control circuit used for benchmark tests

pulse to the injector driver. The timing of this pulse and the associated pulse width were set on the SRS and corresponded to the required SOI setting. Synchronisation of the encoder TDC signal and the physical TDC were fixed once the engine could be turned, by dial gauge indicator on the piston crown and a cathode ray oscilloscope (CRO) trace of the encoder signal.

A small suction pump was attached to the dipstick hole of the Lister engine to draw oil-laden gas out of crankcase and reduce the likelihood of oil passing up through the gap in the PEEK ring and smearing the quartz windows.

6.3 Instrumentation

The engine was instrumented so that its performance could be checked against data obtained by Jaguar from a single-cylinder emissions research engine fitted with a similar cylinder head.

See Figure 6-5 for locations of instrumentation on engine. To measure air

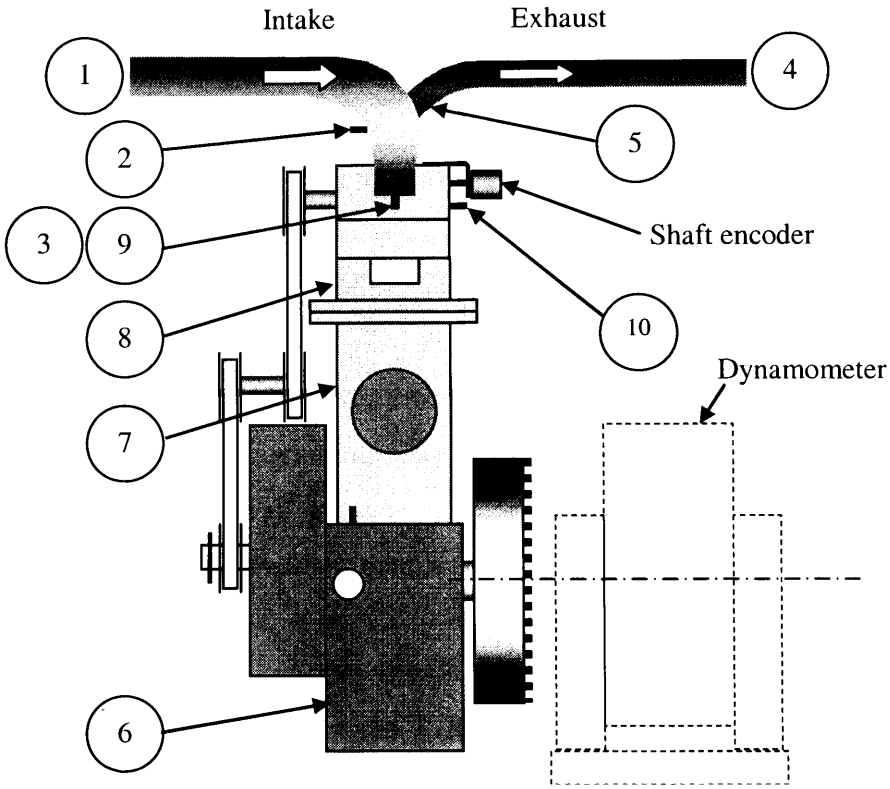

Ref	Instrument	Property	Unit
1	Hot wire anemometer	Air flow rate	Kg/s
2	U-tube manometer	Intake manifold pressure	mm Hg
3	Pressure gauge	Fuel pressure	bar
4	Exhaust gas analyser	Exhaust gas concentration	various
5	UEGO sensor	Air fuel ratio	-
6	Thermocouple	Lister sump temperature	deg C
7	Thermocouple	Water jacket temperature	deg C
8	Thermocouple	Optical block temperature	deg C
9	Thermocouple	Fuel temperature	deg C
10	Piezoelectric pressure sensor	Cylinder head pressure	bar

Figure 6-5 Location of instrumentation on optical engine, shown in side elevation

flow rate, a Ford hot wire anemometer (HWA) was fitted in the short length of pipe leading up to the plenum chamber, ie just before the throttle. The output was displayed as volts on a voltmeter and a calibration chart provided conversion to mass flow rate (see Appendix A). A U-tube mercury manometer was used to measure air inlet manifold depression. A standard pressure gauge was fitted in the high pressure side of the fuel system to indicate fuel pressure in bar. Engine speed in rev/min and load applied by the dynamometer in Nm were displayed on the dynamometer control box. Values

of UHC in ppm and CO as % volume were measured using a Horiba MEXA - 321E CO.HC infra-red gas analyser, attached to a tapping in the exhaust pipe.

To measure AFR directly, provision was made in the exhaust manifold for an unheated exhaust gas analyser (UEGO) λ sensor. The instrument was connected to a voltmeter and calibration charts from the supplier (see Appendix A) used to convert to AFR. Data from the HWA and the injector calibration experiment provided a cross check of the AFR value. The injectors used during the test programme were calibrated by pulsing them at a fixed frequency over a range of pulse widths and collecting the injected fuel in a measuring cylinder. Further details and calibration graphs are given in Appendix A.

Thermocouples were fitted in the Lister sump and optical engine block to measure lubrication oil temperature and cooling water temperature respectively. Further thermocouples were used to measure the optical block temperature and the temperature of the fuel just before it entered the injector. A Kistler 6041A pressure transducer was located in the cylinder head and was used to record combustion chamber pressure. It was connected to a CRO via a charge amplifier and pressure was determined using the sensitivities of the transducer, amplifier and oscilloscope, ie pC/bar, mv/pC and volts/div respectively. Gauges were also included to monitor the pressures of the dynamometer cooling water and compressed air supply to the fuel ram. In addition, test cell ambient air temperature, pressure and humidity could be recorded.

6.4 Benchmark tests

Once the engine was commissioned (see Appendix B) the benchmark tests could be carried out to check engine performance against results achieved by Jaguar using their version of the engine. Large discrepancies would indicate the existence of serious problems with the UCL optical engine and the need for investigation. The tests also helped to define the operating envelope to use for the optical work. Once the engine was performing satisfactorily, settings were noted and instrument values recorded to act as a reference position to return to after converting the engine to optical mode.

Jaguar's experience was that the spark should occur between about 20 and 35 CAD BTDC (before top dead centre) firing and end of injection (EOI) must lie between 50 and 65 CAD, ie between 655 and 670 CAD based on Figure 6-6. These figures were used in conjunction with pulse width to choose EOI, having first established the relationship between time and CAD.

Jaguar's choices of SOI 66 CAD and 74 CAD and EOI 56 CAD and 60 CAD at 1500 rev/min, equated to pulse widths of 1.1 and 1.6 ms. These values were used as a guide for initial runs, although conditions leading to good running would become the basis of the values chosen for the optical work.

The method employed by Jaguar was to fix the intake camshaft phasing, exhaust camshaft phasing and throttle setting, and carry out a sweep of ignition timings for each condition. A comprehensive engine performance map was not required for the benchmark tests, instead, strategic test points were chosen and the range of spark timings in Jaguar's test matrix was explored.

The procedure was to set the spark timing and motor the engine up to 1500 rev/min. The fuel system pressure was set to 100 bar and power to the injector and spark plug were switched on. Then the SOI and pulse width were adjusted until the engine was combusting without misfires. Once stable combustion was detected, the motor speed was reduced and checks made for signs that the engine could sustain itself. Finally, the motor was switched off (disengaging via a sprag clutch) which left the engine powering the dynamometer, whose load reading thus corresponded to torque developed at the crankshaft. Once the engine was self-sustaining at steady speed, a set of values was recorded as per Table 6-2. The engine was returned to rest and modifications made as necessary, before beginning the next run.

6.5 Data analysis

In total, there were 13 parameters, 6 of which were fixed, ie intake valve MOP (mid-opening point), exhaust valve MOP, EGR, SCV and fuel rail pressure.

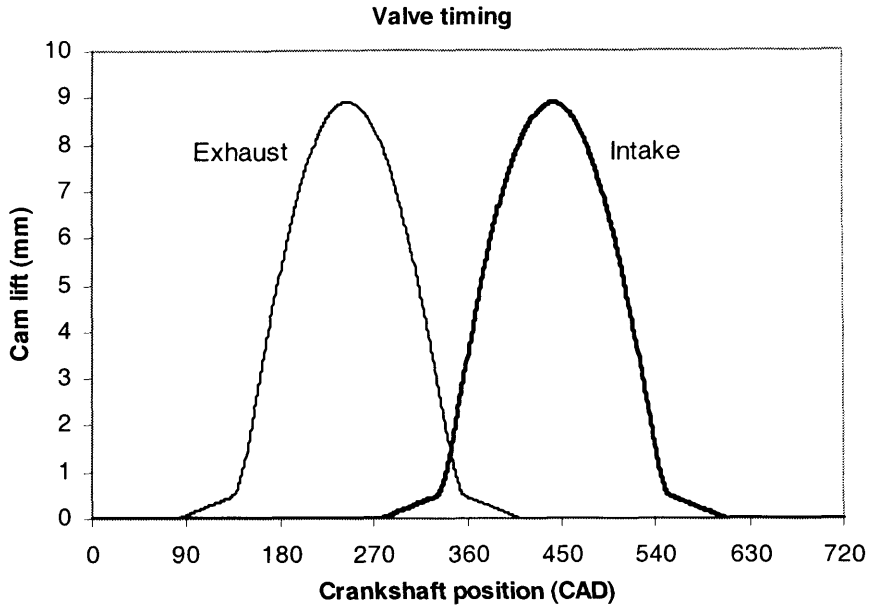

Figure 6-6 Valve opening times, where 720 CAD is TDC firing

The variables were spark timing, SOI and pulse width. Several quantities were measured: speed, torque, inlet manifold absolute pressure, AFR, air mass flow rate.

The following points should be noted about the test readings:

1) Speed was initially set by motor control, but once self-sustaining, could drift somewhat although close to 1500 rev/min was preferred.

2) The main method of obtaining air/fuel ratio was from the airflow meter reading and the injector calibration. The manufacturer's calibration of the UEGO sensor fitted in the exhaust did not continue any leaner than 18:1 and so its readings were only useful for the richer settings of the engine. In fact there was a suspicion that the UEGO sensor was not functioning correctly since its readings were not consistent with the calculated values under homogeneous running conditions. Tests 22 and 23 gave implausibly low values of AFR. A check calculation for the AFR in test point 18 is included in Appendix A.

6.6 Discussion of benchmark test results.

The main differences between the engines used by Jaguar and UCL relate to EGR and the piston rings. The UCL engine did not use re-circulation of the

Test run	Speed (rev/min)	BMEP (bar)	map (kPa)	AFR (measured)	AFR (calculated)	EGR rate (% total)	SCV (deg)	SOI (CAD ATDC)	EOI (CAD BTDC)	Spark advance (CAD BTDC)	Fuel pressure (bar)
Jag	1500	1	75	29.83		34	18	66	56	21-31	100
Jg 2	1500	2.62	90	25.17		29	0	74	60	26-36	100
Jg 3	1500	5.5	87	14.6		24	0	320	300	31-41	100
Jg 4	1750	4	76	14.6		26	0	340	320	41-52	100
Jg 5	2000	7	93	14.6		17	0	310	280	17-28	100
Jg 6	2500	5	80	14.6		19	0	300	270	31-41	100
Jg 7	3500	6	95	14.6		12	0	325	270	20-30	100
UCL	995	2.05		11		0	18	220	181	30	100
2	997	1.46		14.5		0	18	91	79	30	100
3	996	0.23		16		0	18	91	80	30	100
4	997	0.56	52	17		0	18	71	60	30	100
5	1000	0.08		18	19.71	0	18	71	60	30	100
6	1030	0.18	81	18	19.14	0	18	74	63	30	100
7	1004	0.64	81	18	17.93	0	18	72	61	30	100
8	914		84	18	19.69	0	18	72	62	30	100
9						0	18		0	30	100
10	990	0.13	84	18	19.91	0	18	72	61	30	100
11	1007	0.15	81	18	19.58	0	18	72	61	25	100
12	1031	0.15	81	18	17.46	0	18	72	61	25	100
13	895	0.13	81	18	20.11	0	18	72	62	25	100
14	920	0.13	81	18	19.57	0	18	72	62	25	100
15						0	18		0	34.5	100
16	779	0.10	87	18	20.91	0	18	72	64	34.5	100
17						0	18		0	34.5	100
18	1490	0.49	93	18	28.19	0	18	74	56	20	100
19	1490	0.46	99	18	37.39	0	18	67	51	26	100
20	1000	0.20	97	18	34.29	0	18	62	51	21	100
21	968	0.05	100	18	40.73	0	18	59	49	21	100
22	1280	0.36	63	12		0	18	220	197	28	100
23	1290	0.61	63	13		0	18	220	197	28	100
24	1340	0.59	63	18		0	18	245		28	100
25	1380	0.41	63	18		0		220		28	100
26	1260	0.15	63	18		0	18	195			

Note: in all cases, inlet MOP = 84 CAD ATDC (after top dead centre) and exhaust MOP = 111.5 CAD BTDC.

Table 6-2 Results of Jaguar (denoted "Jag" or "Jg") and UCL benchmark tests)

exhaust gas, ie EGR, since there were doubts whether this could be set up in a stable and controlled manner during the relatively short periods of firing with UCL's optical engine. The single, PEEK piston ring compared to the standard three steel piston ring pack of the Jaguar engine, meant that the compression ratio was reduced and blowby could occur. In addition, the metal blanks used in place of the quartz windows, increased the crevice volume since their edges were not an entirely perfect fit. The BMEP values of the UCL engine were consistently below the 2.62 bar value of the standard Jaguar test condition. This could be attributed to two causes:

i) the loss of compression due to blowby past the PEEK ring

ii) the probable extra frictional losses of the UCL optical engine compared to the single-cylinder Jaguar, meaning that the indicated mean effective pressures (IMEP) of the two engines were likely to be more similar than their BMEPs. No calculations were performed on the cylinder pressure traces of the UCL engine, but they were checked for consistent firing. The majority of test points of the UCL engine were set with the engine running in the stratified charge (late injection) mode, but test points 22 to 26 were set with the engine in its homogeneous (early injection) mode. It was immediately apparent that the engine was far less sensitive in this mode to changes in its parameters (injection timing, pulse width, ignition timing) than in SC mode.

Taking into account the unavoidable shortcomings of an optical engine, the behaviour recorded indicated no serious problems and that the engine was ready for use in the optical studies.

6.7 Summary

The layout of the test bed and development of the instrumentation have been described. Results of the benchmark testing have been included and discussed. The characteristics of the engine in stratified charge mode were found to be in reasonable agreement with data from the manufacturer's performance map so that no major changes were needed. The behaviour of the engine for mid-range settings was deemed good enough to be the start point for the Mie study, in Chapter 7.

Chapter 7
A Mie study

7.1 Introduction
Earlier chapters have shown the benefits of using optical methods to explain interaction phenomena in engines and concluded that the Mie scattering and LIF techniques are most applicable to the current work. The design of an optical engine suitable for such techniques was detailed in Chapter 5. Chapter 6 described the test bed, instrumentation and benchmark testing necessary to prepare for the Mie study. Now Chapter 7 presents the findings of the Mie study. It begins by outlining the aims of the study, describes the equipment used, the set-up and the experimental methods. The chapter concludes with a presentation and brief discussion of the images.

7.2 Aims and scope of testing
The overall aim of the Mie study was to obtain sets of images of the fuel interactions in the firing engine. Unacceptable levels of UHC emissions were found during testing by Jaguar Cars Limited. Tracing the path of the fuel should provide the basis of a theory to explain these emissions.

The engine used in Chapter 6 provided benchmark results and showed that the optical engine in its non-optical configuration behaved in a reasonably similar way to the version used by Jaguar Cars Limited to produce their engine map. Following the benchmark tests, the metal engine was converted to full optical mode for the Mie study.

The Mie process is the inelastic scattering of light from small particles, such as droplets in a fuel spray (see § 4.4.3.) Analysis of Mie scattered light can therefore give information on droplet sizes and droplet density. Images were recorded at a range of settings and conditions to match the benchmark tests and the Jaguar map.

At each injection timing, images were recorded over a range of delays in the illuminating laser light. This indicated how the spray developed and interacted with the piston surface, although the sequence was false since the images could not be recorded from the same cycle. Fortunately the

repeatability at a particular timing was found to be good, thus allowing a representative sequence to be recorded.

The engine variables included: fuel pressure, head/block temperature and amount of swirl. The majority of testing was performed at a single engine running condition, namely the worldwide mapping point: 1500 rev/min 2.62 bar BMEP. Injection timing was varied over a greater range than used by Jaguar, namely EOI 65 to 45 CAD before top dead centre (firing). Even with tests limited to one image per test point, the full test matrix would require around 250 tests to complete each of the Mie and LIF studies. A more manageable test matrix was made possible by identifying a 'standard' configuration and investigating each variable in turn. Interpretation and analysis of results showed if additional or re-testing was required.

7.3 Equipment

See chapter 6, "Test Bed", for a description of the main engine elements. The additional equipment used for the Mie study comprised the laser, camera and image capture hardware and software, see Figure 7-1 and description below.

7.3.1 Laser

The laser was a Nd:YAG Surelite Continuum III, capable of delivering pulses of 1064 nm wavelength light with a repetition rate of 10 Hz. This standard repetition rate was altered by the manufacturer to give 12.5 Hz which equated to one discharge per engine cycle at 1500 rev/min to match the WWMP. A separator unit, SSP-1, was used in conjunction with the laser. Unwanted wavelengths were passed into a beam dump whilst the desired wavelength was transmitted by the unit. The laser could be switched on and off remotely using an RS232 connection from a personal computer (PC) and triggering was from the engine control unit (§ 7.6).

The laser's fundamental wavelength of 1064 nm was deep in the infra-red range and therefore invisible to the human eye. Harmonic generators can be installed, though, which double, triple or quadruple the fundamental

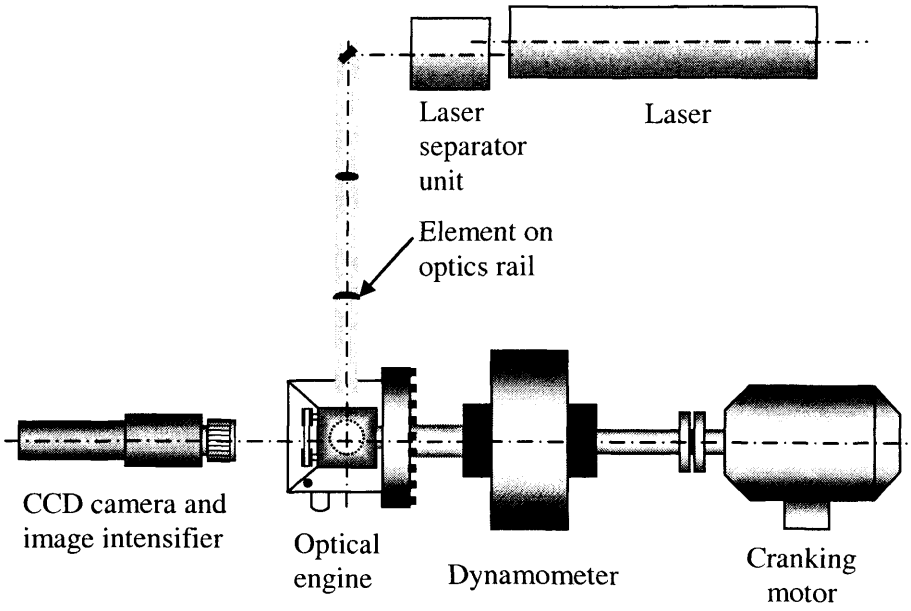

Figure 7-1 Layout of main equipment used for Mie study

frequency. This produces the second, third or fourth harmonic of the frequency, or wavelengths of 1064/2 = 532 nm, 1064/3 = 355 nm or 1064/4 = 266 nm. The second harmonic, 532 nm, was chosen since it is in the visible range and thus ideal for Mie scattering work. The second harmonic generator unit was installed in front of the emerging fundamental beam which then passed into the separator unit. The harmonic generator was 97% efficient at producing the desired wavelength, ie 532 nm. Next, dichroics in the separator removed 95% of unwanted wavelengths so that the light emerging from the laser was composed of approximately 92% the 532 nm wavelength. No steps were needed to prevent the unwanted 1064 nm wavelength light entering the optical engine since any effects it may have produced (eg fluorescence or phosphorescence) would be overwhelmed by Mie scattered light effects (§ 4.2). The presence of 1064 nm light merely represented a slight attenuation of power of the 532 nm wavelength light.

7.3.2 Elements on optics rail

The beam emerging from the separator was turned through 90^0 in the horizontal plane by a mirror, see Figure 7-2. A spherical lens on the optical rail then converted this beam into a cone, striking the cylindrical lens further along the optical rail. This generated the sheet of light which was focused onto the mirror in the optical engine cross bore

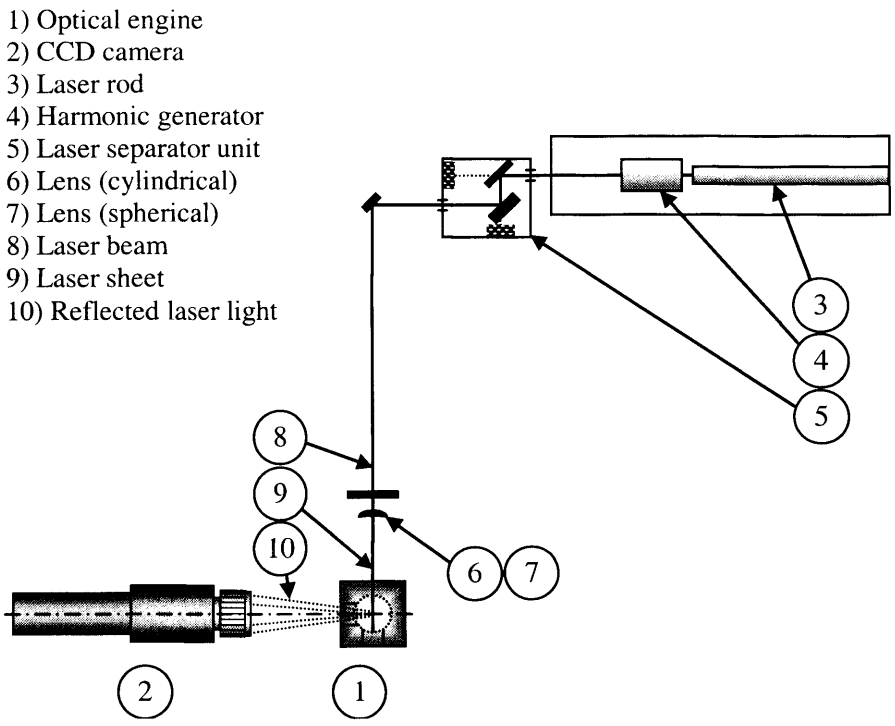

Figure 7-2 Layout of optical elements used to create light sheet in the optical engine cross-bore.

7.3.3 Camera

The camera was a Photonic Science Coolview 12 with 512x512 pixel resolution. This was a broadband model, able to capture visible and ultra violet (UV) light. It was fitted with a Nikon AF Micro Nikor 1:2.8 D lens, with aperture set to f/22.

7.4 Method of image capture

A standard desktop PC was used to store and post-process images and for remote activation of the laser for each run. A Matrox Imaging Corona-II frame grabber was installed in the PC. Image Pro Plus (IPP), version 3.0, software was used to control image capture, storage and post processing.

7.5 Conversion of metal engine to optical mode

The metal blanks were removed from the cylinder block and replaced with quartz windows giving two main windows in the optical block and a pent window in the cylinder head. The initial approach used was to bond the windows in place using Permabond ESP-110 applied in a 1 mm gap between the windows and the machined cavity. This bonding agent proved to be very strong to the extent that the windows cracked due to differential thermal expansion after cooling down from the curing temperature of 60^0C. This

setback caused a significant delay to the test programme while another approach was developed. It was decided to use a more flexible agent, namely RTV (room temperature vulcanising) manufactured by Pacer Technology who specified that the agent could be used up to a maximum temperature of 370^0C. A gap of 0.25 mm was left between the quartz and the cavity sides. The RTV bonded well to metal and quartz alike, and was resistant to attack by oil and gasoline. It had sufficient elasticity to accommodate differential thermal expansion between the metal block and the quartz windows.

The all-metal piston crown was substituted by the crown containing the slot of quartz. The quartz was supported by sitting on the ledge and RTV was used to bond and seal, rather than Permabond due to the experience with the block. The profile of the piston bowl was practically the same as the original all-metal design.

The next step involved the physical alignment of the 532 nm beam emerging from the laser separator unit, that is to say making it orthogonal and level with the engine centrelines. Once this was achieved, the ramp mirror was installed in the optical engine cross-bore and the beam was then confirmed as striking this mirror dead centre in both axes. Additional elements were then placed on the optics rail next to the reflecting mirror in order to produce the light sheet.

The slot of quartz in the piston lay on the centreline of the crown and thus also on the centreline of the combustion chamber. The axis of the injector body lay in this same plane. The Mie study required the light sheet to pass up the hollow of the Bowditch piston, through the slot of quartz in the piston crown and to enter the combustion chamber on its centreline. The light sheet thus intersected the fuel entering the injector. The optics rail elements were adjusted to tune the portion of the light sheet in the combustion chamber which was adjacent to the optical block quartz windows. This meant making the light sheet as wide as the combustion chamber, ie the sheet occupied the full length of the piston crown quartz slot, but was as thin as possible compared to the width of the quartz (see Figure 7-3). The camera was positioned to be orthogonal to the optical block main quartz window and an area of interest (AOI) was chosen. This careful alignment ensured that the

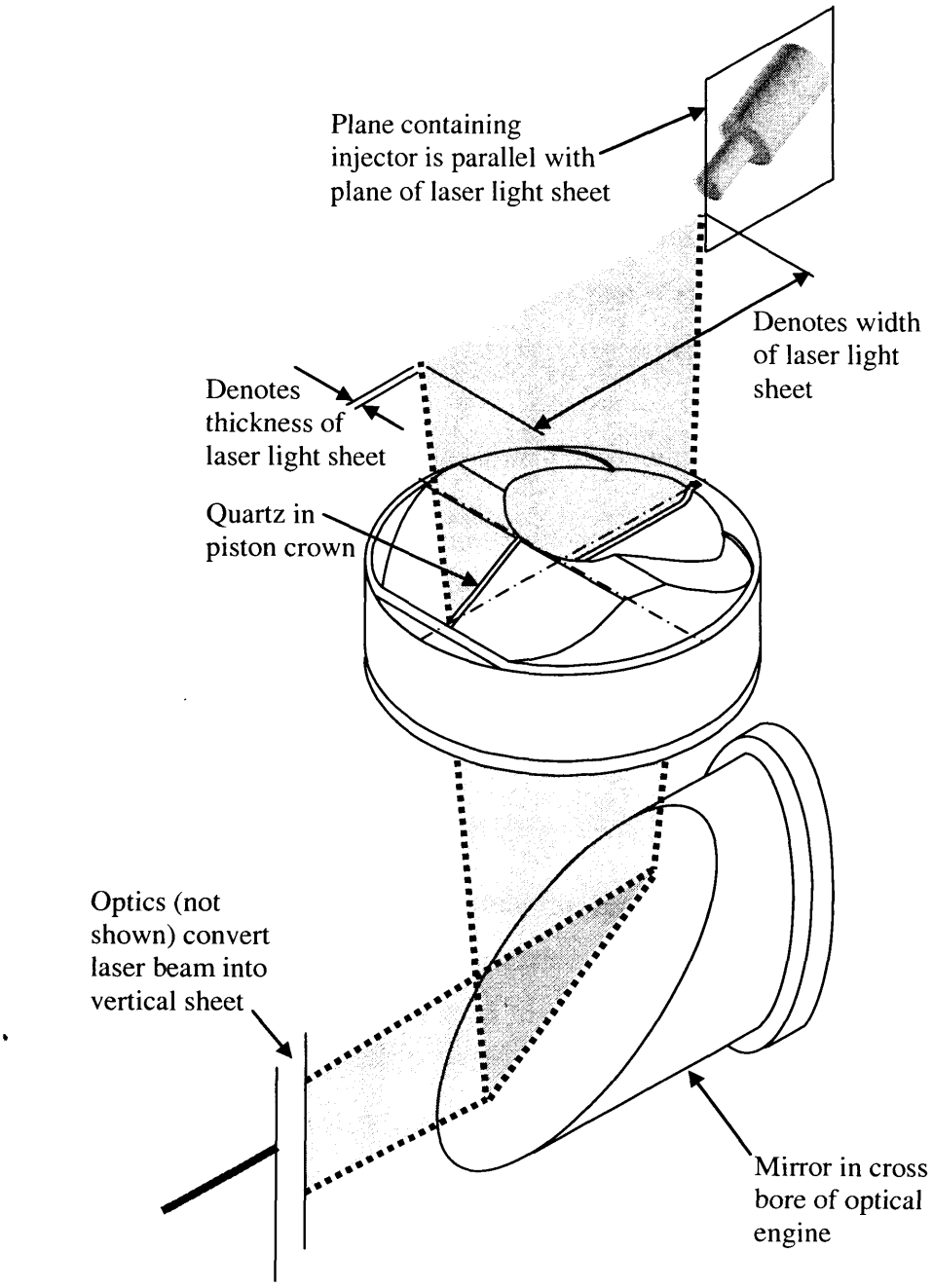

Figure 7-3 Relationship of light sheet to mirror, piston and injector

focal plane of the camera could be fixed on the plane of the light sheet, and interactions there captured in sharp focus. See §7.10.2 for a discussion of focal planes and obfuscation by particles out of the focal plane.

Finally the harmonic generator was adjusted to maximise the power of the light sheet using a Coherent P10i power meter, plugged into an oscilloscope and placed in the light sheet. This fine alignment was achieved by rotating the

screw for crystal phase-matching on the generator until the trace reached a maximum value.

As pointed out in Chapter 6, the engine, dynamometer and electric motor support steelwork was bolted to the plinth which was attached to the laboratory floor slab via an anti-vibration mat. This ensured that vibration from the engine was not transmitted to other equipment in the cell. As an additional measure, the camera and laser tables both had pneumatic, anti-vibration pads to minimise any movement of these items.

7.6 Control of engine and instrumentation

Synchronisation of the injector, engine, laser, camera and computer was achieved using a shaft encoder and electronic signal generating units. Note that in the following description 'integration' refers to making the camera chip active, whereas 'gating' is equivalent to opening and closing the shutter of a film camera. Furthermore, 720 CAD is defined as TDC (firing).

The aim was to gate the camera while the laser flashed, all within the CCD integration period of the chip in the camera. The Hohner shaft encoder was connected to the camshaft and used to provide a TTL engine timing signal (synchronised with the physical TDC using a CRO as described in Chapter 6). This TTL signal acted as a trigger for two SRS signal generator units, which formed the heart of the control system (Figure 7-4). The SRSs each provided two outgoing TTL signals, totalling four signals, one each to the computer, camera, injector and laser. A delay and pulse width could be set for each signal. The equipment was triggered every cycle in the case of the laser, but only when other switches were activated in the case of the computer, camera and injector.

The SRS was selected as it has an exceptionally high specification in terms of precision of the timing of its signals. The selectable delays had a resolution of 5 ps, channel to channel jitter was less than 50 ps and insertion delay (ie the delay between receipt of an external trigger and initiation of the output signal) was approximately 85 ns.

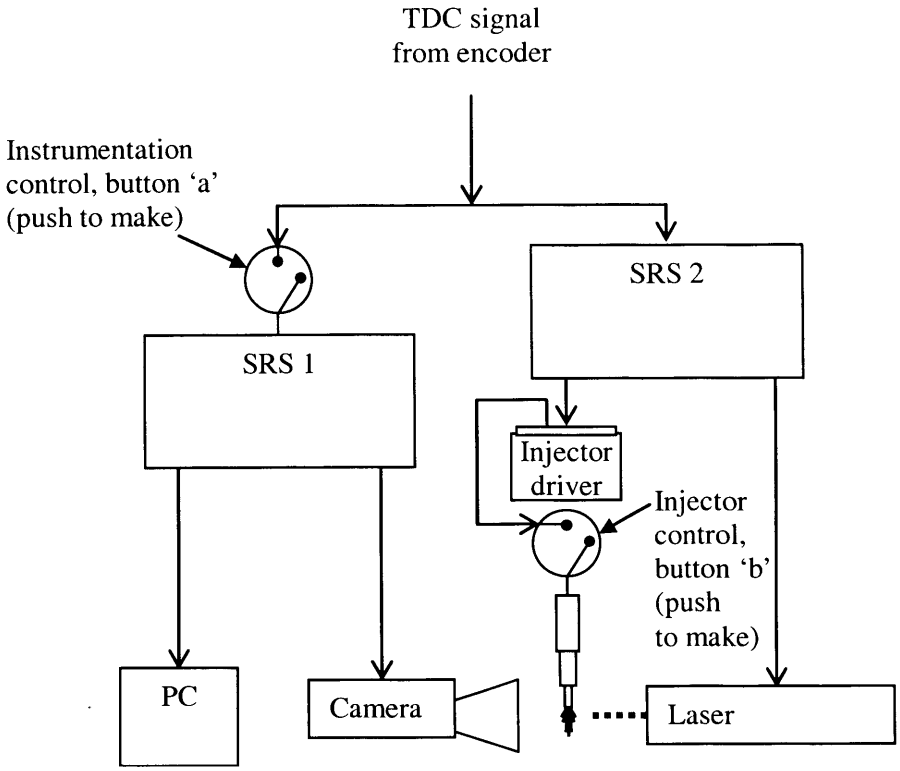

Figure 7-4 Equipment for control of instrumentation

7.6.1 Laser

A signal was needed to trigger each laser discharge. The SRS signal was of a nominal width since the rising edge was sufficient to trigger the laser. The delay to the signal rising edge was chosen to be a certain number of CADs after the triggering of the injector to capture the developing spray.

7.6.2 Computer

The camera's chip integration was controlled by the Image Pro Plus (IPP) software on the computer and initiated by a short duration signal from the SRS. The delay and integration time were set in IPP and the sequence started by pressing the instrumentation control button. When the instrumentation control button was pushed, the circuit was made and once the SRC received the next TDC from the encoder, IPP accepted the 'snap' command, waited for the expiry of any delay and began the integration period. Once the period set in IPP had elapsed, the integration period ended. For the Mie study, a delay of 40 ms and a pulse width of 80 ms combined to make the integration period 80 ms, equally spaced about the TDC (firing) position, see Figure 7-5.

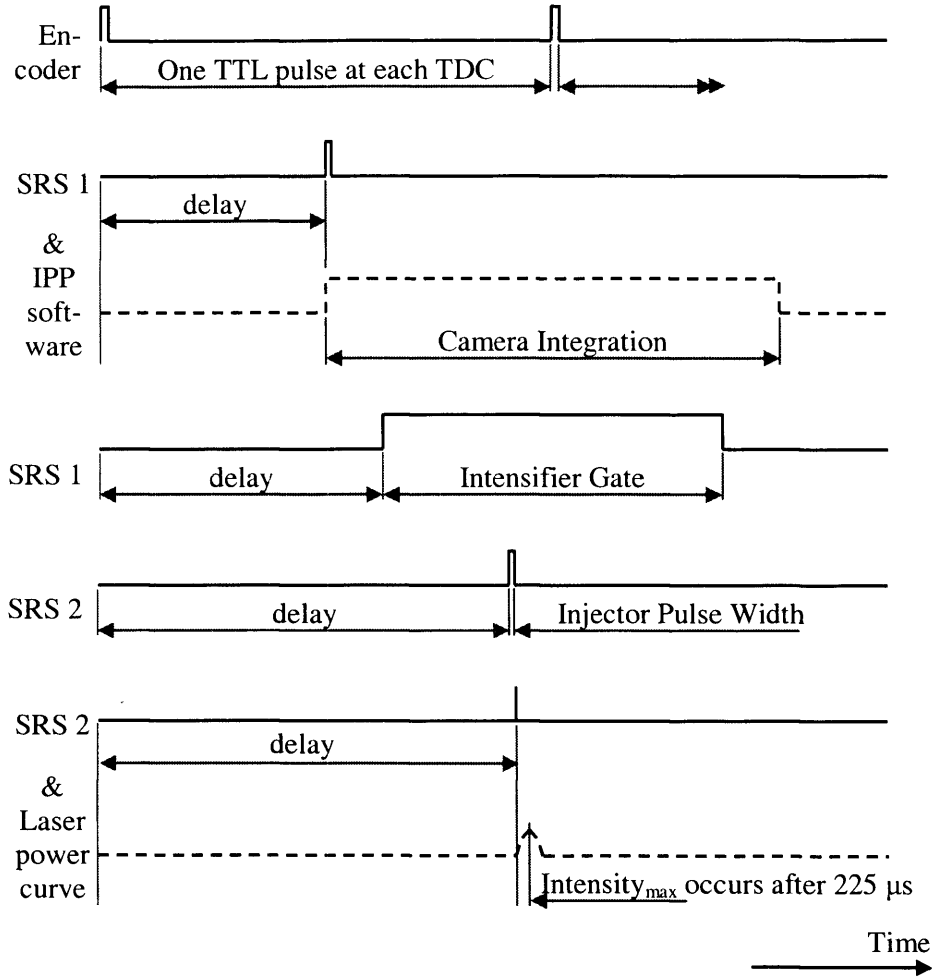

Figure 7-5 Timing of events using SRSs (Stanford Research Systems signal generators)

7.6.3 Camera Gating

The camera gating was controlled directly by the signal generator SRS 1. Once the first encoder TDC signal was received after the push of the control button, the delay and pulse width were such that the gate was open for 60 ms, straddling the TDC (firing) position.

7.6.4 Injector

The timing and pulse width of the injector were set by the second signal generator, SRS2. This in turn activated the Bosch HSDEV injector driver circuit. When the active pin in the driver was high, the solenoid in the injector was off. When the active pin went low, the solenoid was energised and the pintle withdrawn from its seat, allowing the pressurised fuel to flow through the injector. The pintle closed again when the SRS2 made the driver active pin high again. For the injector, the SRS pulse width directly corresponded to

the injector pulse width and the delay corresponded to the SOI in CAD of the test point being used. The injector control button (push to make switch 'b') was included in this circuit so that the injection of fuel and thus engine firing could be closely controlled. Firing must be closely controlled in an optical engine since prolonged running can cause damage to the windows through a combination of thermal- and cylinder pressure-induced stress. The approach adopted was to use the electric motor to turn the engine at the required speed, check that all engine controls were correctly set, initiate firing through pushing the injector control button and then take images once the engine was running consistently by pressing the instrumentation control button. The injector control button was released soon after the images had been recorded.

7.7 Experimental methods

The first part of the practical work consisted of preliminary tests and the commissioning of the optical engine. The sequencing of the laser and camera was tested by monitoring the behaviour of the systems while using a simulation of the engine. A function generator was set to reproduce the shaft encoder's TTL pulse at 12.5 Hz and a storage oscilloscope was used to confirm that the triggers, delays and pulse widths were working as expected. The simulated engine was also useful for carrying out some datum testing of the injector under quiescent conditions at atmospheric pressure. A camera position was selected, the optical engine was broken at the flange and the cylinder head and optical block were raised out of the way. A rig was used to clamp the injector, spark plug and the quartz main window in their respective 'engine' positions. The simulated engine then permitted the injector to be fired across what would have been the combustion chamber. By this means, the camera could be moved to frame the image and focusing and aperture (f-stop) settings could be investigated. Images were taken with various injector delay values to assemble a library of ambient condition reference images of the injector (see Appendix C).

Generally the optical engine ran at the same settings as the all-metal engine, although at some settings it took longer before stable firing was established.

7.8 Mie tests

Having confirmed that all systems operated satisfactorily and that combustion was stable, the Mie scattering testing began. The overall procedure for a single test point can be summarised as follows:

- Motor engine up to 1500 rev/min
- Apply load (dynamometer)
- Check laser flashes in synchronisation with engine using oscilloscope
- Select 'snap' in IPP software
- Press and hold push to make switch 'b' (injector control button)
- Press and hold push to make switch 'a' (instrumentation control button)
- Once image downloaded to computer, release both buttons
- Motor engine down to 0 rev/min
- Save image
- Clean quartz windows
- Select signal generator settings for next test point
- Begin next run

The images required some post-processing after they were saved. The IPP software permitted inversion and saving to 8-bit format. The latter allowed the images to be manipulated and displayed in standard packages such as Microsoft Word.

7.9 Results

The results of the Mie study are presented in the following pages as TIFF (Tagged Image File Format) images. The full set of images appears in Figure 7-6 to provide an overview. This includes a sequence of ambient air injections using the slotted quartz crown. In Figure 7-7, all the SOI 639 CAD images are grouped together, Figure 7-8 features the SOI 654 CAD images and the SOI 675 CAD images are in Figure 7-9. Note that no images were obtained at delta 45 CAD and delta 63 CAD using the start of injection 675 CAD, since the piston was at or beyond top dead centre at this timing and thus almost entirely filling the viewing area. "Delta" refers to the number of CAD since the signal was sent to the Bosch injector to initiate injection. An alternative means of viewing the same images is provided by grouping like deltas together, Figure 7-10, Figure 7-11 and Figure 7-12 All the results shown were taken with a cylinder block temperature of 40^0C, pump gasoline and a spark

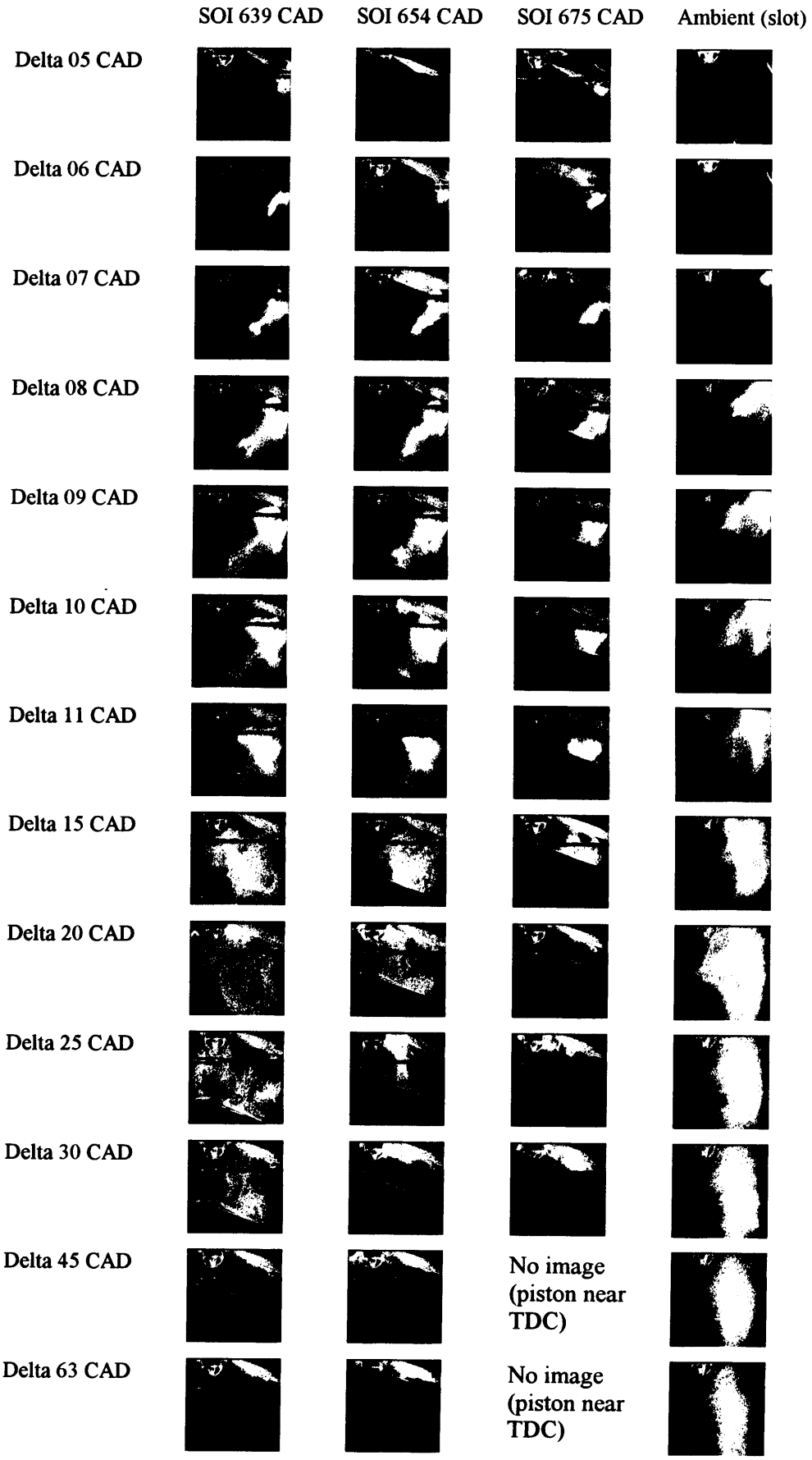

Figure 7–6 Thumbnails of Mie scattering images in firing engine, SOI 639, 654 and 675 CAD, alongside ambient air images.

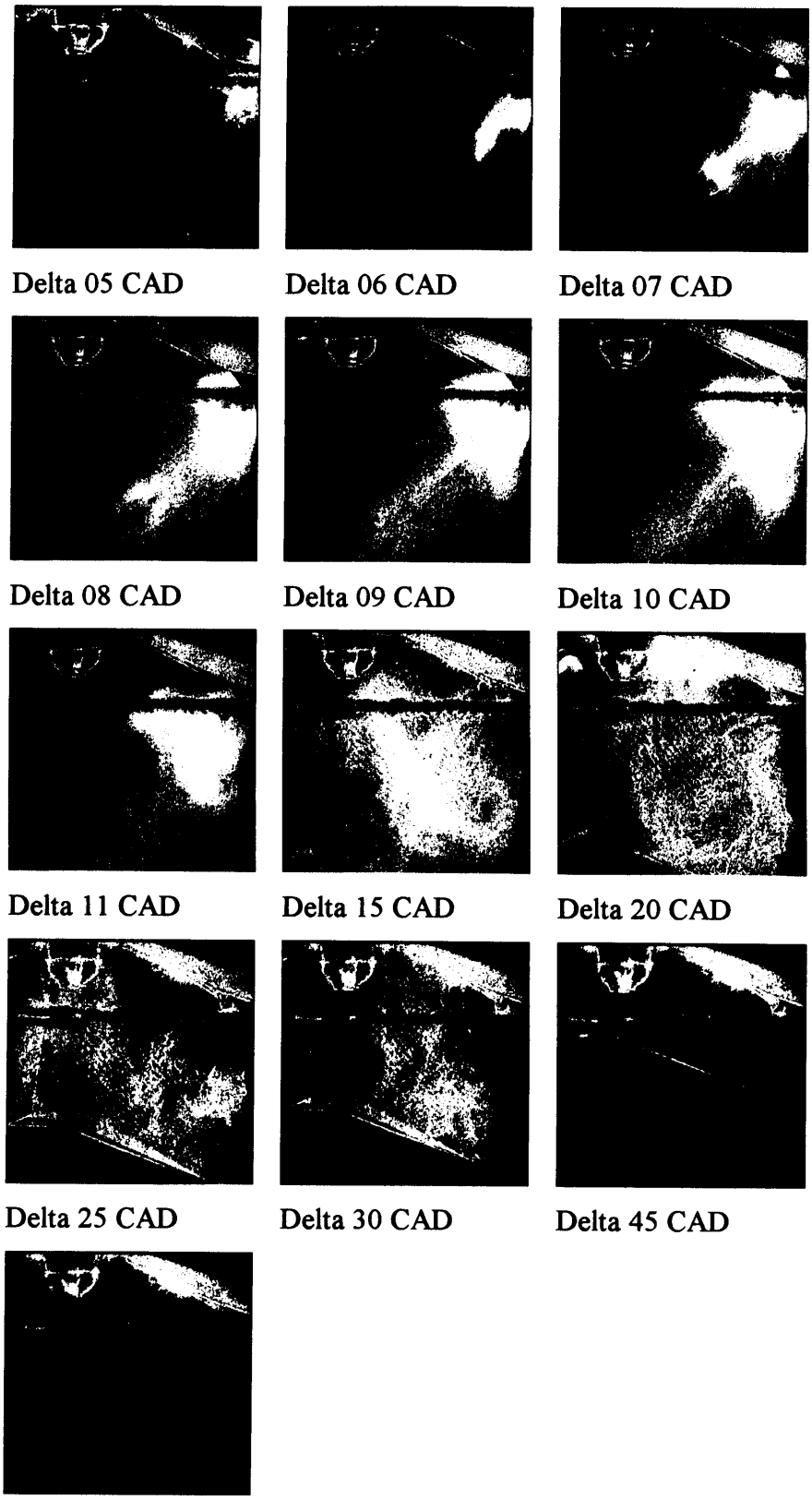

Figure 7–7 Mie scattering images in firing engine, SOI 639 CAD

Delta 05 CAD

Delta 06 CAD

Delta 07 CAD

Delta 08 CAD

Delta 09 CAD

Delta 10 CAD

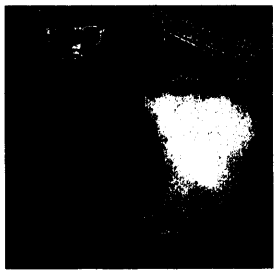

Delta 11 CAD

Delta 15 CAD

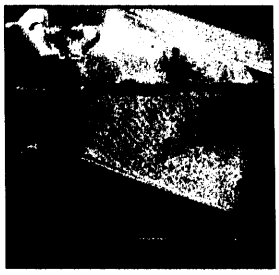

Delta 20 CAD

Delta 25 CAD

Delta 30 CAD

Delta 45 CAD

Delta 63 CAD

Figure 7–8 Mie scattering images in firing engine, SOI 654 CAD

Delta 05 CAD

Delta 06 CAD

Delta 07 CAD

Delta 08 CAD

Delta 09 CAD

Delta 10 CAD

Delta 11 CAD

Delta 15 CAD

Delta 20 CAD

Delta 25 CAD

Delta 30 CAD

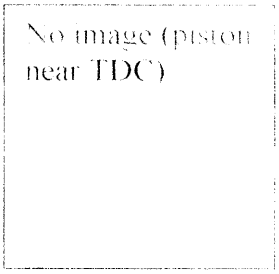

Delta 45 CAD

Delta 63 CAD

Figure 7–9 Mie scattering images in firing engine, SOI 675 CAD.

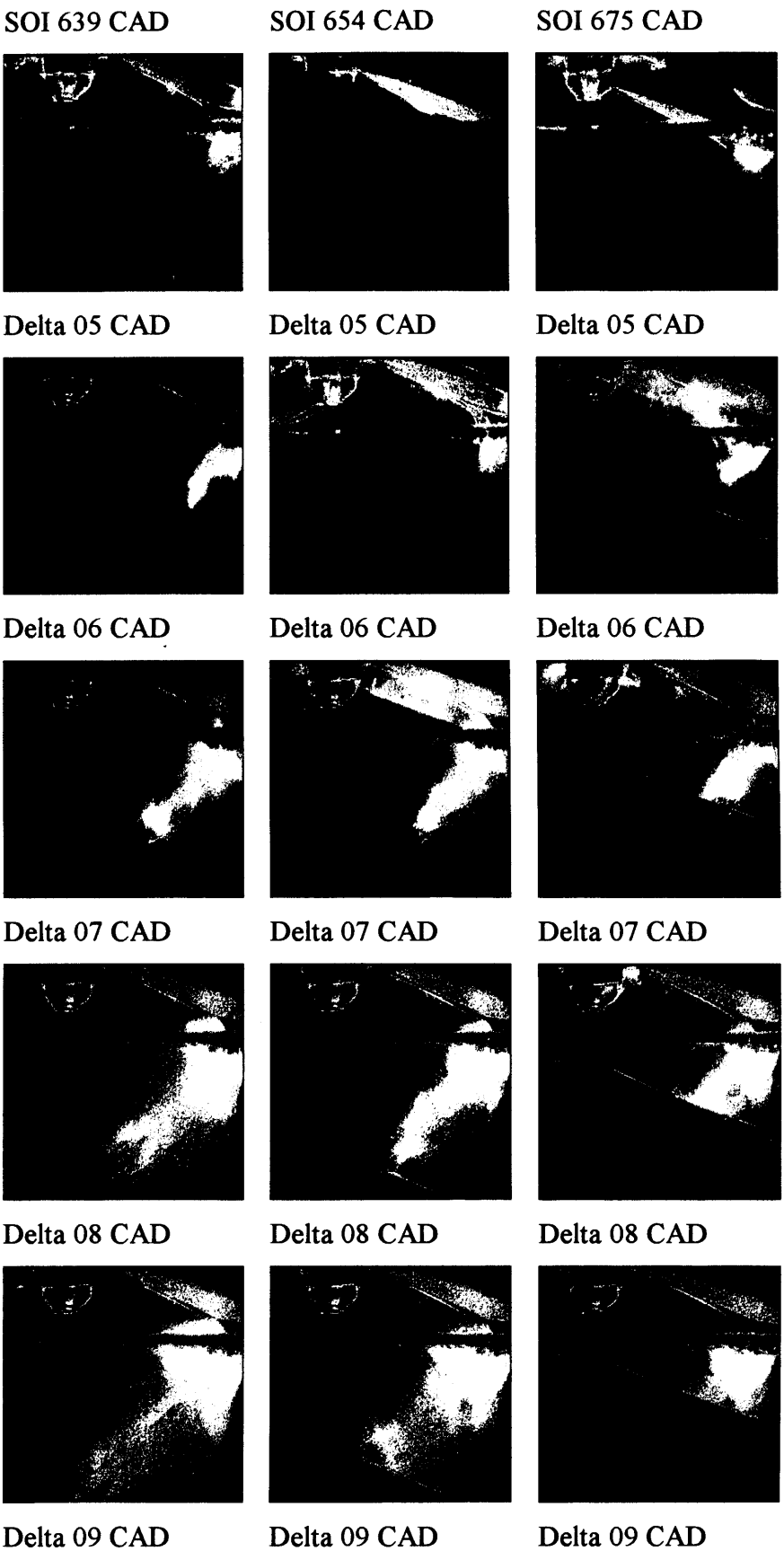

Figure 7–10 Mie scattering images in firing engine, delta 05, 06, 07, 08 and 09 CAD

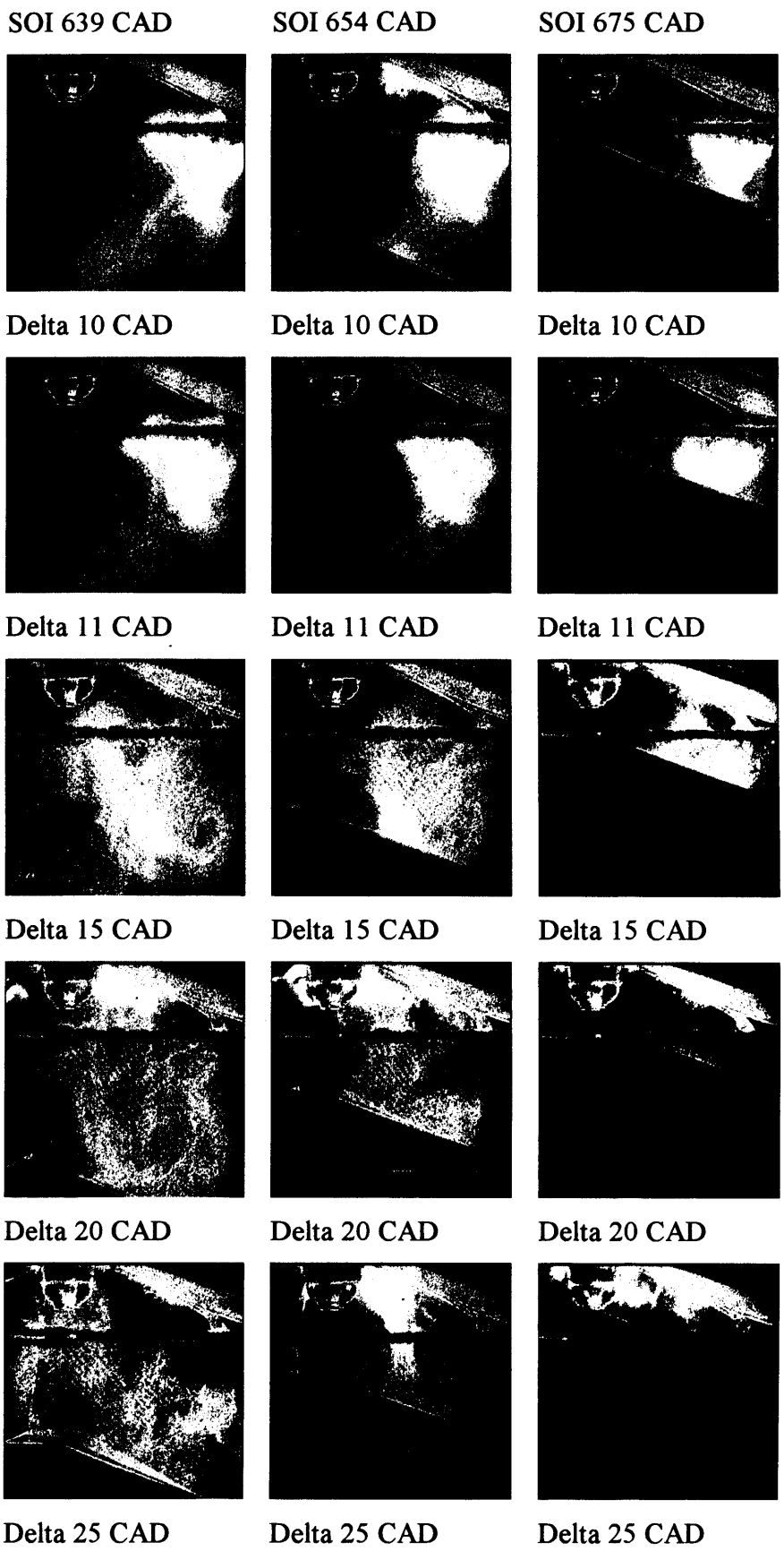

Figure 7–11 Mie scattering images in firing engine, delta 10, 11, 15, 20 and 25 CAD.

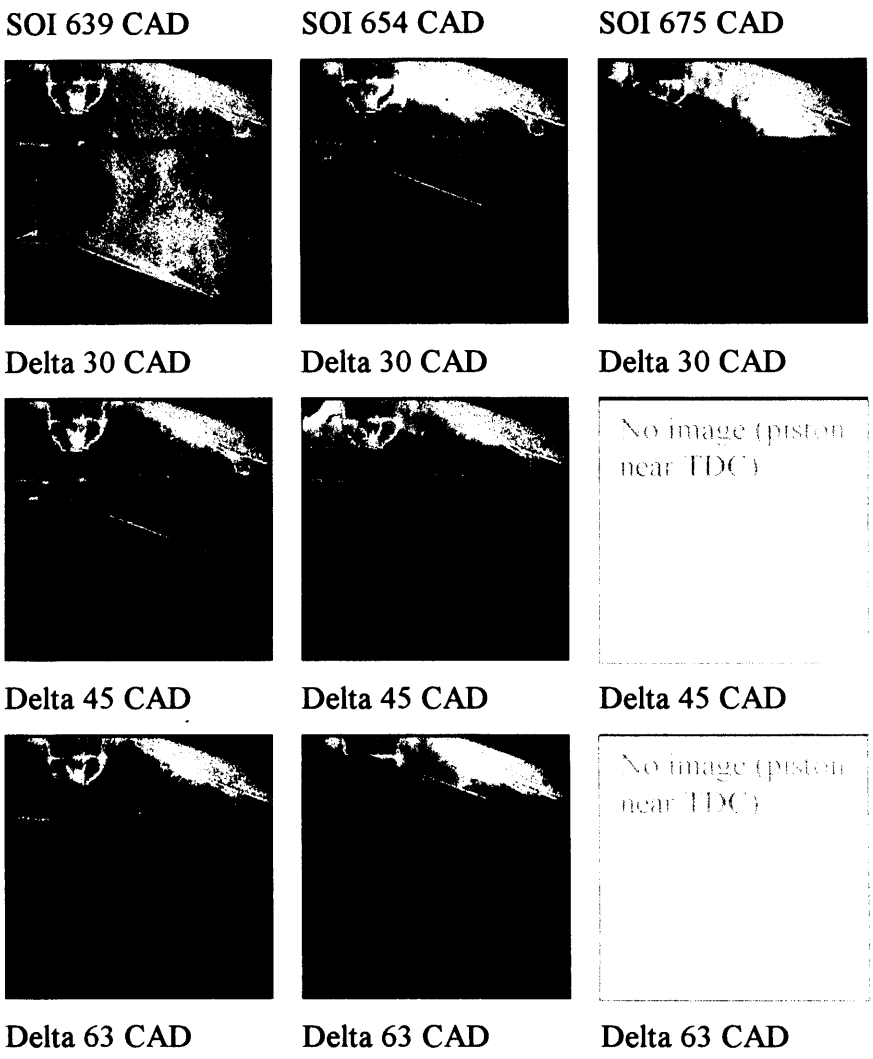

Figure 7–12 Mie scattering images in firing engine, delta 30, 45 and 63 CAD.

timing of 27 CAD BTDC (firing). The engine speed was 1500 rev/min (± 10 rev/min) and a minimal load was set on the dynamometer to reproduce WWMP as closely as possible. The swirl control valve was in the 18^0 position (see Figure 6-3 for definition) and the engine lightly throttled (as in the benchmark tests). Single shots were taken using 80 ms gating time on the camera (the laser pulsewidth was 5 to 7 ns duration and this effectively controlled the exposure of the image). The lens was set at f/22 aperture and focus was fixed on the combustion chamber centreline (the image plane) using a target device inserted through the spark plug hole. The Mie images were converted to 8-bit, greyscale, TIFF before being imported into Microsoft Word.

7.10 Discussion

7.10.1 Introduction

A comprehensive discussion of these studies is presented in Chapter 8 along with a comparison with the LIF results. An appraisal of the Mie images alone follows.

Figure 7-13 and Figure 7-14 show the relationship of the quartz windows to the main engine components and indicate how the field of view relates to both. Since the main and pent roof quartz windows had their inner surfaces machined to match the bore of the combustion chamber and their front surfaces were flat, they acted as plano-convex lenses. These do not distort in the vertical plane, but in the horizontal plane a distortion is introduced, varying according to distance from the vertical centreline of the window. No steps were taken to compensate for this distortion since the work was mainly qualitative. The establishing shots, taken once through the quartz window and once without the window in place, illustrate this point (see Figure 7-15).

7.10.2 Observations

A first inspection of the images shows a good overall intensity of light, adequate clarity and most of the features within the combustion chamber are visible. Note that the main source of illumination is by the laser light sheet entering the combustion chamber through the slot of quartz in the piston crown. It is possible that some stray light entered the combustion chamber

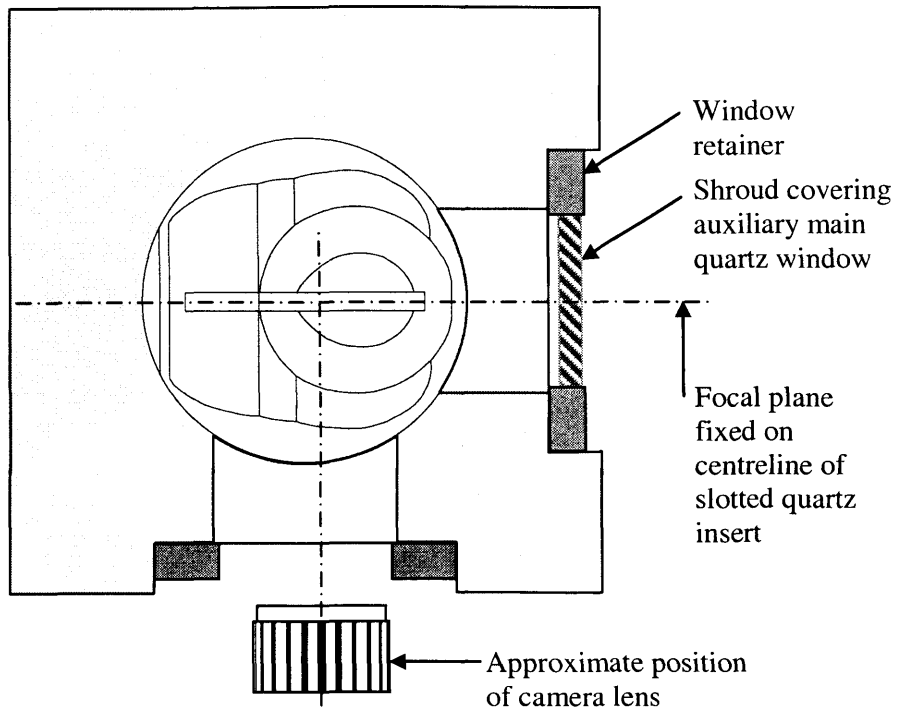

Figure 7-13 Layout of quartz windows and camera

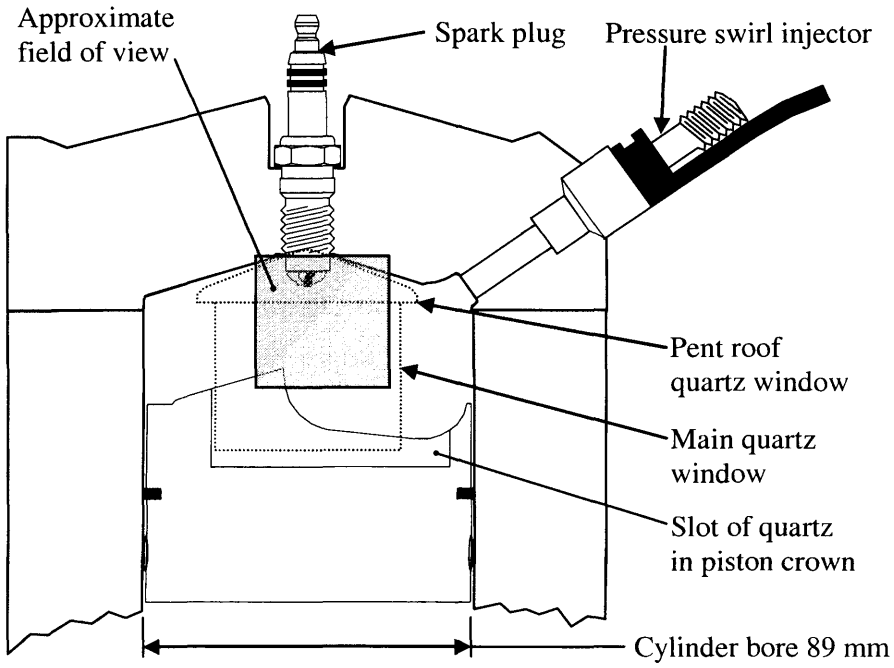

Figure 7-14 Field of view superimposed on combustion chamber

through the main windows, but it is likely that it was very low in intensity compared to the sheet emanating from the slot.

Some clear bright areas are visible in the images as well as areas of less intensity or even a misty appearance. The bright areas are from fuel in the

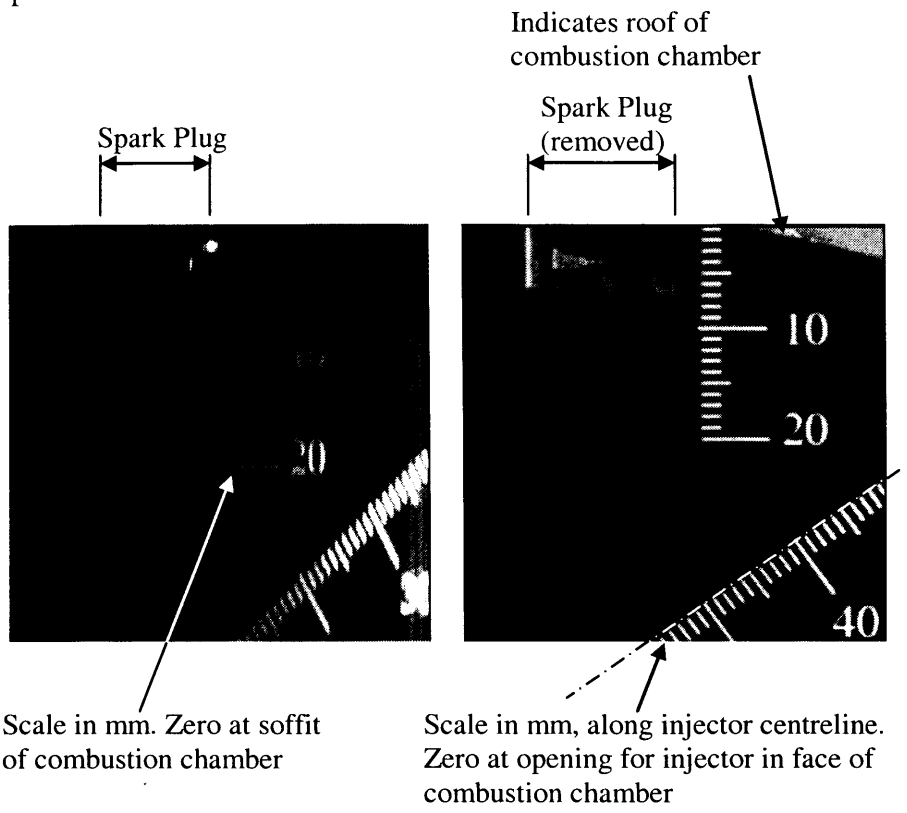

Figure 7-15 Establishing shots of scales in combustion chamber illustrate distortion caused by quartz. Left image taken through main window.

light sheet directly reflecting light toward the camera and reaching it with a minimum of further interactions. One possible cause of the misty areas is firstly due to fuel out of the image plane being illuminated by light scattered from droplets in the image plane. Secondly, fuel between the centreline and the camera would have absorbed light coming from the fuel on the centreline making it of reduced intensity (Figure 7-16 and Figure 7-17).

It should be noted that the images in each set are not a true sequence since they were taken from different cycles. A sequence of multiple shots and cylinder pressure traces were recorded at a single test point to indicate levels of cyclic variability and show whether it was valid to consider the Mie images as pseudo sequences. The output from the Kistler pressure sensor mounted in the cylinder head provided the pressure trace and this was recorded on a two-channel Tektronix TDS1002 CRO. A take-off from the spark plug high-tension lead was fed to the CRO to act as a reference trace. All the tests used the firing engine with SOI 654 CAD and began with runs 1 to 10 with delta set to 6 CAD, then ten runs (i to x) with delta set to 8 CAD and a final run

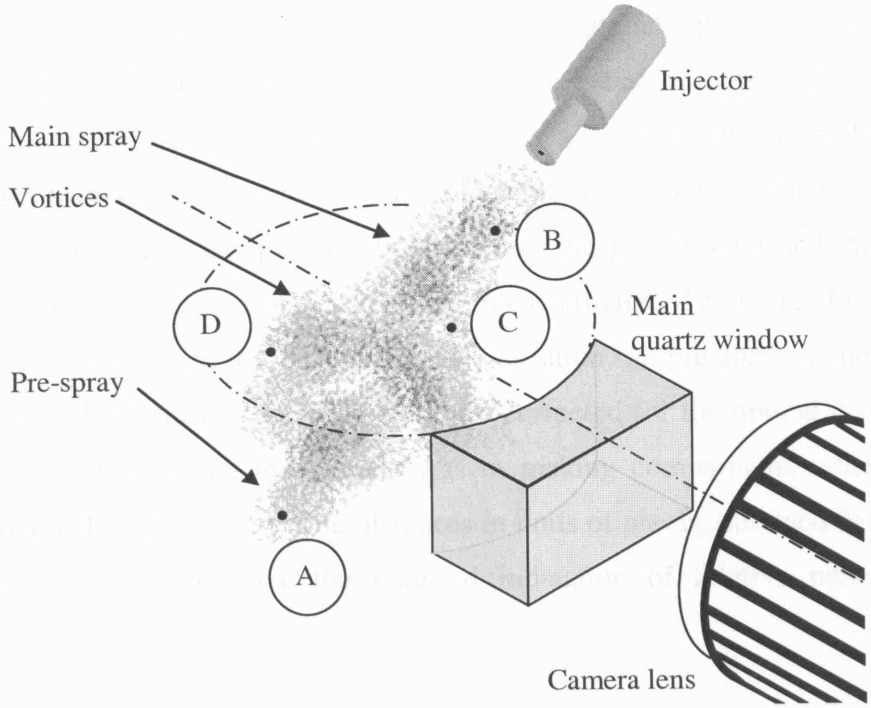

Figure 7-16 Schematic showing typical form of spray cone from pressure swirl injector. Letters A to D refer to cases in Figure 7–17

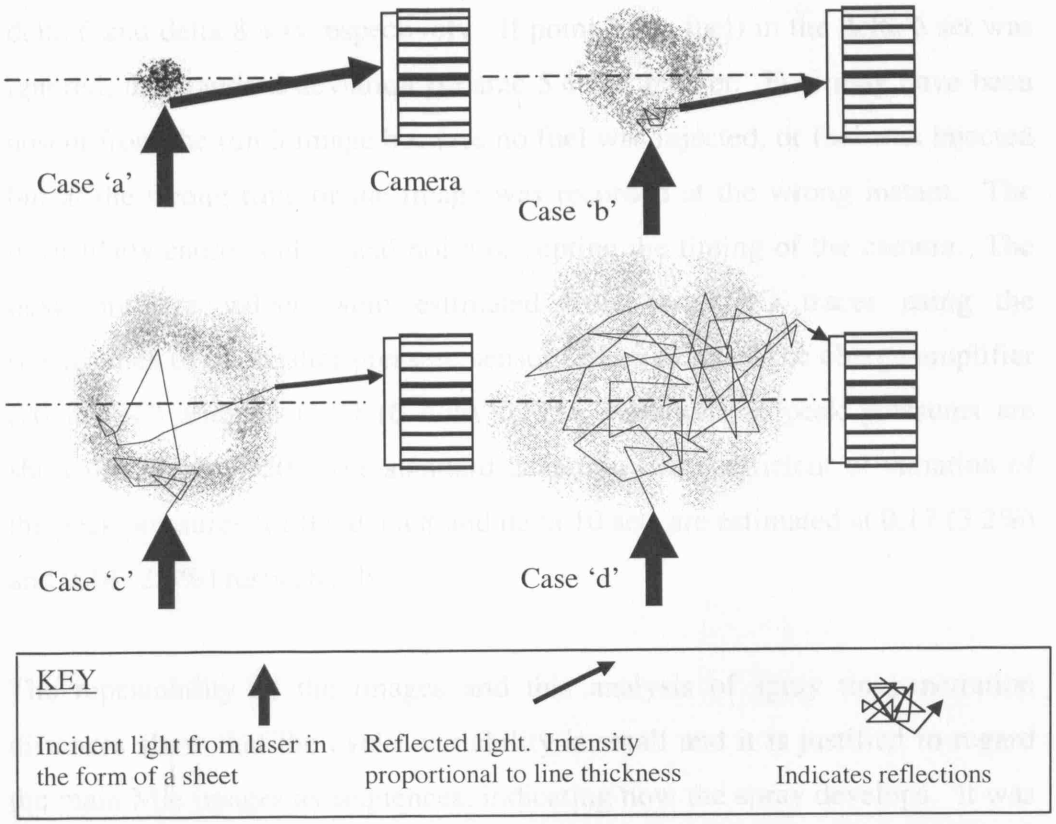

Figure 7-17 Intensity of reflected light according to position in spray cone

(11) with delta again set to 6 CAD. The images and pressure traces are presented in Figure 7-18. The sprays within each set appear reasonably uniform: no spray is evident in run 3 of the delta 6 images, but spray has just emerged from the injector recess in the remainder of the delta 6 images. In the delta 8 images, the pre-spray is about to enter the piston bowl and the main spray is at a similar stage of development in each image. The variability of the spray was quantified by observing the variation in pre-spray penetration distance. The distances recorded were not corrected for the optical distortion mentioned above since the interest was in making comparisons rather than relying on absolute values. The distances in units of pixels, obtained from IPP for the raw images, gave the required indication of relative penetration distances.

This was a valid approach as long as the spray tip was always in the same region of the image. Coordinates for a fixed datum point and the most distant part of the spray were recorded, with the difference in each case shown in Figure 7-19. The standard deviations for the results were 29.0 and 11.5 for the delta 6 and delta 8 sets respectively. If point 3 (no fuel) in the delta 6 set was ignored, the standard deviation became 5.6 for that set. Fuel may have been absent from the run 3 image because no fuel was injected, or fuel was injected but at the wrong time or the image was recorded at the wrong instant. The most likely cause is electrical noise disrupting the timing of the camera. The peak pressure values were estimated from the CRO traces using the sensitivities of the Kistler pressure sensor (20.16 pC/bar), the charge amplifier (20 mv/pC) and the CRO (6 v/div). The variations in peak pressures are shown in Figure 7-20. The standard deviation and coefficient of variation of the peak pressures for the delta 8 and delta 10 sets are estimated at 0.17 (3.2%) and 0.14 (2.6%) respectively.

The repeatability of the images and this analysis of spray tip penetration distances show that the cyclic variability is small and it is justified to regard the main Mie images as sequences, indicating how the spray develops. It was reassuring to observe that the cyclic variability of the peak cylinder pressure

Pre-firing and SOI 654, delta 6 CAD SOI 660 delta 8 CAD and post-firing

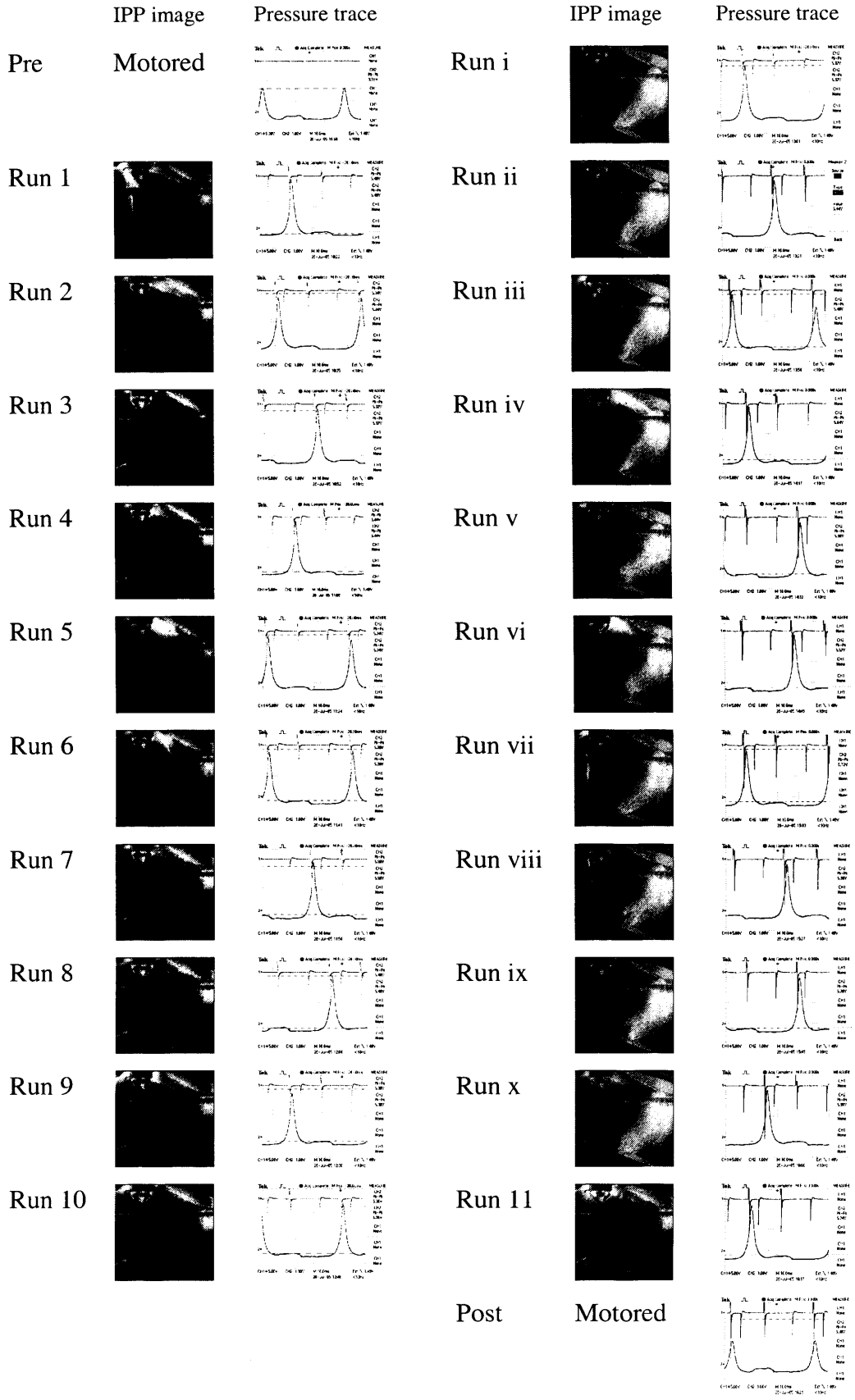

Figure 7–18 Images and pressure traces from repeated runs to investigate cyclic variability

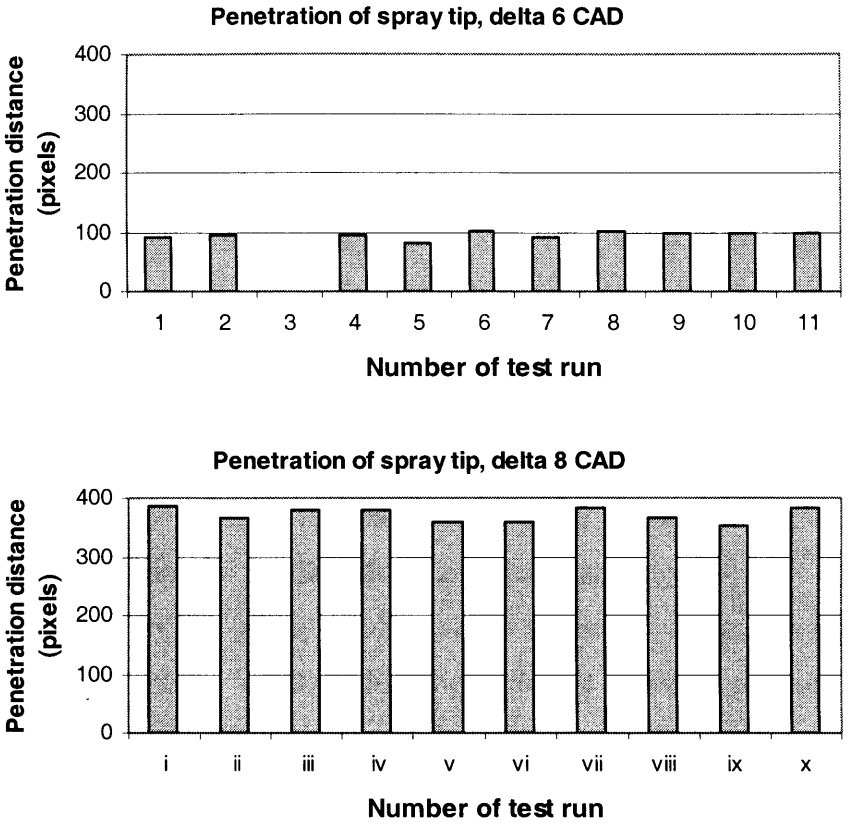

Figure 7-19 Cycle to cycle variation of penetration distance, during firing

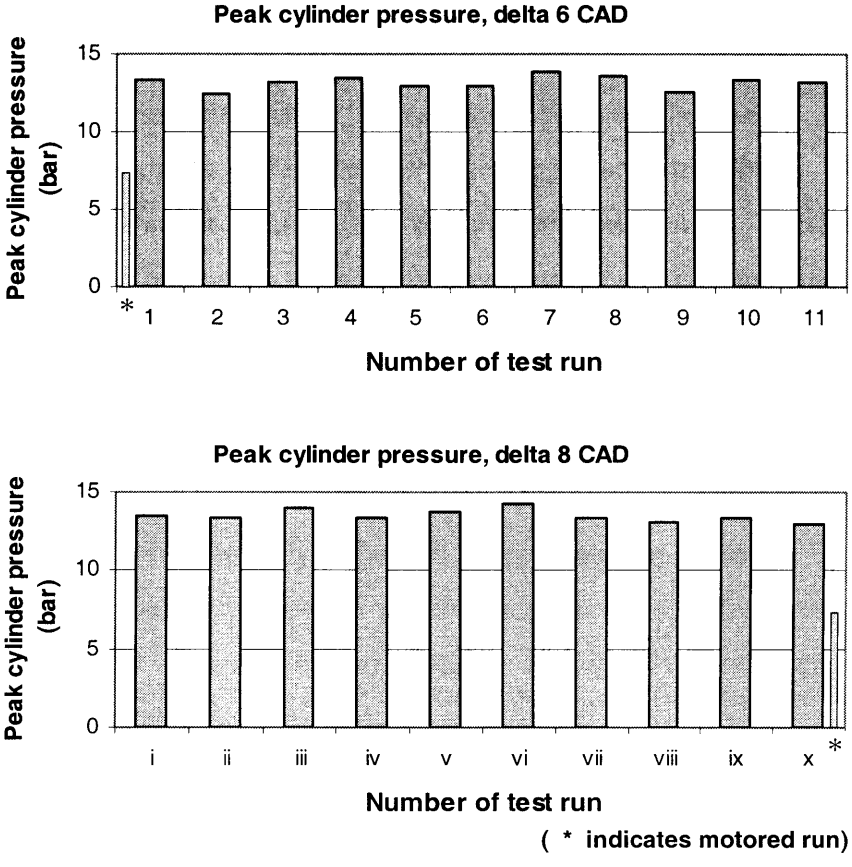

Figure 7-20 Cycle to cycle variation of peak pressure during firing

values was typical of that expected from a stable spark ignition engine.

7.10.3 Features

The first feature of note in the SOI 639 CAD set is the appearance of a pre-spray in the delta 6 image (Figure 7-21). Pre-spray occurs because the swirl injector is unable to impart swirl motion to the earliest emerging fuel. Residing next to the pintle, this fuel exits the injector having travelled a negligible distance along the tangential slots. It therefore has very little angular momentum and it tends to emerge from the injector as an agglomerated mass of fuel with a consequently high penetration rate. A calculation of the penetration rate based on distance (measured on the image) and time (based on the CAD value) is complicated by the fact that the distortion caused by the quartz window varies across its width. An estimate, with approximations for window distortion and the recessed position of the injector, gives a rate of 60 m/s, compared to the range 68 to 86 m/s reported by Zhao et al. [2002]. The observed first emergence of the fuel at 6 CAD after the initiation signal form SRS 2 represents the delays caused by the Bosch driver and the time needed to move the pintle of the injector.

The main spray is visible in image delta 8 for SOI 639 CAD. As the main spray becomes more established, it assumes the classic bell shape expected from an inwardly opening pressure swirl injector [Zhao et al., 2002]. Vortices are clearly visible as the rotating cone entrains air from nearby. A calculation of the penetration rate of the main spray is even more complicated since it is a matter of subjectivity in deciding on a reference point to track.

It is useful to compare the spray shapes from the firing engine with those from the injector in isolation, ie outside the engine, injecting into ambient air, but behind the quartz window. These images are presented in Appendix C. There is considerable similarity between the two sets and any differences can be explained by back pressure and air motion. A more detailed discussion is presented in Chapter 8.

Close observation of the SOI 639, 654 and 675 CAD images shows a dark area in the columns of pixels under the spark plug. This was also seen in the

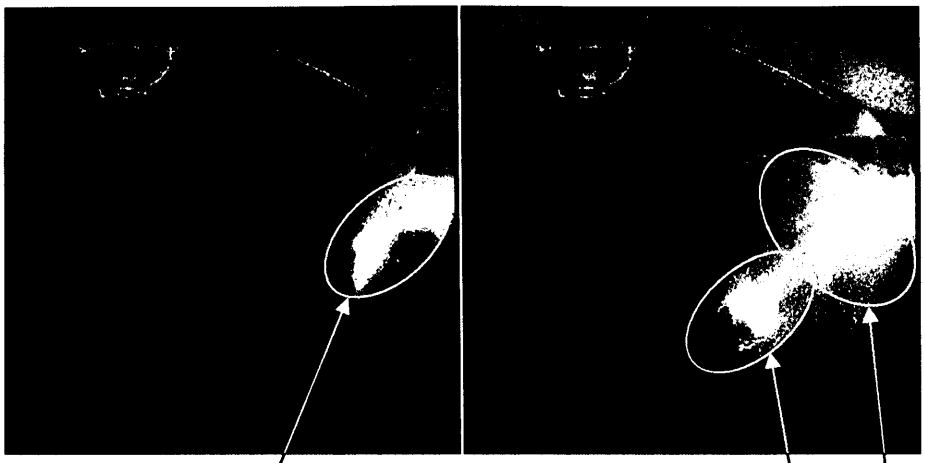

Figure 7-21 Typical pre-spray and main spray

slotted crown ambient air images and was identified as being a consequence of the shape of the quartz. As already mentioned (see § 7.7), prior to testing with a firing engine, a series of free air spray sequences was recorded using an arrangement to simulate combustion chamber geometry. The three sets of free-air spray sequences were: laser sheet passing through disc crown, passing through slotted crown and with piston crown removed (see Figure 7-22). The method used was to simulate the relative positions of the injector, spark plug and quartz windows with the cylinder head raised so that the spray could be seen as it would appear in the motored or firing engine.

A distinct boundary was observed in the ambient disc set corresponding to the limit of the quartz in the piston crown (Figure 7-22). No dark area was apparent in the ambient images with the crown removed, but in the slotted set, columns of reduced intensity were seen. This suggested that the quartz was the cause of the dark areas. This effect was quantified by looking at the variation in pixel intensities along a line drawn across the image, halfway up. The three images for delta 30 CAD were chosen and a line at half height selected. Since each image measured 512 by 512 pixels the 256^{th} row of pixels was isolated in the Matlab software and operated on as 512 by 1 vector. The maximum intensity was found in this vector and all the values were divided by this. However, once plotted, a large amount of scatter was seen. A revised method, based on a band of 40 pixels height extending across each image was adopted. The band was from the 235^{th} to the 275^{th} pixel and it

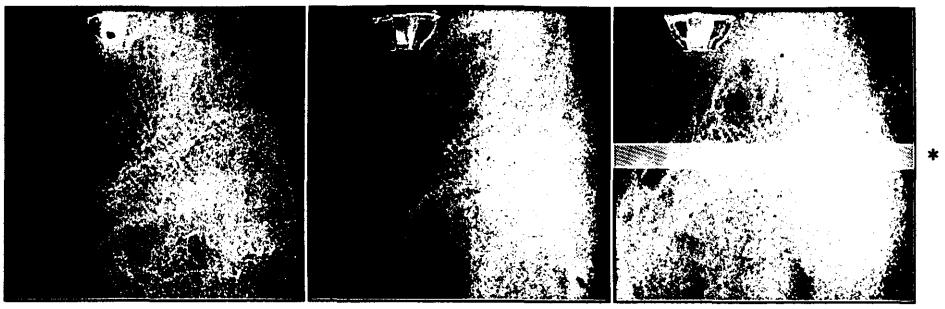

Disc crown, distinct dark area | Slotted crown, columns of variable intensity | No crown, uniform intensity

* Indicates band of pixels sampled for intensity analysis

Figure 7-22 Fresh air images, delta 30 CAD, intensity more uniform in absence of quartz piston crown

produced a 512 x 40 pixel matrix. A mean was taken of each of the 512 40-pixel columns, this was then normalised against the maximum intensity in this column and produced a 512 by 1 vector for plotting. These normalised intensities are shown in Figure 7-23.

It can be seen that the dark regions in the images corresponded with the region of low laser sheet intensity. For the disc set, the intensity in the dark region was 10% of the maximum found in the sample band, and for the slotted set the figure was 20% of the maximum value. For the slotted crown, the near vertical surface of the bowl was likely to cause total internal reflection of the laser light in the quartz and let very little light pass to illuminate the spray. However, this effect was partially disguised in the Mie scattering work by the multiple reflections within the fuel. It was decided not to carry out a light sheet correction for the Mie study, but to keep in mind possible illusions due to the variation of intensity. This issue is discussed further in Chapter 8, the LIF study, where the above intensity percentage values suggest that a light sheet intensity correction should be applied to the LIF images.

An interesting feature of several of the images, eg SOI 639 delta 20 CAD, SOI 654 delta 15 CAD firing (Figure 7-7 and Figure 7-8) and the equivalent ambient shots (Appendix C), is the appearance of concentric lines which seem to have a centre near to the site of the injector. It was thought that these lines were created by an optical effect caused by the lack of co-linearity between the axis of the camera and the axis of the quartz window (Figure 7-24). This is

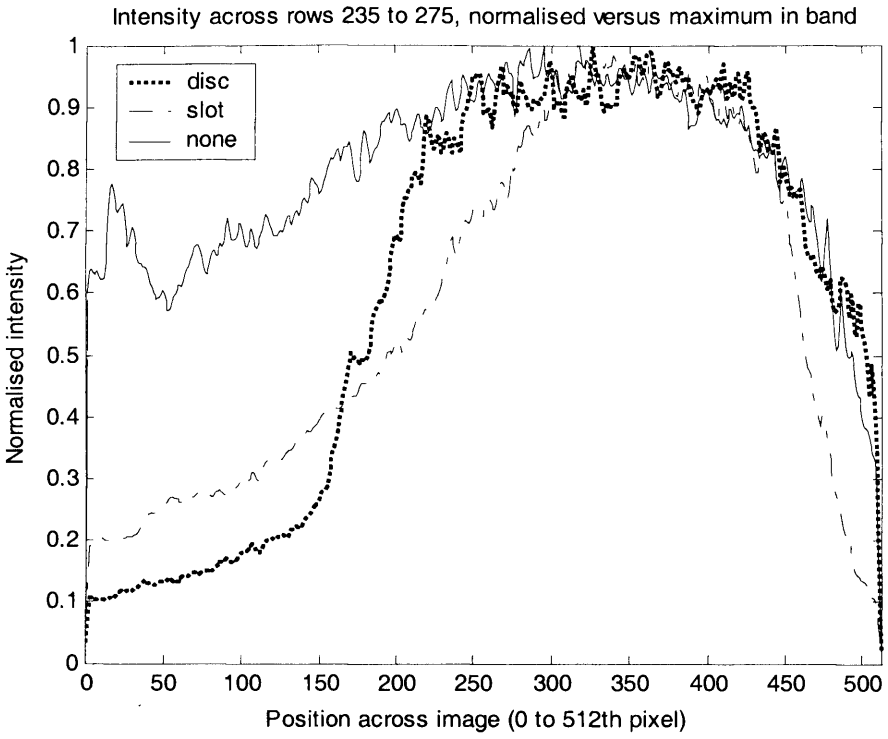

Figure 7-23 Normalised intensities for band across delta 30 CAD images

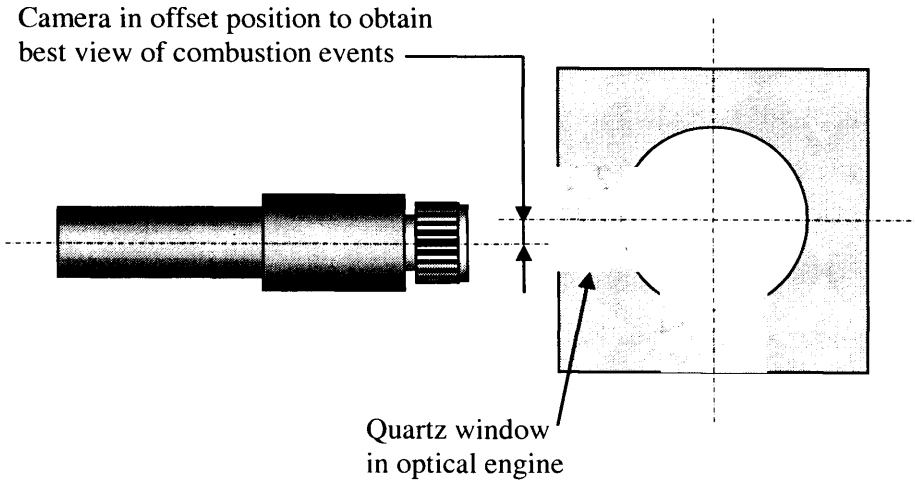

Figure 7-24 Layout of camera and engine to show offset between axes

supported by their appearance in work by Davy [2000] using a similar but independent arrangement.

7.10.4 Comparisons

A comparison of the full range of images allows conclusions to be drawn about the mechanisms that produce a stratified charge.

The intake ports of the original design of wall-guided direct injection engine, the Mitsubishi G-DI [Zhao et al., 2002], are near vertical which induces so-called reverse tumble (air motion in a similar direction to its fuel injection). The majority of port-injected engines use near horizontal ports to promote tumble in the opposite direction (conventional tumble). The Jaguar engine has ports which are mid-way between (Figure 5–3), but a study of the geometry suggests that conventional tumble, if any, is likely to predominate. In addition the bifurcated ports contain a swirl valve which, when closed, would superimpose a swirling motion around the cylinder axis. Even though the intake valves have been closed since approximately 610 CAD, the charge motion would still be expected to retain some vestiges of tumble and swirl. It would be useful to have to hand information on actual air motion within the cylinder, but this was not available although some inferences can be made from CFD data supplied by Jaguar which show predicted air velocity contours (Chapter 8).

A first appraisal of the Mie data suggests the following:

(i) Compared to the Mitsubishi G-DI engine, less fuel from the main part of the spray impinges on the piston, although there is strong evidence of pre-spray impingement.
(ii) The fuel spray appears to be kept away from the left hand side (exhaust valve side) of the engine, quite possibly by an air flow motion (conventional tumble) in the opposite direction to the emerging fuel spray.
(iii) The momentum of the fuel spray carries it away from the right hand side (inlet valve side) of the cylinder.
(ii) and (iii) combine to produce a concentration of fuel in the centre of the chamber, which is carried upwards towards the spark plug by the ascending piston.

7.11 Conclusions

The Mie study has provided clear images of the fuel spray in the firing engine at a variety of settings. The use of the images as sequences was validated by comparing with multiple shots at single test points. The engine appears to be effective at keeping the fuel spray in the centre of the combustion chamber,

although it appeared that the piston bowl was not fully utilised. Uncertainty exists about fuel activity in a dark region caused by total internal reflections in the quartz piston insert. It is likely that compensation for low light intensity in the region will be required in the LIF study.

Chapter 8 contains the results of the LIF study and a full discussion of the Mie and LIF work.

Chapter 8

A LIF study and further analyses

8.1 Introduction

This chapter is concerned with locating fuel vapour and maximizing data from the engine to explain spray phenomena. LIF is the second of the two optical methods chosen for their suitability in studying fuel spray interactions. The Mie images in Chapter 7 enabled the path of liquid droplets to be tracked during combustion. It was hoped that fluorescence would reveal something of the behaviour of fuel vapour as well as liquid fuel. The results are discussed and compared with some CFD predictions. Next, an intensity analysis of the Mie, LIF and ambient air raw images was completed. The chapter concludes with a different approach to post-processing images in an attempt to obtain further information.

8.2 Aims

The main aim of the LIF work was to study the formation and dispersion of fuel vapour in the firing engine. The LIF images would also provide further information about the motion of liquid fuel. A set of LIF images at the same test points as used in the Mie study would be a useful tool in understanding the interactions of the fuel spray in the combustion chamber. Images from additional tests, eg in stratified charge mode with water at 80^0C in the engine cooling jacket, during homogeneous running and at timings close to spark should provide a fuller picture of the overall behaviour of the engine. An intensity analysis of the LIF images was intended to quantify the development of the plume of spray by calculating the mean intensity of light in each image. The main aim of the velocity analysis was to look for any coupling between the velocities of the piston, fuel and air. These analyses would reveal how well the engine was set up and in particular its suitability for running in stratified charge mode.

8.3 Theory: Sprays in G-DI engines

For a G-DI engine in stratified charge mode, a near stoichiometric mixture of vaporised fuel and air must be formed in the vicinity of the spark plug for when the spark occurs, while the rest of the combustion chamber should be as

free from fuel as possible. As discussed in Chapter 3, the global AFR will be very lean. To achieve this, the injector must deliver the correct quantity of fuel in a spray of droplets with a precise degree of penetration. The temperature and pressure in the combustion chamber and the fuel pressure largely determine the degree of penetration of the spray and the droplet size, which in turn affect evaporation rates. The quantity of fuel is controlled by the pulse width of the fuel injection process. The location of the charge is governed by injector location and air motion and, in the case of the Jaguar design, possibly also by the interaction between the spray and the profiled piston crown. These events must occur as planned right across the envelope of load and speed operation for stratified charge running. Thus synchronisation of the positions of the fuel spray and the piston crown is crucial. If the spray is too early, it misses the bowl, no re-direction is possible and the far wall of the combustion chamber may become wet with fuel. If the spray is too late, there is insufficient time for evaporation and a pool of liquid fuel in the bowl may result. The LIF images will help confirm whether these requirements for good stratified charge combustion are being met.

8.4 LIF study

8.4.1 Selection of dopant and base fuel

The physics behind laser induced fluorescence is well understood. Whereas Mie scattering is an elastic effect, LIF involves absorption and emission. With Mie scattering, when photons of light collide with particles, they bounce off, but with LIF the photons collide, are absorbed and then re-emitted. Fluorescence is very useful in the context of tracing vapour at low concentrations, but it is also a rare phenomenon. Some components of gasoline are reported to fluoresce when excited by some wavelengths of laser light [Weaver et al., 2003], [Smith and Sick, 2005]. However, it is poorly understood which component or components of this extremely complex fluid are fluorescing. There would be little value in fluorescence results from gasoline since it would be unclear which part of the evaporation range was being represented. Very wide variations occur in the composition of gasolines resulting from differences in the crude oil from which they originate, the refining technique, the method of blending and their additives. These

variations make the use of gasoline even more questionable as the source of fluorescence. Furthermore, gasoline as a whole strongly absorbs light in the UV range [Wagner et al., 1999], [Wermuth and Sick, 2005] which precludes using it as a base fuel to which a fluorescing dopant is added. Instead, more control is possible if a single hydrocarbon fuel or mix of hydrocarbon fuels is chosen whose evaporation characteristics are a reasonable match to those of a typical gasoline. This component or components can be chosen to be non-fluorescent, but a fluorescing dopant can be added in a low concentration. The dopant can be selected to co-evaporate with one of these components (most usefully one in the middle of the range) and not adversely affect the base fuel as regards combustion.

In evaluating suitable dopants, the principal properties to consider are the evaporation temperature, and the absorption and emission characteristics. The boiling point must match that of a component in the base fuel which must itself be midway in the range of boiling points of gasoline constituents. The laser being used must be able to deliver light in the dopant's excitation wavelength range and the emitted light must be easily distinguishable from the excitation light.

Since the absorption/re-emission process involves electrons attaining a higher quantum level then returning to a lower quantum level, certain energy values suit certain level transitions. The wavelength of light and the energy of the photons of which it is composed are directly related. It follows that certain lasers suit certain dopants. Quantum theory shows that the wavelength of the emitted light is shifted from the wavelength of the absorbed light allowing separation by use of suitable filters (see § 8.4.5).

As stated above, the range of boiling points of the base fuel component or components must approximate that of gasoline and each component must be non-fluorescing at the dopant's exciting wavelength. Many researchers used a single base fuel, with iso-octane the most commonly chosen [Wagner et al., 1999], [Han and Steeper, 2002], [Lin and Sick, 2002], [Smith and Sick, 2005]. Graf et al. [2001] used two components, and Van der Wege and Hochgreb

[2005a] argued that five would be required. Styron et al. [2000] employed a numerical model to match the distillation curve of their four selected components with California Phase II gasoline. Davy [2000] suggested that a mixture of three components could adequately replace gasoline, one each for the light and heavy ends and an intermediate one. In the 2000 study, carried out at UCL, Davy used 10% by volume of 2,3-Butanedione (known as Biacetyl) as a dopant in a base fuel consisting of 10% n-nonane, 20% iso-pentane and 70% iso-octane (all by volume). The success of that project and the constraint of having to use Davy's laser led to the selection of the same dopant and base fuel mix for the current studies.

The boiling point of Biacetyl, 88^0C, is close to that of iso-octane, 99^0C, and is towards the mid-range of gasoline. It absorbs light in the range 340 to 470 nm, with a peak at 417 nm, and it emits light in the range 420 to 520 nm with a peak at 478 nm (see Figure 8-1 and Figure 8-2). The Nd:YAG laser has a fundamental wavelength of 1064 nm, the frequency can be tripled to produce light of 355 nm wavelength which is an absorption cross section of approximately 1.5×10^{-20} cm^2 compared to the peak of 7.6×10^{-20} cm^2 (see Figure 8-1).

8.4.2 Laser

In order to obtain light of 355 nm wavelength from the laser, the third harmonic of frequency was needed. A harmonic generator tripler unit was installed in the main laser body. In addition, the 532 nm dichroics in the SSP-1 separator unit were replaced with the set for the 355 nm wavelength.

8.4.3 Optical elements

Some of the optical elements were suitable for narrow ranges of wavelengths only, so the main reflecting mirror and the cylindrical and spherical lenses from the Mie study were replaced by components suitable for 355 nm use. The fused silica in the quartz windows (main, pent roof and slot) was suitable for both 355 nm and 532 nm light.

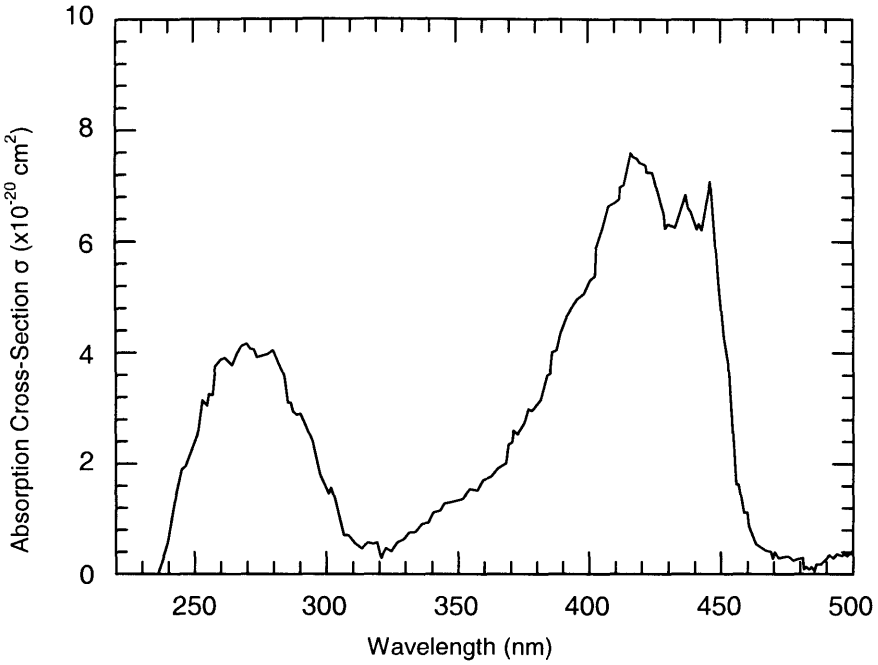

Figure 8-1 Measured values of the biacetyl absorption cross-section [Lozano, 1992

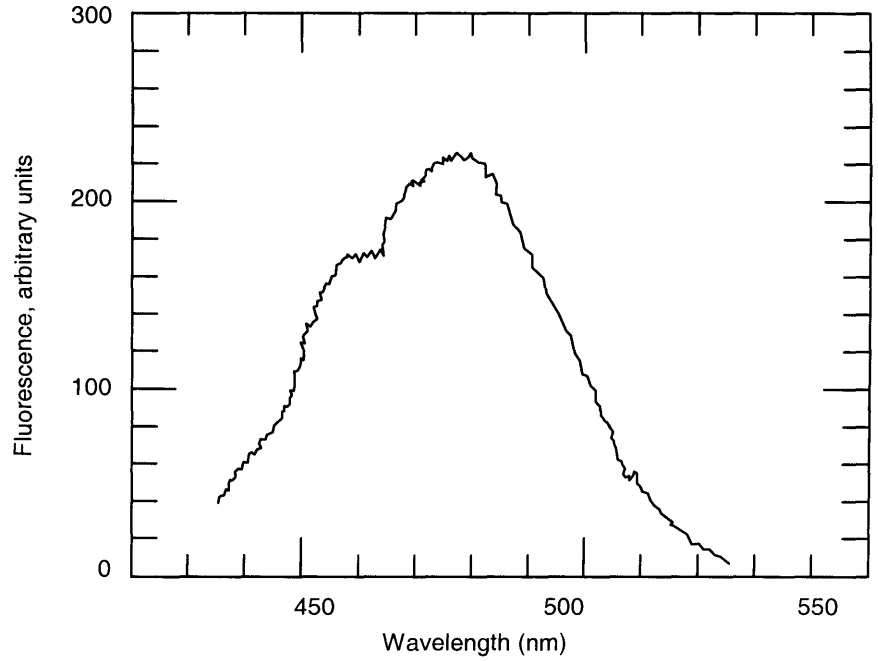

Figure 8-2 Biacetyl fluorescence emission spectrum. Ordinates in arbitrary units [Lozano, 1992]

The cross-bore mirror, also suitable for both 532 nm and 355 nm wavelengths, had sustained some damage to the silvering which had been partially burned on its centreline. The damage was probably cumulative and caused by spots of engine oil on the surface acting as lenses and concentrating the energy of

the laser sheet to values exceeding the threshold of the silvering. The mirror from the Davy [2000] project was adapted and fitted as a replacement. Since some oil spatter appeared to be unavoidable, a more rigorous regime of monitoring and cleaning was adopted.

8.4.4 Camera

The Coolview 12 camera was broadband and thus able to capture visible and UV emissions. The camera settings were the same as for the Mie work, except that the lens aperture was f/4. A Wratten 2E filter was fitted in front of the lens (see §8.4.5) in order to cut out light of the exciting frequency (355 nm).

8.4.5 Filters

It was possible for Mie scattered light to be present during the LIF study. The main cause was stray 532 nm light (escaping light at double the base frequency) and this effect was not restricted to droplets directly illuminated by the light sheet since additional collisions could result in light reaching the camera (see §7.10.2). However, with the set-up used, LIF could only be produced by molecules of dopant struck by 355 nm laser light in the light sheet. The presence of stray 532 nm light in the combustion chamber could cause enough Mie scattered light to overwhelm any LIF effects. Therefore, careful consideration had to be given to the types and positioning of filters chosen. Based on the absorption and emission curves for Biacetyl (Figure 8-1 and Figure 8-2), laser light of 355 nm should produce reasonable fluorescence, shifted to the range 420 to 520 nm and peaking at 478 nm. The ideal setup would result in high intensity 355 nm (but no other wavelength) entering the combustion chamber and all of the light emitted by the Biacetyl (but no other wavelength) entering the camera. In theory once the harmonic generator tripler and dichroics were fitted, the laser should produce only 355 nm light. However, the transmission efficiencies of these elements meant that some light at the 1064 nm and the 532 nm wavelengths left the laser separator unit, along with the desired 355 nm light. The original elements on the optics rail transmitted some of this 1064 nm and 532 nm light, so the band-pass filter UG-5 (see Figure 8-3) was fitted to block most of the 1064 nm and 532 nm

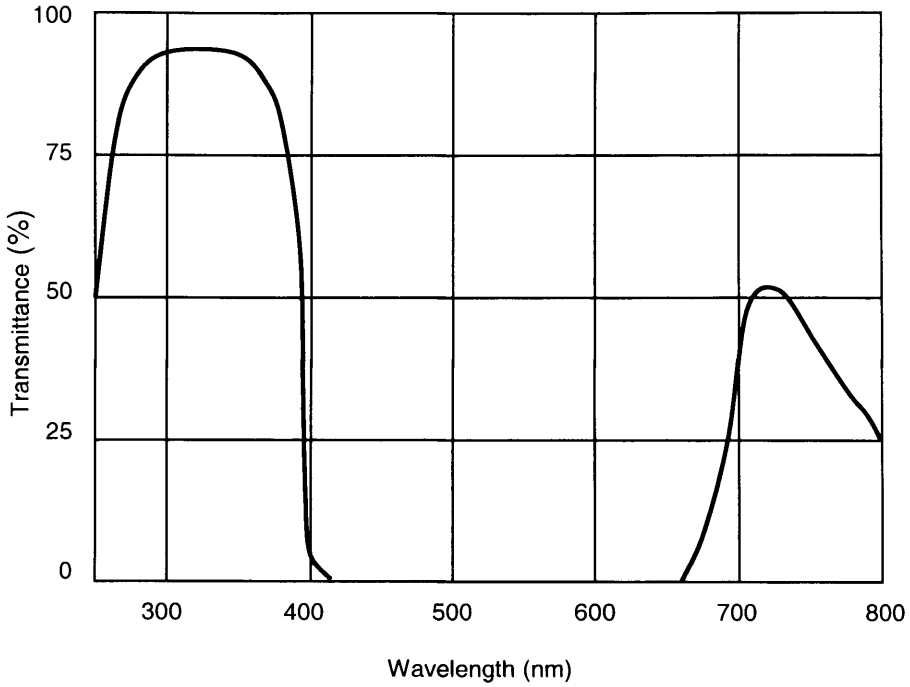

Figure 8-3 Percentage transmittance of UG-5 bandpass filter [Comar Instruments, 2004]

light, hence the majority of light entering the optical engine via the cross-bore mirror was 355 nm. The high-pass filter, Wratten 2E, in front of the camera lens began transmitting at 450 nm, thus the 355 nm exciting frequency should be blocked and the 420 to 520 nm emitted frequency (fluorescence) reached the CCD chip. The Wratten filter also unfortunately allowed any stray 532 nm light to reach the chip (see Figure 8-4). The use of beam dumps, shrouds (for example blocking off the unused main quartz window), and application of matt black paint to reflecting surfaces helped to maintain 355 nm light as the dominant light interacting with the doped fuel (see Figure 8-5).

8.4.6 Control of equipment

The requirement was to synchronise the injector, engine, laser, camera and PC. The method used was generally the same as for the Mie study, see § 7.6.1 to 7.6.4. The main difference was with the means of image capture (see § 8.4.7).

8.4.7 Method of image capture

As with the Mie study, a standard desktop PC was used for remote activation of the laser. A Matrox Corona-II frame grabber was installed in the PC and, along with Image Pro Plus (IPP) version 3.0 software, it was used to control image capture and storage. The lower levels of light from LIF made image

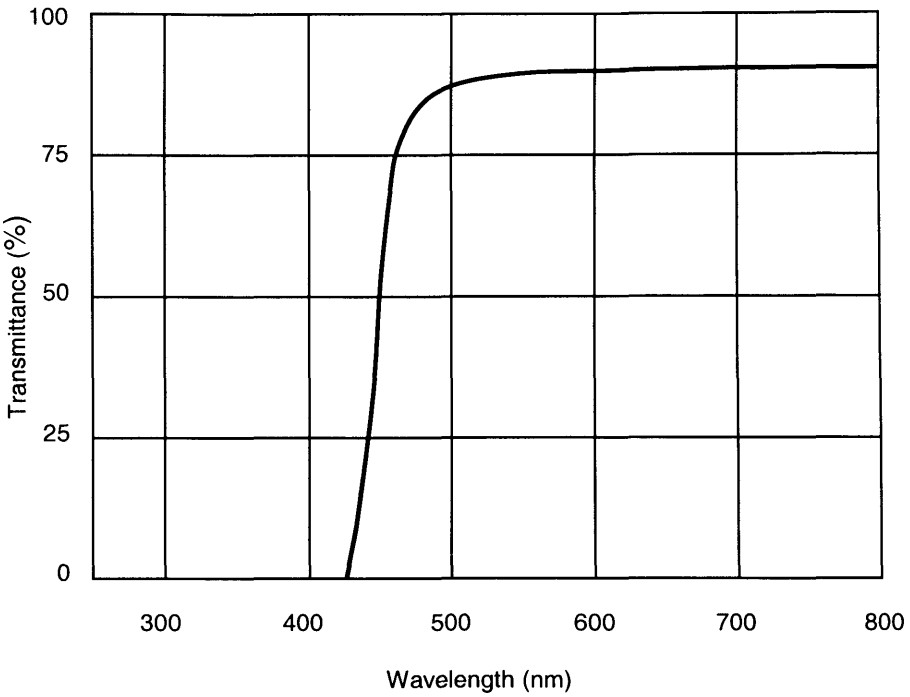

Figure 8-4 Percentage transmittance of gelatine filter Wratten number 2E [Comar Instruments, 2004]

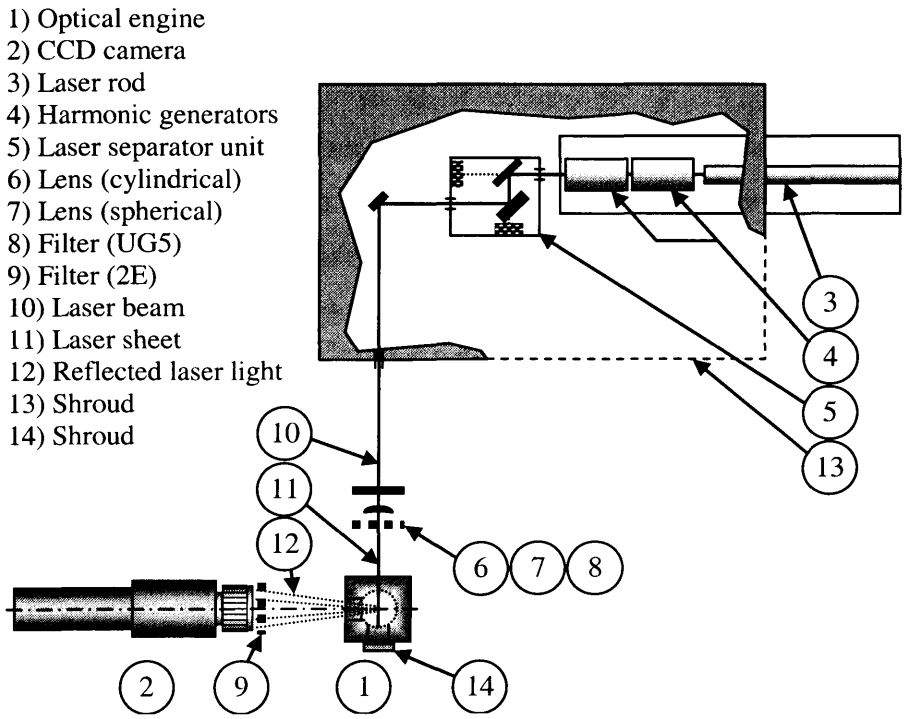

Figure 8-5 Plan showing main elements used to introduce 355 nm laser light into optical engine.

capture and post-processing much more complex than for the Mie study and several iterations were needed to develop the final method.

The intensity of light from LIF depends on the molar concentration of the

dopant in the measurement volume and the photophysical and chemical properties of the specific dopant molecule [Davy, 2000]. In order to get a sufficiently strong signal, output from a number of cycles had to be accumulated to obtain a suitable LIF image, whereas a single cycle gave sufficient light for a Mie scattering image.

In order to compare LIF images, account needs to be taken of variations in dopant concentration, charge temperature and cylinder pressure throughout the cycle, also the shot-to-shot variations of laser intensity and sheet profile [Davy 2000]. This was achieved by taking the average of many images and applying post-processing. The number of images chosen was 50, where this is a convenient number exceeding the statistically valid minimum sample size of 30 [Frank and Althoen, 1994]. Thus, if fuel was in region 'a' and no fuel was in region 'b' for the majority of these 50 laser flashes, the resulting image would contain fluorescence at 'a' and none at 'b'.

The relatively long gating time meant that deposits could accumulate on the quartz windows during the image collection and reduce quality. The correction was to take background images before and after the firing image and subtract the mean of the pre- and post-firing images from the firing image. This approach also reduced the effect of bright background features.

At the low light levels encountered with LIF, spatial non-uniformity of the light sheet could become critical. Important features might be lost because they coincided with dark areas in the light sheet. A light sheet correction image could boost the intensity in these areas and prevent loss of detail. An average was taken from a number of static images of the sheet and this provided, in effect, a 'look-up' table of factors to apply to the LIF image. The result of this was that several images needed to be taken for each LIF test point, namely those for pre-firing, firing, post-firing and for sheet correction. For post processing see § 8.4.8.

Some initial work was required before attempting to record LIF in the firing engine. The optics were adjusted to produce a laser sheet across the width of

the combustion chamber which was less than 1 mm thick in the image plane. This was brought to focus halfway up the quartz main window and the power maximised by adjusting the harmonic generators and monitoring with a power meter. Note that UV light is invisible to the human eye, so small white cards (containing chemicals which fluoresce in UV light) were used to track the position of the beam or sheet. Engine simulation was used as before (§ 7.7) to fire the laser and trigger the camera without the need to run the engine. The cylinder head was raised and a false combustion chamber set up, with the camera focused on the image plane. A vaporiser was filled with a 50:50 mix (by volume) of iso-octane and dopant and the vapour was directed into the false combustion chamber to disperse through the image plane. It was seen that the dopant/iso-octane vapour resulted in an image, but pure iso-octane (known to be non-fluorescing) did not. The shot without dopant showed only dimly lit background features (illuminated by reflections and stray light) and naturally fluorescing features, such as the tip of the vaporiser device. The shot with dopant also showed the background features but in addition, definite illumination in the form of a cloud emerging from the tip of the vaporiser. Pure dopant in the vaporiser resulted in a much more intense image than with the iso-octane/dopant mix. With the system optimised in this way, one could be confident that dopant carried in the base fuel and entering the combustion chamber through the injector would disperse through the image plane and be captured by the camera.

8.4.8 Post-processing

For each Mie picture, the single gating period of 40 ms and the integration period of a single 4 ns flash of laser light reflecting off the fuel, had enough intensity to form a useful image without the need for post-processing. However, post-processing was required for the LIF images for several reasons. Firstly, the low intensity of light when using the LIF technique meant that light had to be accumulated from a number of cycles and a mean image formed. Secondly, these long firing periods resulted in a significant amount of oil being deposited on the quartz windows with a consequent reduction in image quality, making background correction essential to prevent loss of data. Such a correction would also compensate for anomalies (for example the spark

plug insulation material was found to fluoresce) and reflections caused by stray light. Thirdly, light sheet non-uniformity could be critical at low light levels, so a light sheet correction procedure was needed to ensure data was not lost if it happened to occur in regions of low light sheet intensity. Mathwork's Matlab software (version 6.1) was the main post-processing tool. It operates on matrices and arrays, and treats each IPP image downloaded from the CCD chip as a grid of numbers each corresponding to the intensity of a unique pixel. The post-processing was simple manipulation of these matrices and displaying them as images was performed by assigning the resultant intensity values back to the relevant pixels. For the accumulated images, Matlab produced a mean by adding the images pixel by pixel and dividing the totals by the number of images in the set. To apply background correction, the mean of the pre- and post-firing images was subtracted from the mean of the firing images. The mean images were assembled as described above, then subtraction was carried out pixel by pixel.

Any light sheet will have variations in its intensity. If a light sheet image is loaded into Matlab, the pixel of maximum intensity (I_m) can be found. All other pixels can have their intensity compared to this value, producing a matrix of correction factors, based on I_m / I_i, where I_i is the intensity of each pixel. A firing image taken using this light sheet could then be loaded into Matlab and each pixel could be multiplied by the intensity factor, I_m / I_i, for that pixel location. This would compensate for the light and dark areas in the laser light sheet.

Variations in the intensity of the light sheet were present for a number of reasons, firstly the original beam and the light sheet forming optics did not produce a uniform sheet. Then there were further changes caused by the beam passing into the engine. If the quartz had been a disc of constant thickness the light sheet would have been uniform (if the original sheet had been uniform) even if the disc were tilted (ie its optical surfaces not parallel with the piston surface). Such a light sheet would require a single sheet correction image,

providing a single correction factor matrix which could be applied to each firing image for pixel by pixel correction, regardless of the piston position.

The quartz sliver of the slotted piston had variable thickness, though, so it refracted light to a greater or lesser extent according to where the incident light struck it. This was apparent as several fans of light emerging from the piston surface (see Figure 8-6) and included a distinctly dark area. The latter corresponded to the vertical edge of the piston bowl, where total internal reflections in the quartz prevented most of the light from emerging. Since some of these areas were triangular with their bases on the quartz surface, the height of the piston determined where the light and dark areas occurred in relation to a fixed point, say the spark plug. The consequence of this was that a sheet correction matrix was required each time a firing image was taken with the piston captured in a different position. Each sheet correction image served as a 'lookup table' of factors to apply to the relevant firing image and was stored in a library ready to be called by the Matlab controlling program.

The method of obtaining a sheet correction matrix for both slotted and disc crowns was to fill the combustion chamber with dopant vapour, allow it to disperse, then take an image. One set was completed with the windows and mirror left unclean after a typical firing run and another set with them freshly cleaned. The procedure was to place cotton wool soaked in Biacetyl in the bowl of the piston and ensure it was fully concealed. Then the cylinder head was lowered and bolted in place, water at 40^0C was pumped through the engine cooling jacket and the Biacetyl vapour was allowed to disperse for 2 hours.

For the disc crown, the piston was lowered enough to be out of view, the laser was initiated with the engine in simulation mode, the camera triggered and the image saved. For the slotted crown, the piston was set to the required position, the laser started with the engine in simulation mode, the camera triggered, the image saved and the flywheel rotated to set the piston position for the next image and so on.

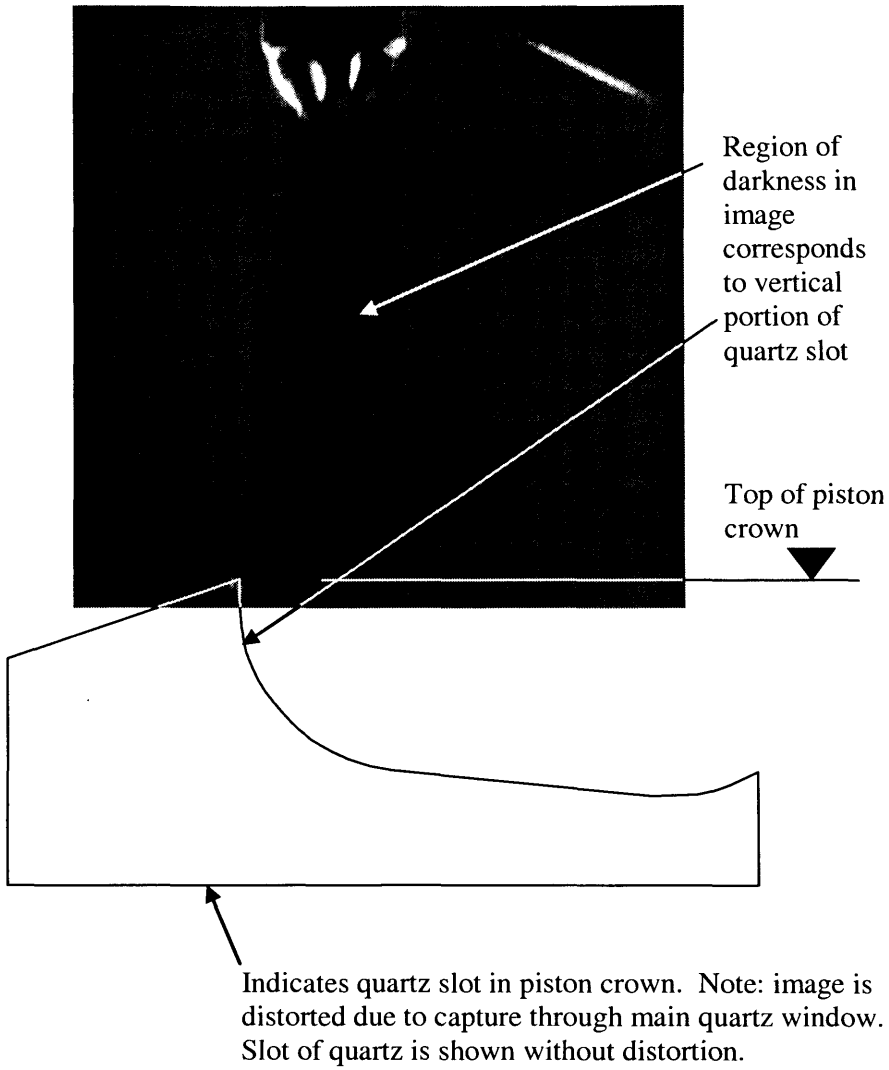

Figure 8-6 Light sheet correction image (corresponding to SOI 543 CAD) showing influence of quartz slot in piston crown on transmitted light.

The programs used by Matlab for the post-processing were:

- Background Correction program
- Beam Profile Correction program
- Figure Generation program
- Pentroof function
- Piston function
- Mask function

The function programs served two purposes:

Firstly, the area from which Matlab looked for a maximum value was restricted to regions where LIF could occur. If the whole image were scanned, a bright reflection in a non-LIF region may represent the image's highest value, say 3000 bits. Thus if areas of LIF measuring 100 bits and background measuring 30 bits were also present in the image, they would be indistinguishable from each other compared to the maximum of 3000 bits. The second use of the functions was in the Figure Generation programs, where they generated zero values (black) in regions other than the potential LIF regions. The Pentroof and Piston functions were written by noting the pixel references for the outline of the pentroof, the spark plug and piston respectively with the image displayed in IPP. The defining matrix to blank out the piston was linked to the SOI and delta values so that it could be accurately superimposed on the physical piston for each image. The controlling program was given a reference value to superimpose the piston blank over the physical piston according to the point in the cycle when the image was taken, ie using SOI plus delta.

The Mask function was used with the disc crown but not the slotted crown. The disc of quartz reached only part of the way across the piston, thereby only illuminating the right hand (intake) region of the combustion chamber. Thus, the left hand region was excluded from consideration in choosing the maximum (Beam Profile Correction program) and was replaced with zeros (black) in the results from the Figure Generation program.

All the information and raw data necessary for producing a processed image were now in place. The sequence of the complete process was as follows:

- Background Correction program, input: pre-firing, firing and post-firing images. Purpose: to find mean values and to subtract background from firing image. Output: background corrected image.
- Beam Profile Correction program, input: background corrected image. Purpose: to apply sheet profile factors. Output: beam profile corrected

image. The Beam Profile program acted as the controlling program, calling the Pentroof, Piston and Mask functions.

- Figure Generator program (first run), input: beam profile corrected images. Purpose: to choose AOI from possible fluorescence sites. Output: table of maximum values.
- Figure Generator program (second run), input: beam profile corrected images. Purpose: to adjust settings. Output: false-coloured image in jpeg (Joint Photographic Experts Group) format.

See flowchart, Figure 8-7. Note that a log scale was used because a large range of intensities existed in each image and the fluorescence was close to the background values. Using a natural log scale compressed this range and preserved the low level features. The Wiener filter helped with noise-removal. It was a low-pass filter which worked by applying a Wiener method pixel by pixel, based on statistics estimated from the local neighbourhood of each pixel. The false-colouring linked colours to intensities, and the colour-map was set to 'hot', with warm colours corresponding to high intensities. The colour-bar included with each image acted as a legend.

Note that the first run of the Figure Generator program listed the maximum intensity in each image. Then the batch processing in the second run could set all the images to the maximum of these maxima. Finally, the jpeg format was chosen since it was straightforward to import and manipulate in standard software, eg Microsoft Word.

8.4.9 Refining the LIF procedure

The initial processed images suffered from an ill-fitting lens adaptor which had to be replaced. Further problems were encountered caused by droplets of engine lubrication oil lying on the silvered mirror, acting as lenses, with the result that light locally exceeded the power threshold of the silver. A replacement mirror was installed and a better inspection/cleaning regime instituted. A further problem encountered was blockage of the fuel system. Waxy deposits occurred in the fuel ram, the pipework and the injector. A bad batch of dopant was the most likely cause, since the problem reduced when a

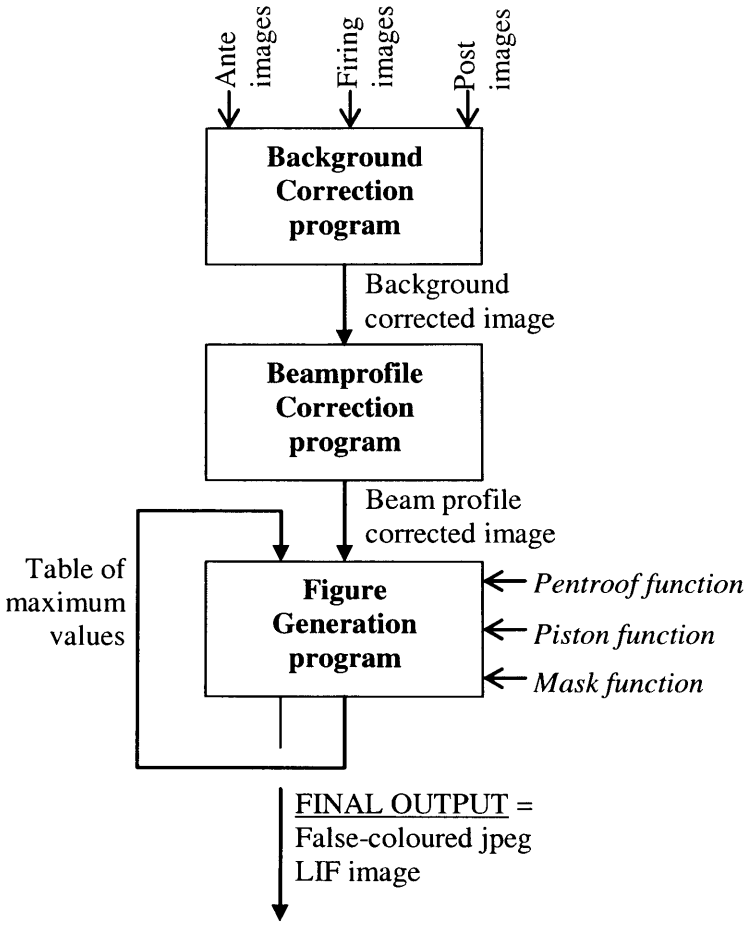

Figure 8-7 Flowchart showing use of Matlab programs for post-processing LIF images

new batch was tried. In addition, a regime of draining down the fuel system after testing and filling it with gasoline overnight improved matters.

The next batch of images was rejected due to low LIF intensity, so higher quality optics were installed, namely a spherical lens of focal length 500 mm and a cylindrical lens of focal length -25 mm. In addition, more thought was given to the CCD gating time. It must be long enough to capture all of the possible fluorescence signals, but short enough to minimise the amount of light captured from other sources. This was particularly important since the intensifier was near to its maximum setting and able to transmit light of minimal intensity to the CCD chip. The requirement was for the shortest gating time which could still capture the fluorescence. The theoretical delay between triggering the laser and the end of fluorescence was calculated. This included the delay until peak power for the laser (228 μs) was reached (see Figure 8-8) and the lifetime of the fluorescence from Biacetyl (15 ns) [Davy,

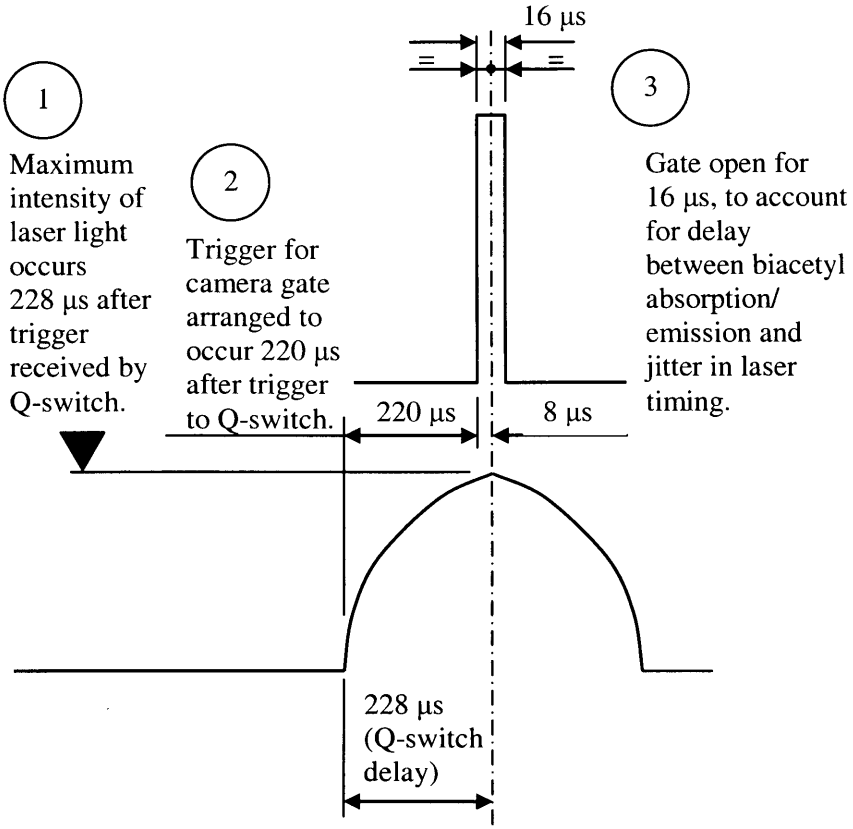

Figure 8-8 Timing of camera gating used to maximise the amount of fluorescence captured by camera

2000]. Test images using various delays and gating times close to the theoretical ones showed that the best fluorescence yield was obtained with a gate of 16 µs, equally spaced about the peak power of the laser pulse. These measures were adopted and used with the firing engine.

Some of the areas in the resulting processed images had intensities of 4096 bits. Since the camera was a 12-bit model and $2^{12} = 4096$, this indicated saturation. Saturation is unacceptable because of the uncertainty it introduces. For an integration period of 4 seconds (using light from 50 laser flashes) it was impossible to tell at which point the total light gathered reached saturation. The opposite extreme would be to take 50 individual shots (each of one laser flash), but the time required to do this was unacceptable for the optical engine. It was also very demanding on computer storage space. A combination of 13 images and 320 ms integration time, ie 4 exposures each, was found to be a good compromise between brevity of firing and chip saturation.

8.4.10 Finalised procedure

The overall procedure for a typical LIF test point can be summarised as follows:

- Motor engine up to 1500 rev/min
- Apply load (dynamometer)
- Check laser flashes in synchronisation with engine using oscilloscope
- Select 'snap' in IPP software (for 'Ante' image)
- Press and hold push to make switch 'a' (instrumentation control button)
- Release push to make switch 'a' (instrumentation control button)
- Select 'snap' in IPP software (for 'Firing' image)
- Press and hold push to make switch 'a' (instrumentation control button)
- Press and hold push to make switch 'b' (injector control button)
- Release push to make switch 'b' (injector control button)
- Release push to make switch 'a' (instrumentation control button)
- Select 'snap' in IPP software (for 'Post' image)
- Press and hold push to make switch 'a' (instrumentation control button)
- Release push to make switch 'a' (instrumentation control button)
- Motor engine down to 0 rev/min
- Clean quartz windows
- Select signal generator settings for next test point
- Begin next run

Having confirmed that all systems operated satisfactorily and that combustion was stable, the LIF testing began.

8.4.11 LIF tests

Five studies were attempted using the LIF technique. These are set out in Table 8-1.

I) Study number one, referred to as P1_SC_FL_T40, was directly equivalent to the Mie set and used the 'slotted' piston, a light sheet across the full width of the combustion chamber and water at 40^0C passing through the engine cooling jacket. The test matrix consisted of SOIs 639, 654, 675 CAD and delta values of 5, 6, 7, 8, 9, 10, 11, 15, 20, 25, 30, 45, 63 CAD. Thus, for the first test point, the laser flash occurred at (639+5)=644 CAD etc.. Note that no

Study number	Piston (0=disc/1=slot)	Strategy (Homo/stratified)	Test points (full set/near spark)	Temp (Deg C)
I	P1	SC	FL	T40
II	P1	SC	NR	T40
III	P0	SC	FL	T40
IV	P1	HC	FL	T40
V	P1	SC	FL	T80

Table 8-1 Conditions used for studies using LIF technique

images were taken for the last two deltas in the SOI 675 series, since (675 + 45) and (675 + 63) exceeded 720 CAD and the piston obscured most of viewing area.

II) The second study was similar to study (I), but concentrated on events just before and just after spark. The location of fuel vapour becomes critical for a direct injection engine in stratified mode in the moments leading up to ignition. The study employed the slotted piston and SOIs of 639, 654 and 675 CAD, but the deltas equated to the laser flash occurring at 684, 687, 690, 693 and 696. The spark timing was 693 CAD.

III) The third study was designed to look at events within the piston bowl which, in studies (I) and (II), were obscured by the wall of the bowl. Increased optical access into the bowl was possible by machining away some of this wall. Of the two optical piston crowns available, the slotted one would be more useful for the later studies so the disc crown was chosen for the machining operation. The remainder of the settings were similar to study (I).

IV) For the fourth study, the slotted piston was re-installed, water at 40^0C was circulated through the engine cooling jacket and SOIs for homogeneous charge running were used. Benchmark data was available for this mode to compare with the images and it was also interesting to note the degree of homogeneity at the time of the spark. Delta values were chosen to show the spray developing, then at wider intervals up to ignition.

V) The fifth study was similar to study (I) and the Mie work, except that water at 80^0C was pumped through the water jacket. Information on the behaviour of the fuel at this much higher temperature would be valuable given the importance of flash boiling to the behaviour of fuel sprays.

8.4.12 Results

All the static sheet correction images for the slotted and disc piston crowns were recorded. These were saved in a library ready to be called by the Matlab controlling program. The experience in applying these correction images is as follows.

For test 1 (study I), the raw images of pre-firing, firing and post-firing showed good consistency within the set, light levels were adequate and the degree of definition acceptable. The background correction worked well, producing higher definition images and significant fluorescence was apparent. When sheet corrections were applied to the background corrected images, ie making use of the sheet correction images, the results deteriorated. There was little fluorescence in areas where fuel vapour should have been present and the patterns of what little fluorescence was present did not seem plausible. Exhaustive efforts were made to isolate the fluorescence so that its presence correlated, as it should, with the presence of fuel. This included adjusting the maximum setting for the correction algorithm, adopting a log scale and applying filters. All of these attempts proved unsuccessful.

A similar outcome to test I was found with test II, ie the sheet correction routine produced very poor results. However, even the background corrected images for this test displayed very little evidence of fluorescence.

For test III, the raw images were good, and the background correction routine improved the definition, revealing a strong LIF signal. Sheet correction resulted in even more improvement.

The ante-firing, firing and post-firing raw images were acceptable for test IV, but the sheet corrected and even the background corrected images were again of low quality. Little evidence of fluorescence was seen in the later images.

The results for test V were similar to test I, ie sheet corrected images were of poorer quality than the background corrected ones.

Results from tests I, III and V are presented on the following pages labelled from Figure 8-9 to Figure 8-18 (results from tests II and IV added no extra information and are omitted). The first page contains all the images and acts as an index. Thereafter, each page contains results from one SOI, ie there are three pages for each test. Post-processing is as described in § 8.4.8. The intensities are normalised against a maximum of the maxima and the colour-bar gives the range compared to this maximum.

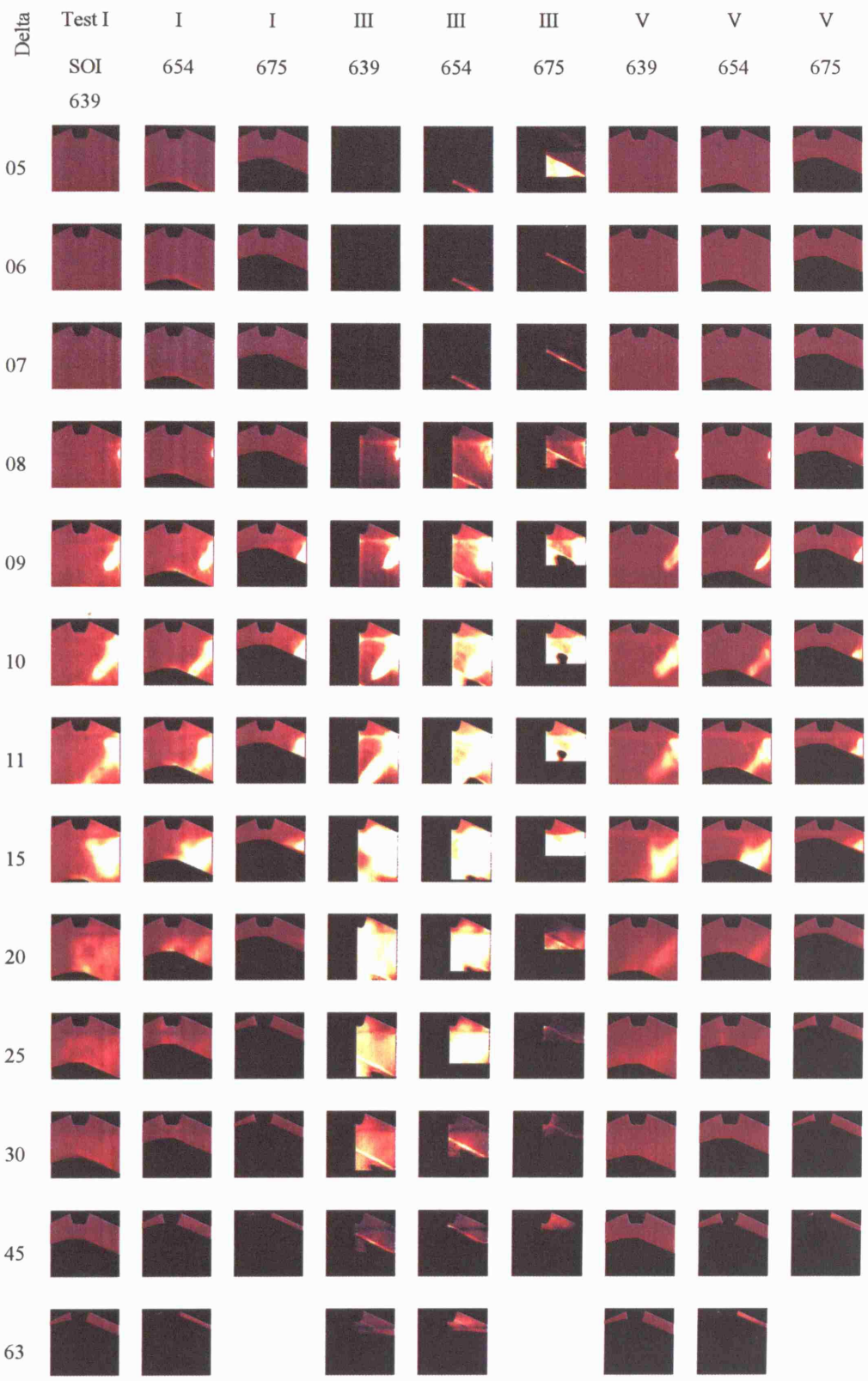

Figure 8-9 Thumbnails of LIF tests I, III, V, for SOI 639, 654 and 675 CAD

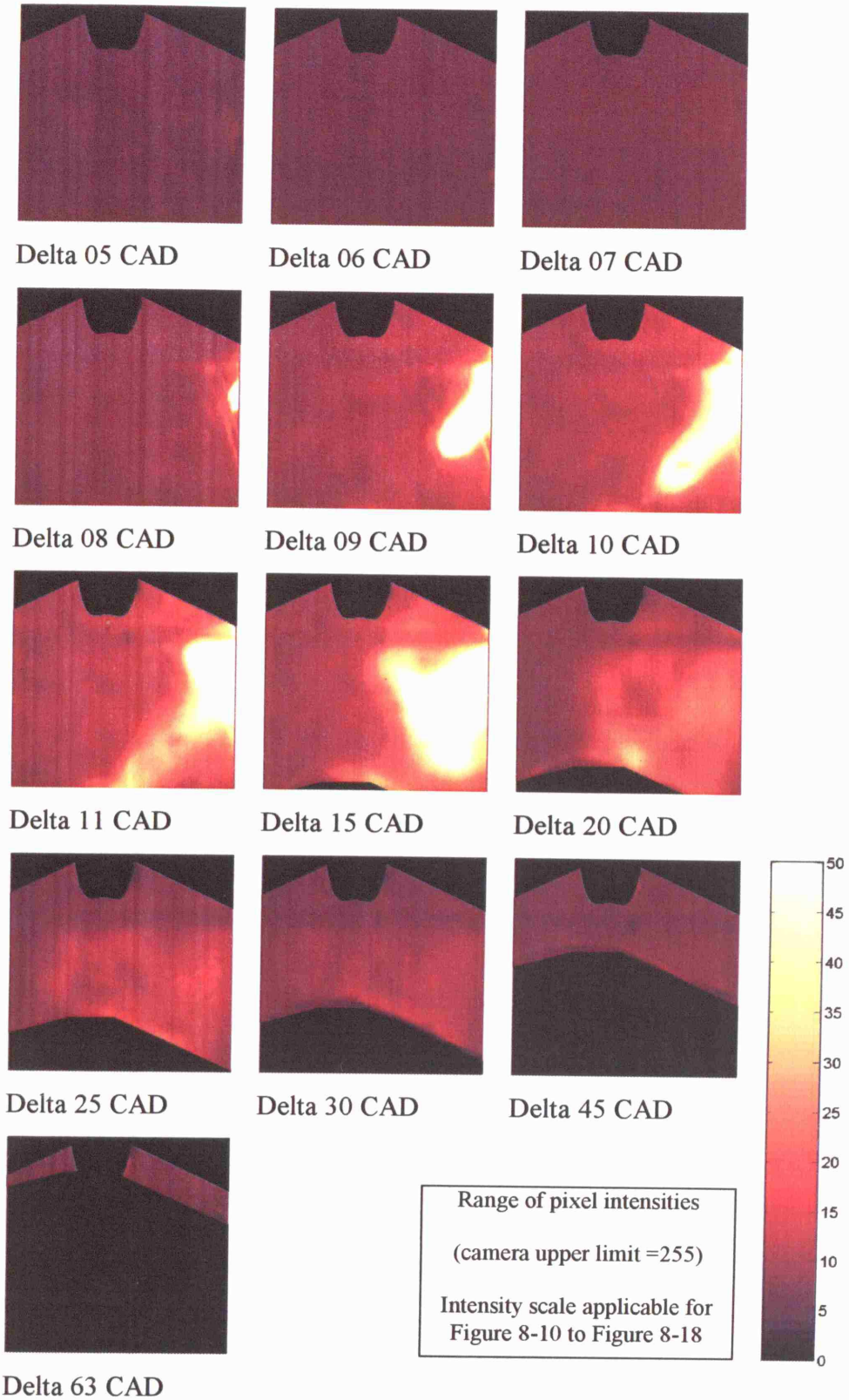

Figure 8-10 Post-Processed Images for LIF Test I, SOI 639 CAD

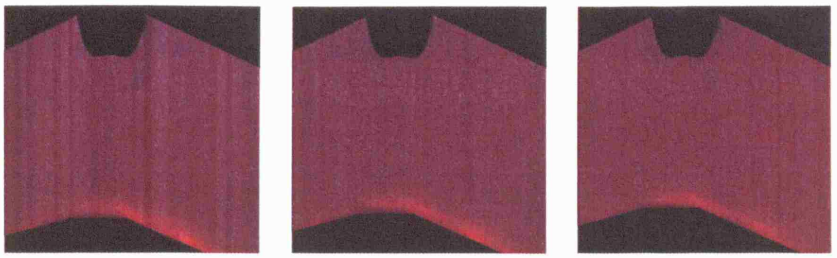

Delta 05 CAD Delta 06 CAD Delta 07 CAD

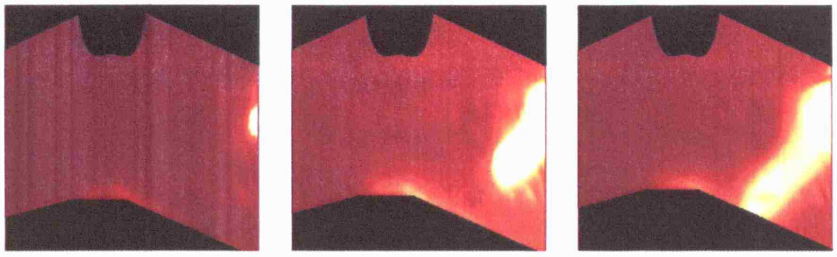

Delta 08 CAD Delta 09 CAD Delta 10 CAD

Delta 11 CAD Delta 15 CAD Delta 20 CAD

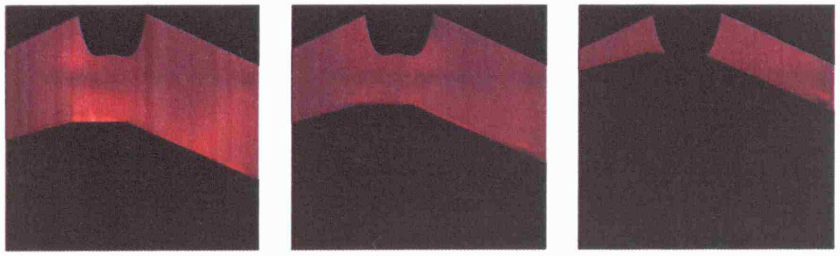

Delta 25 CAD Delta 30 CAD Delta 45 CAD

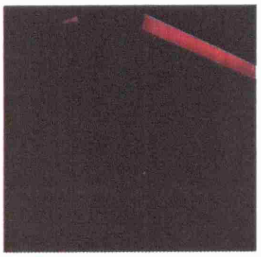

Delta 63 CAD

Figure 8-11 Post-Processed Images for LIF Test I SOI 654 CAD

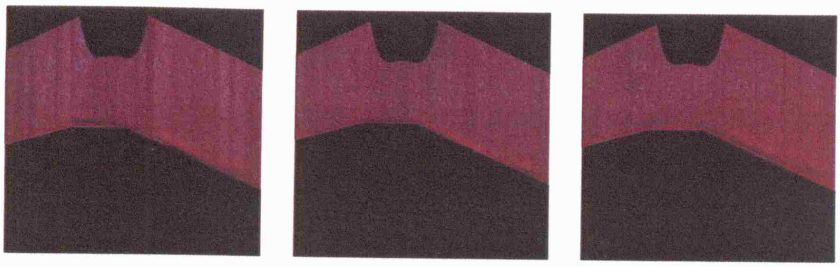

Delta 05 CAD Delta 06 CAD Delta 07 CAD

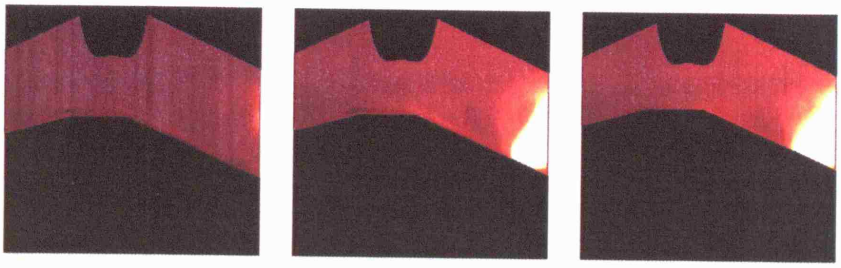

Delta 08 CAD Delta 09 CAD Delta 10 CAD

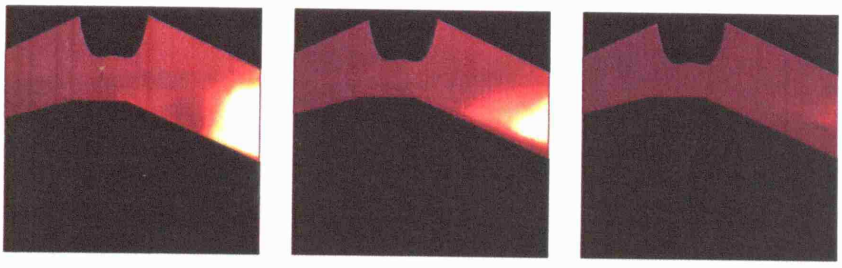

Delta 11 CAD Delta 15 CAD Delta 20 CAD

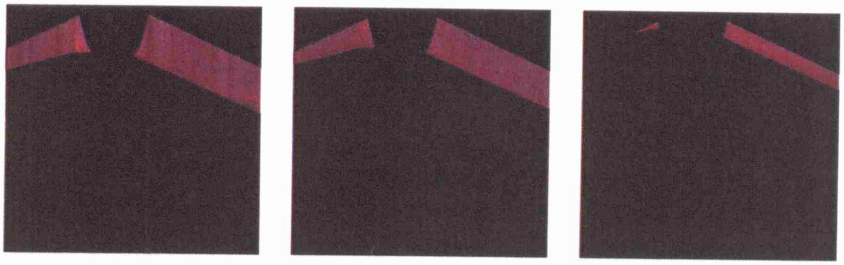

Delta 25 CAD Delta 30 CAD Delta 45 CAD

No image (piston near TDC)

Delta 63 CAD

Figure 8-12 Post-Processed Images for LIF Test I SOI 675 CAD

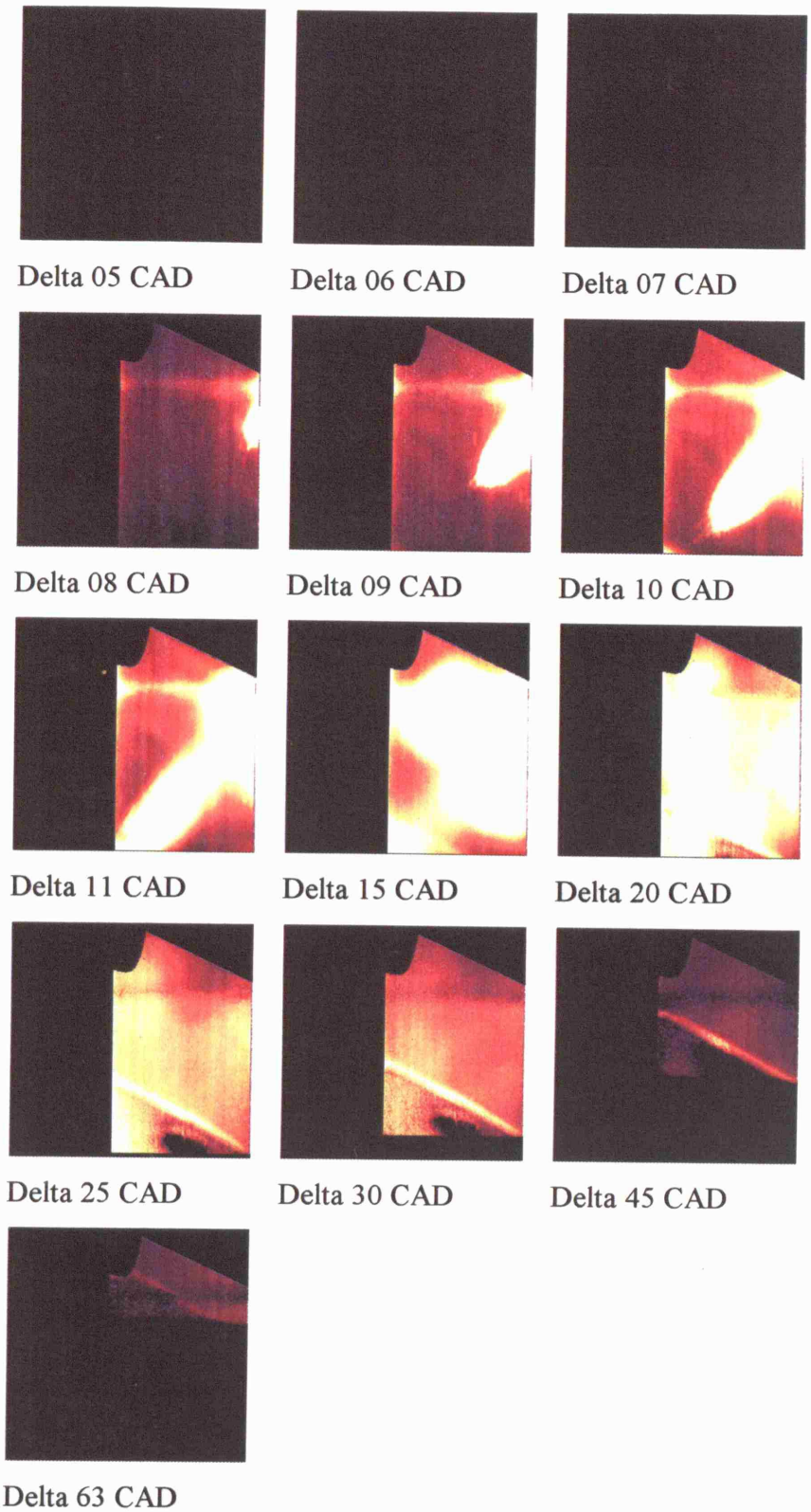

Figure 8-13 Post-Processed Images for LIF Test III SOI 639 CAD

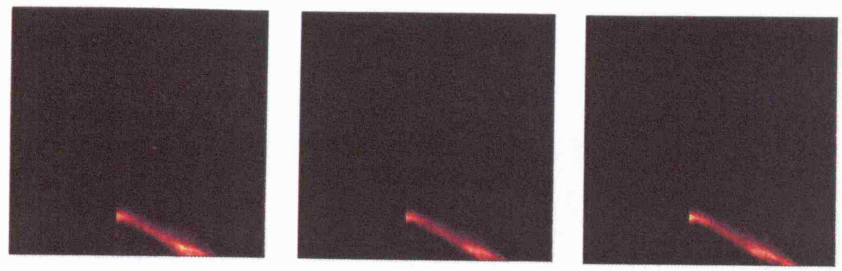

Delta 05 CAD Delta 06 CAD Delta 07 CAD

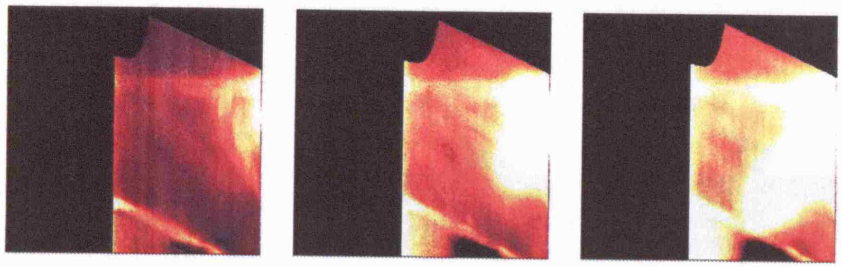

Delta 08 CAD Delta 09 CAD Delta 10 CAD

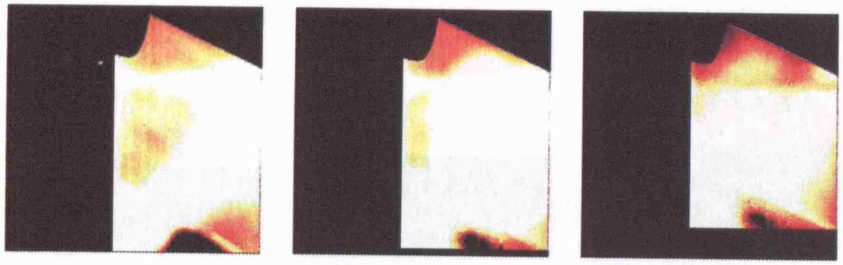

Delta 11 CAD Delta 15 CAD Delta 20 CAD

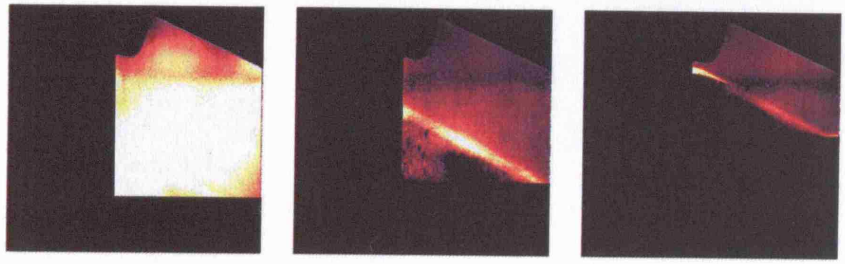

Delta 25 CAD Delta 30 CAD Delta 45 CAD

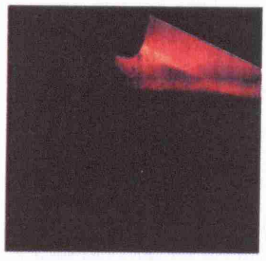

Delta 63 CAD

Figure 8-14 Post-Processed Images for LIF Test III SOI 654 CAD

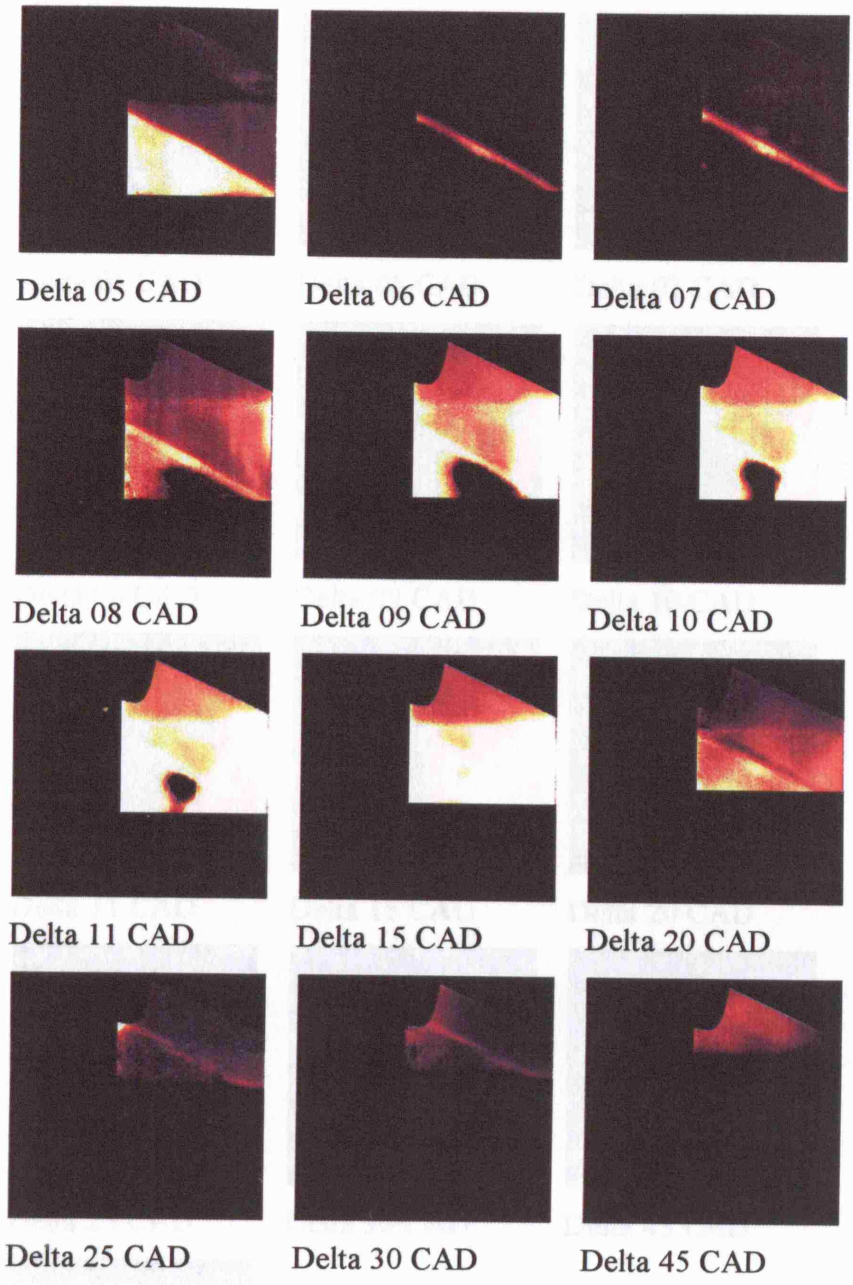

Figure 8-15 Post-Processed Images for LIF Test III SOI 675 CAD

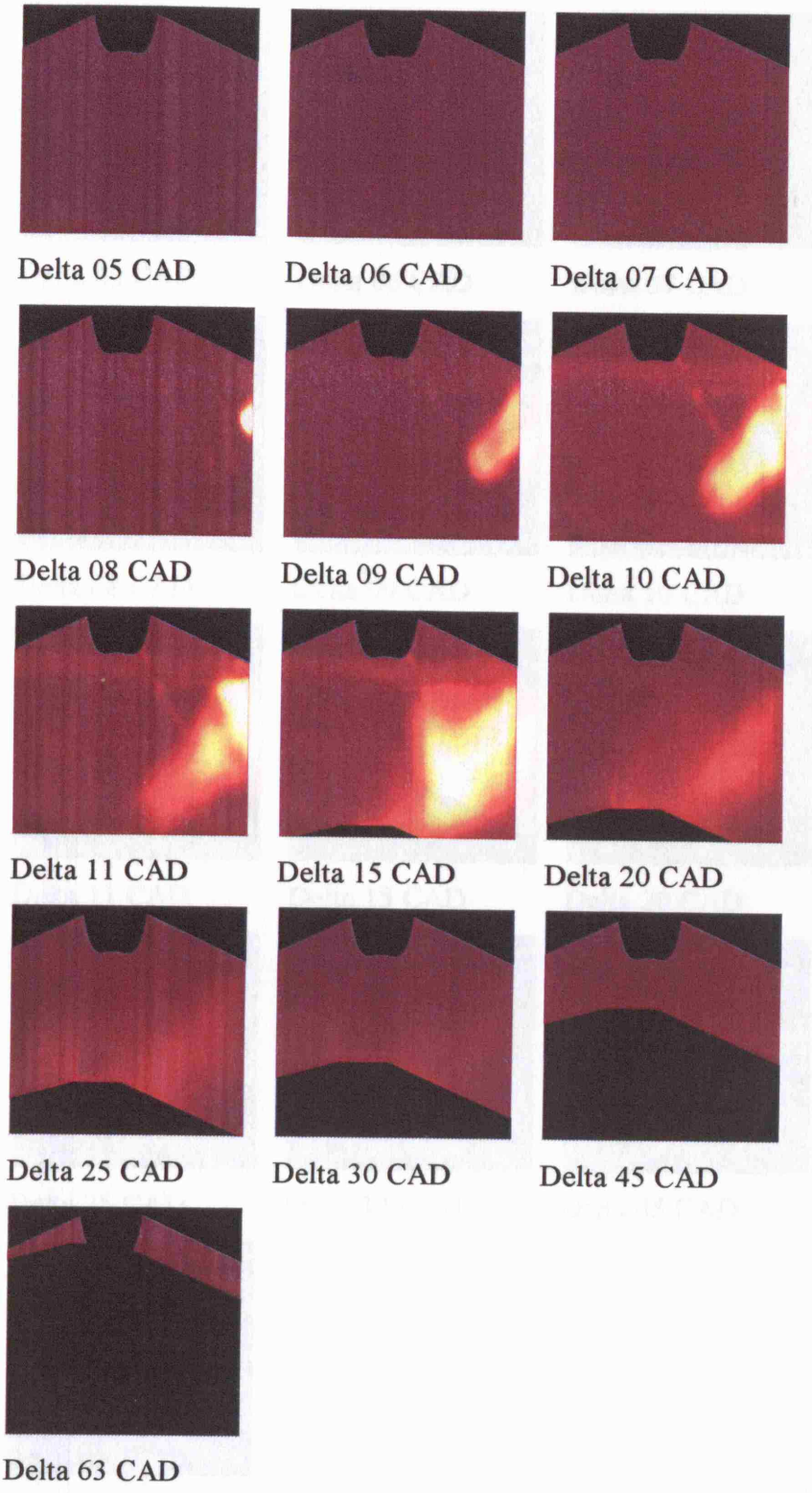

Figure 8-16 Post-Processed Images for LIF Test V SOI 639 CAD

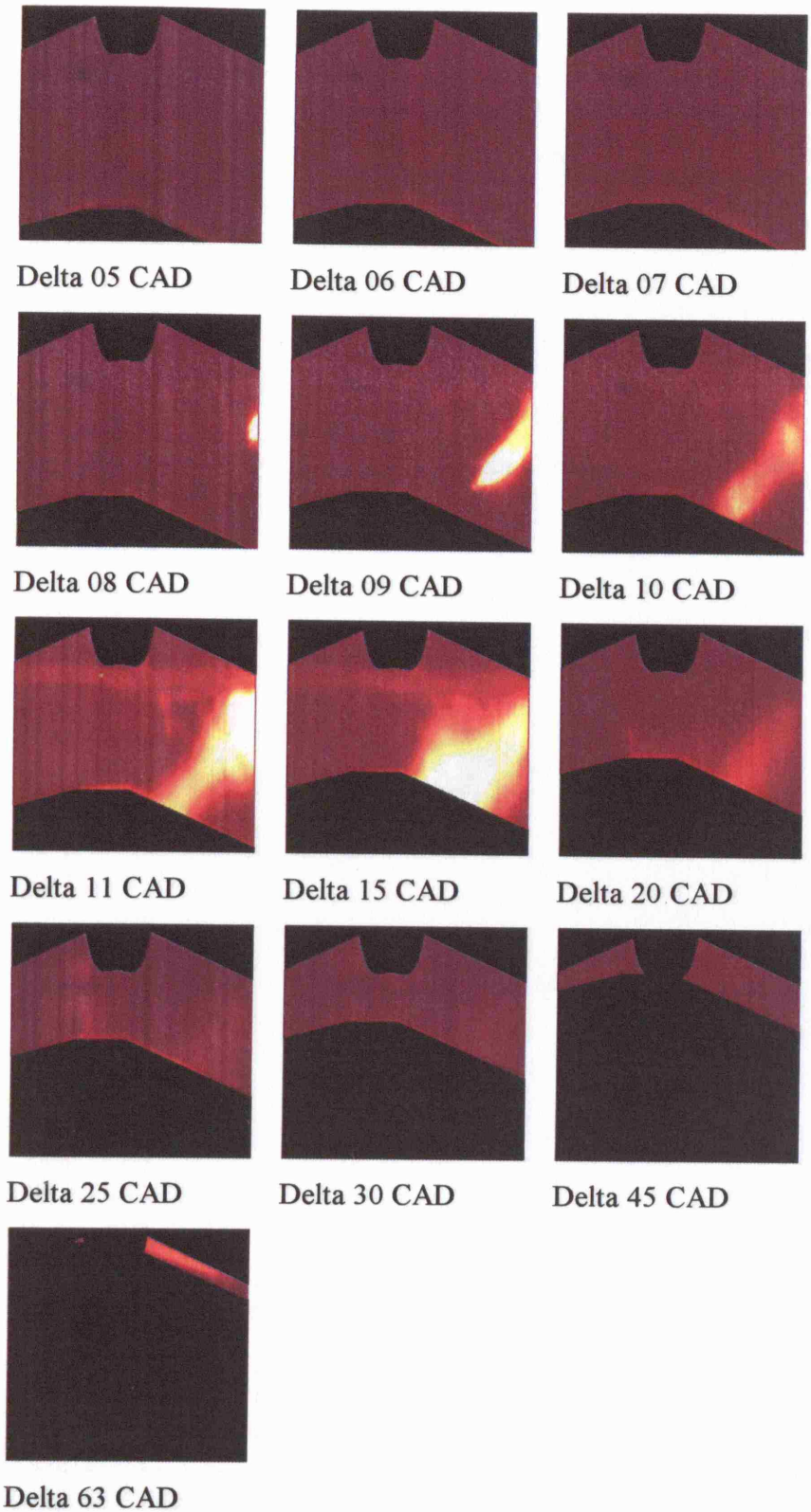

Figure 8-17 Post-Processed Images for LIF Test V SOI 654 CAD

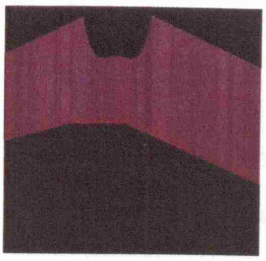

Delta 05 CAD

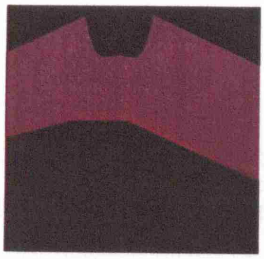

Delta 06 CAD

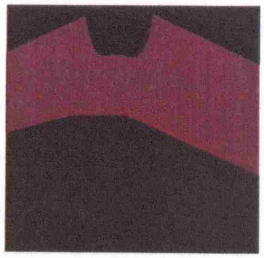

Delta 07 CAD

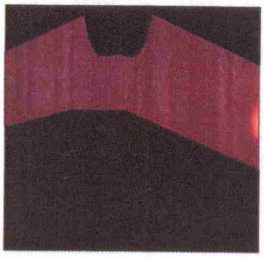

Delta 08 CAD

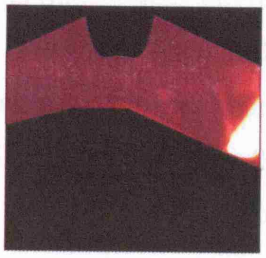

Delta 09 CAD

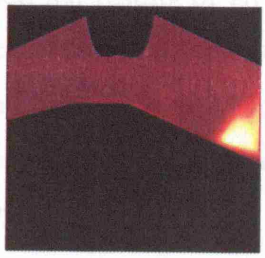

Delta 10 CAD

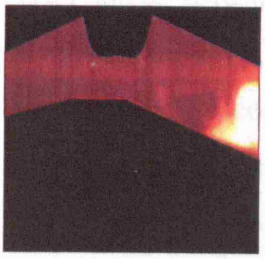

Delta 11 CAD

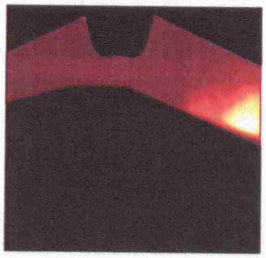

Delta 15 CAD

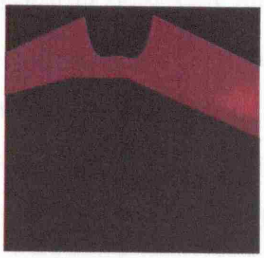

Delta 20 CAD

Delta 25 CAD

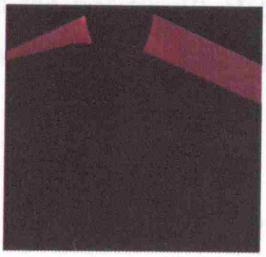

Delta 30 CAD

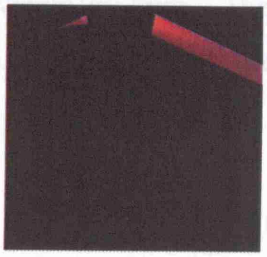

Delta 45 CAD

No image (piston near TDC)

Delta 63 CAD

Figure 8-18 Post-Processed Images for LIF Test V SOI 675 CAD

8.4.13 Discussion of LIF results

The best results were produced from test III, with the images being improved at each stage of post-processing as planned, ie from the raw images, to the background corrected and finally the beam profile corrected.

The use of sheet correction images degraded the results of all the tests apart from test III and consideration needs to be given to possible reasons. It has already been noted that a dark region caused by total internal reflection in the quartz insert existed in all images using the slotted crown, indeed this was the reason for attempting to apply the sheet correction images.

The contrast between this region and the adjoining ones was much larger than for the disc images, where the plain piece of quartz gave little distortion to the light sheet. A comparison of sheet intensities across disc and slot sheet correction images is shown in Figure 8-19. Any misalignment between the sheet correction and the firing images meant the use of wrong factors and the large discrepancies (due to contrast) at the dark region boundaries of the slotted set introduced the possibility of division by zero. The discrepancies also made it difficult to choose a maximum value to suit the whole set of images.

It would have been possible, although extremely difficult, to develop correction procedures to rectify the misalignment, but it was apparent that there was an even more fundamental problem. In spite of hopes to the contrary, the intensity of illuminating light at 355 nm wavelength reaching the 'dark' region was too low to cause significant fluorescence. Thus the multiplying factors to allow for the low illumination could not produce sensible results where little or no fluorescence was occurring. It was reluctantly decided to accept that there would be regions within each image where the illumination was too low to expect significant fluorescence. The light sheet correction images did prove helpful in identifying the low intensity region for each firing image. The boundaries of these regions were transposed onto the sample firing image and shown as white lines (Figure 8-20).

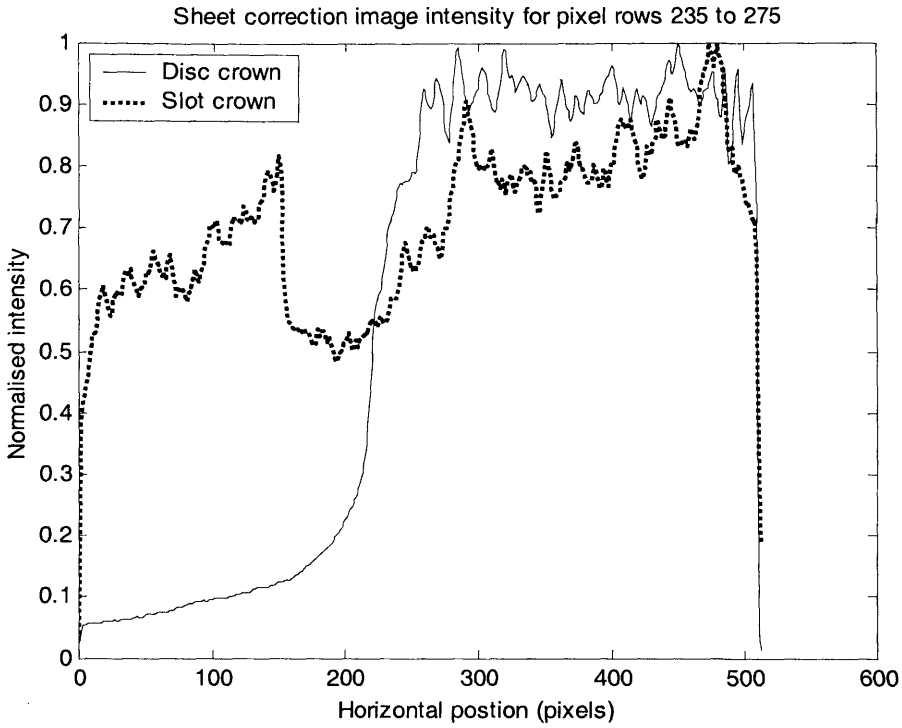

Figure 8-19 Mean intensity for a band of pixels across the sheet correction images, using the disc crown and the slot crown

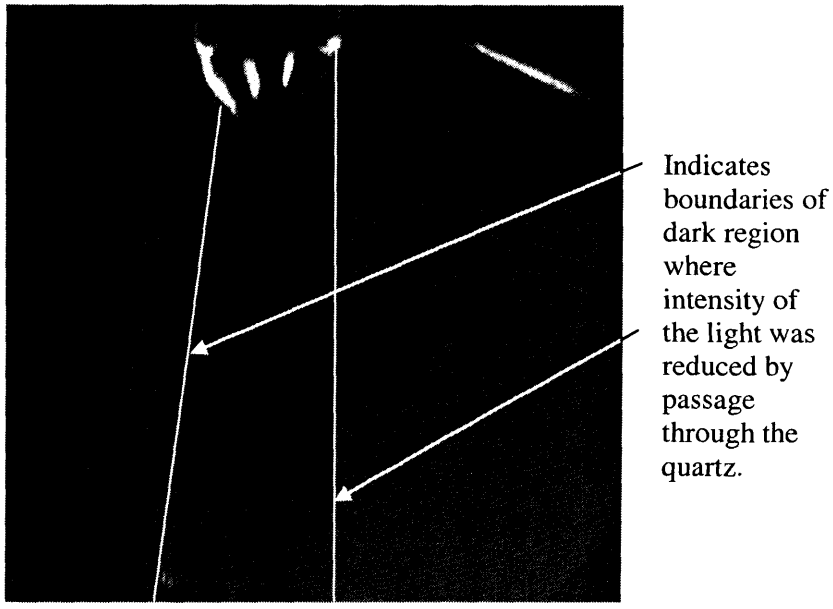

Figure 8-20 Dark region caused by quartz refracting the light sheet

Figure 8–21 to Figure 8–41 contain the LIF images, tests I, III and V, displayed alongside the earlier Mie and ambient air injector images for comparison. The intention was to use the SOIs and deltas as a time reference. Inspection of the images in that format revealed a timing anomaly, apparent as the non-arrival of pre-spray at CAD timings when it was expected to be seen

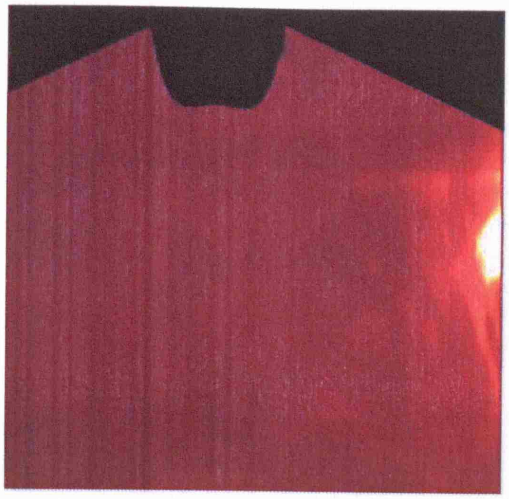

LIF test I, TFA 0 (Delta 08)

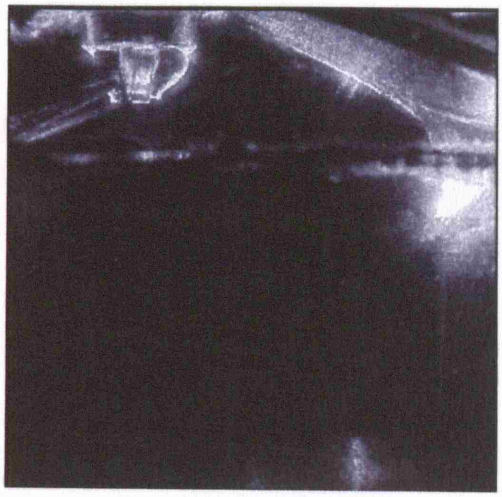

Mie, TFA 0 (Delta 05)

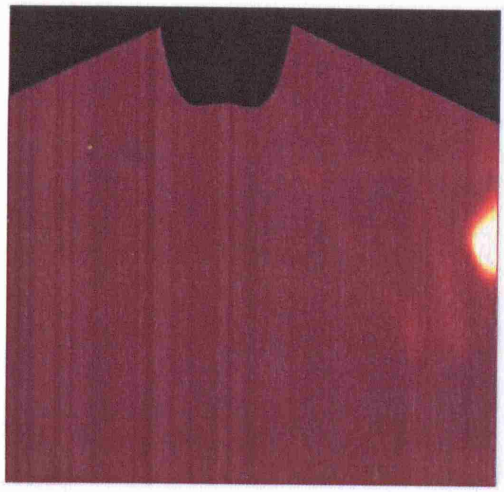

LIF test V, TFA 0 (Delta 08)

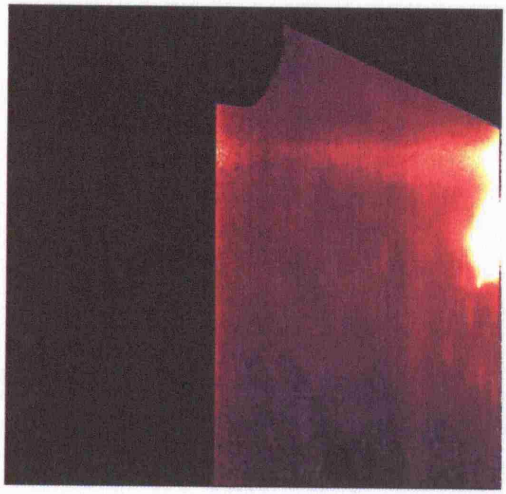

LIF test III, TFA 0 (Delta 08)

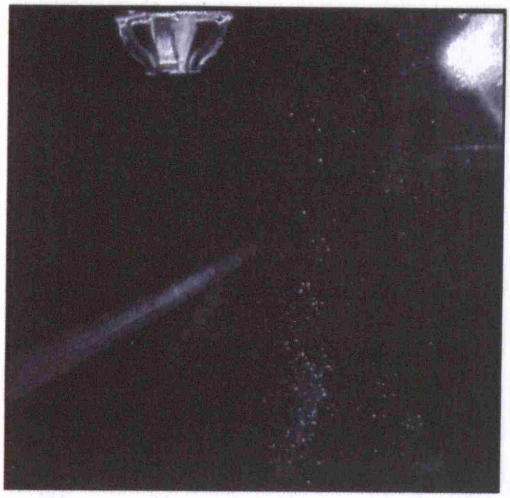

Ambient air, slotted, TFA 0 (Delta 07)

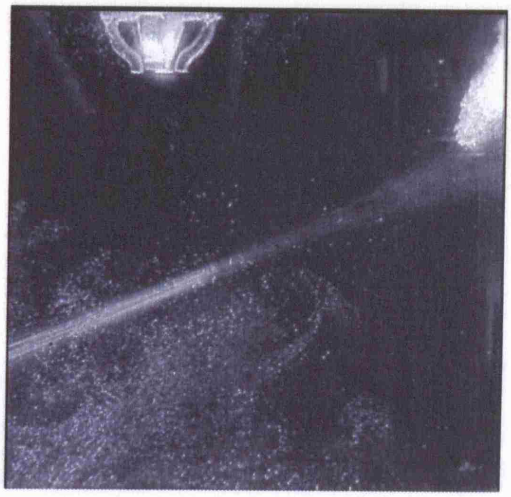

Ambient air, none, TFA 0 (Delta 07)

Intensity scale for LIF results is in Figure 8-10

Figure 8-21 Grouped results, LIF, Mie, Ambient Air, for SOI 639 CAD, TFA (A)

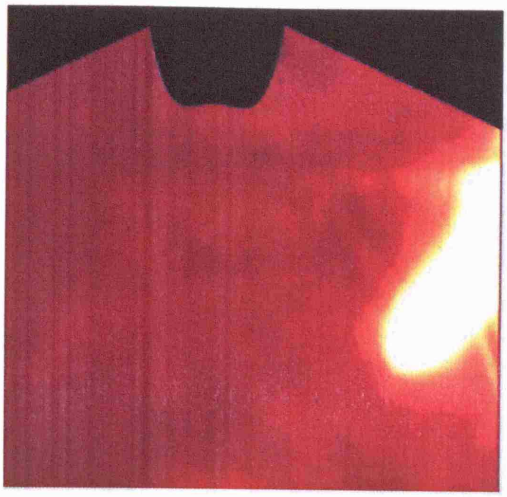

LIF test I, TFA 1 (Delta 09)

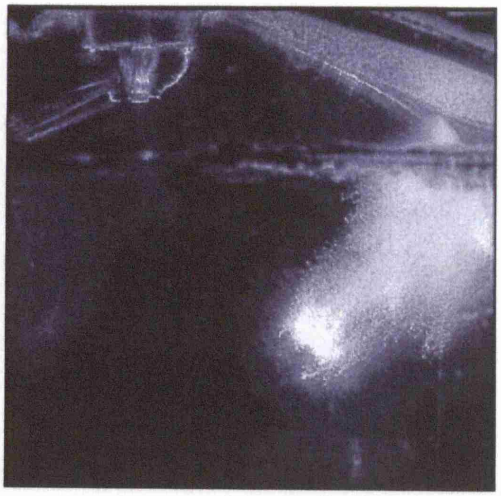

Mie, TFA 2 (Delta 07)

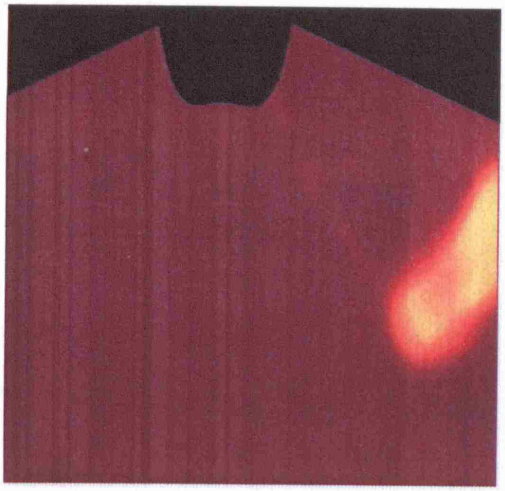

LIF test V, TFA 1 (Delta 09)

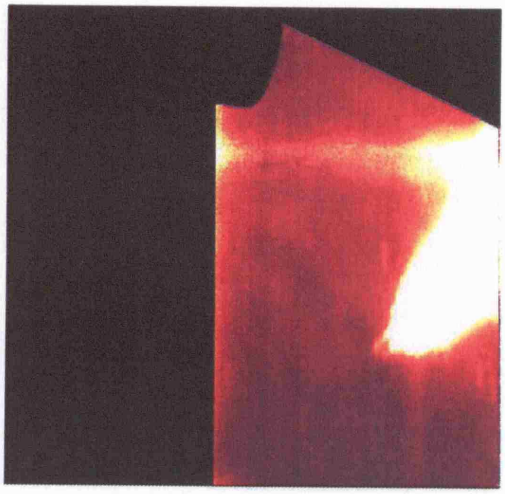

LIF test III, TFA 1 (Delta 09)

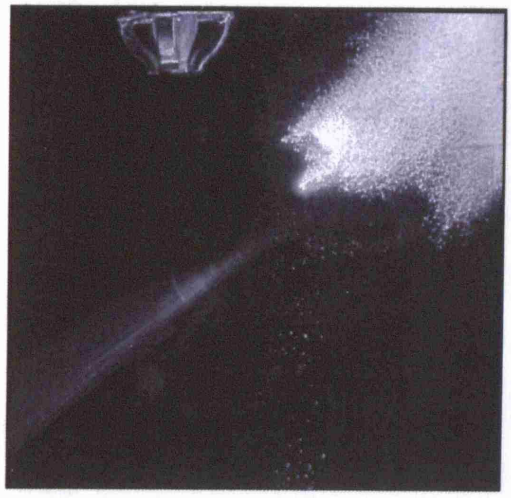

Ambient air, slotted, TFA 1 (Delta 08)

Ambient air, none, TFA 1 (Delta 08)

Figure 8-22 Grouped results, LIF, Mie, Ambient Air, for SOI 639 CAD, TFA (B)

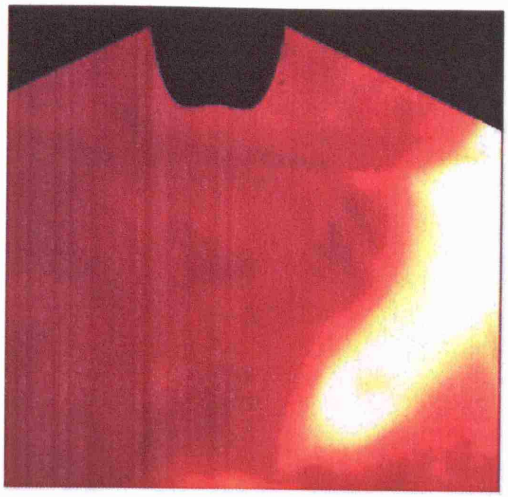

LIF test I, TFA 2 (Delta 10)

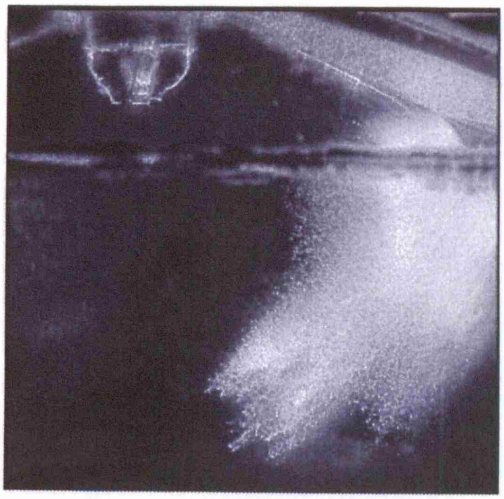

Mie, TFA 3 (Delta 08)

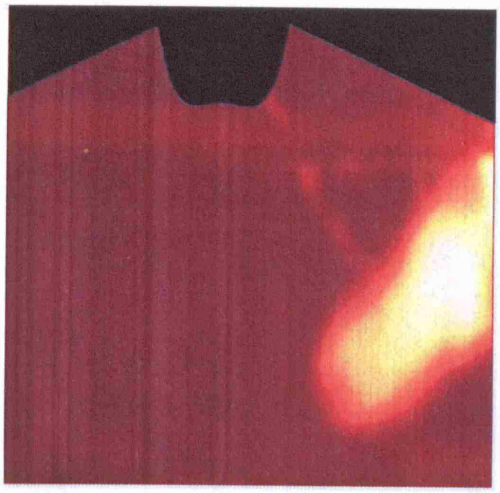

LIF test V, TFA 2 (Delta 10)

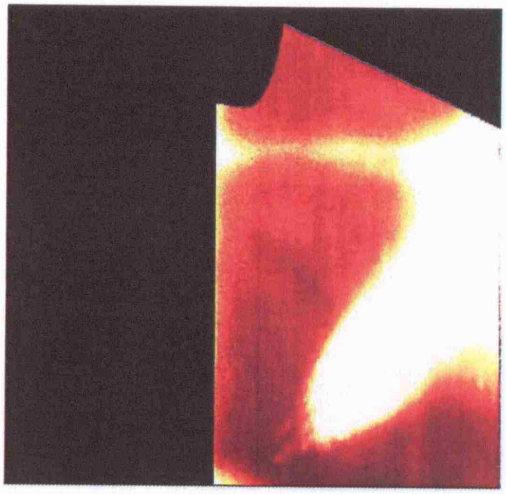

LIF test III, TFA 2 (Delta 10)

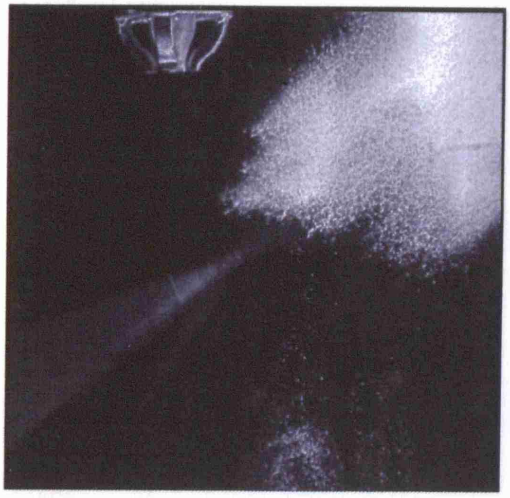

Ambient air, slotted, TFA 2 (Delta 09)

Ambient air, none, TFA 2 (Delta 09)

Figure 8-23 Grouped results, LIF, Mie, Ambient Air, for SOI 639 CAD, TFA (C)

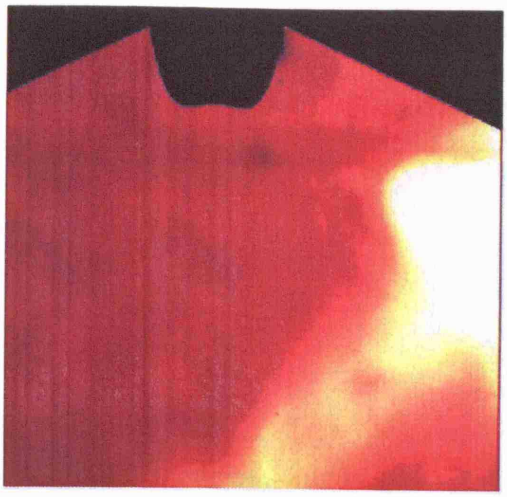

LIF test I, TFA 3 (Del 11)

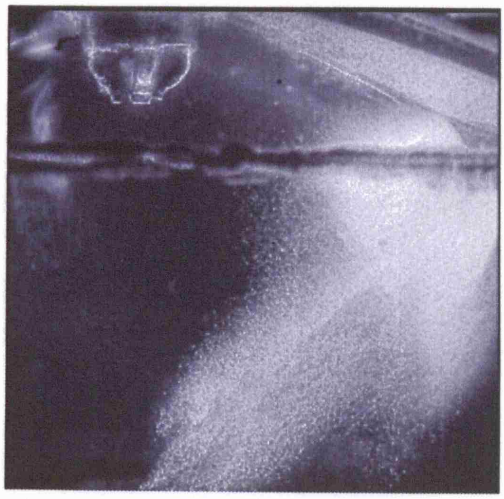

Mie, TFA 4 (Del 09)

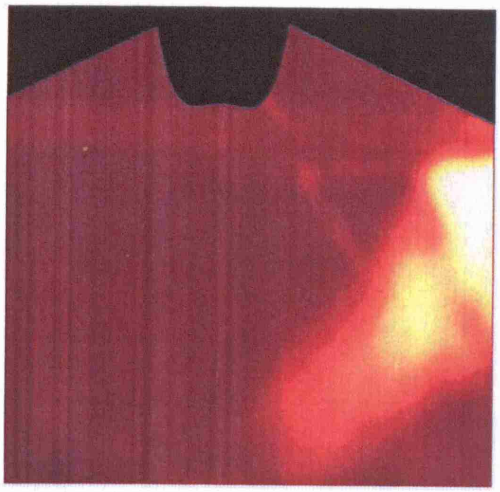

LIF test V, TFA 3 (Del 11)

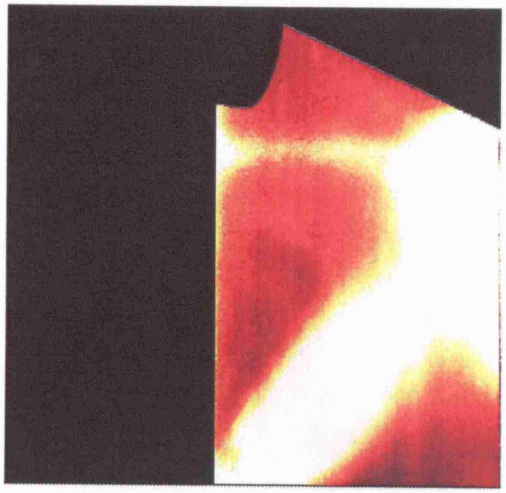

LIF test III, TFA 3 (Del 11)

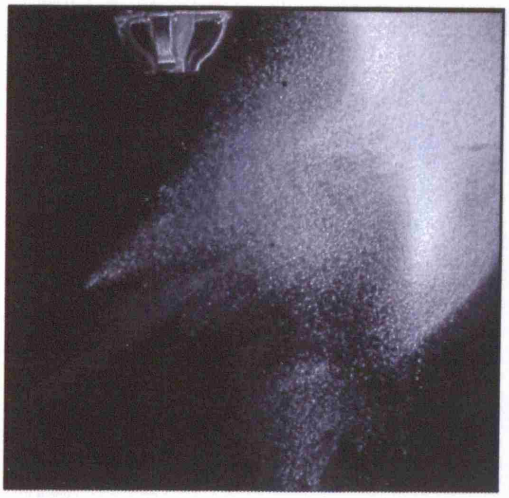

Ambient air, slotted, TFA 4 (Del 11)

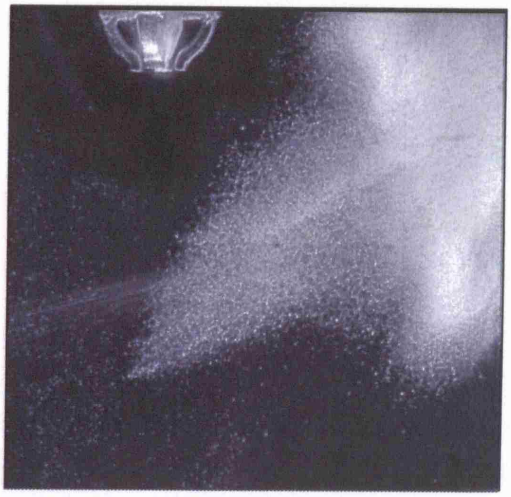

Ambient air, none, TFA 4 (Del 11)

Figure 8-24 Grouped results LIF, Mie, Ambient Air, for SOI 639 CAD, TFA (D)

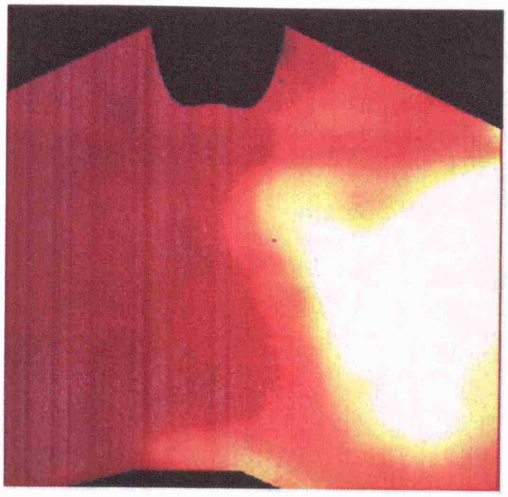

LIF test I, TFA 7 (Del 15)

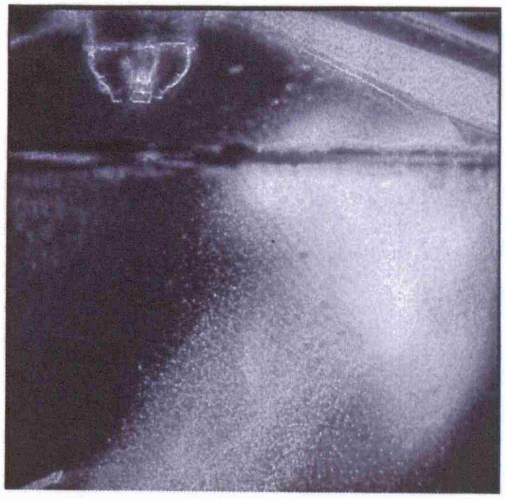

Mie, TFA 6 (Del 11)

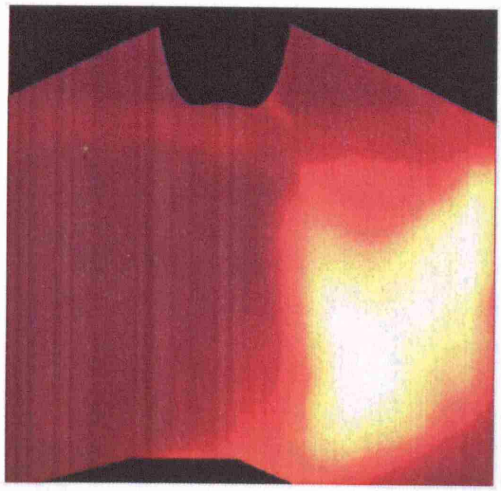

LIF test V, TFA 7 (Del 15)

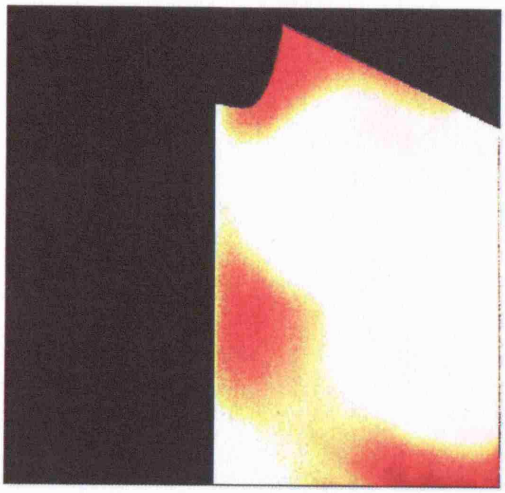

LIF test III, TFA 7 (Del 15)

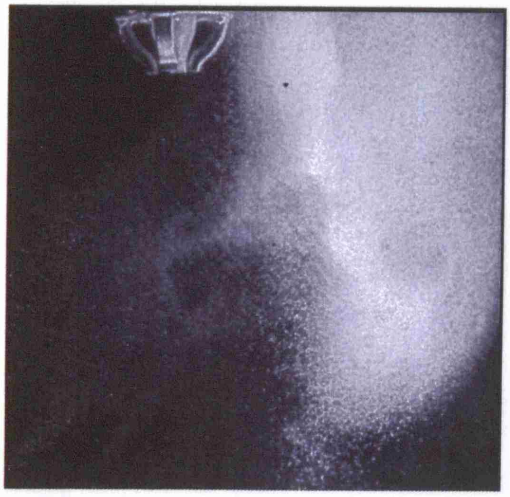

Ambient air, slotted, TFA 8 (Del 15)

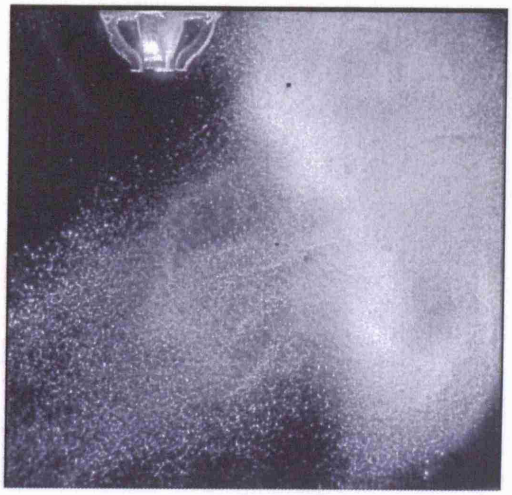

Ambient air, none, TFA 8 (Del 15)

Figure 8-25 Grouped results LIF, Mie, Ambient Air, for SOI 639 CAD, TFA (E)

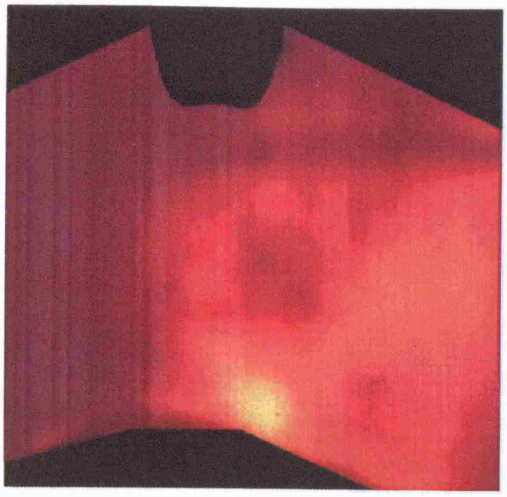

LIF test I, TFA 12 (Del 20)

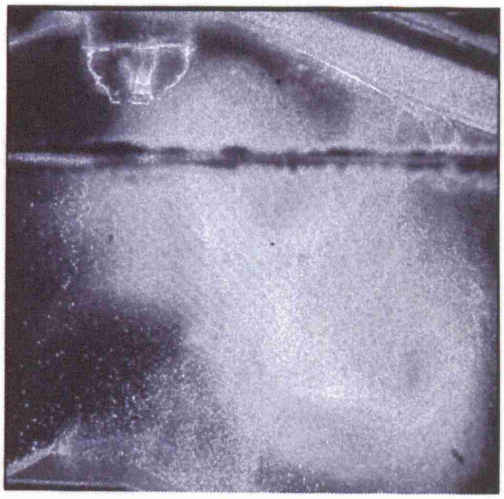

Mie, TFA 10 (Del 15)

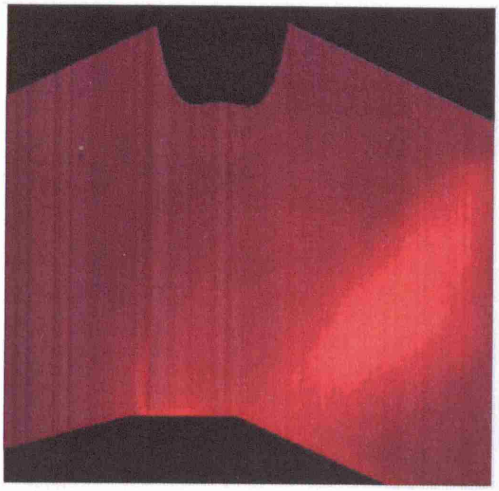

LIF test V, TFA 12 (Del 20)

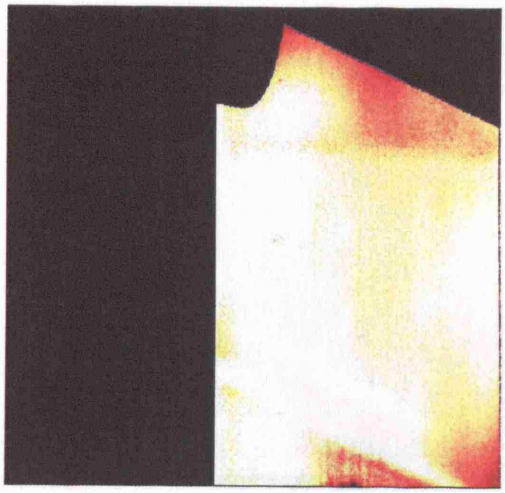

LIF test III, TFA 12 (Del 20)

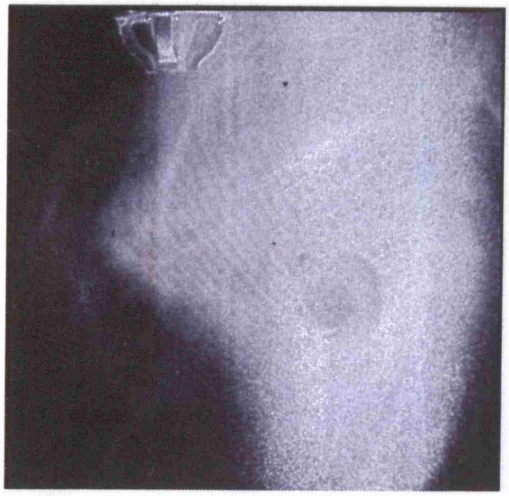

Ambient air, slotted, TFA 13 (Del 20)

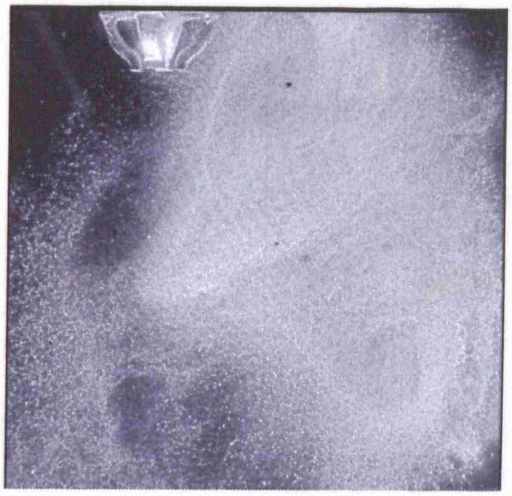

Ambient air, none, TFA 13 (Del 20)

Figure 8-26 Grouped results LIF, Mie, Ambient Air, for SOI 639 CAD, TFA (F)

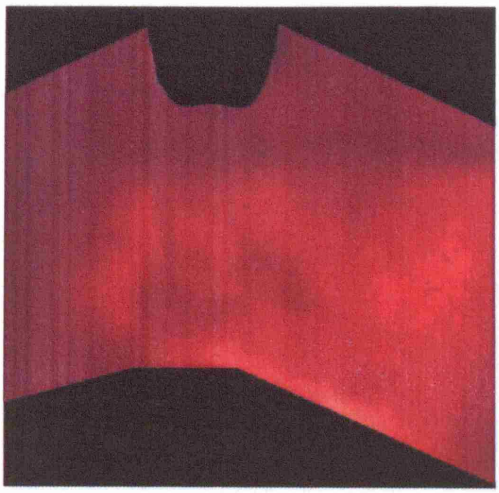

LIF test I, TFA 17 (Del 25)

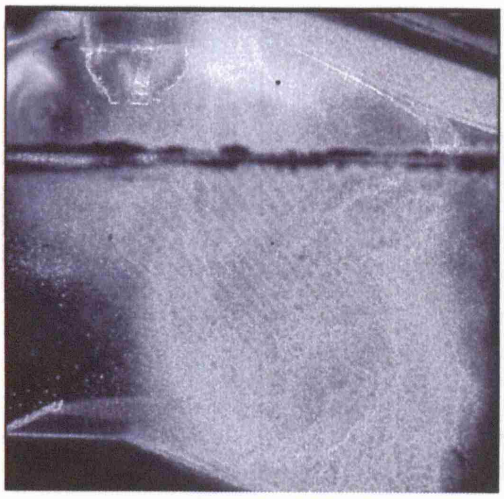

Mie, TFA 15 (Del 20)

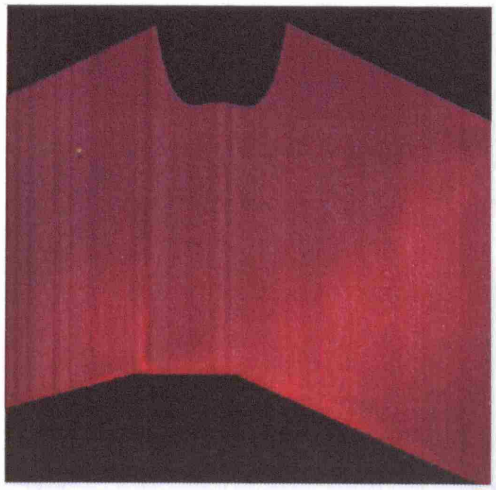

LIF test V, TFA 17 (Del 25)

LIF test III, TFA 17 (Del 25)

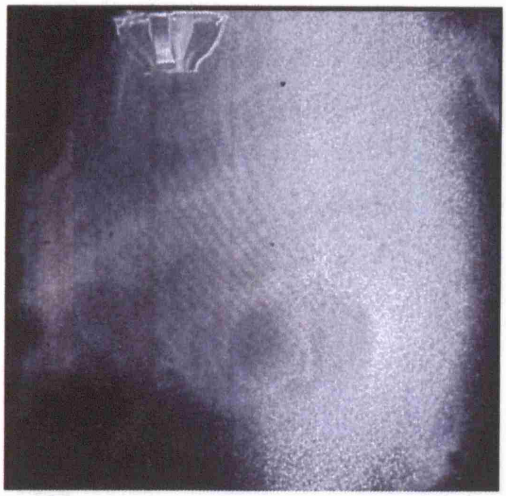

Ambient air, slotted, TFA 18 (Del 25)

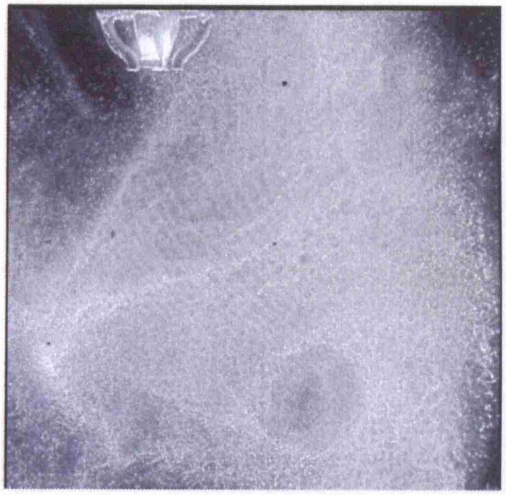

Ambient air, none, TFA 18 (Del 25)

Figure 8-27 Grouped results LIF, Mie, Ambient Air, for SOI 639 CAD, TFA (G)

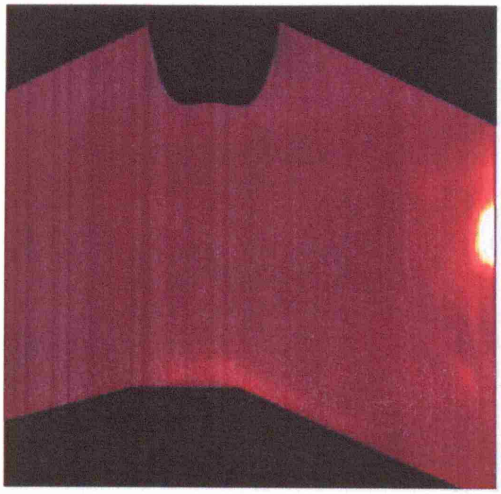

LIF test I, TFA 0 (Del 08)

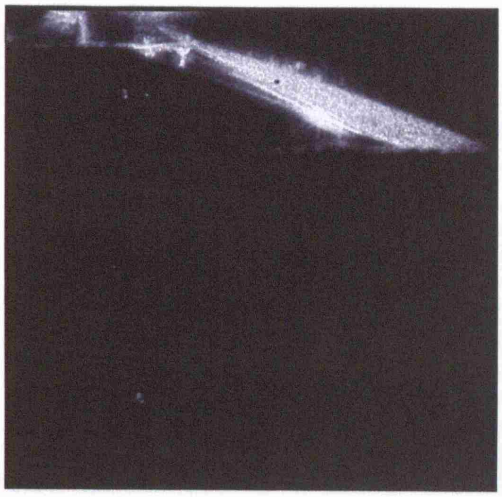

Mie, TFA 0 (Del 05)

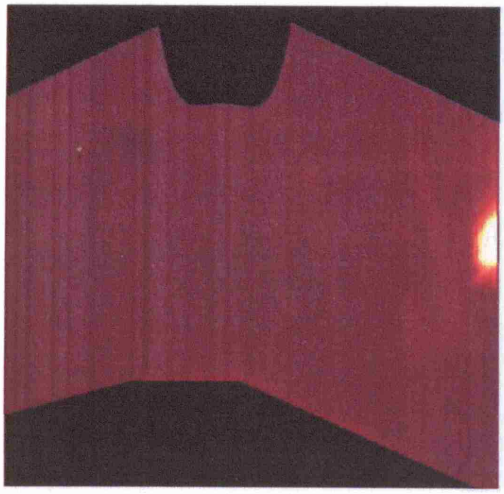

LIF test V, TFA 0 (Del 08)

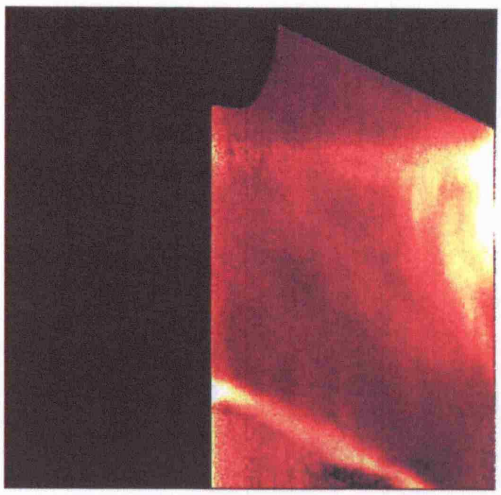

LIF test III, TFA 0 (Del 08)

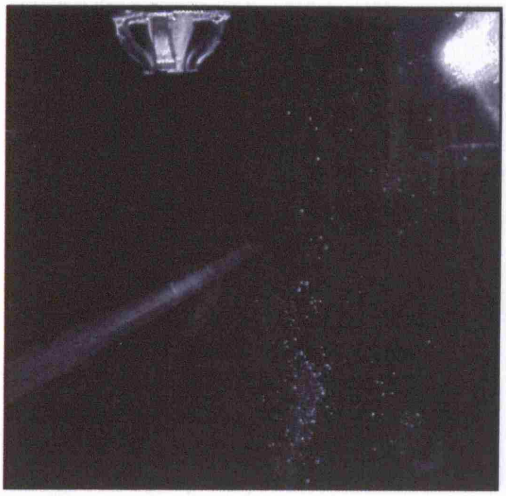

Ambient air, slotted, TFA 0 (Del 07)

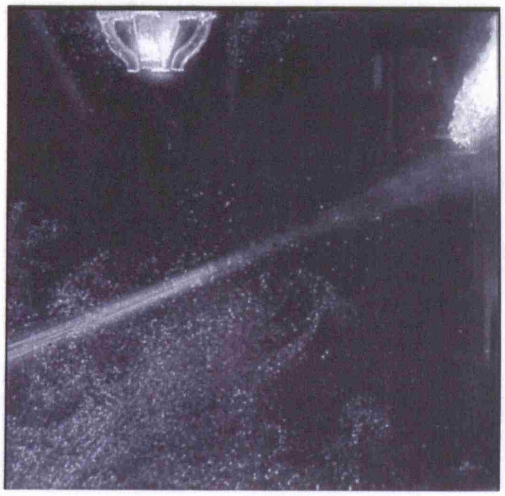

Ambient air, none, TFA 0 (Del 07)

Figure 8-28 Grouped results LIF, Mie, Ambient Air, for SOI 654 CAD, TFA (A)

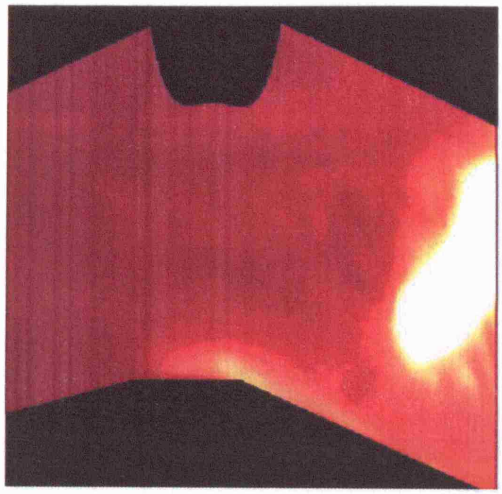

LIF test I, TFA 1 (Del 09)

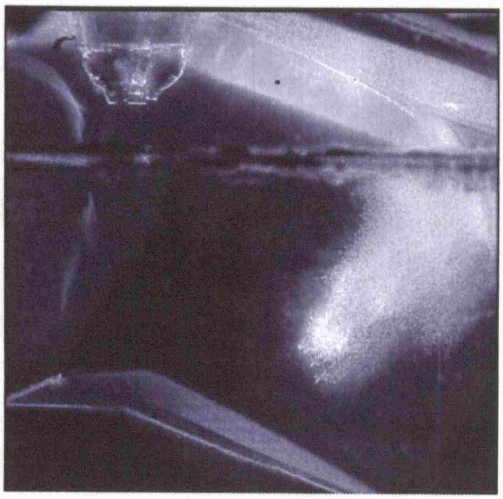

Mie, TFA 2 (Del 07)

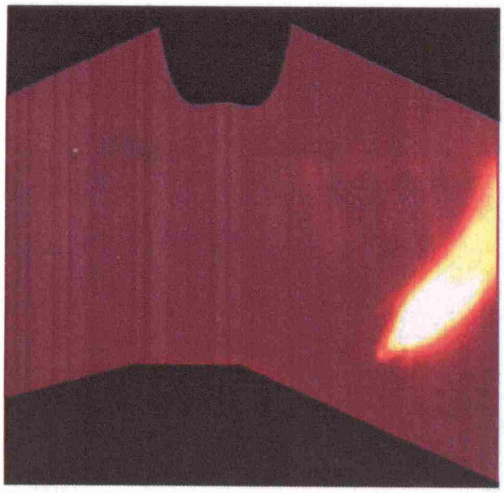

LIF test V, TFA 1 (Del 09)

LIF test III, TFA 1 (Del 09)

Ambient air, slotted, TFA 1 (Del 08)

Ambient air, none, TFA 1 (Del 08)

Figure 8-29 Grouped results LIF, Mie, Ambient Air, for SOI 654 CAD, TFA (B)

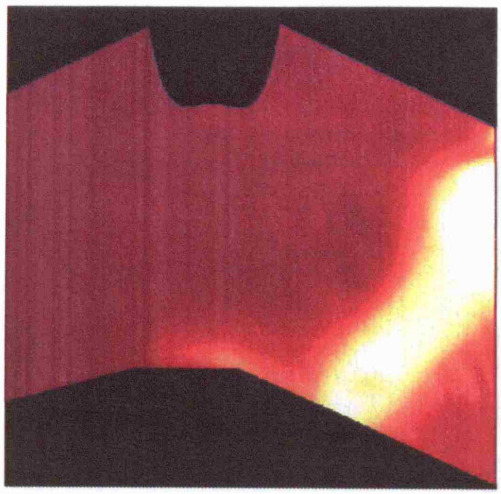

LIF test I, TFA 2 (Del 10)

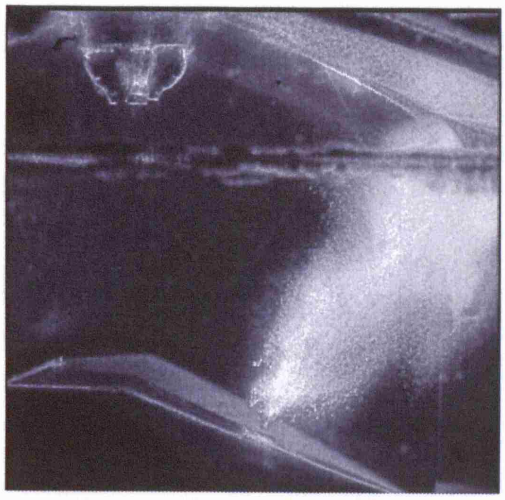

Mie, TFA 3 (Del 08)

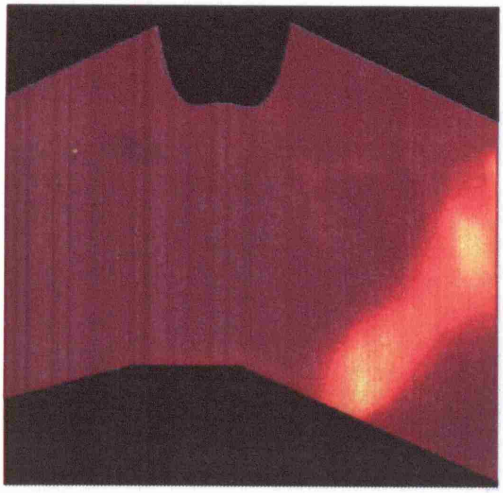

LIF test V, TFA 2 (Del 10)

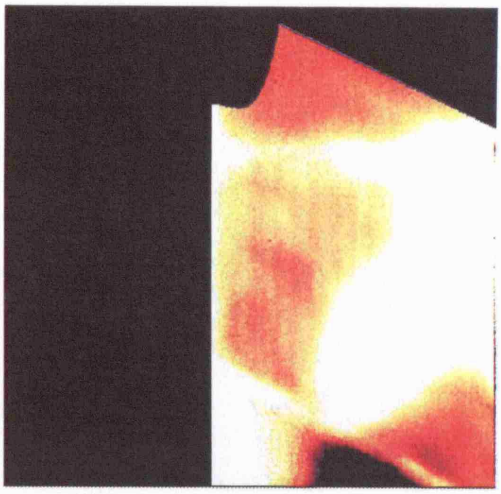

LIF test III, TFA 2 (Del 10)

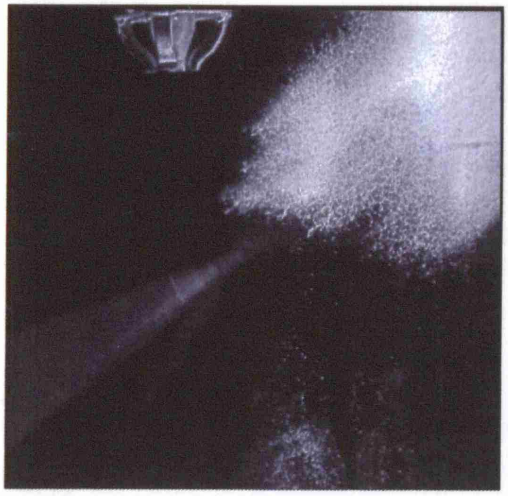

Ambient air, slotted, TFA 2 (Del 09)

Ambient air, none, TFA 2 (Del 09)

Figure 8-30 Grouped results LIF, Mie, Ambient Air, for SOI 654 CAD, TFA (C)

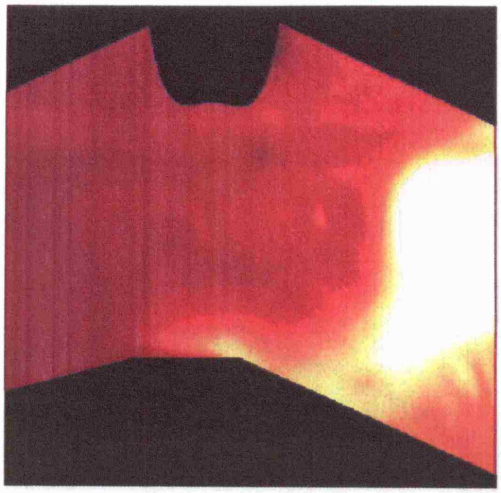

LIF test I, TFA 3 (Del 11)

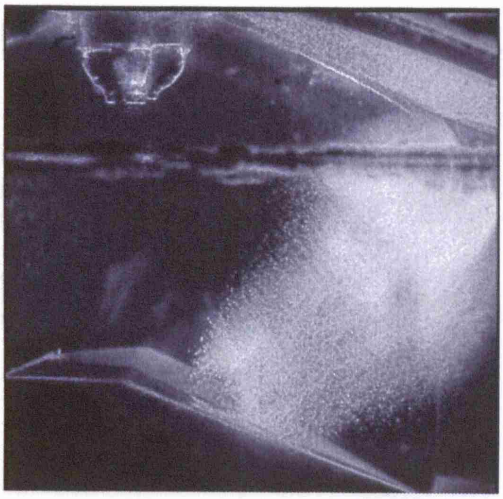

Mie, TFA 4 (Del 09)

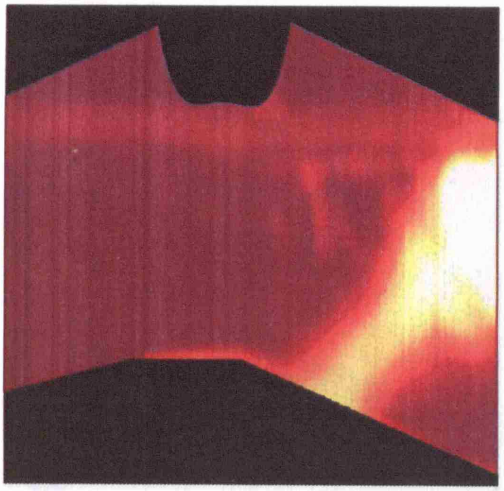

LIF test V, TFA 3 (Del 11)

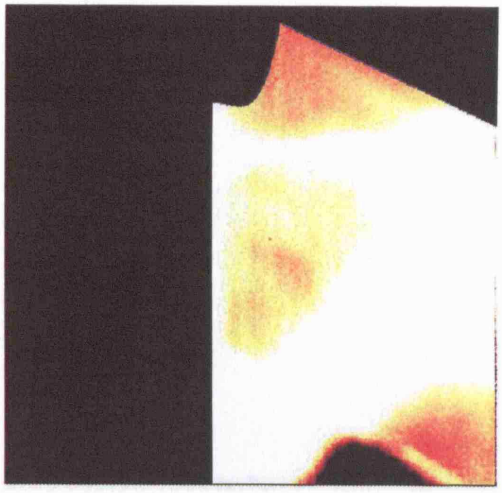

LIF test III, TFA 3 (Del 11)

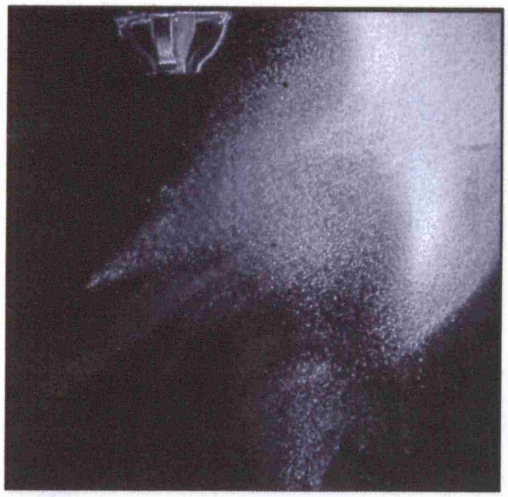

Ambient air, slotted, TFA 4 (Del 11)

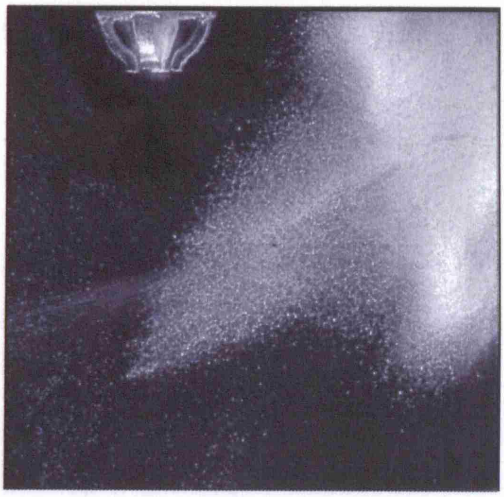

Ambient air, none, TFA 4 (Del 11)

Figure 8-31 Grouped results LIF, Mie, Ambient Air, for SOI 654 CAD, TFA (D)

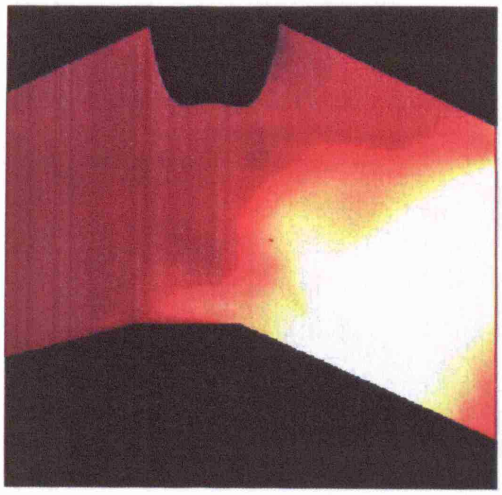

LIF test I, TFA 7 (Del 15)

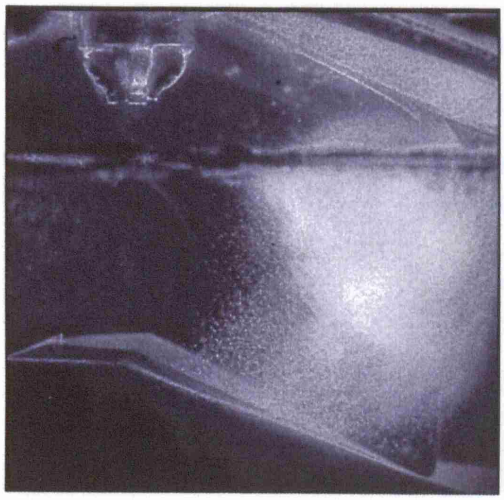

Mie, TFA 6 (Del 11)

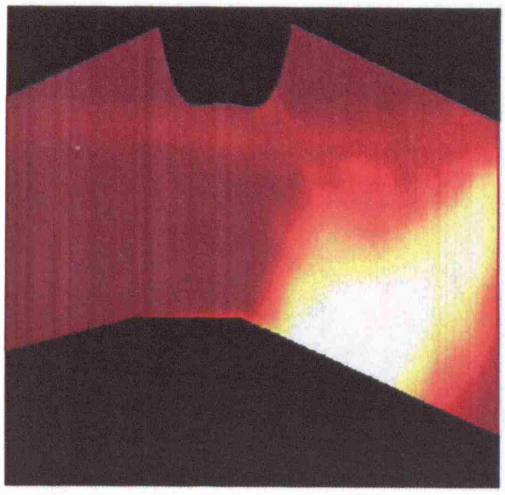

LIF test V, TFA 7 (Del 15)

LIF test III, TFA 7 (Del 15)

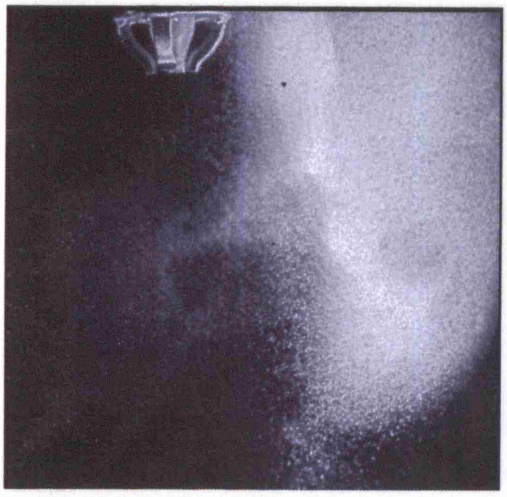

Ambient air, slotted, TFA 8 (Del 15)

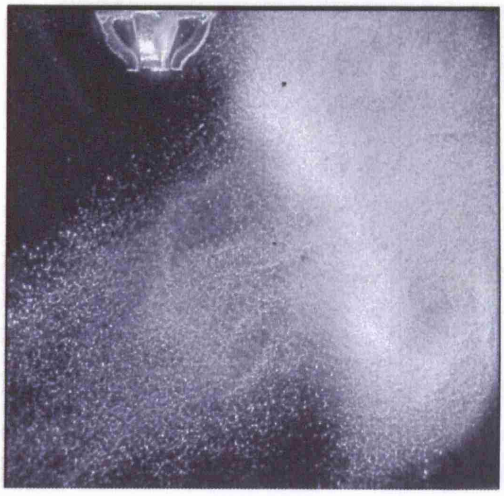

Ambient air, none, TFA 8 (Del 15)

Figure 8-32 Grouped results LIF, Mie, Ambient Air, for SOI 654 CAD, TFA (E)

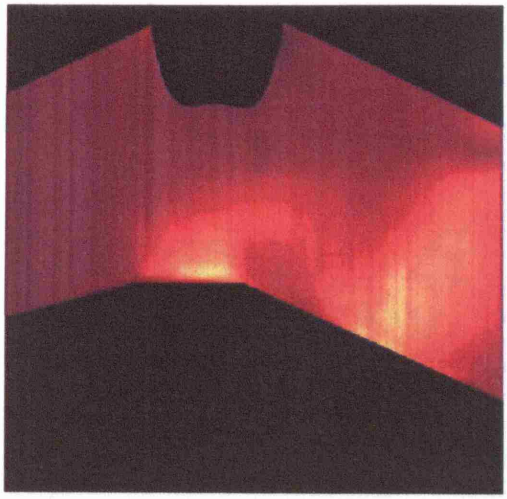

LIF test I, TFA 12 (Del 20)

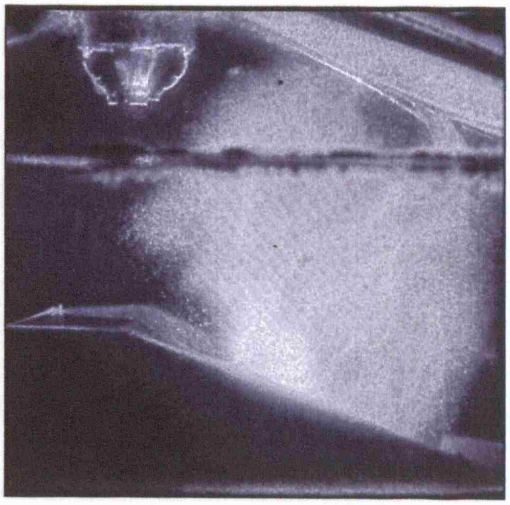

Mie, TFA 10 (Del 15)

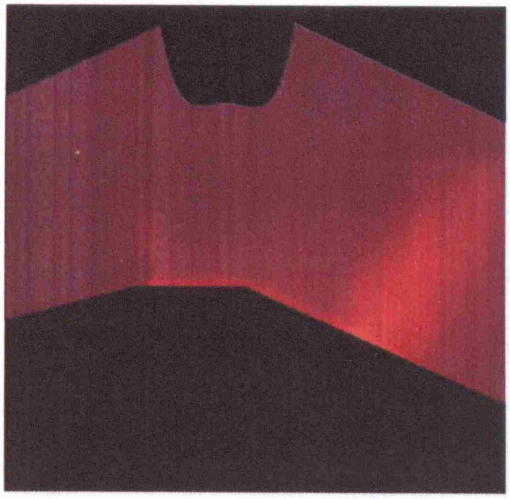

LIF test V, TFA 12 (Del 20)

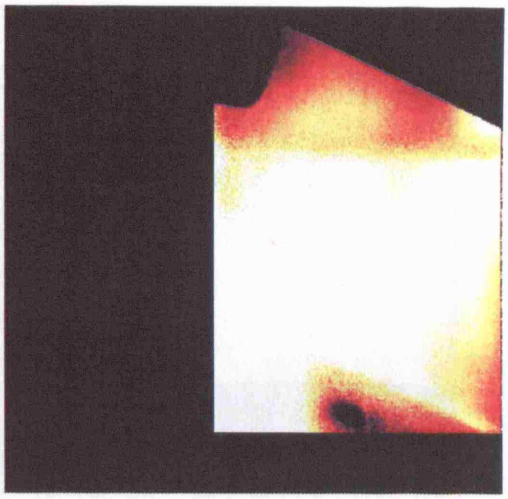

LIF test III, TFA 12 (Del 20)

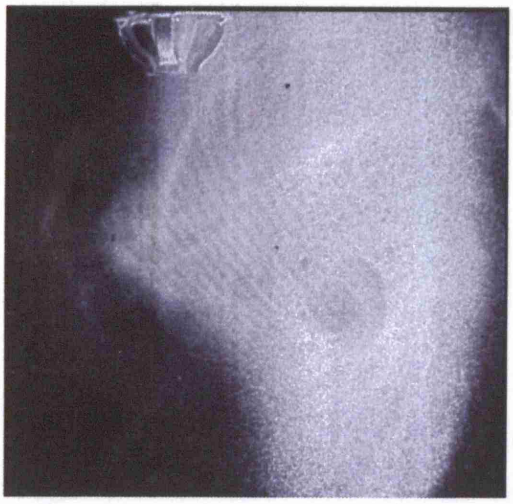

Ambient air, slotted, TFA 13 (Del 20)

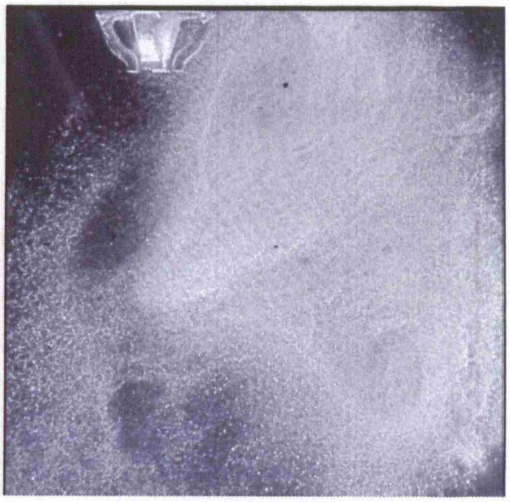

Ambient air, none, TFA 13 (Del 20)

Figure 8-33 Grouped results LIF, Mie, Ambient Air, for SOI 654 CAD, TFA (F)

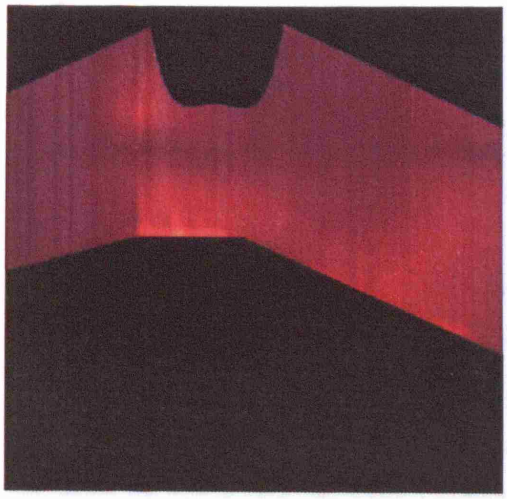

LIF test I, TFA 17 (Del 25)

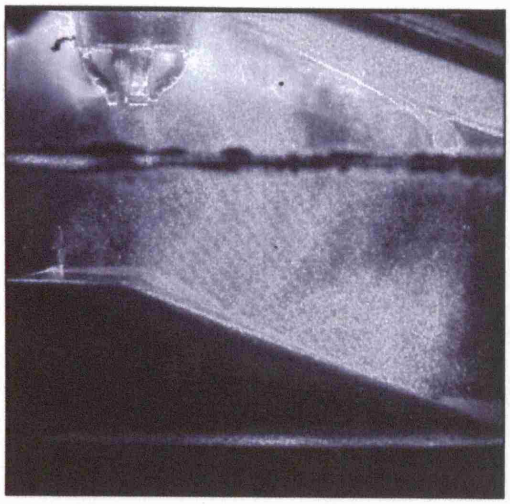

Mie, TFA 15 (Del 20)

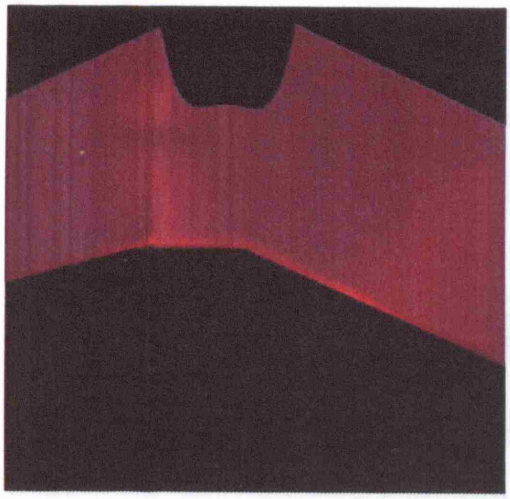

LIF test V, TFA 17 (Del 25)

LIF test III, TFA 17 (Del 25)

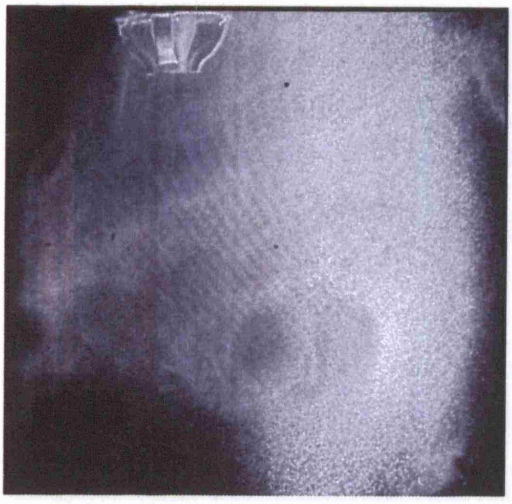

Ambient air, slotted, TFA 18 (Del 25)

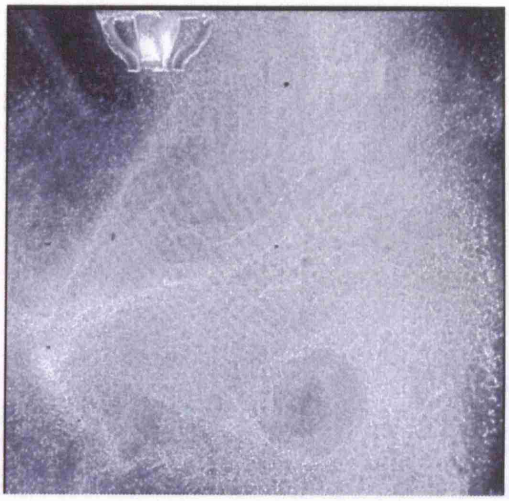

Ambient air, none, TFA 18 (Del 25)

Figure 8-34 Grouped results LIF, Mie, Ambient Air, for SOI 654 CAD, TFA (G)

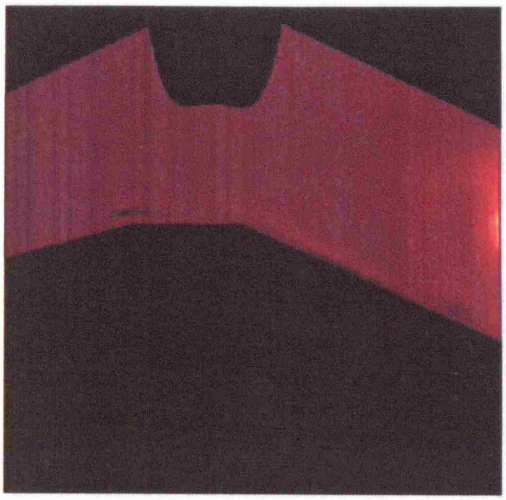

LIF test I, TFA 0 (Del 08)

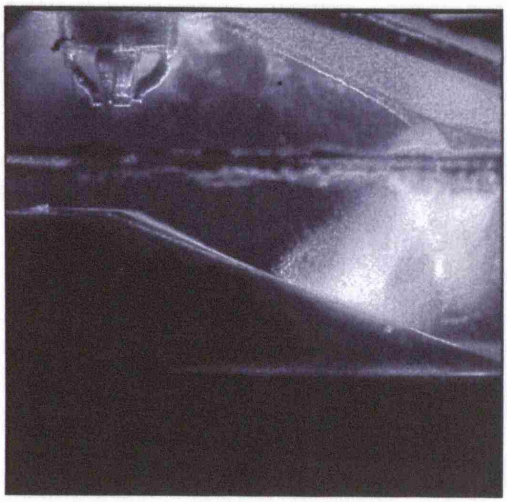

Mie, TFA 0 (Del 05)

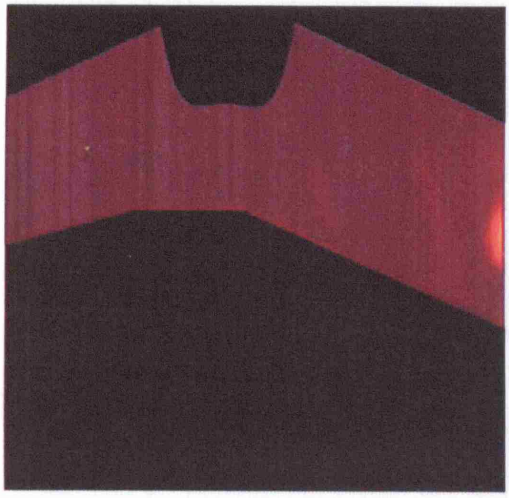

LIF test V, TFA 0 (Del 08)

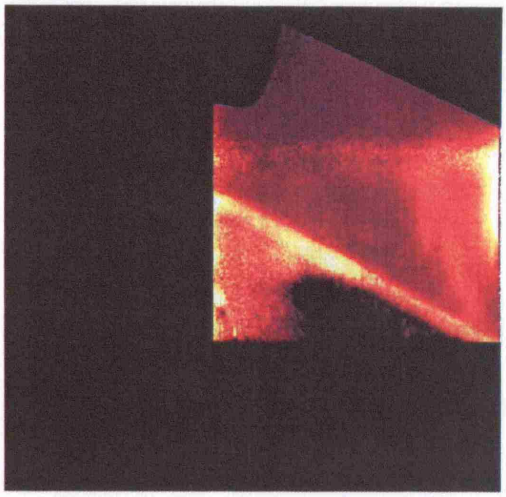

LIF test III, TFA 0 (Del 08)

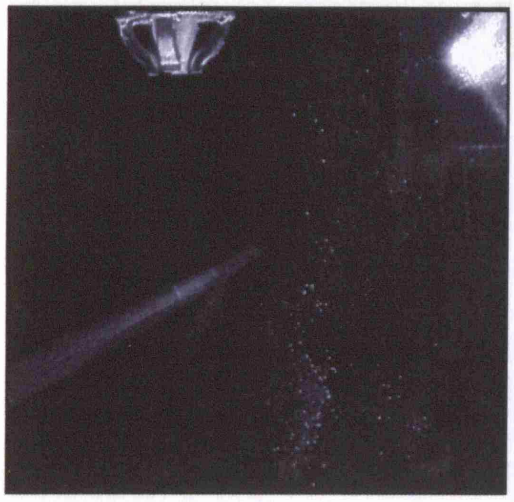

Ambient air, slotted, TFA 0 (Del 07)

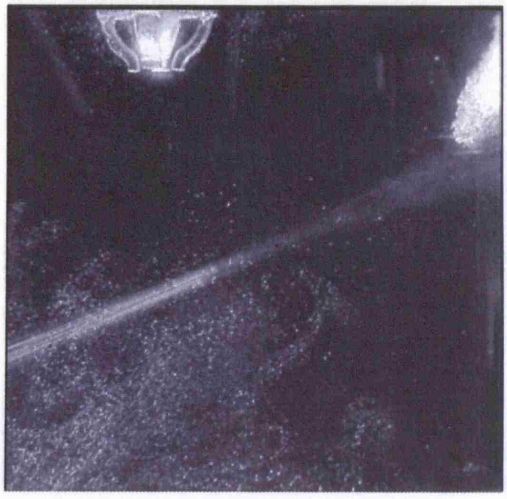

Ambient air, none, TFA 0 (Del 07)

Figure 8-35 Grouped results LIF, Mie, Ambient Air, for SOI 675 CAD, TFA (A)

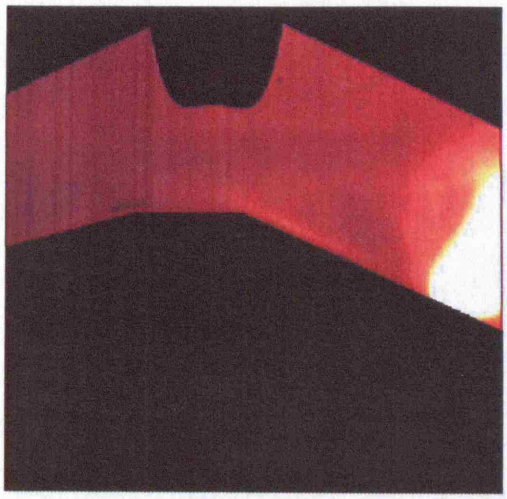

LIF test I, TFA 1 (Del 09)

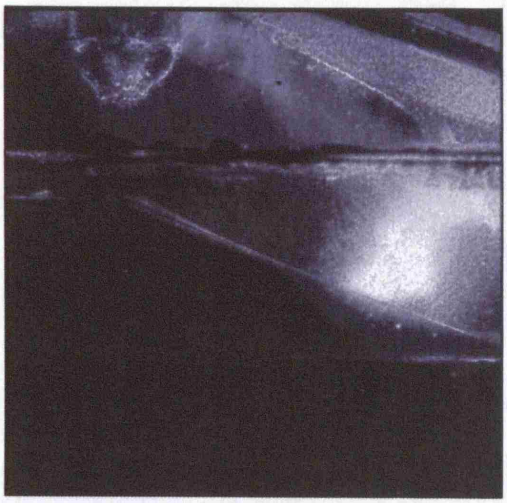

Mie, TFA 2 (Del 07)

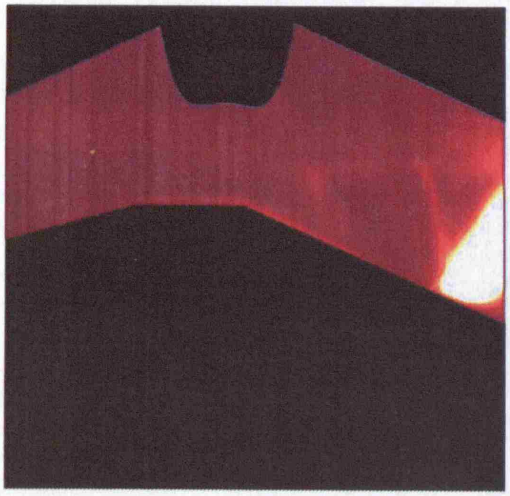

LIF test V, TFA 1 (Del 09)

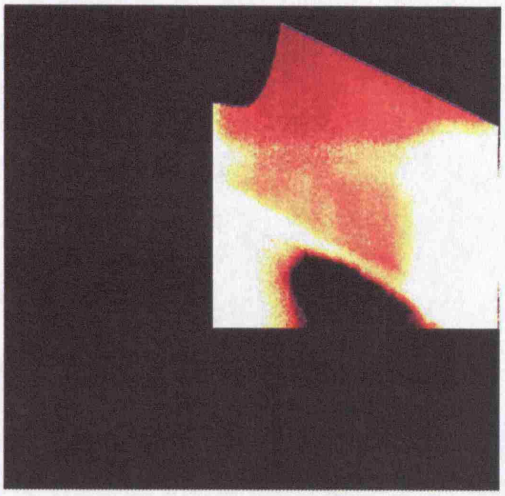

LIF test III, TFA 1 (Del 09)

Ambient air, slotted, TFA 1 (Del 08)

Ambient air, none, TFA 1 (Del 08)

Figure 8-36 Grouped results LIF, Mie, Ambient Air, for SOI 675 CAD, TFA (B)

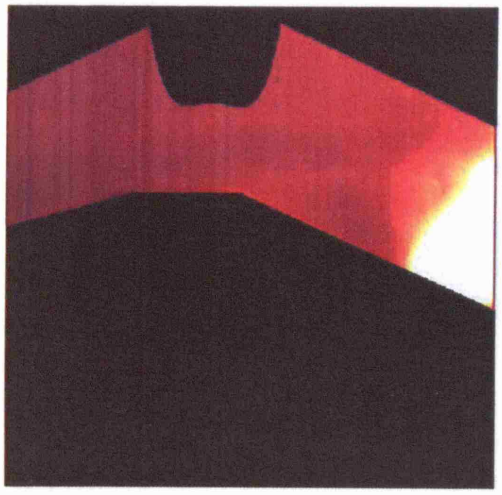

LIF test I, TFA 2 (Del 10)

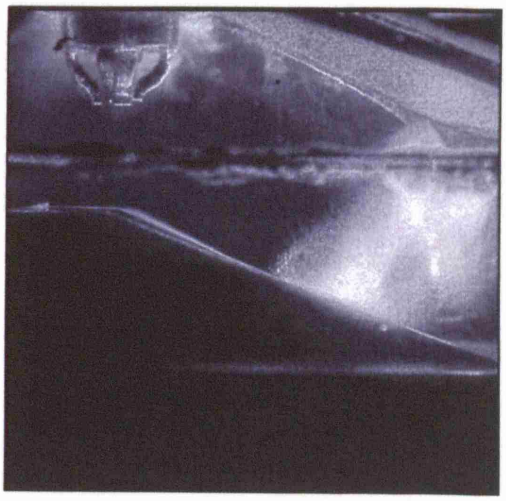

Mie, TFA 3 (Del 08)

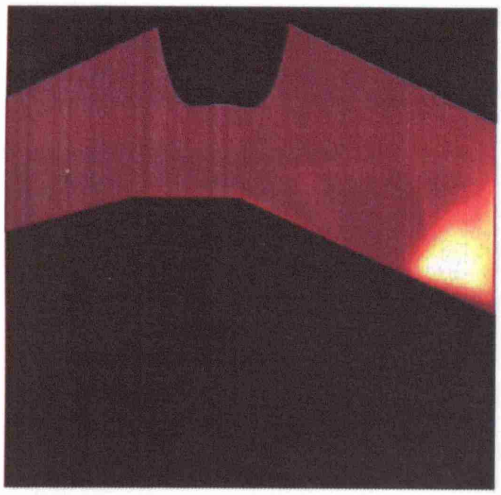

LIF test V, TFA 2 (Del 10)

LIF test III, TFA 2 (Del 10)

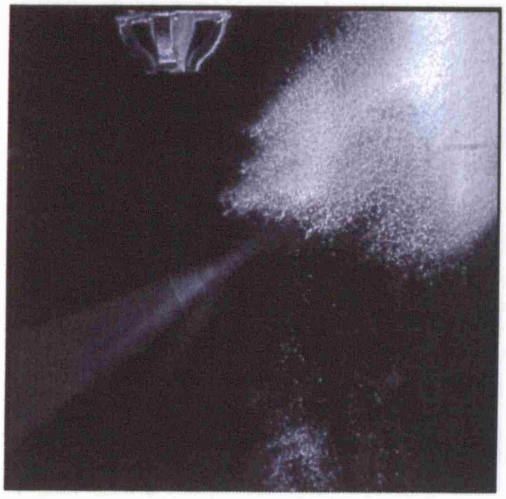

Ambient air, slotted, TFA 2 (Del 09)

Ambient air, none, TFA 2 (Del 09)

Figure 8-37 Grouped results LIF, Mie, Ambient Air, for SOI 675 CAD, TFA (C)

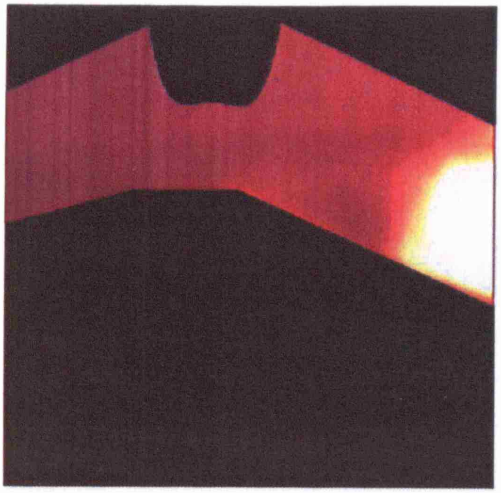

LIF test I, TFA 3 (Del 11)

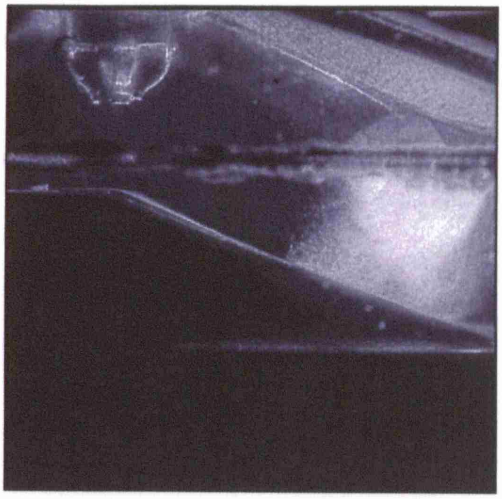

Mie, TFA 4 (Del 09)

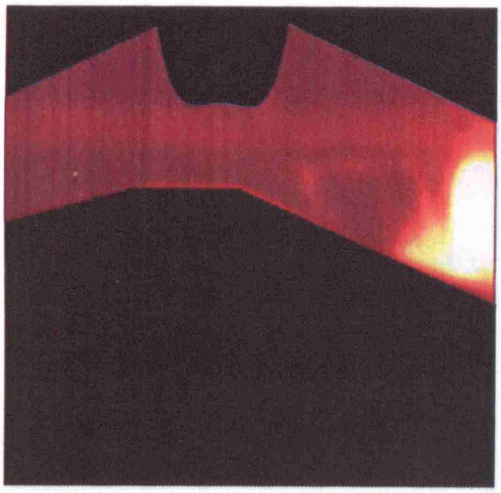

LIF test V, TFA 3 (Del 11)

LIF test III, TFA 3 (Del 11)

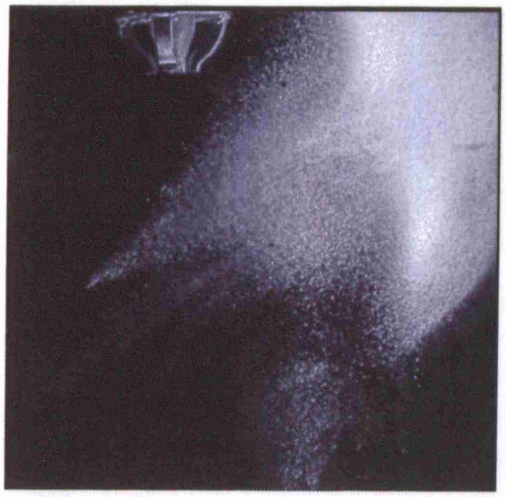

Ambient air, slotted, TFA 4 (Del 11)

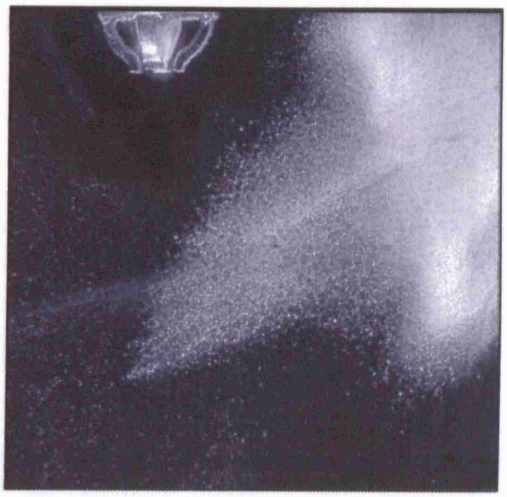

Ambient air, none, TFA 4 (Del 11)

Figure 8-38 Grouped results LIF, Mie, Ambient Air, for SOI 675 CAD, TFA (D)

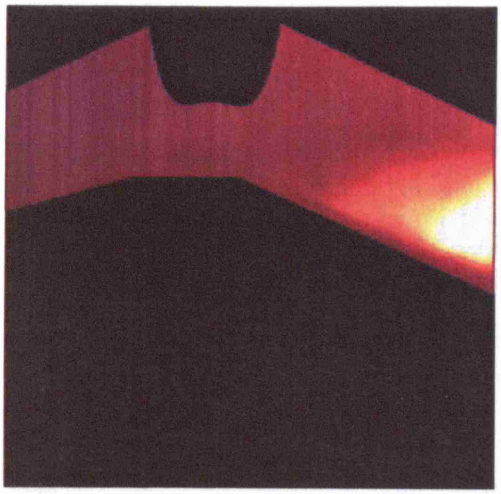

LIF test I, TFA 7 (Del 15)

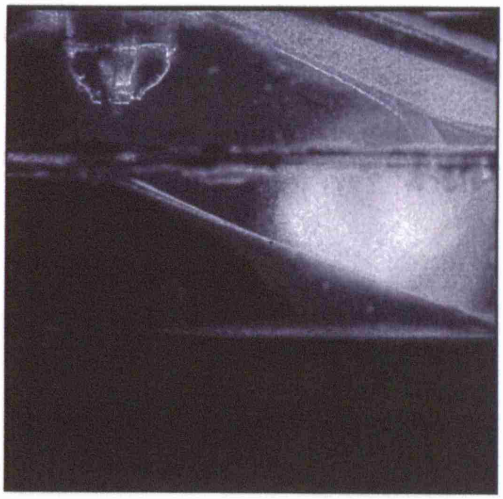

Mie, TFA 6 (Del 11)

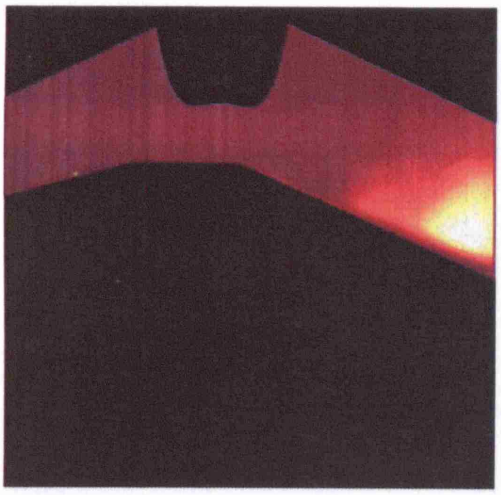

LIF test V, TFA 7 (Del 15)

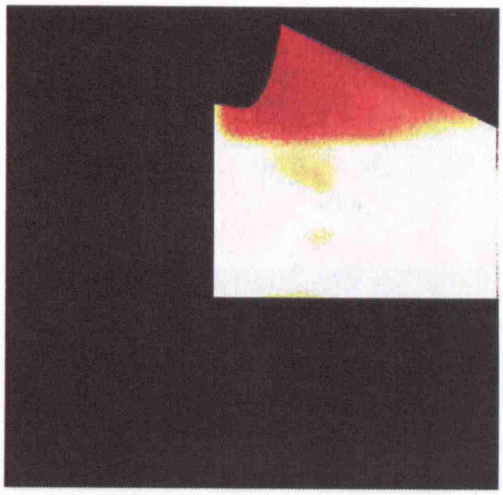

LIF test III, TFA 7 (Del 15)

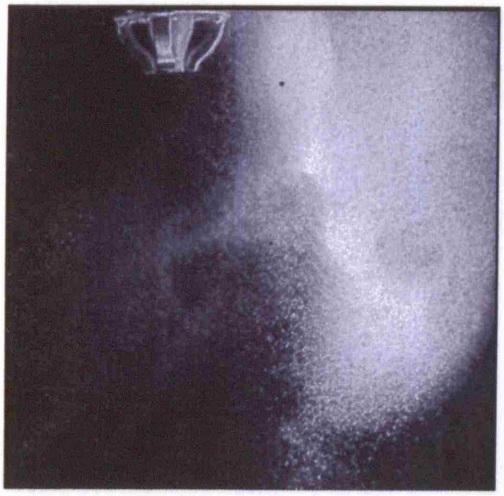

Ambient air, slotted, TFA 8 (Del 15)

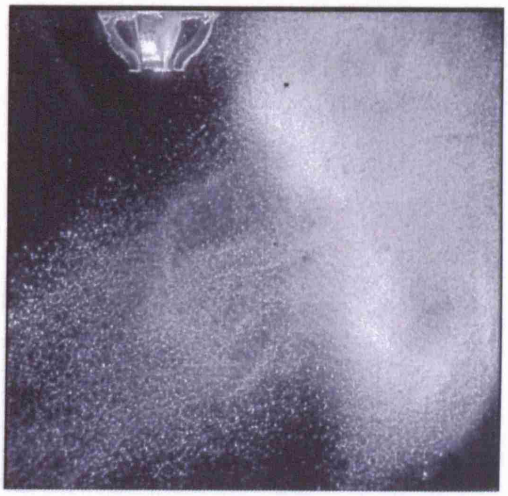

Ambient air, none, TFA 8 (Del 15)

Figure 8-39 Grouped results LIF, Mie, Ambient Air, for SOI 675 CAD, TFA (E)

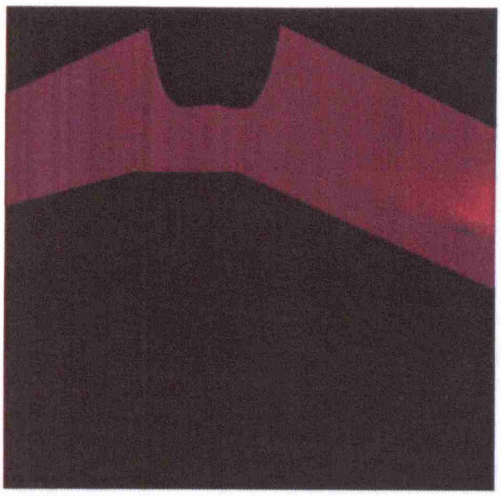

LIF test I, TFA 12 (Del 20)

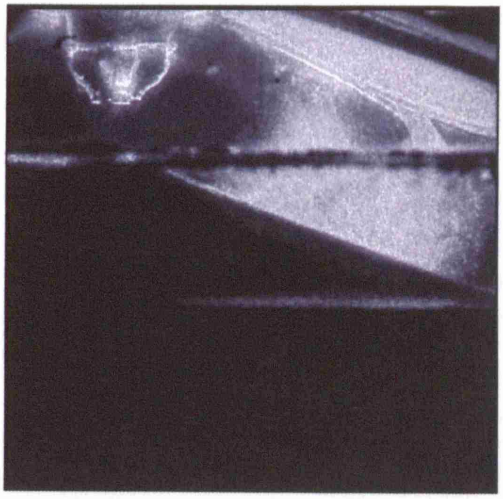

Mie, TFA 10 (Del 15)

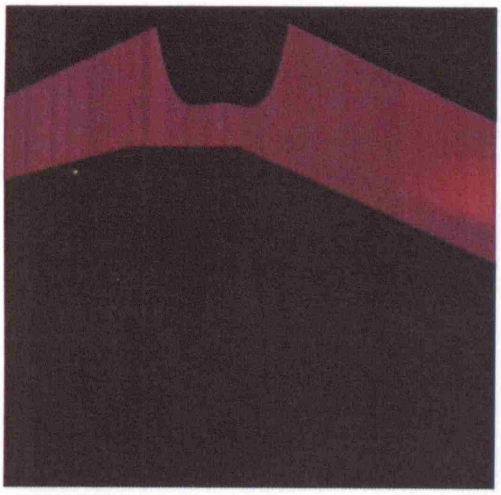

LIF test V, TFA 12 (Del 20)

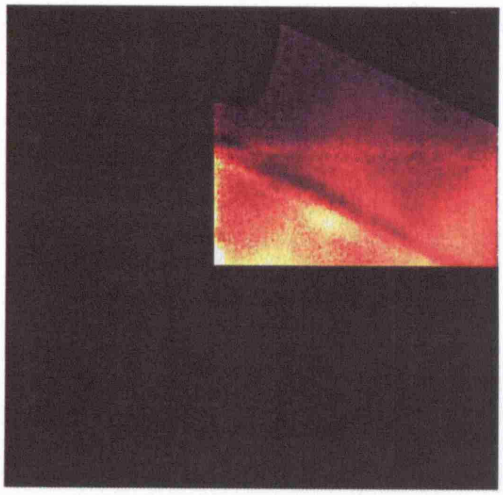

LIF test III, TFA 12 (Del 20)

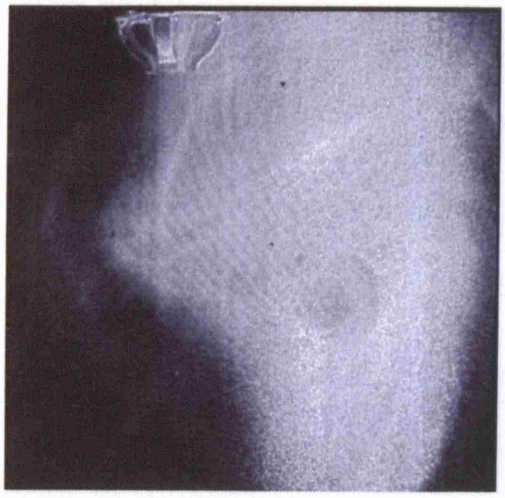

Ambient air, slotted, TFA 13 (Del 20)

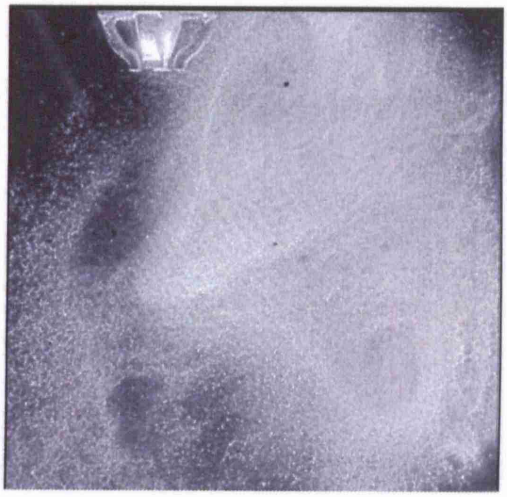

Ambient air, none, TFA 13 (Del 20)

Figure 8-40 Grouped results LIF, Mie, Ambient Air, for SOI 675 CAD, TFA (F)

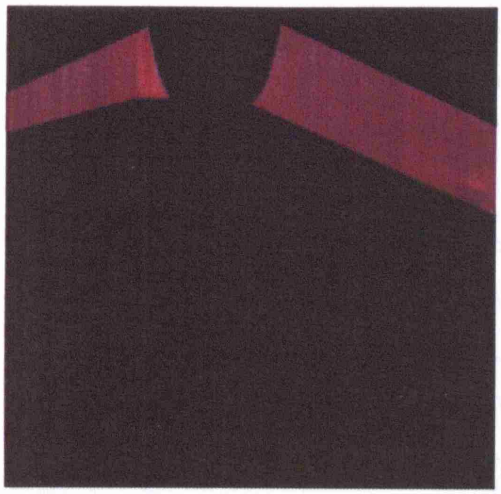

LIF test I, TFA 17 (Del 25)

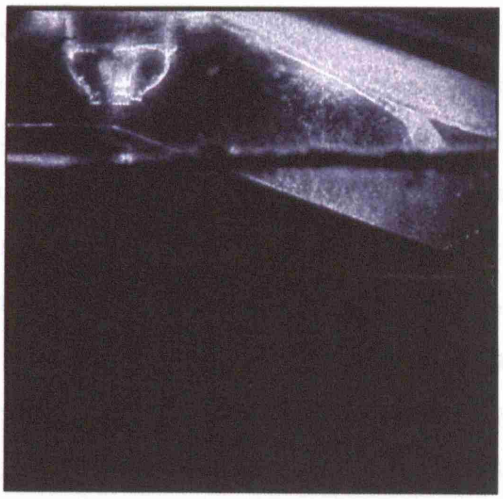

Mie, TFA 15 (Del 20)

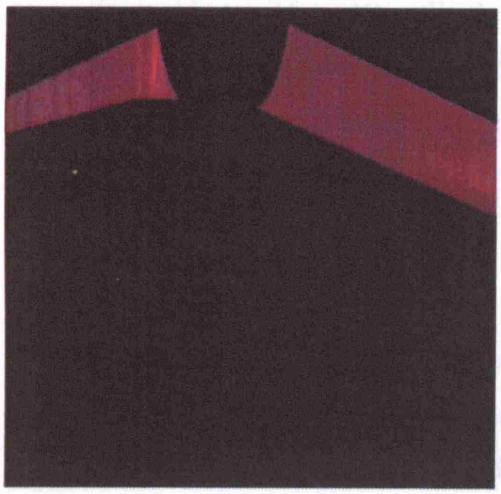

LIF test V, TFA 17 (Del 25)

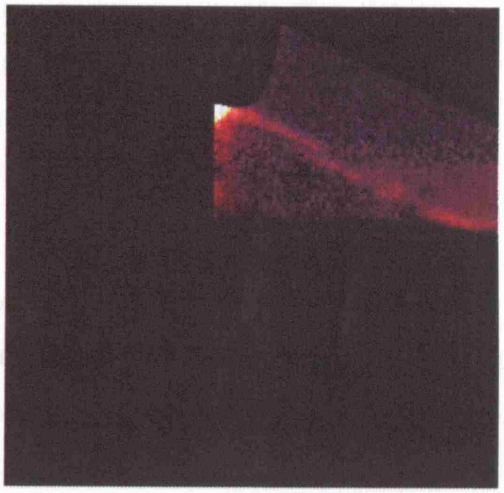

LIF test III, TFA 17 (Del 25)

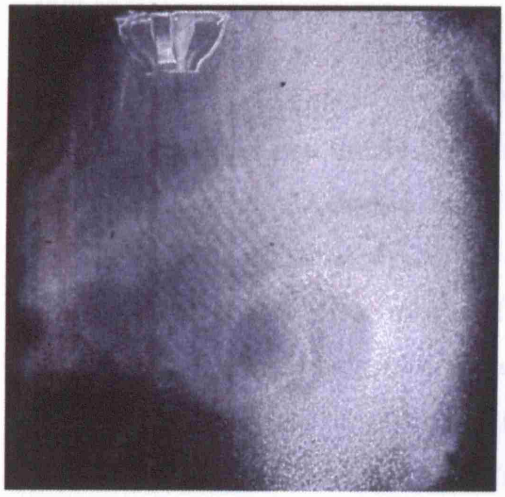

Ambient air, slotted, TFA 18 (Del 25)

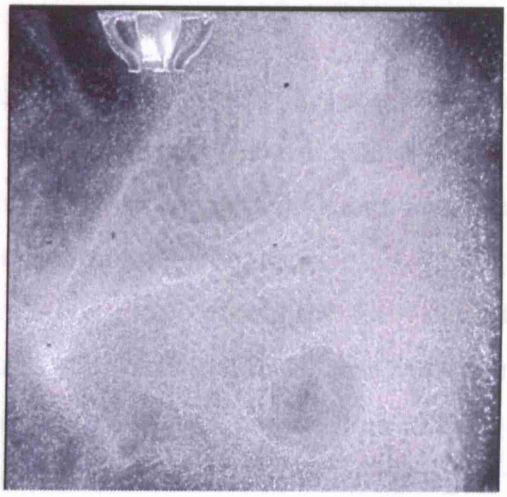

Ambient air, none, TFA 18 (Del 25)

Figure 8-41 Grouped results LIF, Mie, Ambient Air, for SOI 675 CAD, TFA (G)

This was most likely due to inconsistency in the engine re-build between the Mie and LIF experiments. The teeth on the timing belt were quite coarse and so there could be approximately ± 2 CAD difference in position of the camshafts (and hence shaft encoder) relative to the crankshaft dependent on relative tooth position. To aid visual comparison, it was decided to choose the best Mie and ambient air images at each test-point to agree with the spray development seen in the LIF images and to use the term TFA (time from appearance of fuel). The images in Figure 8-21 (the first SOI 639 set) were chosen because the fuel was just emerging, so each image has TFA 0 and this set is labelled TFA (A). Figure 8-28 is labelled TFA (G) and the images range from TFA 15 to TFA 18. With the adjustment made for the timing discrepancy, the form and development of the spray in the LIF and Mie images is similar. The next section describes some analysis that was performed on the images to obtain a better understanding of results.

8.5 Intensity analysis

Visual inspection of images may be misleading, so a more scientific approach, based on the average intensity of each image, was used. Such an analysis could reveal, for example, how the plume of spray developed as the piston ascended. It was kept in mind that the images are a two-dimensional representation of a three-dimensional event.

8.5.1 Theory

For Mie scattering, the sum of the pixel intensities of the image is a function of droplet diameter and the number of those droplets. If the droplet diameter is uniform in a sample, variations of intensity at different locations must be due to droplet concentration, ie fuel concentration. Alexander et al. [2005] argued that droplet diameter changed relatively little during the short period under consideration, so that there was little variation in intensity due to diameter. Any significant intensity changes observed were due to variations of fuel concentration. In their case, fuel was 'squeezed' by the incoming air flow, causing an increase in light intensity.

For the current study, an intensity 'score', ie the mean value of the intensity in an image, could be plotted against delta to observe the way that the spray

developed. This 'score' was found using Mathwork's Matlab software by summing the intensity of all the pixels and dividing by $(512)^2$, ie the total number of pixels. This approach was valid as long as there was no saturation and measures had been taken to avoid this. One complication in the analysis was the moving piston. The piston was a changeable feature, not present in the early images of the SOI 639 CAD set, but obscuring significant parts of the area of interest for later images in the SOI 675 CAD set. To account for this, a mask was made to match the shape of the piston in each image. This matrix contained zeros for the piston and ones elsewhere. Multiplying the matrix for the image by this mask matrix converted any pixels representing the outline of the piston to zeroes. The divisor used to calculate the intensity mean value was adjusted by counting the number of zero pixels required to form the mask matrix and subtracting this from $(512)^2$.

8.5.2 Analysis of mean intensities for Mie scattered images

An analysis as described in §8.5.1 was carried out using Mie scattered images from the firing engine, with SOI 639, 654 and 675 CAD. There were large fluctuations in the values for SOI 675 CAD, which may be due to the small area of interest caused by the high piston position resulting from the very late start of injection. Although a line of best fit for these points had similar trends to the SOI 639 and SOI 654 CAD graphs, this trace will be ignored in this discussion. The graphs in Figure 8-42 shows mean intensity versus delta using Mie scattering in the firing engine for SOI 639 and 654 CAD. The traces for SOI 639 and SOI 654 CAD are similar, with intensity increasing to a maximum value, then reducing, and finally some recovery to the earlier values. These two traces also have a distinctive 'kink'. Probable reasons for the shape of the characteristics are discussed in the following sections.

8.5.3 Discussion of maxima

There are four possible explanations for the traces reducing after reaching a peak value: firstly due to evaporation, secondly due to dispersion of liquid fuel, thirdly due to fuel entering the hidden regions of the bowl and fourthly due to spray entering a dark region which lacks illumination. More and more fuel enters the AOI as the injection continues and thus more and more pixels have positive values. At the end of injection, no more fuel can enter the area

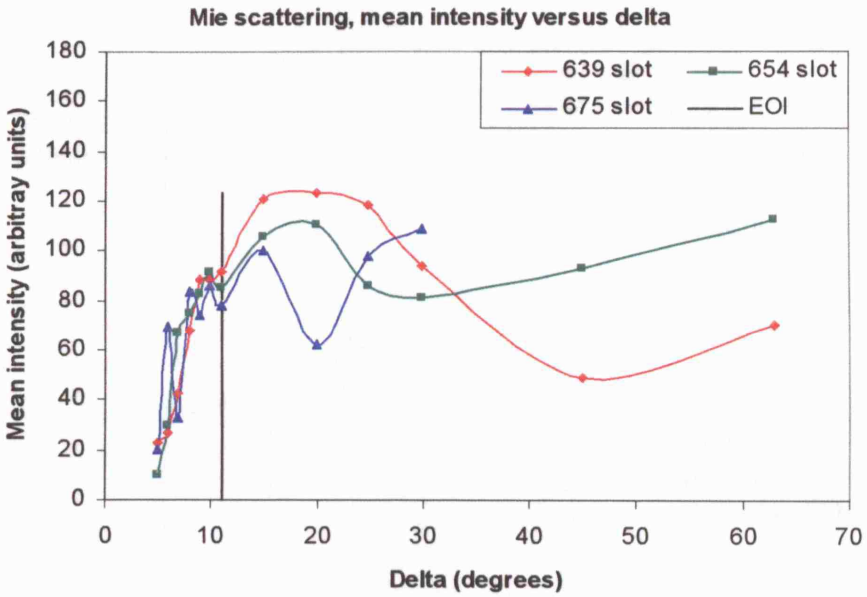

Figure 8-42 Mean intensity of Mie images plotted against time after SOI

of interest and the fuel already there has begun to move out of it, suggesting that the peak will occur at EOI. Lines indicating the EOI on the graphs do not support this, until it is remembered that there is a 'time of flight' delay until the last of the fuel reaches the AOI (Figure 8-43). When this is accounted for, the reduction of mean intensity after the end of injection does seem justified.

At larger delta values, more time has elapsed since the SOI, allowing more fuel to evaporate and since Mie scattered light comes from liquid fuel only, intensity falls at these larger delta values due to this evaporation. Furthermore, the increase of temperature of the charge with increasing pressure as the piston approaches TDC adds to this effect. The second reason for the fall in intensity is dispersion of the liquid fuel. The enclosed combustion chamber means that the fuel is trapped although dispersal from the AOI and the plane of illumination must occur thereby reducing the mean intensity – some of the fuel may enter the hidden regions of the bowl. In addition, the dark region caused by internal reflections in the slotted quartz crown insert will also be a factor. The dark region is on the opposite side of the image from the injector so the fuel is more likely to be in

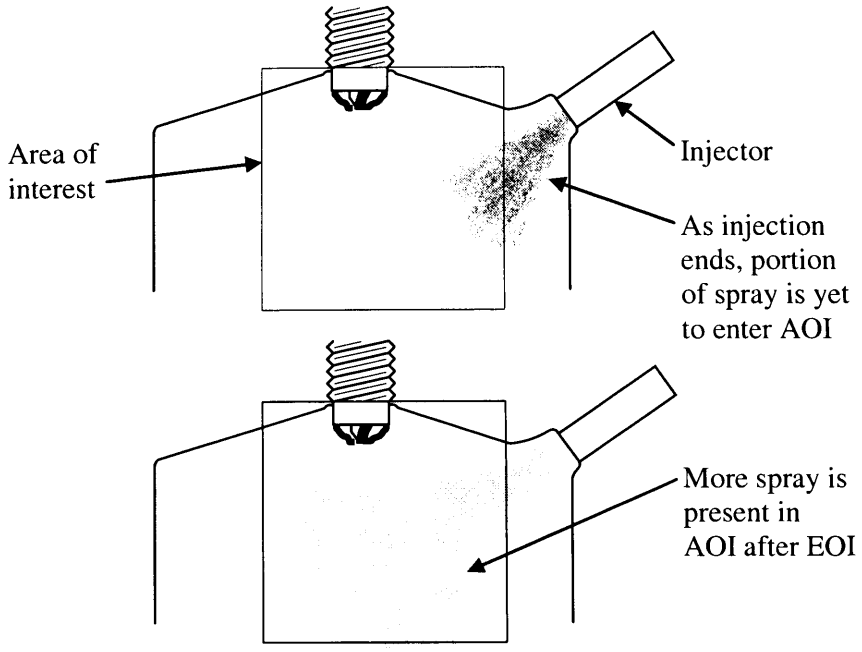

Figure 8-43 Proposed mechanism for mean intensity to rise after EOI

this region at larger delta values. It was thought that comparison with a similar analysis of the ambient air injection images would give some indication of the relative magnitudes of these effects and this is covered in a later section. For the ambient set, there was no enclosing effect from a combustion chamber and one set of images was taken with the piston crown removed.

8.5.4 Discussion of kink

The kink in the traces around delta 9 and delta 10 corresponds to the pre-spray entering the piston bowl. The pre-spray consists of densely packed droplets that are mainly on the combustion chamber centreline and hence directly in the plane of the laser light sheet. Thus, when the pre-spray disappears into the piston bowl, intensity tails off. The pre-spray is moving much faster than the main body of the spray and so will give rise to a distinct event. Meanwhile, more and more main spray has entered the AOI so intensity rises again. It is interesting to note that these characteristics suggest that the pre-spray is 5 – 10% of the main spray whereas the injector manufacturers claim 1%. However, care must be taken in extracting quantitative data from this observation as the pre-spray was likely to have considerably larger droplets than the main spray.

8.5.5 Discussion of recovery after maximum

It can be seen that there is a recovery in the values of intensities which occurs after delta 45 for SOI 639 CAD and after delta 30 for SOI 654 CAD. The recovery may be due to spray re-emerging from the piston bowl. It is not obvious to identify this from studying the sequence of images, so there must be some doubt attached to this explanation. It is not surprising that the recovery happens later with SOI 639 CAD since the spray has to travel further before it enters the bowl.

8.5.6 Analysis of mean intensities for the ambient air images

Figure 8-44 contains the results from analysing the ambient air images in a similar manner to the Mie scattering engine images. For these images, the cylinder head was raised, the injector and spark plug were clamped in place, and the fuel injected was fired into the space which would have been the combustion chamber. The first set used the slotted quartz piston crown and, for the second set, no crown was used. The images were taken through the main quartz window, which was held in the same position as it would have occupied in the engine. The mean values were found by dividing the sum of the individual pixel intensities by $(512)^2$. Both traces can be seen in Figure 8-44 Mean intensity of ambient air images plotted against time after SOI) rising to a maximum value at around delta 20 CAD before tailing off.

The mean intensities for the set with no quartz are higher than those for the set with the slotted quartz insert. This is expected since there is no obstruction to the laser light with the crown absent. Neither trace has a 'kink' in the portion of the graph with a positive gradient and nor would this be expected in the absence of the piston bowl. Maxima occur in both traces corresponding to the end of injection, with the time of flight to reach the AOI factored in. The traces tail off after the maximum due to injection finishing, combined with evaporation and dispersion taking place. Comparison with the engine characteristics of Figure 8-42 shows that the ambient air characteristics fall off less rapidly after the maxima, but show no sign of a subsequent recovery.

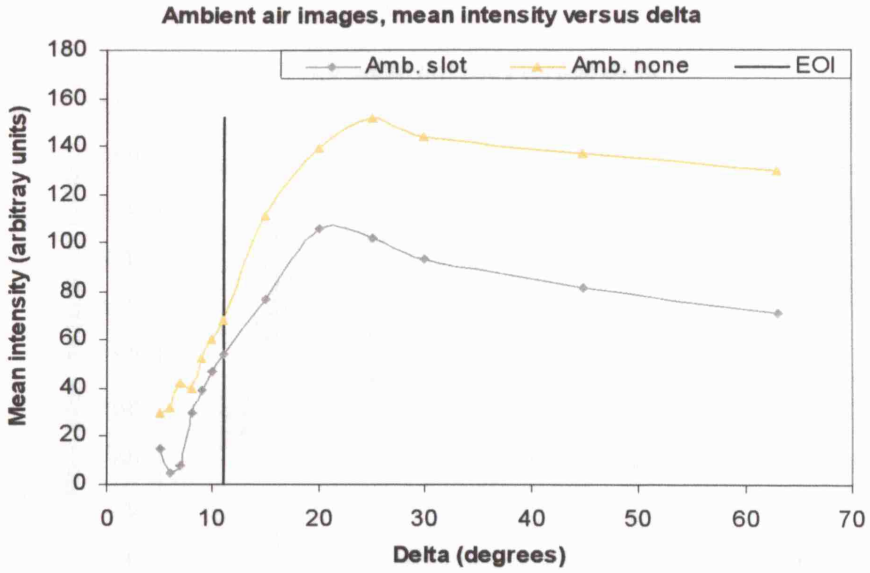

Figure 8-44 Mean intensity of ambient air images plotted against time after SOI

This is consistent with the explanation of some of the main spray disappearing into the bowl and then reappearing, for the engine tests.

8.5.7 Analysis of mean intensities for LIF images

For the LIF images, consideration needed to be given to the location of the spray compared to the laser sheet. For Mie scattering, light could bounce around between droplets, illuminating the entire cone of fuel. For the LIF images, the light did not bounce and in fact quenching effects were likely to occur, thus reducing intensity (see Figure 7–17).

The results of analysing the LIF images are shown in Figure 8-45. The poor quality of images from tests II, IV, V and VI made them unsuitable for analysis. Instead, test I and test III are presented here since the conditions for these tests were closest to those for the Mie series. Images for tests I and III were taken in the firing engine with the engine jacket at 40^0C, using the slotted crown (test I) and disc crown (test III). For the SOI 675 CAD images, the small area of interest caused by the high piston position again made them unreliable and they are not included here. As with the Mie analysis, the piston was masked out and compensation made in the denominator when calculating the mean value. The LIF intensity traces resemble the Mie traces, in terms of

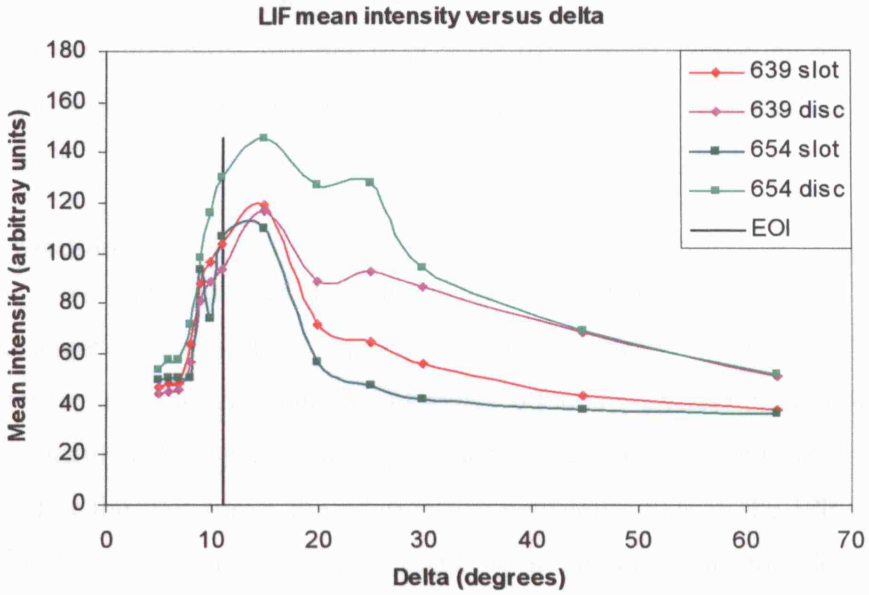

Figure 8-45 Mean intensity of LIF images plotted against time after SOI

peak, kink, and tailing off. Both disc traces have higher intensity values in general than those for the slotted crown. It is surprising that the SOI 654 CAD trace has the greater intensity, since the lower piston position for the SOI 639 CAD set should mean more fuel is introduced before the piston begins reducing the AOI.

The causes of the peak and kink are probably similar to that given for the Mie analysis. There is no evidence of the longer term recovery apparent in Figure 8-42 at the higher deltas. This would be expected in the case of the disc characteristics since most of the hidden area is visible as the side of the bowl was machined away. However, it would not be expected of the characteristics recorded with the slotted piston. One explanation is that since the piston bowl has a three-dimensional geometry, interactions between the spray and the bowl surface would tend to direct the fuel away from the plane of illumination.

8.6 Velocity analysis

An analysis of the piston, fuel and air velocities in the engine would suggest the degree of coupling between them and this would help determine how well the engine was set up to operate in stratified charge mode. CFD routines

carried out by Jaguar Cars Limited provided predictions of the velocity vectors for the air flow while piston velocity was found by calculation. The Mie scattering pictures were analysed to give the true distance travelled by the fuel spray in consecutive images so that the velocity of the fuel could be calculated.

8.6.1 Method

Well-known equations were used to calculate the piston displacement at each crank angle position, knowing the engine geometry, namely its stroke, connecting rod length and crankshaft offset. Differentiation of the displacement with respect to time provided the piston velocity throughout the cycle. For the fuel spray, the relationship between pixels in the IPP pictures and true distance (in metres) in the combustion chamber was complex, due to the lens effect of the quartz window (see appendix D for a detailed discussion of these matters). The results of the fuel velocity analysis, after applying conversion factors to account for optical distortion, are presented. Researchers at Jaguar used a CFD package based on code developed by Ford Motor Company, the details of which were confidential, to predict air flow velocities and directions. The results were obtained from a Microsoft Powerpoint presentation forwarded to the author [Chen, 2005].

8.6.2 Discussion of piston velocity results

The velocity of the piston versus position in the cycle in CAD is shown in Figure 8-46. Maxima occurred near mid-stroke and the maximum value was ± 6.3 ms^{-1}. The calculation was performed for the engine test speed of 1500 rev/min and so the values need to be halved when compared with the CFD predictions which were for 750 rev/min, idle.

8.6.3 Discussion of fuel velocity results

The velocities of the fuel spray elements are plotted versus CAD in Figure 8-47 and Figure 8-48 . 'Pre-spray' refers to the agglomerated collection of droplets which was first to emerge after the injector pintle opened. 'Main spray' refers to the most advanced part of the bulk of the spray, having ignored the pre-spray. If the velocity was calculated using a delta 5 CAD image and a delta 6 CAD image, this was referred to as delta 5.5. Similarly

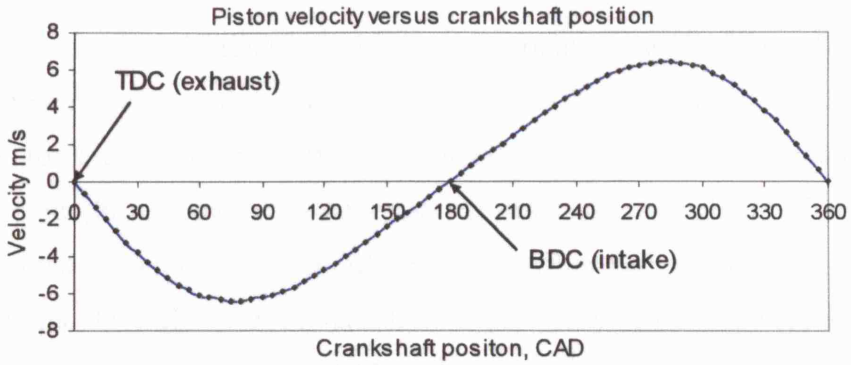

Figure 8-46 Calculated velocity of piston for one crankshaft revolution (1500 rev/min)

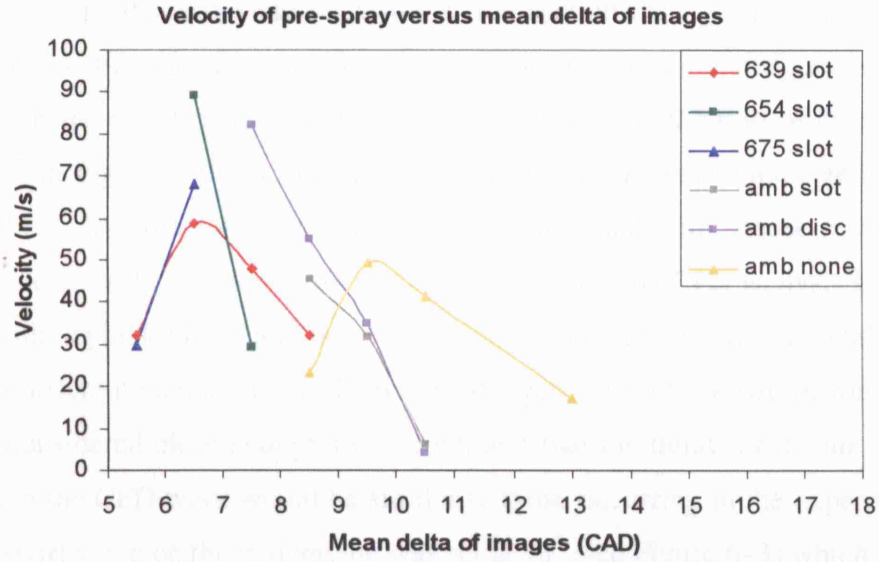

Figure 8-47 Velocity of pre-spray, Mie and ambient air images

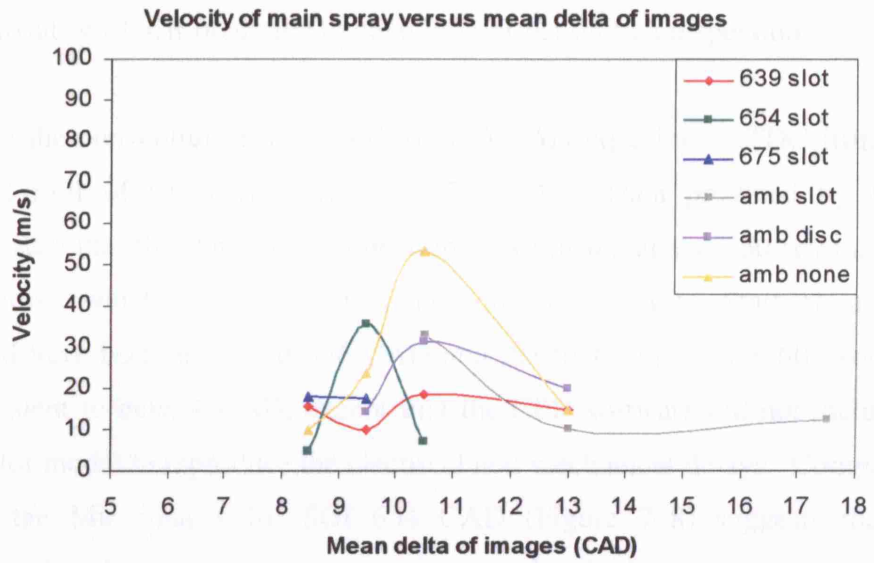

Figure 8-48 Velocity of main spray, Mie and ambient air images

delta 11 and delta 15 images yielded the datapoint delta 13. Hence SOI added to the delta value at the datapoint (both in CAD) showed the absolute CAD value for the mid-point of the interval used to calculate the velocity. The scatter in the results is to be expected since the calculations have been performed using images from different cycles, thus being influenced by cyclic variations. Overall it can be said that the pre-spray velocities were around 50 ms^{-1} and the main spray around 17 ms^{-1}.

8.6.4 Discussion of air velocity results

The CFD predictions were made for a true section through the centreline of the combustion chamber and no optical distortion was simulated. A sequence of predicted results beginning at five crank angles after the start of injection is shown in Figure 8-49. In these images, red dots were used to indicate the fuel droplets. Vectors for air motion were colour-coded with values in cm/s to indicate velocity, and the arrow to show direction. The CFD analysis featured the same cylinder head and injector as used in the current experimental work, but a different piston crown. However, the geometry of the two piston bowls was considered close enough to be confident that the trends of the air motion seen in the CFD work would be similar to those occurring in the experiments. The swirl valve on the real engine was set at 18^0 (see Figure 6–3) which would have induced minimal axial swirl. The computations were carried out for a swirl ratio of 0.83 which is also relatively low. It can be seen in Figure 8-50 that axial swirl was predicted to have little effect on fuel dispersion.

Using the convention in this work of 720 CAD equating to TDC firing, the stated EOI of 61^0 corresponds to 659 CAD. Data provided by Jaguar suggested that the duration of injection was 0.6 ms at the 750 rev/min, idle condition, which corresponds to approximately 3 CAD. Start of injection would have been at around 656 CAD and the first period, ca=660, would be equivalent to delta 4 CAD, except that the CFD software did not include an injector model to reproduce the electrical and mechanical delays. Comparison with the Mie images for SOI 654 CAD (Figure 7–8) suggests that the electrical and mechanical delays were around 4 CAD, meaning that delta 4 CAD (computation) was equivalent to delta 8 CAD (Mie images). The

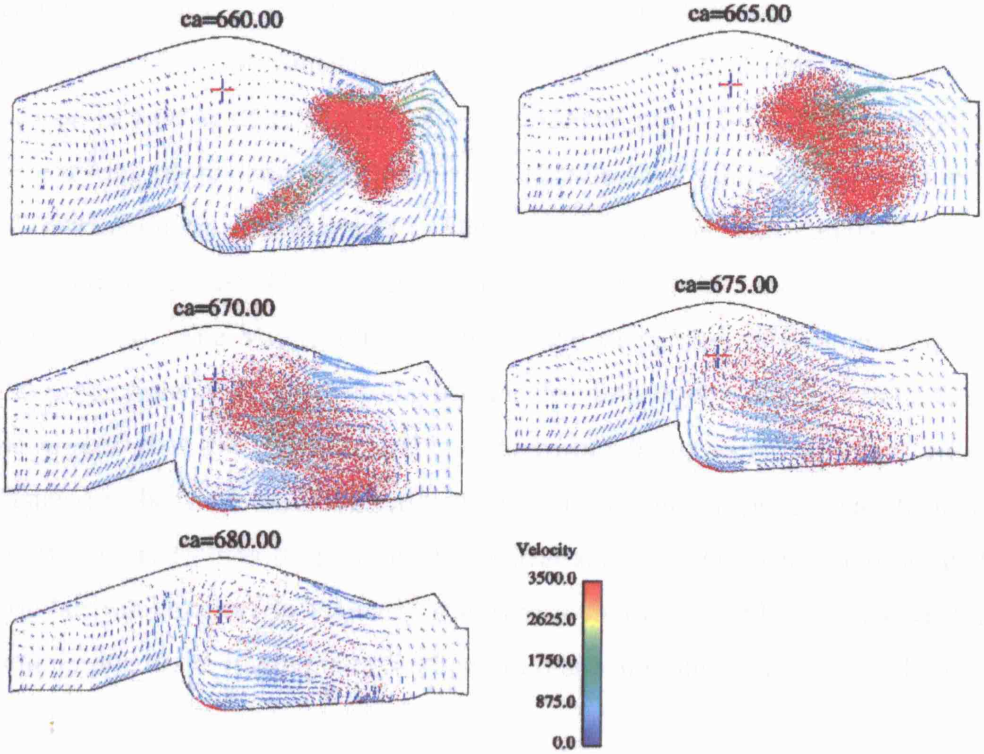

Figure 8-49 Elevations of fuel spray (red dots) and CFD predictions (arrows) of air flow (cm/sec) versus crank angle [Chen, 2005]

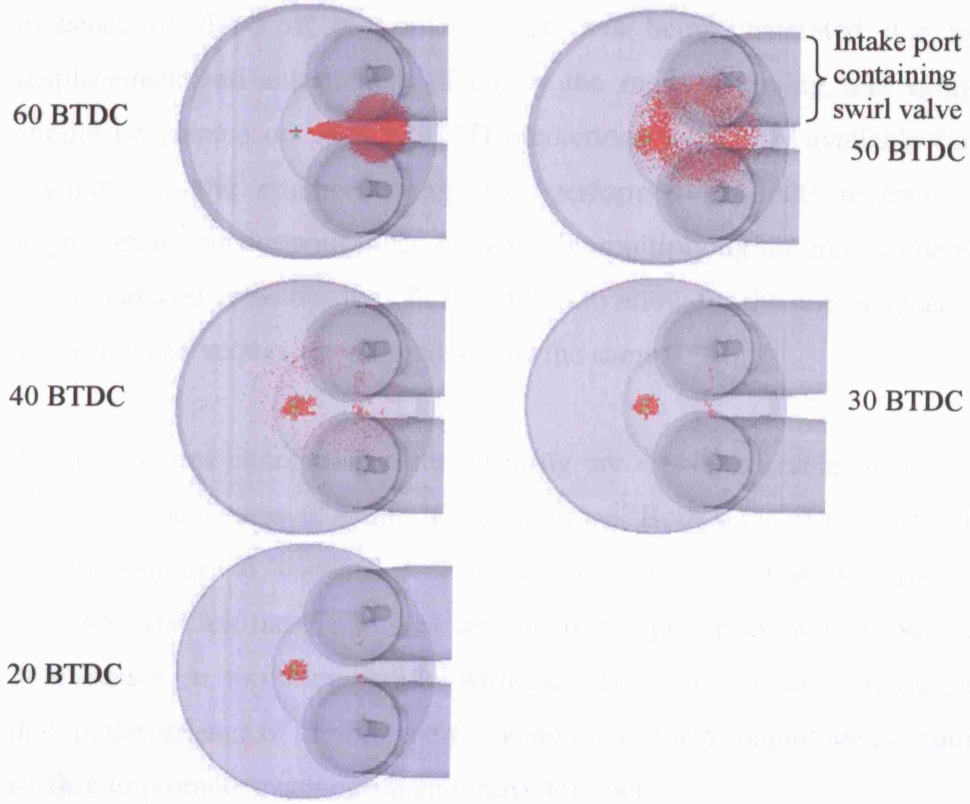

Figure 8-50 Plan view on fuel spray predictions versus CAD [Chen, 2005]

computation at ca=665 was, on the same basis, equivalent to delta 13 CAD (Mie images). Unfortunately there was no Mie result at delta 13 CAD, the nearest two being delta 11 and delta 15 CAD (Figure 7–8). Comparison of the Mie testing results and CFD predictions show encouraging similarity in terms of dispersion of fuel droplets. The last comparison that can be made is between delta 20 CAD (Mie results, Figure 7–8) and ca=670 (CFD predictions). The Mie results suggest greater dispersion of fuel droplets than the predictions, but no really significant discrepancies were apparent. It can be argued that the experimental results would be expected to show greater dispersion because light scattering would illuminate droplets away from the centreline as well as droplets in the central section. The general flow in the combustion chamber in the early stages was characterised by vertical vectors, mainly due to the rising piston with slight distortion due to the crown shape.

There is virtually no sign of any tumble motion being generated during the induction part of the cycle. In terms of magnitude of velocity vectors, it is evident that the most significant effect is due to the injection process. There is evidence of flows of the order of 20 m/s being generated due to the displacement and entrainment of air by the rapidly moving fuel spray. It should be pointed out that the CFD predictions were only available for 750 rev/min yet the engine testing was performed at 1500 rev/min. An approximate transformation can be made by multiplying the magnitude of the piston-induced velocities by a factor of two to allow for the higher speed. The spray induced vectors would tend to stay the same.

The predictions concerning piston wetting are of considerable interest since this would be a cause of high UHC emissions. Both sides of the piston bowl bottom were dry at 'ca=660', and the vectors were normal to the surface. By 'ca=665', the left hand side was wetted by the pre-spray and the vectors at both sides were becoming parallel with the surface. However, it was apparent that, in the absence of tumble, there was no flow of any magnitude to scour the surface to promote evaporation and move the fuel.

8.7 LIF images post-processed using a novel subtraction method

The relatively low levels of LIF emissions meant that background correction was a particularly critical process. The technique described so far of using the average of pre- and post-firing images to perform the background correction, may be termed "the conventional approach". It was decided to investigate an alternative approach to see if it could reveal any more detail about the vapour formed from the evaporating spray. The alternative technique was to use the preceding image to act as the background for the image under investigation. The gains compared to the pre- and post-firing approach were that the background was taken under firing conditions and within a relatively low number of cycles of the image under investigation. These gains were at the expense of having a slightly different pattern of diffracted light due to the difference in piston position and the loss of common areas where fuel was present. The background subtraction routine in IPP version 3.0 was applied and it was based on

$$CI_{x,y} = I_{x,y} - BI_{x,y} + M \qquad (8.1)$$

where

$I_{x,y}$ was a pixel value of the original image at location (x,y);

$BI_{x,y}$ was a pixel value of the background image at location (x,y);

M was the average pixel value of the background image;

$CI_{x,y}$ was the new pixel value in the corrected image [Media Cybernetics, 1994]

8.7.1 Method

For each test point, say SOI 639 delta 05 CAD, thirteen firing raw images had been recorded, each containing four exposures to the laser light. Without performing any other processing, Matlab was used to create one mean image from this sum total of 52 laser flashes. All the remaining processing was carried out in IPP, beginning with conversion of each mean image from 12-bit to 8-bit format. Next, the delta 05 CAD mean image was subtracted from the delta 06 CAD mean image and denoted 'delta 06-05'. Then IPP's pseudo-colouring algorithm was applied, whereby each of the 256 levels of greyscale

were assigned a colour, based on their intensity. Finally, the pseudo-coloured levels were adjusted: the lower level was raised until the background faded, then increased just enough for even the specks of noise to disappear. The upper level was set at 10 above the lower level and raised until no new colours were appearing. This bracketed the displayed levels around the spread of intensities. For images which were generally dark, the upper limit was left at the maximum value, ie 255. The number of divisions was set at 32 throughout to produce a smooth transition between the colours.

8.7.2 Results

No results were presented for the SOI 675 CAD set since they were too indistinct. Figure 8-51 to Figure 8-54 display results from LIF Test I in the firing engine (ie slotted crown, stratified charge, 40^0C engine jacket water), with SOI 639 CAD and SOI 654 CAD, using IPP subtraction and pseudo-colouring. The colours were assigned from blue to red, ie red colours represented the highest intensity light. The numbers on the colour bar can be compared to the full range available (0 to 255) to indicate how many levels had been removed. The greyscale images are included for distinguishing the light and dark areas, ie overlap region, whereas the pseudo-coloured give a better indication of intensity range within a bright region. The sparking plug and the pent roof are visible in most of the images and the outlines of two pistons can be seen, particularly when the difference between delta values is large. The other coloured areas, starting at or near the injector centreline, are assumed to be caused by fluorescing dopant.

8.7.3 Discussion

It should be noted that masking and light sheet correction (see § 8.4.8) were not attempted here. The fact that the plug and piston are visible (against expectations) may be due to wetting or reflections. The areas of high light intensity seen, were caused by the dopant interacting with the laser light sheet, fluorescing and the resulting light was not eliminated by the post-processing routine. A difference between the "subtraction" images and the

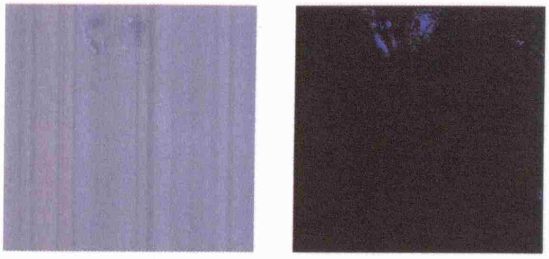

Delta 06-05 greyscale (left), pseudo-colour (4, 255)

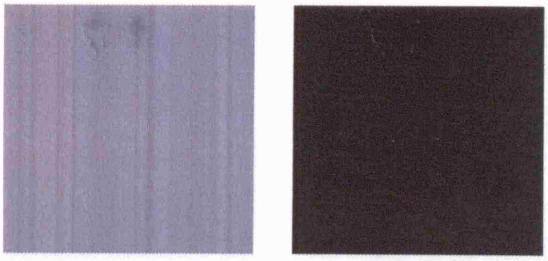

Delta 07-06 greyscale (left), pseudo-colour (4, 255)

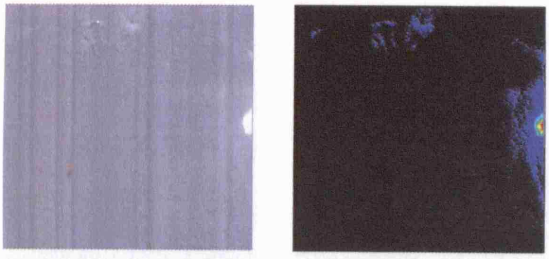

Delta 08-07 greyscale (left), pseudo-colour (8, 68)

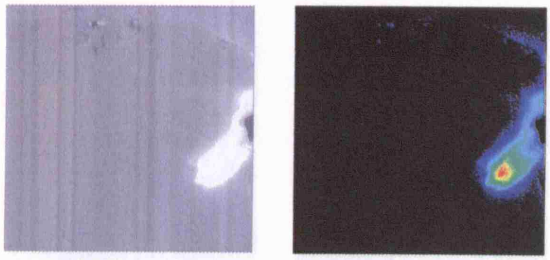

Delta 09-08 greyscale (left), pseudo-colour (7, 64)

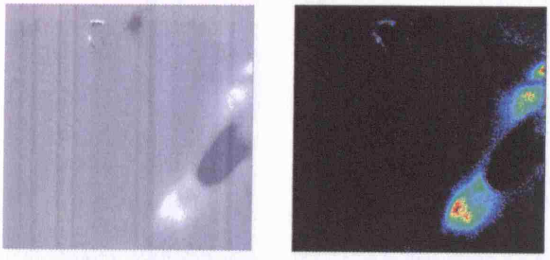

Delta 10-09 greyscale (left), pseudo-colour (8, 23)

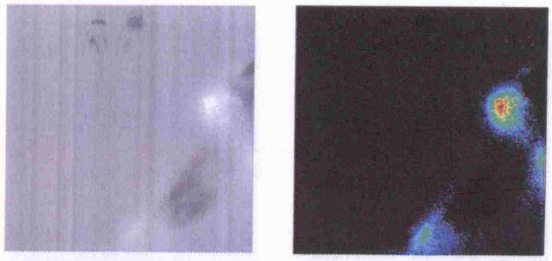

Delta 11-10 greyscale (left), pseudo-colour (8, 19)

NOTE:
Figures in brackets,
eg Del 06-05 (4, 255)

4= lower limit

255 = upper limit

Figure 8-51 LIF "Subtraction" images, SOI 639 delta 6-5 to 11-10 CAD

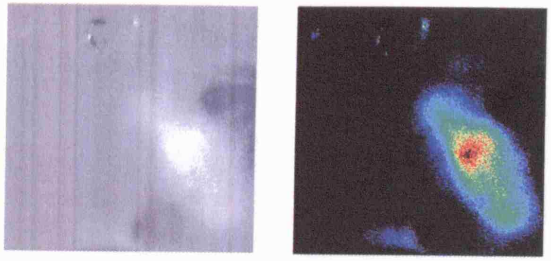

Delta 15-11 greyscale (left), pseudo-colour (8, 21)

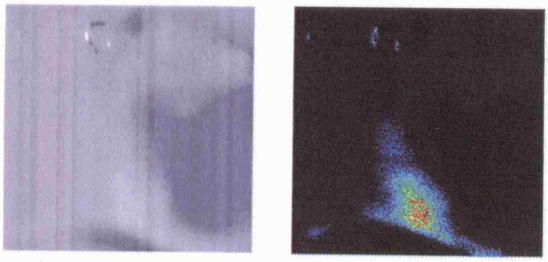

Delta 20-15 greyscale (left), pseudo-colour (8, 12)

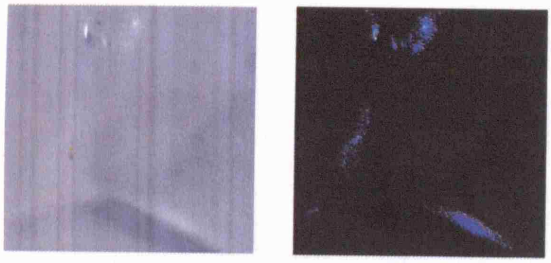

Delta 25-20 greyscale (left), pseudo-colour (6, 49)

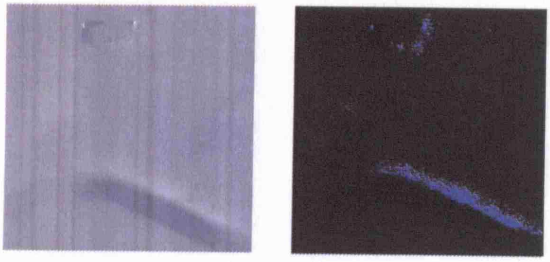

Delta 30-25 greyscale (left), pseudo-colour (5, 255)

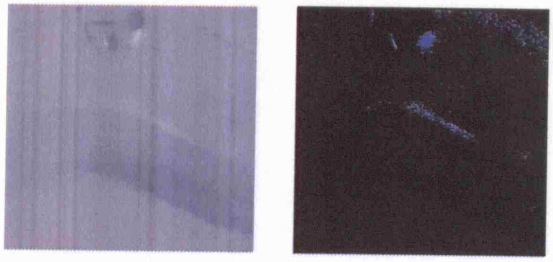

Delta 45-30 greyscale (left), pseudo-colour (4, 255)

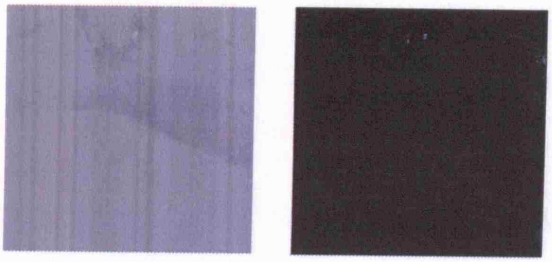

Delta 63-45 greyscale (left), pseudo-colour (4, 255)

NOTE:
Figures in brackets,
eg Del 15-11 (8,21)

8= lower limit

21 = upper limit

Figure 8-52 LIF "Subtraction" images, SOI 639 delta 15-11 to 63-45 CAD

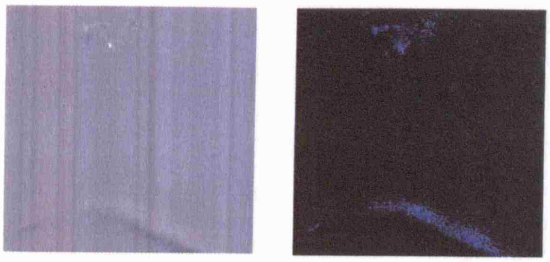

Delta 06-05 greyscale (left), pseudo-colour (4, 255)

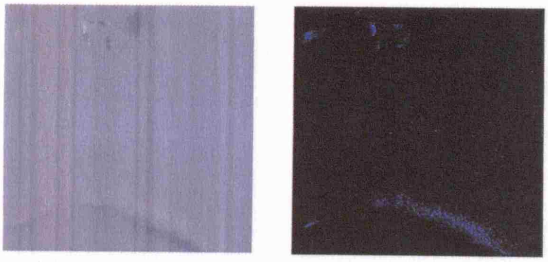

Delta 07-06 greyscale (left), pseudo-colour (4, 244)

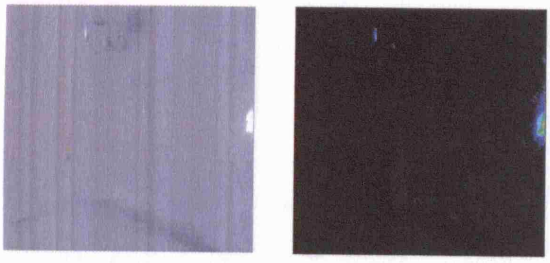

Delta 08-07 greyscale (left), pseudo-colour (5, 60)

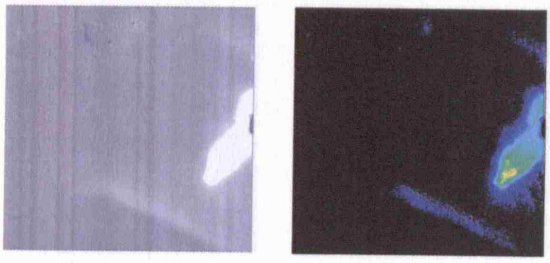

Delta 09-08 greyscale (left), pseudo-colour (7, 81)

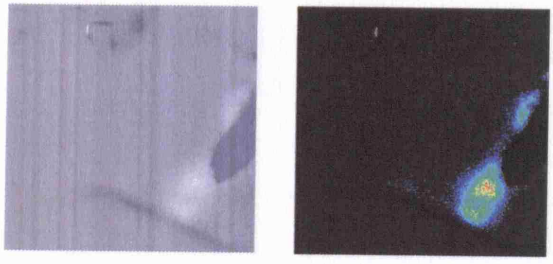

Delta 10-09 greyscale (left), pseudo-colour (6, 17)

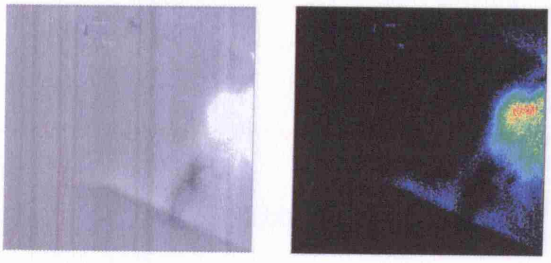

Delta 11-10 greyscale (left), pseudo-colour (8, 29)

NOTE:
Figures in brackets,
eg Del 06-05 (4,255)

4= lower limit

255 = upper limit

Figure 8-53 LIF "Subtraction" images, SOI 654 delta 6-5 to 11-10 CAD

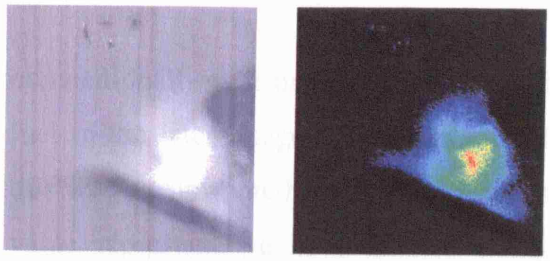

Delta 15-11 greyscale (left), pseudo-colour (8, 30)

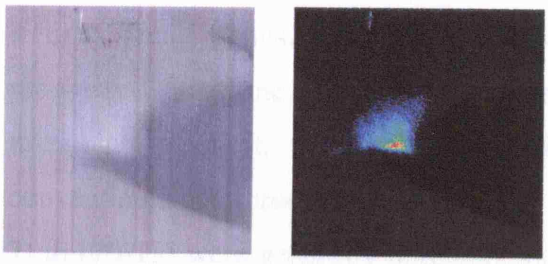

Delta 20-15 greyscale (left), pseudo-colour (7, 13)

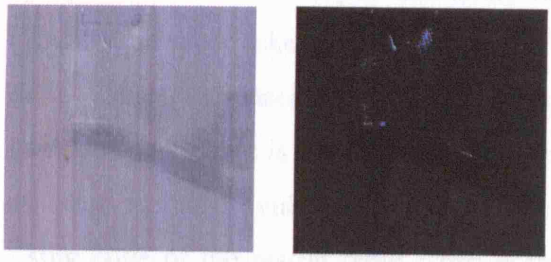

Delta 25-20 greyscale (left), pseudo-colour (5, 14)

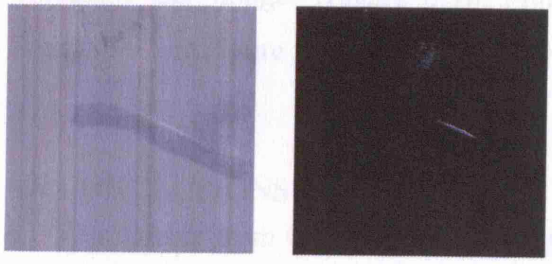

Delta 30-25 greyscale (left), pseudo-colour (4, 255)

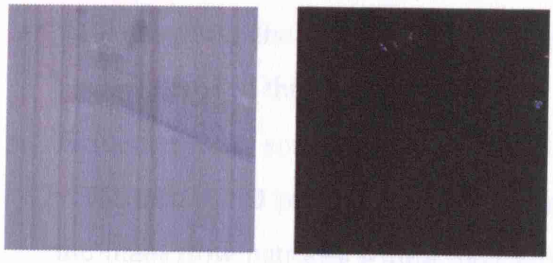

Delta 45-30 greyscale (left), pseudo-colour (4, 255)

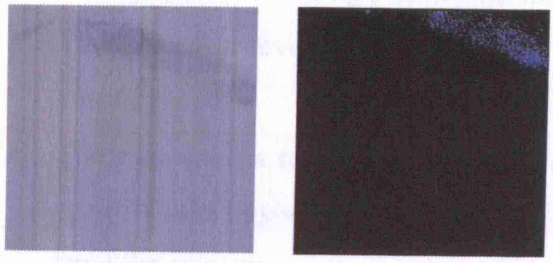

Delta 63-45 greyscale (left), pseudo-colour (3, 255)

NOTE:
Figures in brackets,
eg Del 15-11 (8,30)

8= lower limit

30 = upper limit

Figure 8-54 LIF "Subtraction" images, SOI 654 delta 15-11 to 63-45 CAD

conventionally post-processed previous ones was that when the position of the fuel in the later image overlapped with fuel in the earlier one, IPP assumed this was an unwanted bright spot. Pixels in the overlap region were set to a value representative of a normal background reading. However, if fuel progressed into a new area compared to the previous image, this showed up as a light area. Thus, this revised approach showed how the spray had progressed during the interval between the two frames. Once this difference is taken into account, the results were similar to those obtained from the conventional post-processing method (see § 8.4.12). For both sets, images (8-7) to (20-15) were generally unremarkable: the pre-spray was seen, the main spray followed it, developed and some fuel emerged from the bowl. Images (25-20) and those taken later showed no evidence of fuel. As the difference in delta values increased, it was less justified to use the earlier image as a background. There is a hint of extra information in SOI 654 delta 20-15 CAD as there is more evidence of fuel in the poorly illuminated area above the rising edge of the piston bowl when compared with the conventionally post-processed LIF images (Figure 8-10, Figure 8-11, Figure 8-12, Figure 8-26, Figure 8-33 or Figure 8-40).

8.8 CONCLUSIONS

- The images from the LIF study were generally of poor quality due to low light levels. It was speculated that a particularly 'dark region' existed in the area above the near-vertical part of the quartz slice and a line intensity analysis proved this.
- Evidence was sought for coupling between the piston, fuel and air velocities. CFD predictions performed by Jaguar Cars Ltd. suggested that the main flow patterns within the cylinder before the injection event were mainly due to the rising piston with no indication of significant tumble.
- The injection event stirred up the flow by the fuel displacing and entraining air.
- The engine tests results appeared to validate the CFD predictions that the spray would linger in the region near the spark plug and somewhat away from the injector.

- The CFD results suggested that the main spray was arrested by the drag on the small droplets moving against a modest vertical air flow caused by the rising piston. These predictions increased confidence that the images recorded on the engine had not missed significant fuel activity in the region above the rising piston lip because of poor illumination.
- An analysis of mean intensities of the images showed that all traces had a peak as intensity rose due to the developing plume, then fell away due to evaporation, dispersal and fuel entering a dark region.
- A 'kink' was apparent in the traces when pre-spray entered the piston bowl. The fall in intensity was of the order of 5 – 10% indicating that the volume of pre-spray was not insignificant. It should be noted that the fall in intensity cannot be linked directly to the quantity of fuel since droplet diameter also determines intensity of scattered light. The pre-spray is believed to consist of relatively large droplets.
- The recovery in average intensity visible at the larger delays for the Mie scattering engine firing tests was thought to be due to fuel re-emerging out of the bowl. The fact that it was evident in the Mie scattering tests led to the conclusion that it was still in liquid form.
- A novel post-processing routine was tried. This approach to background correction did not reveal significantly more information than the conventional approach. There was no sign of the elusive vapour that would be leaving the evaporating spray.

One of the objectives of this research was to identify the source of high UHC emission in the prototype versions of the Jaguar engine. One reason for these elevated emissions appeared to be pre-spray. It was probable that the pre-spray impacted on the piston crown due to its high penetration rate. If so, full evaporation would be unlikely in the short time available, particularly during engine warm-up, and this portion of the fuel would not be combusted. A second reason for high UHC emission could be the absence of a distinct airflow pattern to constrain the fuel spray to the region around the spark plug. This would result in pockets of mixture which were too lean to burn.

Another objective was to understand the physical processes which determined the limits of injection timing for satisfactory stratified charge combustion. The late limit could be linked to the proximity of the piston. Some of the fuel reached the region below the spark plug but the majority was prevented from doing so by the motion of the piston, and there was a risk that some of this fuel was liable to remain unburned. The early limit could be linked to the lack of distinct air pattern, where the fuel spray dispersed so much that the mixture around the spark plug at ignition was too lean to burn.

The final chapter, 9, consolidates the conclusions of the benchmark, ambient air and cycle to cycle testing, the Mie and LIF studies and the intensity and velocity analyses. It sets out the claims of originality and suggests possible future work.

Chapter 9

Summary and conclusions, claims of originality, recommendations for future work

9.1 Introduction

A literature review was presented in Chapters 1 to 3, discussing the present and future of the automobile, future automotive prime movers and gasoline direct injection engines. In Chapter 4, the optical methods were selected for investigating fuel spray interactions in the Jaguar G-DI engine, subject of this thesis. Chapter 5 described the design of the optical engine built around the Jaguar cylinder head. Chapter 6 reported on the test bed, instrumentation, commissioning and benchmark tests required to prepare for the main experiments. The Mie study was presented in Chapter 7. The equipment used and the method of image capture were described and the results presented. A comprehensive discussion of the Mie and LIF studies, in conjunction with the benchmark, cycle to cycle and injector ambient air tests and Jaguar's CFD work was presented in Chapter 8. This final Chapter summarises the findings, sets out the claims of originality and makes recommendations for future work.

9.2 Summary and conclusions

- Demand for cars will continue to rise due to demand in the developing world.
- There will be a continued need for IC engines to power the cars.
- G-DI engines combined with VVT are believed capable of meeting future emissions regulations. In fact, emissions regulations have become significantly more stringent than the Euro 3 regulations reported in the literature survey carried out at the start of the research. The current and future limits may be seen in Appendix E. The conclusion remains that G-DI combined with VVT are technologies that will help meet the challenge of theses regulations.
- Fuel spray/wall interactions are crucial in G-DI engines in determining the completeness of combustion.

- Jaguar's version of a G-DI engine has some emissions problems in the stratified charge mode.
- The optical techniques of Mie scattering and laser induced fluorescence were chosen as suitable for studying fuel-air mixing on an optically-accessed version of the Jaguar G-DI engine.
- The cyclic repeatability of the injection process was good so that it was possible to build up a picture of spray progression by taking images from different cycles, taken at different delay settings, and assembling them into a pseudo-sequence.
- A Mie study was performed and clear images obtained which were assembled into sequences. They showed that the combustion chamber design appeared to be effective at keeping spray in the centre of the combustion chamber and thereby in the region of the spark plug. However, there was certain impaction of the pre-spray on the top surface of the piston.
- Variations in the intensity of the illuminating light sheet were encountered during the Mie scattering investigation. In particular, a dark region was found to exist above the near vertical part of the quartz slice let into the piston to pass the illuminating light sheet.
- The lack of uniformity in the light sheet caused particular problems with the LIF study for which it was important to have uniform illumination of a reasonably high intensity.
- A technique was evolved for the LIF study in which images were compiled from 52 cycles to obtain the average behaviour at a particular test condition. The 52 cycles were accumulated by averaging 13 batches of images integrated over 4 consecutive gating periods. Four periods were found to be sufficient to obtain a sufficiently strong signal without saturating the camera.
- Pre- and post-firing background images were recorded to compensate for window fouling during each of the LIF tests.
- A further correction was included to allow for variation in intensity across the spread of the light sheet. It was a particularly important correction due

to the prismatic effect of the contoured quartz in the slot in the piston. A different correction was employed for each piston position.

- Jaguar provided some CFD predictions for the prototype cylinder head. The CFD results had to be extrapolated to cover the 1500 rev/min, WWMP, test condition of the engine.
- Evidence was sought for coupling between the piston, fuel and air velocities. The CFD predictions suggested that the main flow patterns within the cylinder before the injection event were simply due to the rising piston with no indication of significant tumble.
- The injection event stirred up the flow by the fuel displacing and entraining air. The maximum velocities predicted were on the order of 35 m/s and were in the air near the region of developing fuel spray.
- The engine test results appeared to validate the CFD predictions that the spray would linger in the region near the spark plug and somewhat away from the injector.
- The CFD results suggested that the main spray was arrested by the drag on the small droplets moving against a modest vertical air flow caused by the rising piston. These predictions increased confidence that the images recorded on the engine had not missed significant fuel activity in the region above the rising piston lip because of poor illumination.
- An analysis of mean intensities of the images showed that all traces had a peak as intensity rose due to the developing plume, then fell away due to evaporation, dispersal and fuel entering the dark region.
- A 'kink' was apparent in the traces when pre-spray entered the piston bowl. The fall in intensity was of the order of 5 – 10% indicating that the volume of pre-spray was not insignificant. It should be noted that the fall in intensity cannot be linked directly to the quantity of fuel, since droplet diameter also determines intensity of scattered light. The pre-spray is believed to consist of relatively large droplets.
- The recovery in average intensity visible at the increased delays for the Mie scattering engine firing tests was thought to be due to fuel re-

emerging out of the bowl. The fact that it was evident in the Mie scattering tests led to the conclusion that it was still in liquid form.

- A novel post-processing routine was tried. This approach to background correction did not reveal significantly more information than the conventional approach. There was no sign of the elusive vapour that would be leaving the evaporating spray.
- One reason for high UHC emissions from the engine appeared to be as a result of liquid fuel on the piston due to the highly penetrating pre-spray. Another reason could be the absence of distinct airflow pattern so that the fuel spray was not constrained to the region around the plug.
- The late limit for stratified charge injection may be explained by the proximity of the piston which reduced the amount of fuel reaching the region below the spark plug. The early limit could be linked to the dispersal of fuel arising from the lack of distinct airflow pattern. This dispersal would lead to an excessively lean air/fuel ratio around the spark plug under stratified charge operating conditions.

9.3 Claims of originality

It is believed that previous optical investigations of wall-guided G-DI engines have included one or more simplifications. The engines were either run in firing mode with modifications or were just motored. Where the engines were fired, the piston geometry was revised or a single component fuel was used. The testing reported here used an engine with the correct piston geometry and the running conditions were realistic. Gasoline was used for the Mie tests, and for the LIF work it was replaced by a three-component fuel with similar evaporation characteristics to gasoline.

The research engine itself was designed with a number of features that were either novel individually or in combination. The cylinder head raising mechanism permitted rapid cleaning of the optical surfaces. The valve timing could be preserved during these cleaning operations by careful design of the camshaft drive system. The quartz windows were retained by a flexible sealant compound capable of accommodating differential thermal expansion

whilst maintaining a gastight seal. At the concept stage, it was decided that the piston crowns would be interchangeable to cover commissioning, thermodynamic benchmark work and the optical studies. One crown had a contoured slice of quartz which closely followed the topography of the piston bowl.

The post-processing routines applied to the LIF images contained elements that again were either novel individually or in combination. Images were averaged to avoid saturation of the camera and combined with pre- and post-firing background shots and light sheet correction images. The method of having a light sheet correction image for each piston position is believed to be novel. The attempted approach of using the preceding image as a background correction rather than the pre-/post-firing method is thought to be novel.

9.4 Recommendations for future work

It is recognised that CFD predictions alongside optical results form a powerful analytical approach. It was unfortunate that project scheduling prevented CFD work being carried out in parallel with the optical studies, although some general conclusions could be drawn from the small amount of CFD data that was available. A comprehensive CFD study using engine conditions corresponding to the optical studies would help to reveal the fundamental mechanisms of fuel spray interactions in this type of engine.

Further work could still be performed on the interactions between the fuel spray and the piston bowl. One approach would be an iterative study whereby the piston bowl was cut away sequentially and images captured at each stage. This would be time-consuming and require careful machining, but the approach, coupled with the application of CFD, should reveal further information about the spray/piston bowl interactions.

The problems experienced due to the non-uniformity of the laser sheet caused by the prismatic effect of the quartz slice could be avoided by arranging for the laser sheet to enter through optical access on the injector side of the

cylinder wall. Images of the illuminated spray could then be recorded from the same direction as the current study. The view into the top of the combustion chamber would be lost, but most of the important fuel preparation mechanisms appear to occur within the cylinder bore, at least for the earlier two injection timings. One side of the bowl would need to be machined away, as above, for the study to look into the bowl of the piston. The light sheet could be traversed away from the centre line of the cylinder axis to reveal more information about the spread of the spray.

Finally, a stand-off microscope lens, capable of magnification to produce a very small area of interest, could be used. This would be quite difficult to set up and light levels would be low, resulting in low definition images. However, sensitive cameras are now available and the crucial test points are already known as well as the approximate location of the fuel vapour.

The preceding points have concentrated on possible developments to the experimental techniques. The observations made during this research have indicated possible design changes to the combustion chamber which should help reduce UHC emissions. The most obvious change is to adopt a type of injector that eliminates the production of pre-spray such as the latest multi-hole injectors [Delphi, 2007]. A change of injector would require a reconsideration of the air flow patterns towards the end of the compression stroke. Efforts should concentrate on creating more distinct air flow patterns (as compared to the relatively quiescent flow of the engine used in this study). This could be achieved through more advanced forms of VVA that allow lift and durations to be controlled. Such a change would mean that the injector arrangement would become classified as an air-guided G-DI system.

Chapter 9 Summary and conclusions, claims of originality, recommendations for future work

Appendix A

Equipment lists and calibration

A1 Equipment

Table A-1 lists the hardware used in the tests.

Description	Make	Model No.	Serial No.
Engine	Jaguar	Single optical prototype	-
Fuel injector	Bosch	100 Wdgn	034
Injector driver	Bosch	HDEV-1	JGT17667
Spark plug	Bosch	HGR 7 LQPEO	048366
Spark timing optical switch	Lumenition Optronics	PMA 50	-
DC eddy current dynamometer	Froude Consine	AG80	8005918/2
Variable speed drive motor	Brook-Hansen	WD180L	D937366
Digital delay/pulse generator	Stanford Research Systems	DG535	08233
Shaft encoder	Hohner	W8C90R	310801
Hot-wire anemometer	Ford	AFH60-02A	3C16
Cylinder pressure sensor	Kistler	6041A	1309768
Charge amplifier	Kistler	566	2466
Inlet manifold pressure sensor	Druck	PDCR910	1070024
UEGO sensor	ECM	AFM-1000	-
Exhaust gas analyser	Horiba	MEXA -321E	E40489
Digital oscilloscope	Nicolet	4094-2	-
Digital storage oscilloscope	Tektronix	TDS1002	C046582
Thermocouples	Radio Spares	K-type	-
Nd:YAG laser	Continuum	Surelite III	3133
Intensified CCD camera	Photonic science	CV12/500	70506
Camera lens	Nikon	AF Micro Nikor 1:2.8	-
Spherical lens	Comar	f300	-
Cylindrical lens	Comar	f-25	-
Light power meter	Coherent	P10i	-
Frame grabber	Matrox Imaging	Corona-II	-

Table A-1 Hardware used in tests

A2 Calibration

The following graphs contain calibration information for the UEGO sensor, (Figure A-1, from manufacturers' literature) and for the hot wire anemometer (HWA), Figure A-2 and the Bosch injector, Figure A-4 (both determined experimentally). The Ford air flow meter was converted for use only at low flow and calibrated against a rotameter.

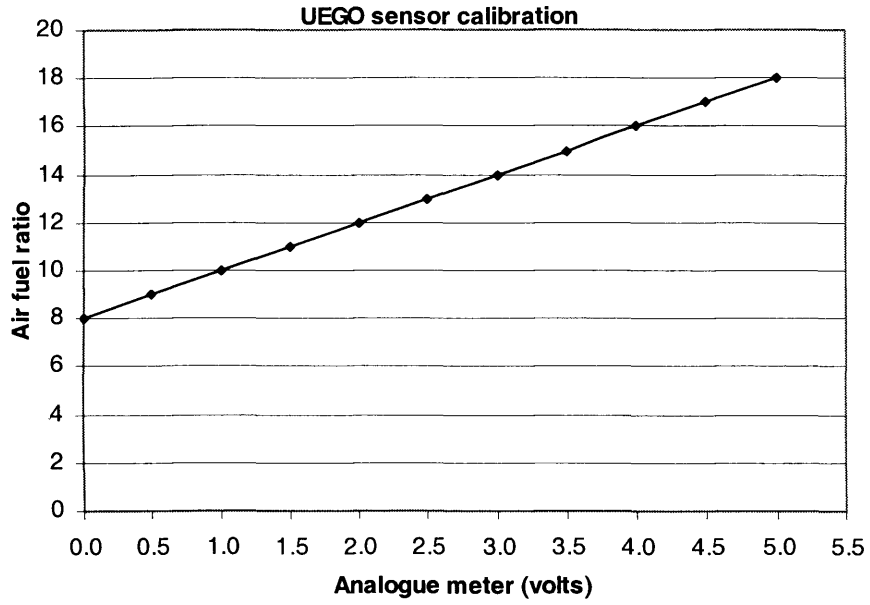

Figure A-1 Calibration graph for UEGO air fuel ratio sensor

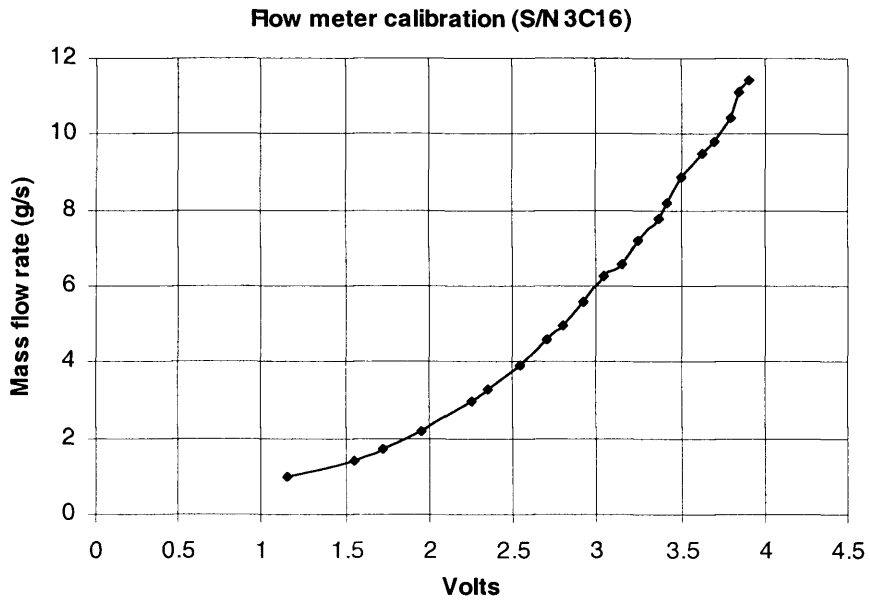

Figure A-2 Calibration graph for Ford hot wire anemometer

The injector had to be calibrated to determine its flow rate characteristics and for this, a simulated engine was used. The shaft encoder was disconnected and replaced by a function generator, which produced TDC signals to act as triggers in the SRS while avoiding the need to run the engine (See Figure A-3). Since the encoder was designed to be mounted on the engine camshaft, it produced one TDC pulse for every two crankshaft revolutions. So to simulate the engine running at 1500 rev/min, $\frac{1500}{2}$ pulses per minute were needed, or $\frac{1500}{2\times 60}$ pulses per second, ie the function generator was set to 12.5 Hz. The injector was fired into a collecting vessel and the mass of fuel determined for a known number of injections, across the range of pulse widths.

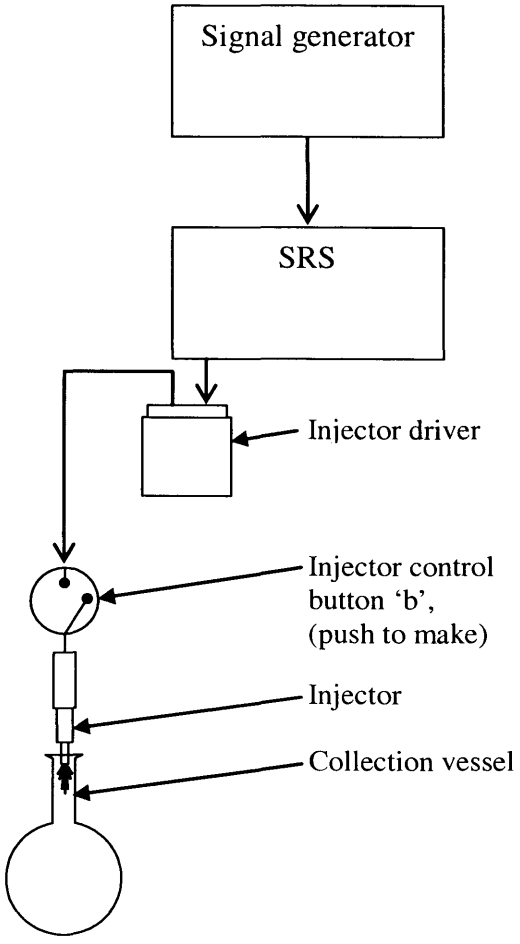

Figure A-3 Arrangement of equipment for injector calibration

The results of the injector calibration are graphed in Figure A-4.

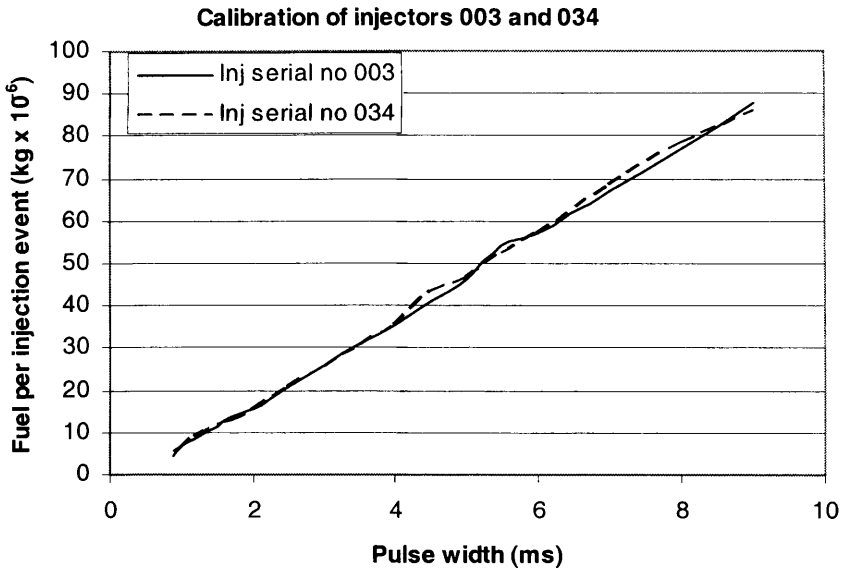

Figure A-4 Calibration of Bosch inwardly opening pressure swirl injector.

A3 Sample calculation of air fuel ratio

For the benchmark testing, AFR was measured directly using the UEGO sensor. It was interesting to compare the values with ones calculated using air flow and the injector calibration data. For test point 18 (Table 6-2, § 6.5), an injector pulse width of 2 ms was used, Figure A-4 shows that 1.60×10^{-5} kg fuel was delivered per injection event. At the engine speed of 1490 rev/min this equated to: $1.60 \times 10^{-5} \times \frac{(1490 \times 1000)}{60 \times 2} = 0.199$ g/s .

The HWA reading of 2.9 volts represented 5.6 g/s of air flowing into the plenum, based on Figure A-1. Thus the AFR was $\frac{(5.6)}{0.199} = 28.19$.

It is interesting to compare this value with a figure using the intake air mass flow rate based on 100% volumetric efficiency, ie

$$\frac{\text{swept vol} \times \text{density of air} \times \text{engine speed}}{60 \times 2}$$

First, the density at the assumed ambient conditions of 1 bar pressure and 20^0C was found, using:

$$PV = mRT$$

$$\rho = \frac{P}{RT} = \frac{10^5}{287 \times 293} = 1.19 \text{ kg/m}$$

Hence, theoretical air flow = $490 \times 10^{-6} \times \frac{1490}{60 \times 2} 1.19 \times 10^3 = 7.24$ g/s.

In combination with the fuel mass flow rate estimated above, the air fuel ratio assuming 100% volumetric efficiency is $\approx \frac{7.24}{0.199} \approx 36.44$

Appendix B

Engine commissioning

B1 Engine commissioning

Commissioning was required before the engine was ready to begin the benchmark tests. A check was made that the lubrication oil system was full. The fuel ram was filled with pump unleaded gasoline (to B.S.7070) and a pressure of 50 bar attained. Air was bled from the system and the pressure was increased and stabilised at 100 bar. The dynamometer water system was pressurised and the crankcase suction pump was switched on. Two revolutions of the flywheel were completed by hand to ensure there were no clashes between the valves and piston. Mains power for the ignition system, motor and dynamometer were switched on but with the zero load option selected for the dynamometer and the injector remained switched off. The cathode ray oscilloscope (CRO) was switched on. As the motor speed was increased, encoder TDC signal and Kistler pressure sensor traces on the CRO confirmed the correct synchronisation of the encoder TDC pulse and the physical top dead centre. A check was made that the crankcase suction pump was working correctly and visual inspection showed that the HWA, U-tube manometer, Horiba analyser, UEGO sensor and all pressure gauges and thermocouples were working. Speed was increased to achieve the WWMP value of 1500 rev/min. Load was gradually applied from the dynamometer and the CRO traces and instruments behaved as expected. Values for SOI and pulse width from an intermediate position on the Jaguar engine map were selected. Traces from the injector and spark plug leads were added to the CRO. The injector was switched on and the CRO confirmed that the injector and spark events were correctly timed and combustion occurred, albeit with misfires. Heated water was piped to the engine jacket and combustion quality improved. Settings were tried from more extreme points on the engine map and satisfactory combustion was found. A plumb bob suspended above the engine showed that displacement due to the torque reaction was less than 2 mm and vibration was also minimal. This proved the integrity of the test bed fixings and demonstrated the efficiency of the anti-vibration mat, which would

help maintain image quality. The engine was ready to begin the benchmark tests. Additional commissioning work for the Mie and LIF studies is described in Chapters 7 and 8 respectively.

Appendix C

Ambient air injection images

C.1 Introduction

Images of the injector firing into ambient air were recorded, using various delays (delta values) between the injector firing and the camera gating. These were recorded to form a library of reference images for comparison with images from the firing studies.

C.2 Method

The setup was intended to replicate as closely as possible the arrangement used for the firing work and each image was taken through the quartz main window. Two identical injectors were available and the options for the piston crown were: slot of quartz, disc of quartz and no quartz. The camera and laser were in their standard positions. The engine head was raised and the spark plug, injector and main quartz window were clamped in the same positions that they would occupy in the firing engine. The engine simulation electronics were prepared and the relevant delay chosen. The unleaded gasoline was pressurised, the laser switched on, the simulation started, the camera gated and the image captured. The quartz surfaces were cleaned, the next delay was set and another image recorded. This was repeated for each delta, using all piston crown options and finally every setting repeated for the spare injector. The resulting images are presented in Figure C1 to Figure C13. Each page is for one delta setting (eg delta 05 CAD for Figure C1) and contains six images, three for each injector, serial numbers (s/n) 003 and 034. For the top pair of images, the piston crown containing the slot of quartz was used. For the middle pair, the disc was in place and for the bottom pair, the piston crown was absent. For every image, the fuel pressure was 100 bar and the injector pulse width was 0.9 ms.

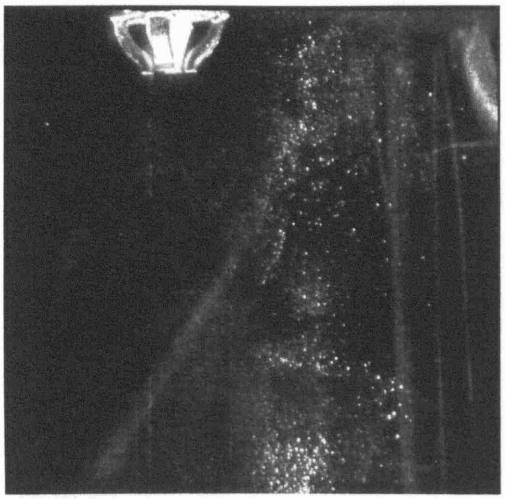

Injector s/n: 003, "slot" crown

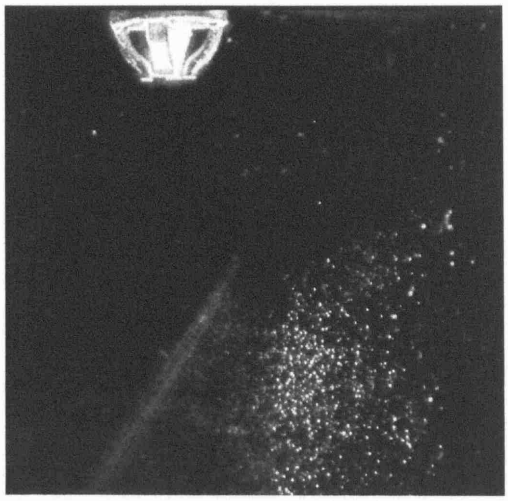

Injector s/n: 034, "slot" crown

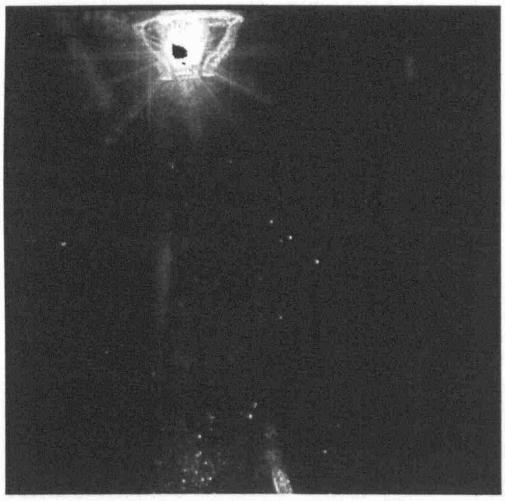

Injector s/n: 003, "disc" crown

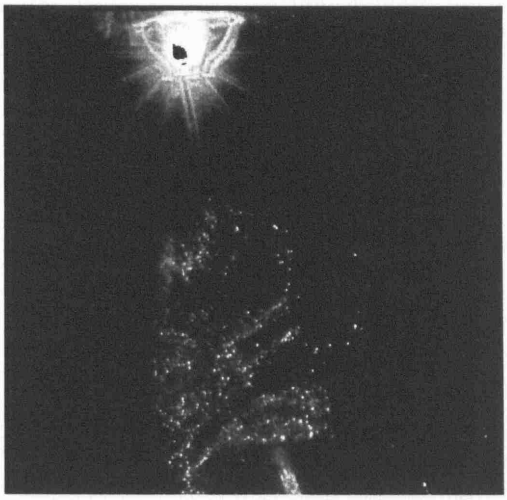

Injector s/n: 034, "disc" crown

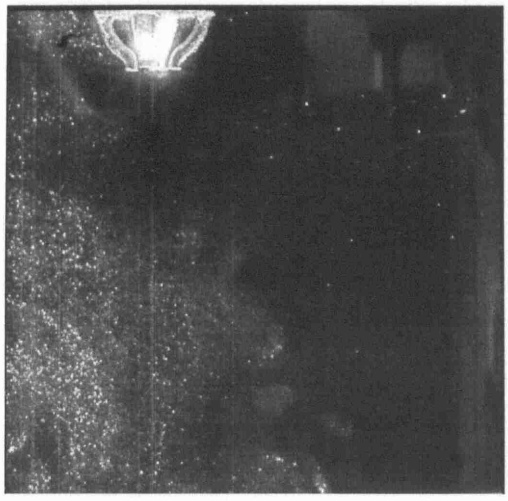

Injector s/n: 003, no crown

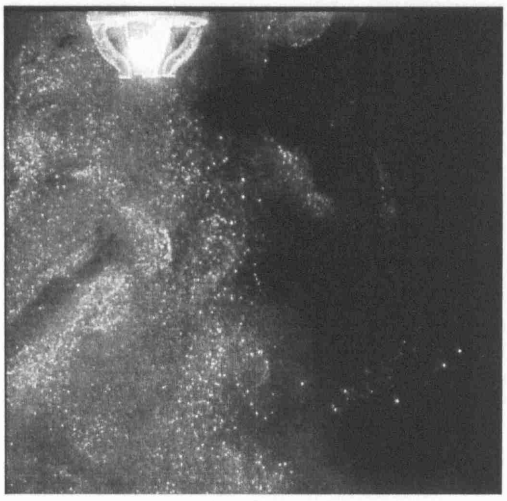

Injector s/n: 034, no crown

Figure C-1, Ambient air images, delta 05 CAD

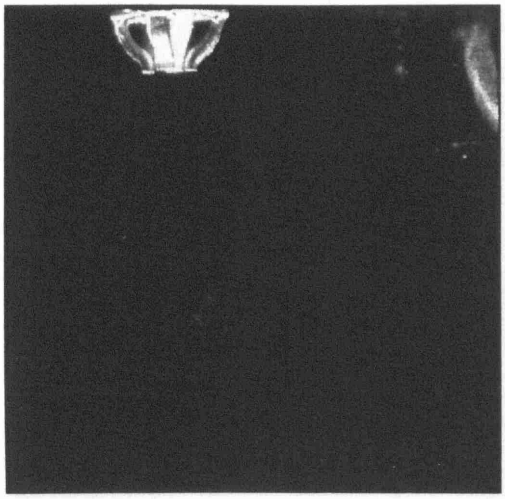

Injector s/n: 003, "slot" crown

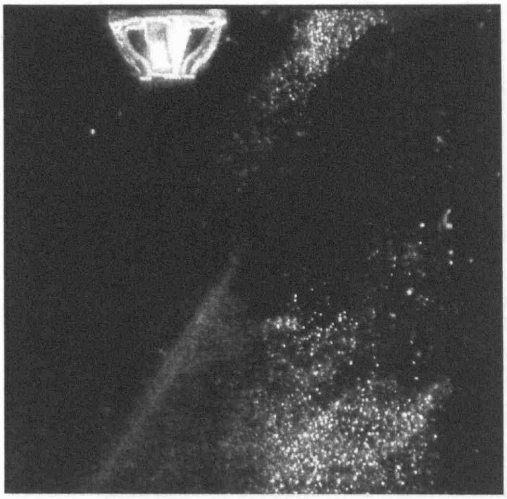

Injector s/n: 034, "slot" crown

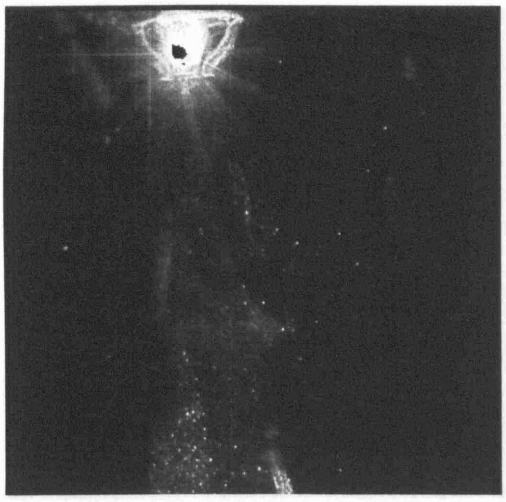

Injector s/n: 003, "disc" crown

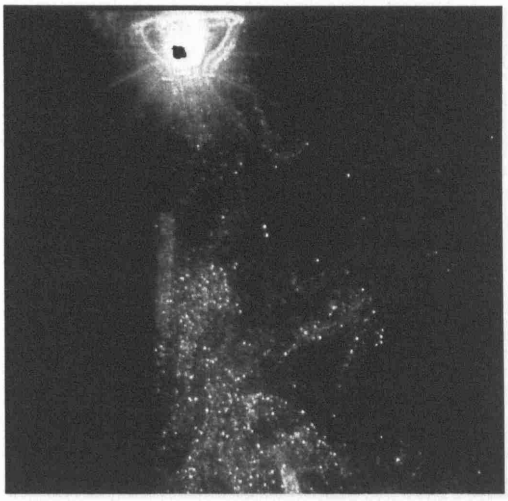

Injector s/n: 034, "disc" crown

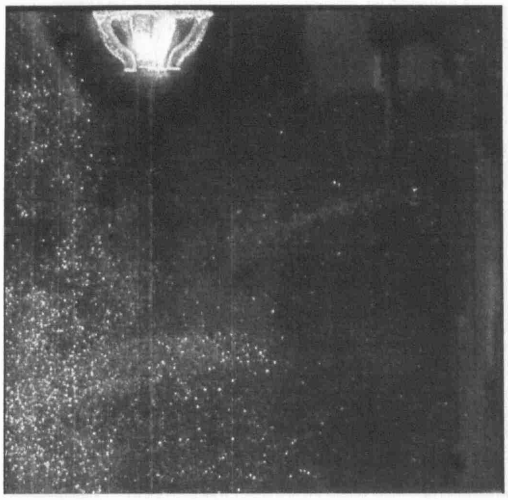

Injector s/n: 003, no crown

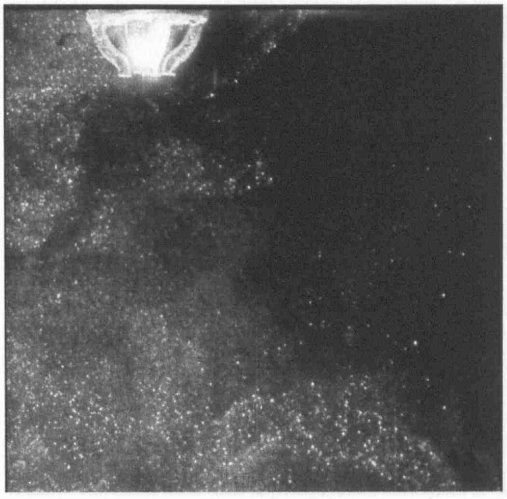

Injector s/n: 034, no crown

Table C-2 Ambient air images, delta 06 CAD

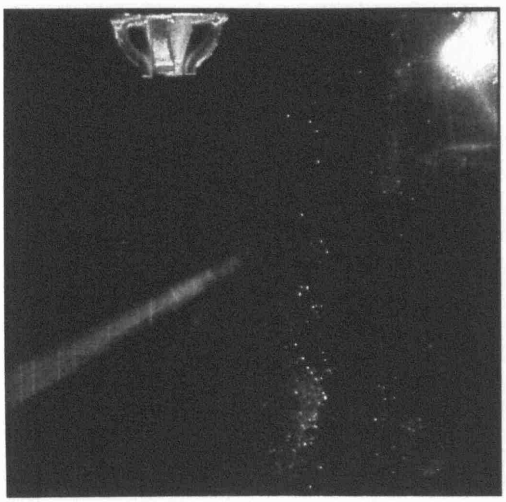

Injector s/n: 003, "slot" crown

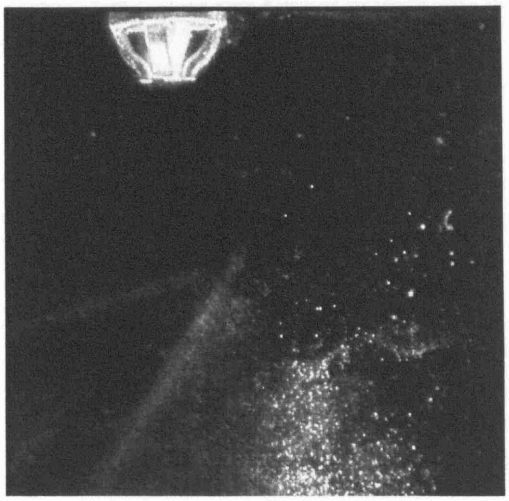

Injector s/n: 034, "slot" crown

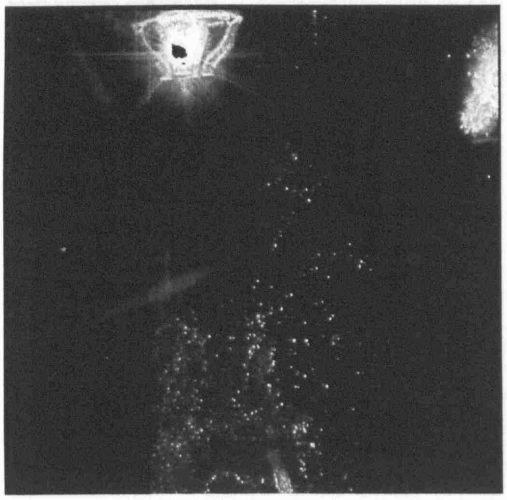

Injector s/n: 003, "disc" crown

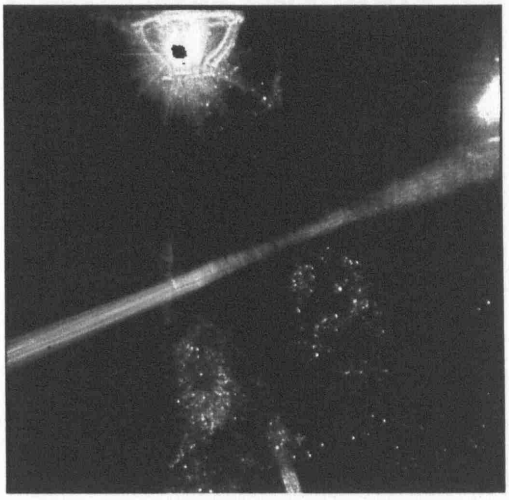

Injector s/n: 034, "disc" crown

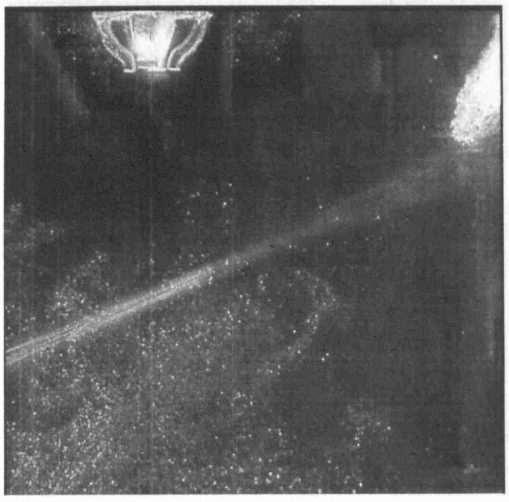

Injector s/n: 003, no crown

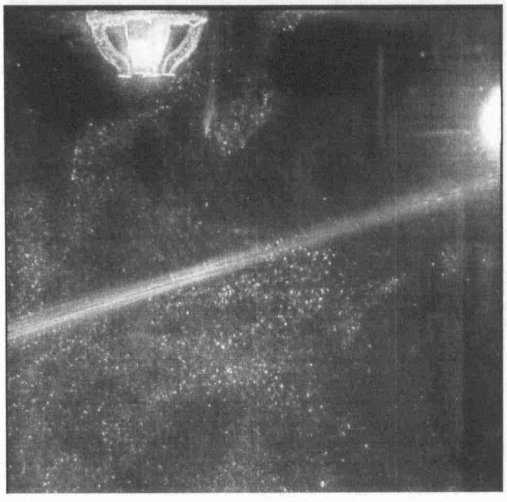

Injector s/n: 034, no crown

Table C-3 Ambient air images, delta 07 CAD

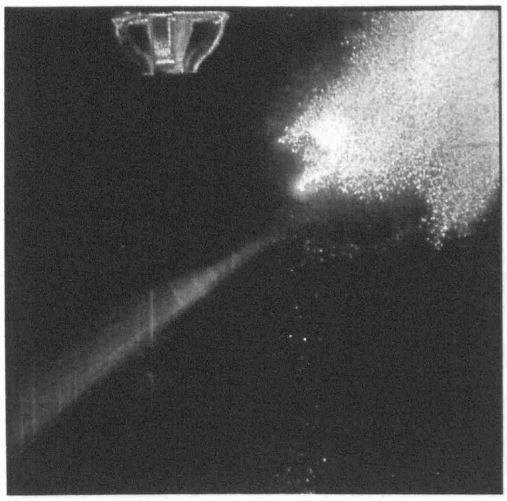

Injector s/n: 003, "slot" crown

Injector s/n: 034, "slot" crown

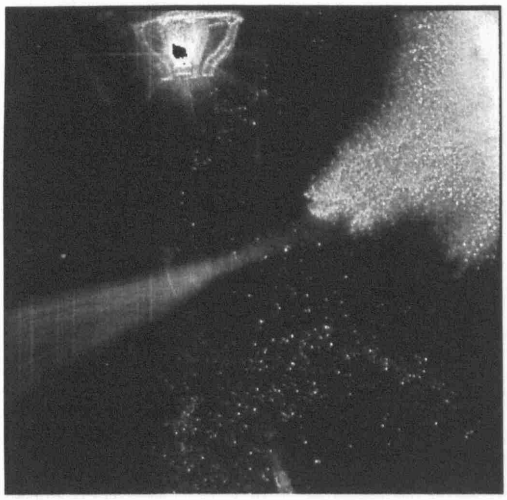

Injector s/n: 003, "disc" crown

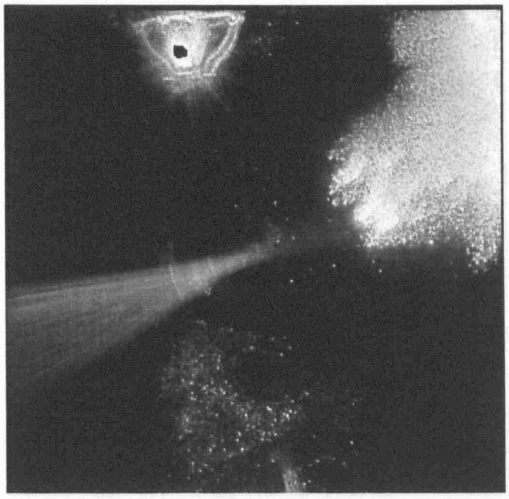

Injector s/n: 034, "disc" crown

Injector s/n: 003, no crown

Injector s/n: 034, no crown

Table C-4 Ambient air images, delta 08 CAD

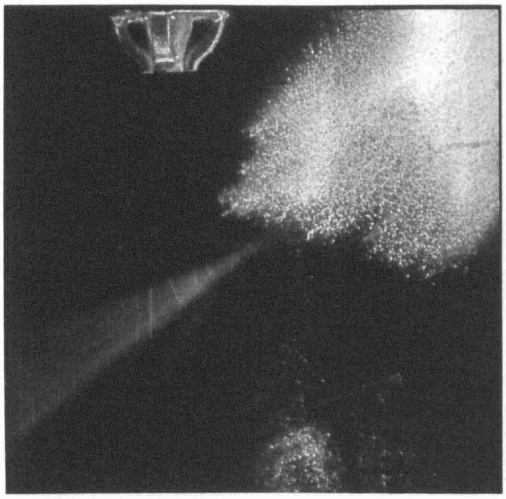

Injector s/n: 003, "slot" crown

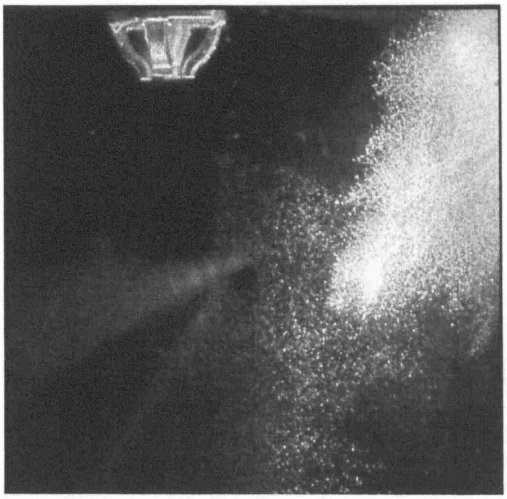

Injector s/n: 034, "slot" crown

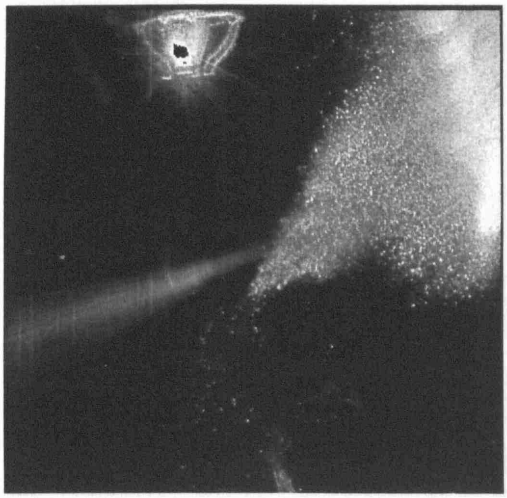

Injector s/n: 003, "disc" crown

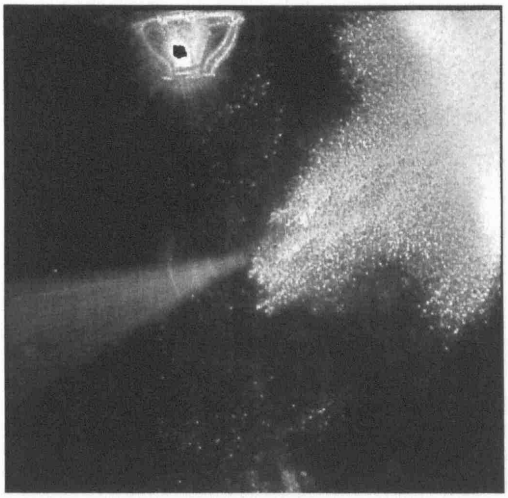

Injector s/n: 034, "disc" crown

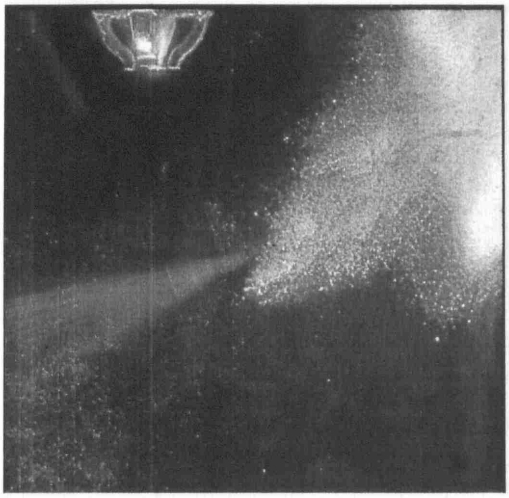

Injector s/n: 003, no crown

Injector s/n: 034, no crown

Table C-5 Ambient air images, delta 09 CAD

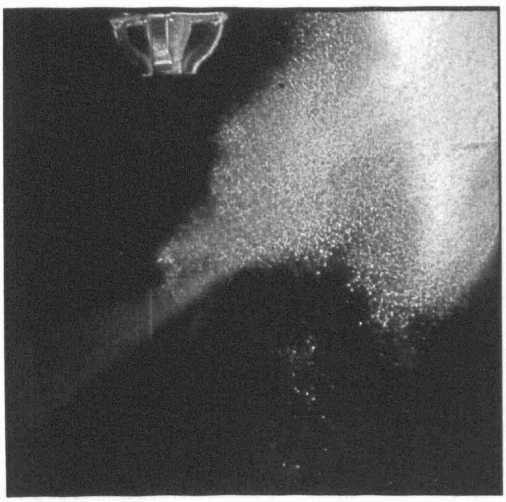

Injector s/n: 003, "slot" crown

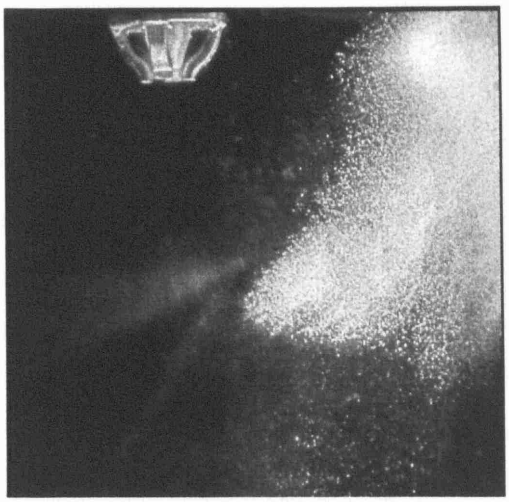

Injector s/n: 034, "slot" crown

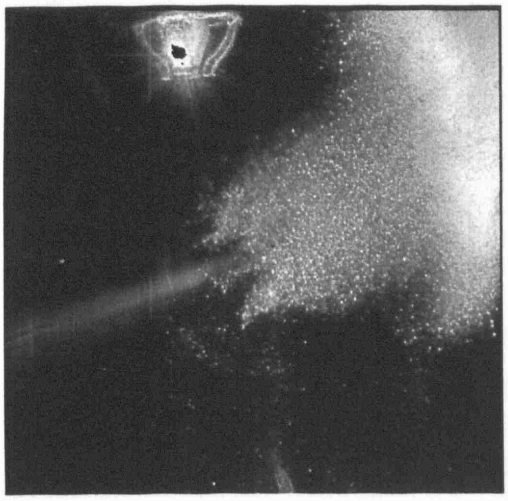

Injector s/n: 003, "disc" crown

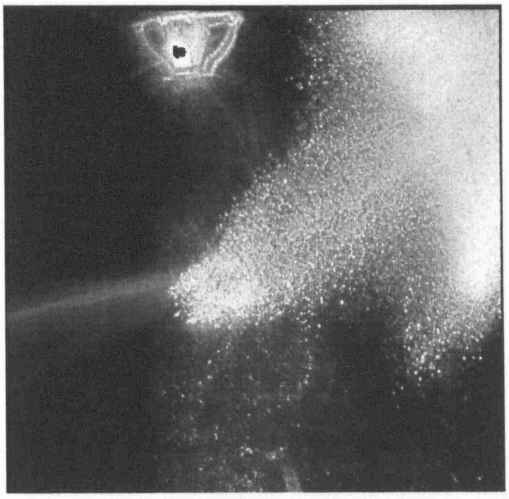

Injector s/n: 034, "disc" crown

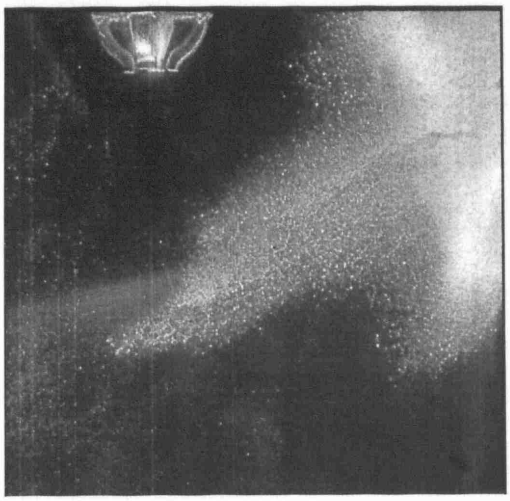

Injector s/n: 003, no crown

Injector s/n: 034, no crown

Table C-6 Ambient air images, delta 10 CAD

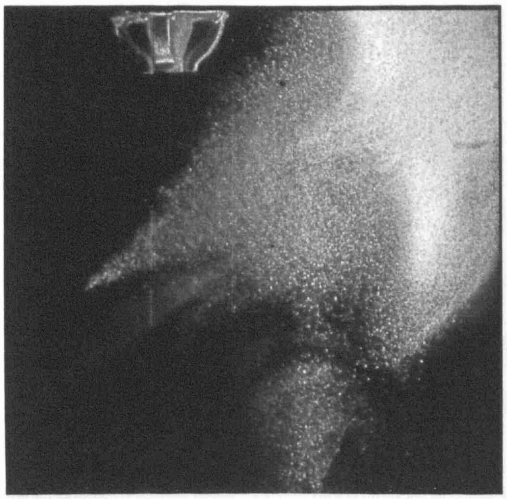

Injector s/n: 003, "slot" crown

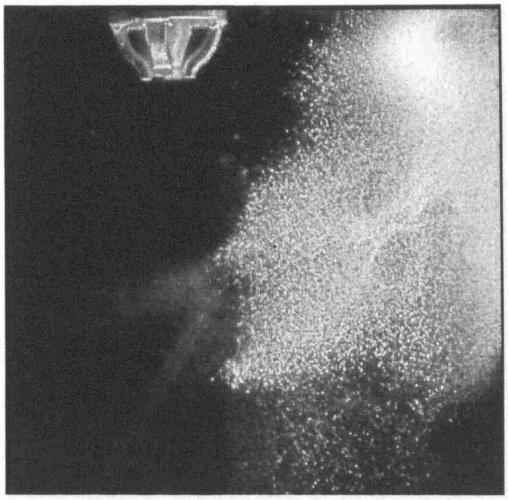

Injector s/n: 034, "slot" crown

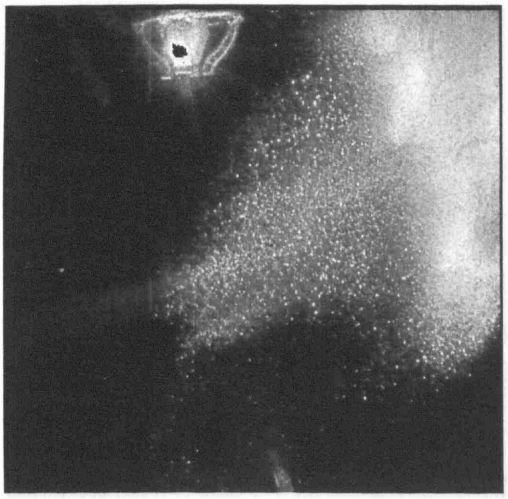

Injector s/n: 003, "disc" crown

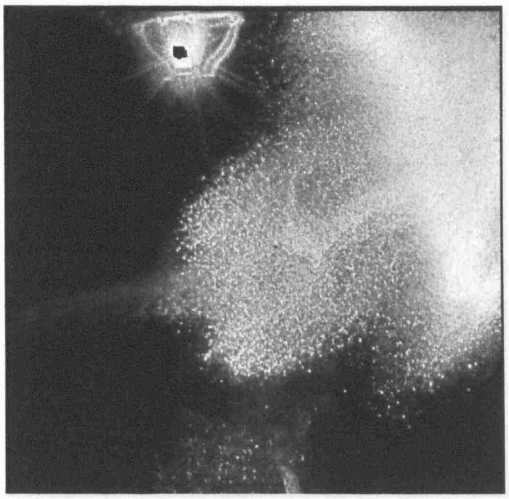

Injector s/n: 034, "disc" crown

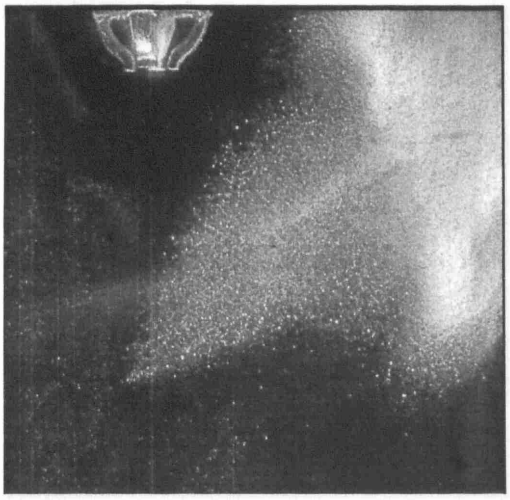

Injector s/n: 003, no crown

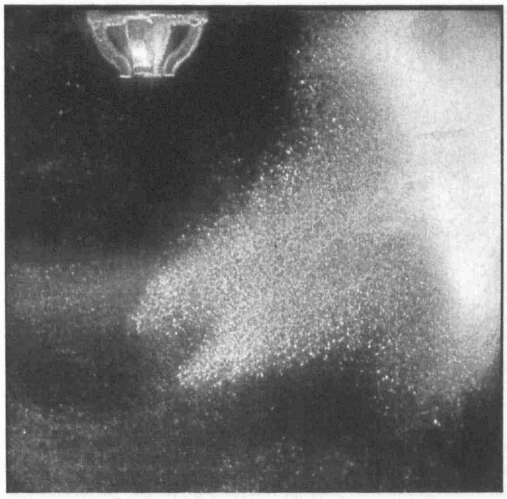

Injector s/n: 034, no crown

Table C-7 Ambient air images, delta 11 CAD

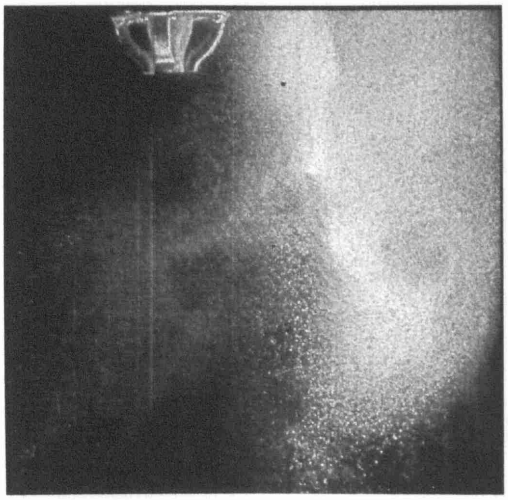

Injector s/n: 003, "slot" crown

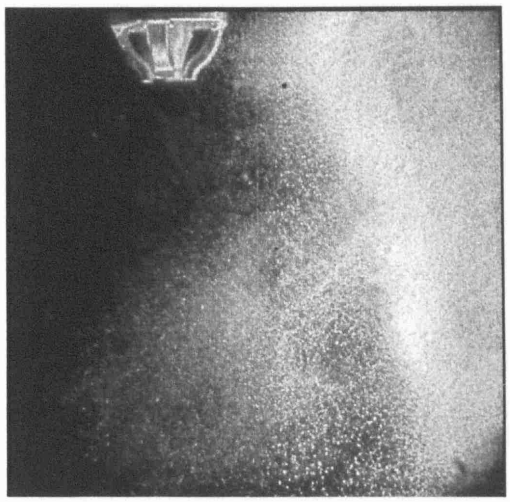

Injector s/n: 034, "slot" crown

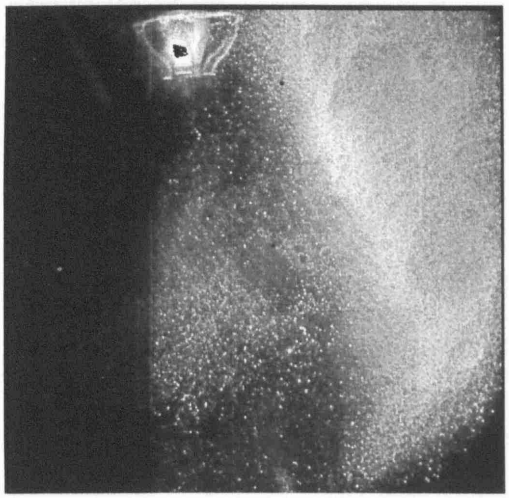

Injector s/n: 003, "disc" crown

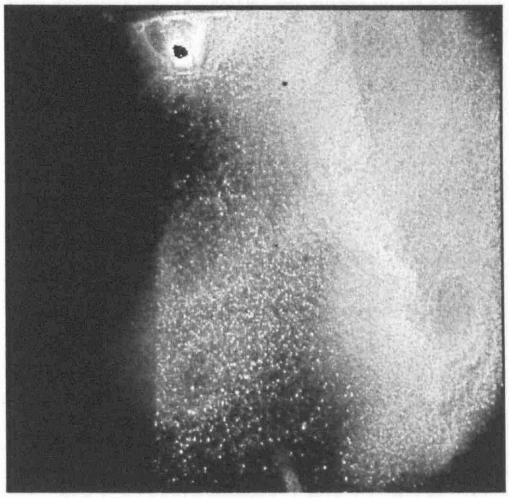

Injector s/n: 034, "disc" crown

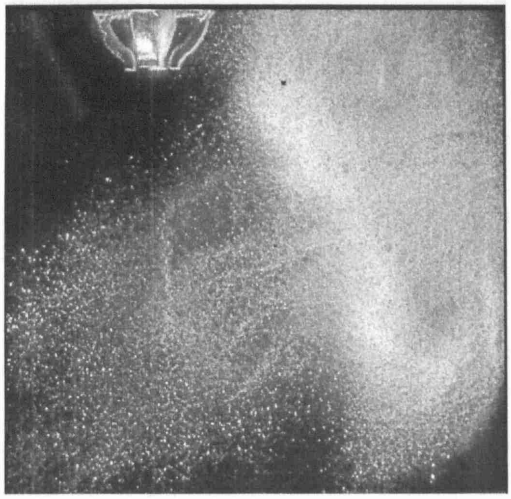

Injector s/n: 003, no crown

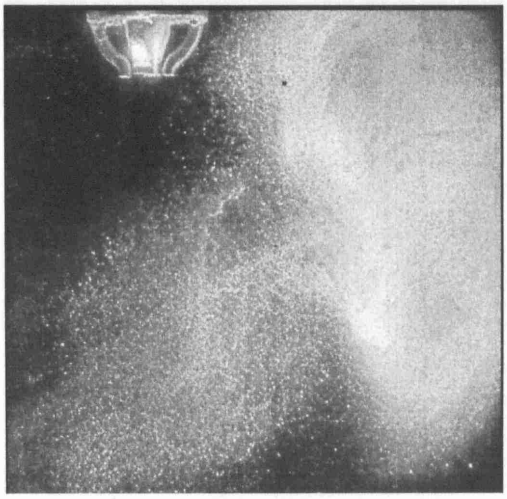

Injector s/n: 034, no crown

Table C-8 Ambient air images, delta 15 CAD

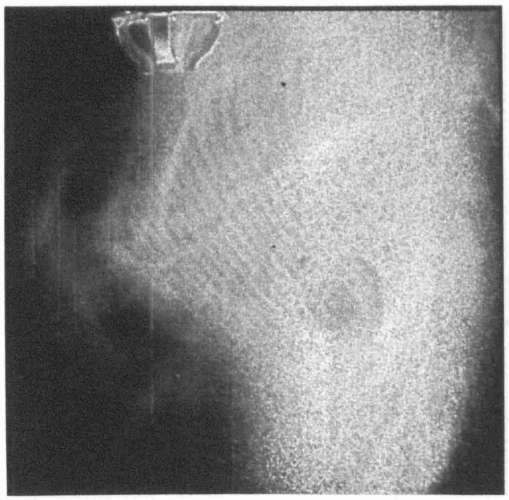

Injector s/n: 003, "slot" crown

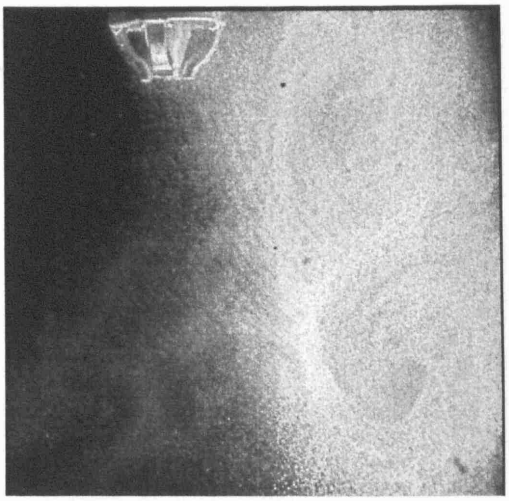

Injector s/n: 034, "slot" crown

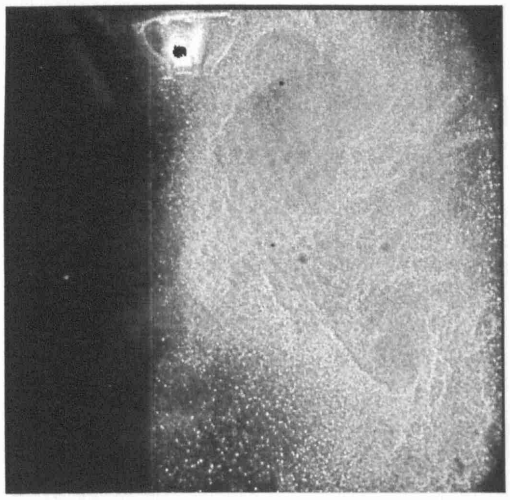

Injector s/n: 003, "disc" crown

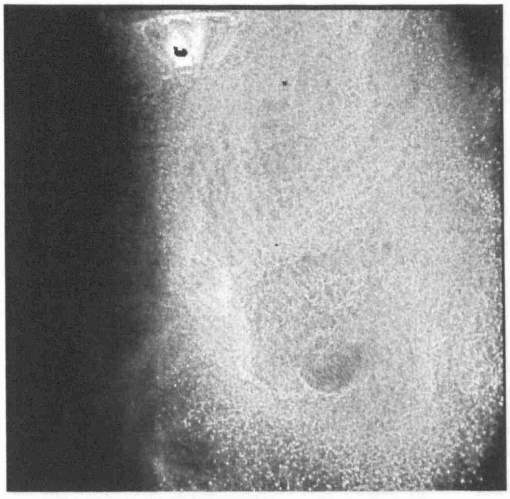

Injector s/n: 034, "disc" crown

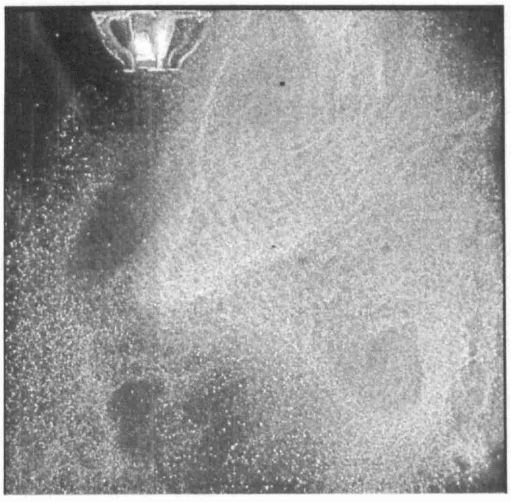

Injector s/n: 003, no crown

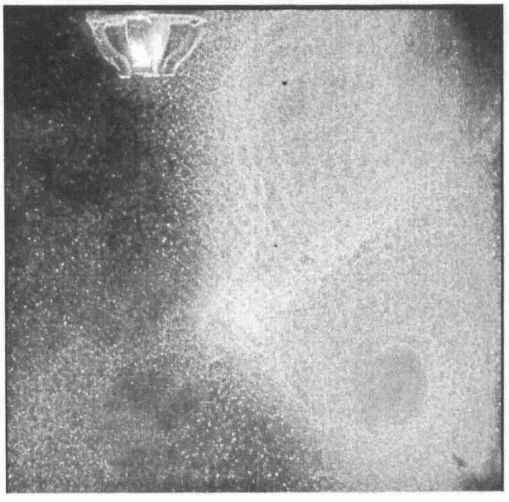

Injector s/n: 034, no crown

Table C-9 Ambient air images, delta 20 CAD

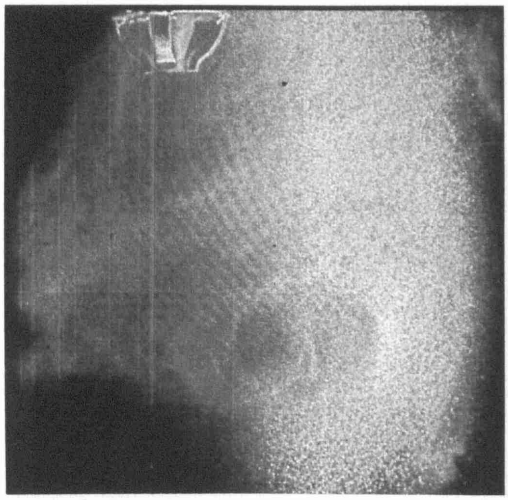

Injector s/n: 003, "slot" crown

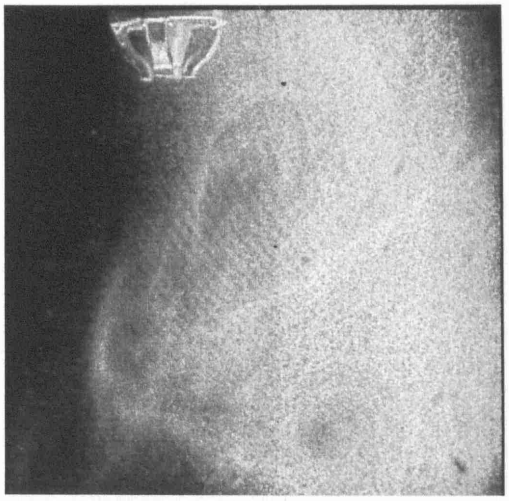

Injector s/n: 034, "slot" crown

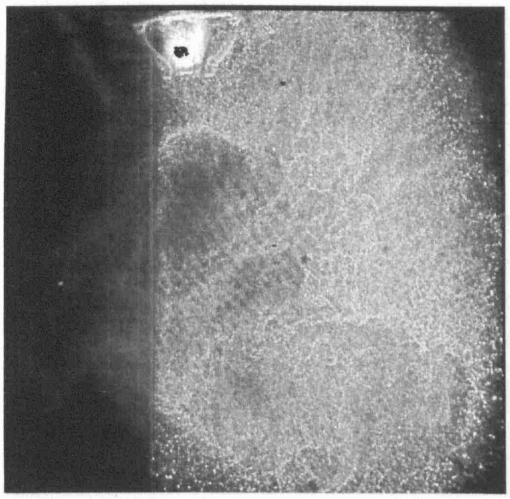

Injector s/n: 003, "disc" crown

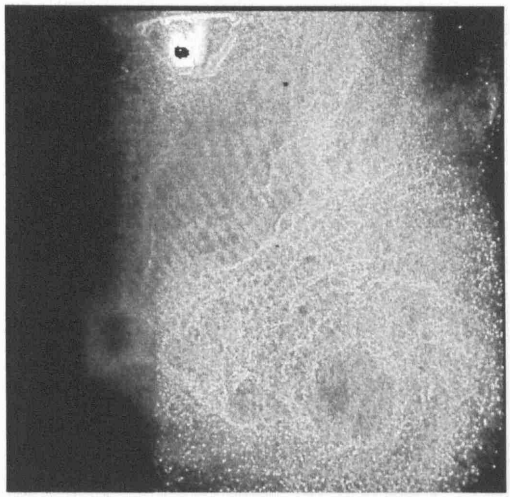

Injector s/n: 034, "disc" crown

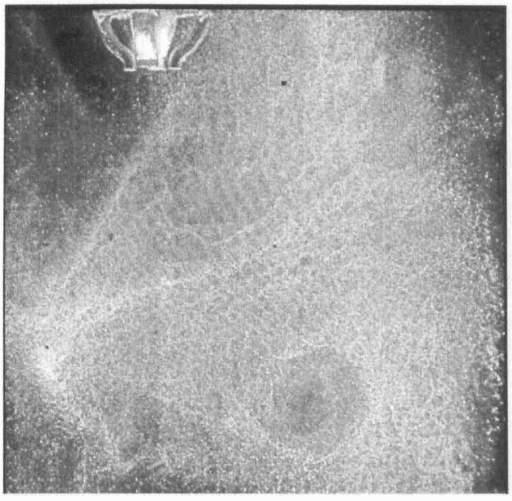

Injector s/n: 003, no crown

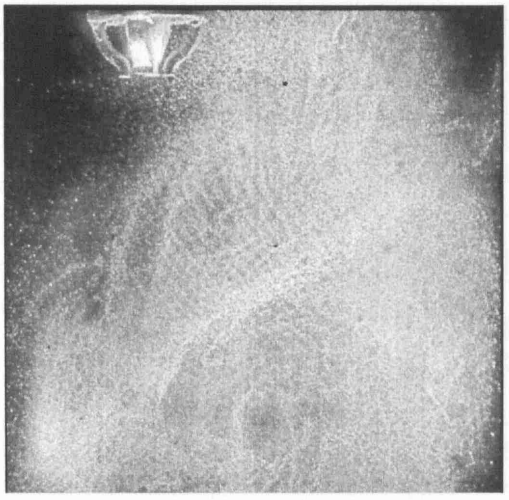

Injector s/n: 034, no crown

Table C-10 Ambient air images, delta 25 CAD

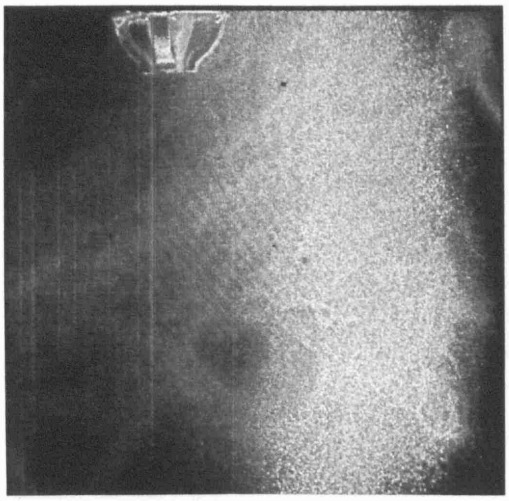

Injector s/n: 003, "slot" crown

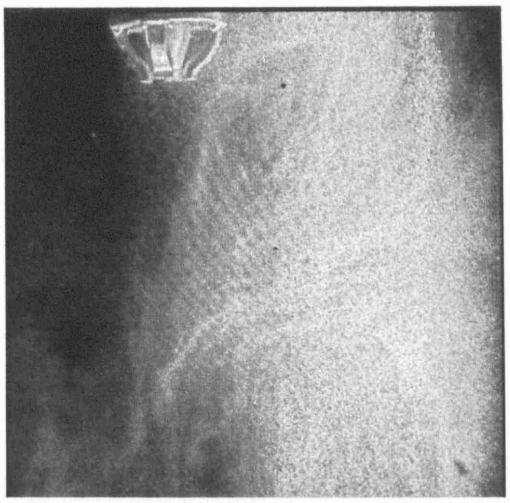

Injector s/n: 034, "slot" crown

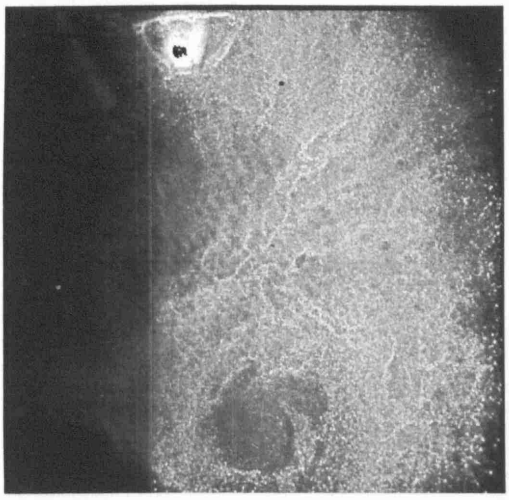

Injector s/n: 003, "disc" crown

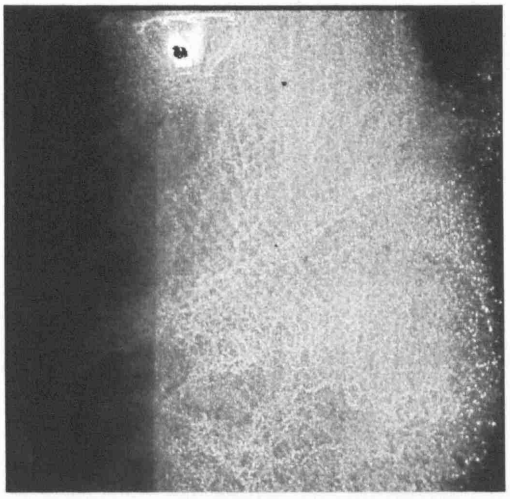

Injector s/n: 034, "disc" crown

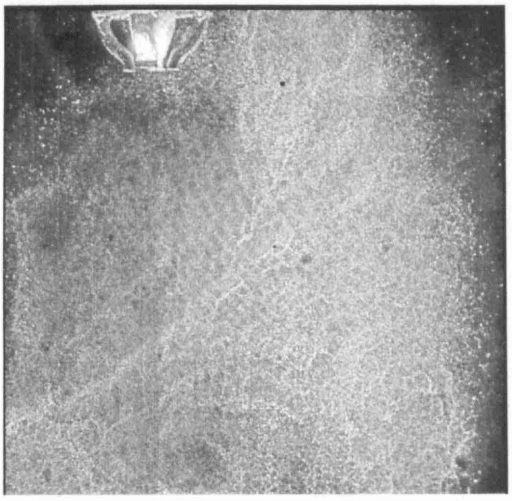

Injector s/n: 003, no crown

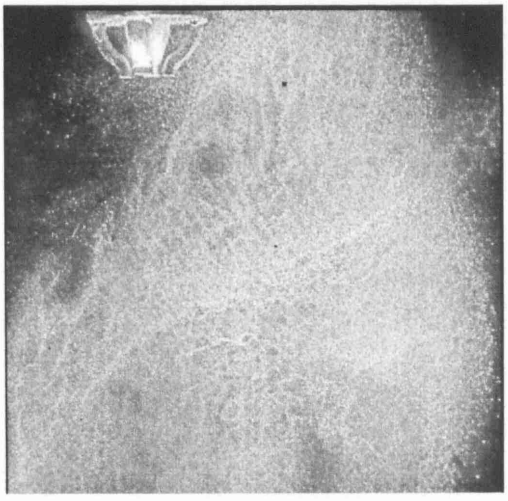

Injector s/n: 034, no crown

Table C-11 Ambient air images, delta 30 CAD

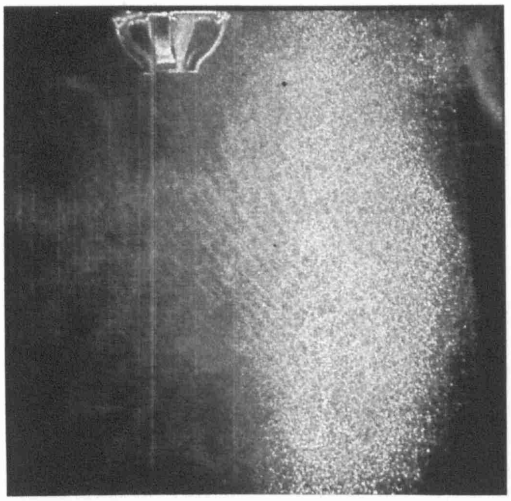

Injector s/n: 003, "slot" crown

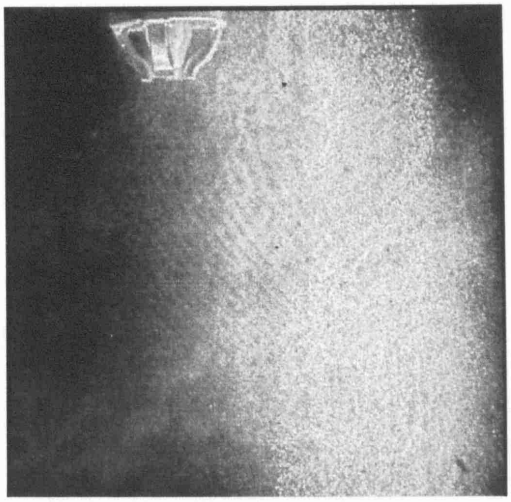

Injector s/n: 034, "slot" crown

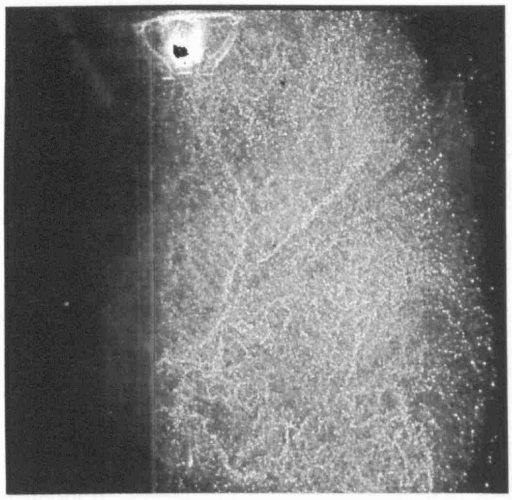

Injector s/n: 003, "disc" crown

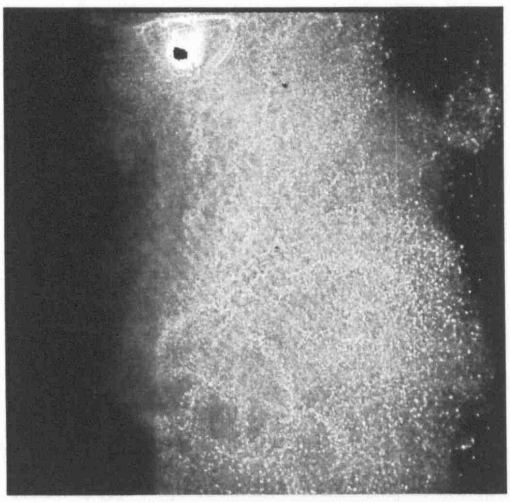

Injector s/n: 034, "disc" crown

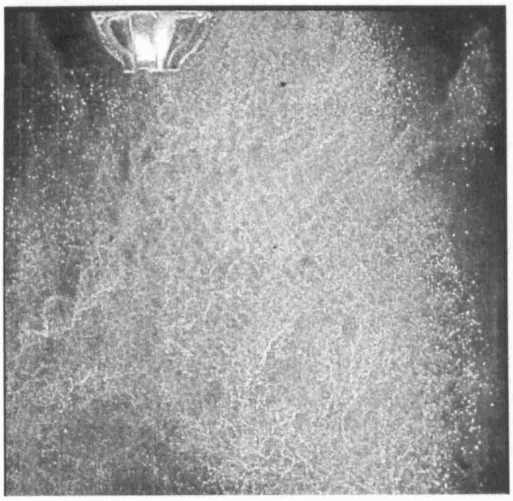

Injector s/n: 003, no crown

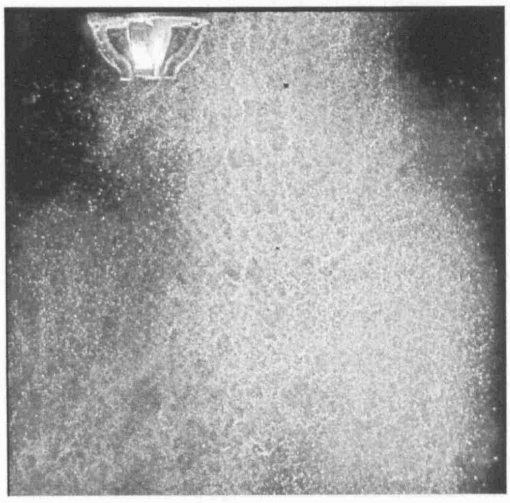

Injector s/n: 034, no crown

Table C-12 Ambient air images, delta 45 CAD

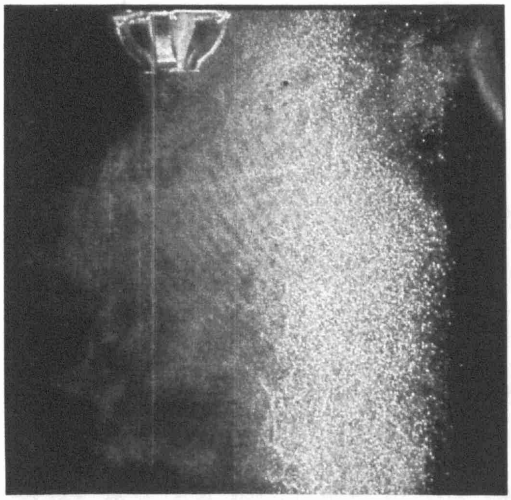

Injector s/n: 003, "slot" crown

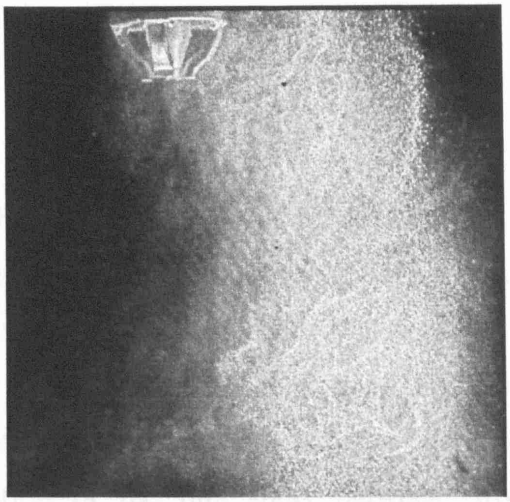

Injector s/n: 034, "slot" crown

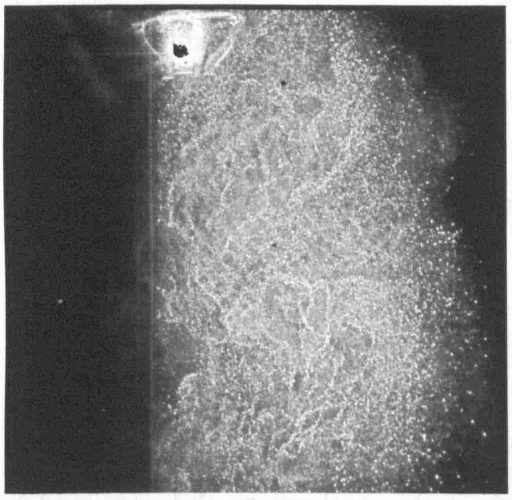

Injector s/n: 003, "disc" crown

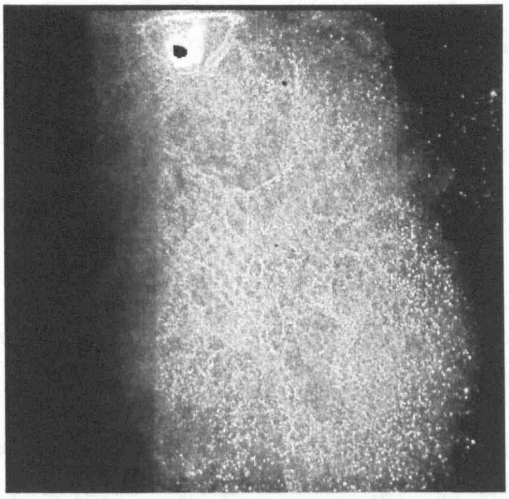

Injector s/n: 034, "disc" crown

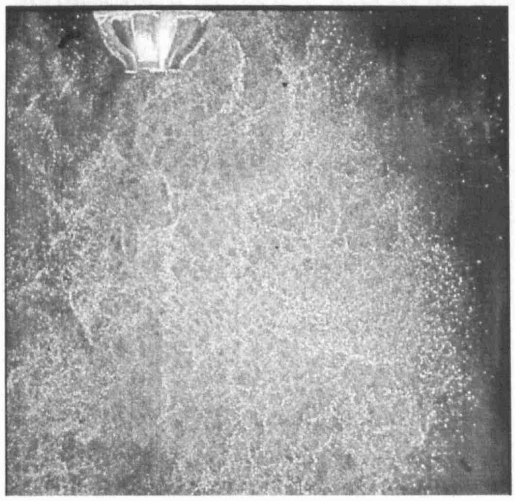

Injector s/n: 003, no crown

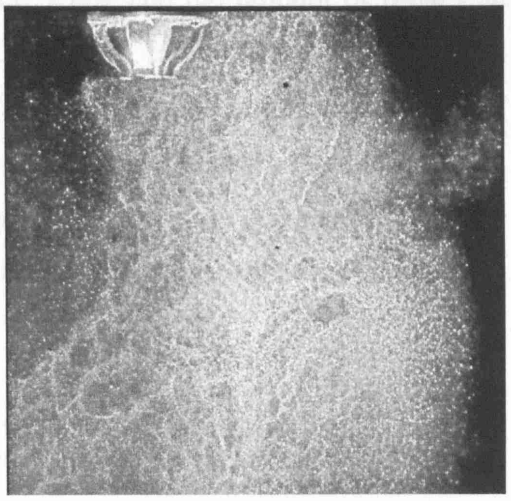

Injector s/n: 034, no crown

Table C-13 Ambient air images, delta 63 CAD

Appendix D

Optical correction

D.1 Introduction

Part of the analysis section of Chapter 8, "A LIF study and further analyses", was to look at the relative velocities of the piston, fuel and air. This was straightforward in the case of the piston and air velocity, but this appendix deals with the difficulty presented by optical distortion in determining the velocity of the fuel spray from the Mie scattering images. The known time delay and the difference in the position of the fuel spray between two consecutive images could be used to find the average velocity of the fuel spray during the interval. However, the quartz main window acted as a cylindrical lens, distorting the image by differing amounts according to location. This meant that correction factors had to be applied to the distances measured on the images. A ray tracing package was used to determine the factors.

D.2 Theory

The quartz main window acted as a cylindrical lens since outside surface was flat but the inside surface was curved to match the combustion chamber. Light rays striking a vertical line on the curved surface were not refracted no matter where they fell on the line. Rays striking a horizontal line across the curved surface were refracted, according to Snell's law and the amount of refraction varied according to their position. Correction factors to account for the refraction were found by tracing rays of light through the system. The optical set-up was drawn using the OSLO software package [Sinclair Optics Incorporated, 2006] and rays were added. The distortion correction factor for each region was determined from the ratio of the separation of the rays before and after the quartz window.

D.3 Physical set-up

Figure D-1 shows the relationship between the CCD chip (512 x 512 pixels), the Nikon lens (nominally 30 mm diameter), the quartz main window (approximately 50 mm wide by 40 mm high) and the area of interest (46mm wide by 25 mm high). This arrangement and the approximate paths taken by

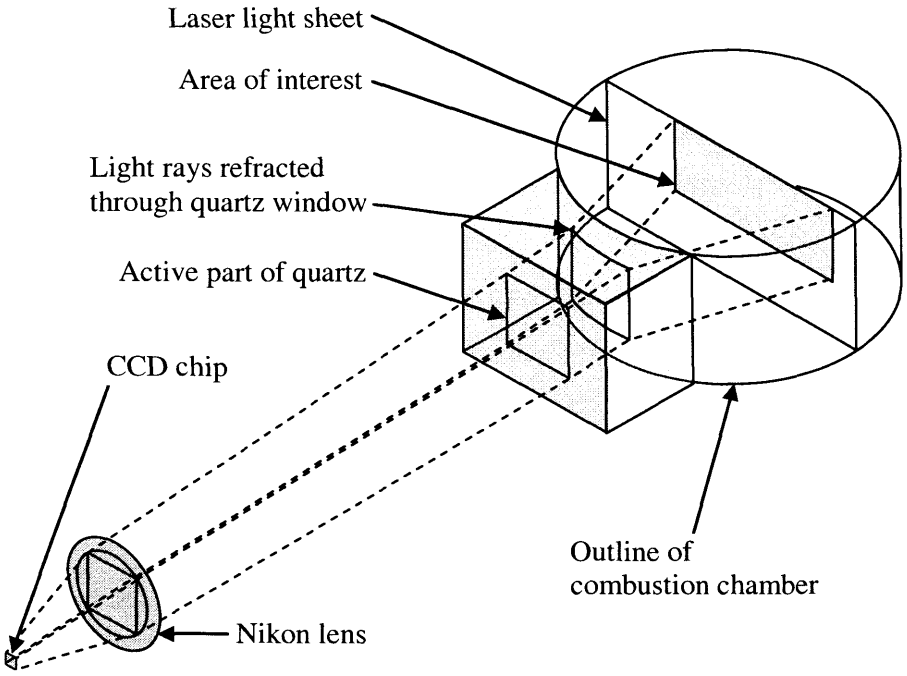

Figure D-1 Set up of optical elements

those rays which struck the CCD chip, having emerged from the extreme edges of the area of interest in the combustion chamber, are also shown in Figure D-1. The set of rays are shown converging slightly as they approach the Nikon lens and this accounts for the slight magnification provided by the Nikon lens.

D.4 The OSLO software

In order to use the OSLO software, it was assumed that the Nikon lens and the quartz window were optically perfect and that the window was accurately made to its manufacturing drawing. It was also assumed that the dimensions and positions were accurate compared to the experimental set up, especially with regard to perpendicularity.

The OSLO software required data on the optical elements, eg material, thickness, radius of curvature and choice of spherical or cylindrical surface. The distance between elements and offsets from the centerline were set and the wavelength of the light was chosen. The 'solve' subroutine then illustrated the path of light rays through the assembled elements. Two options were

available: firstly to assume that the rays were close to parallel after they emerged from the quartz. Secondly, to assume that the rays were converging and the point of convergence was the Nikon lens, which acted as a pinhole. The criterion in the Oslo software for the rays to be considered parallel was for the object to be more than 1 x 10^{20} mm away from the image surface (the area of interest). Diagrams based on each of these options are shown in Figure D-2 and Figure D-3. The actual image to object distance was approximately 300 mm, so while the criterion was not met, the use of near-parallel rays more closely replicated the results from the experimental set up. This was the choice made and the remainder of the analysis was performed on this basis.

D.5 Method of determining correction factors

The area of interest in the combustion chamber filled the IPP image, so the first step was to note down the real dimensions of this area as seen on the IPP image. The known dimensions of the piston crown and spark plug led to an estimate of 46 mm wide and 25 mm high. It was straightforward to determine the correction factors for image distances in the vertical sense, so OSLO was not required. For this case: the 25 mm of the viewing area fell evenly on the 512 pixels of the CCD chip (the quartz did not diffract these rays). Hence, each 1 pixel vertical interval in the IPP image was equivalent to a real distance covered of $25/512$ = 0.049 mm, and this was taken as the vertical distortion factor F_{dv}.

For pixel intervals in the horizontal plane, the conversion factors varied across the width of the quartz, so the 46 mm wide area of interest had to be divided in varying ratios. OSLO was set up with 26 rays, ie 25 intervals of 2 mm each across the 50 mm wide quartz, see Figure D-4. For the first ray interval, rays 1 and 2 were 2mm apart in the parallel region and 3.98 mm apart at the area of interest, ie a basic factor of $2/3.98$ = 0.503. This "bin" accounted for 17 pixels, so an approximation was to assume that each 1 pixel interval in this region had the same factor, ie $0.503/17$ = 0.030 and this was taken as the horizontal distance factor of F_{dh1} for the region. This was repeated for the

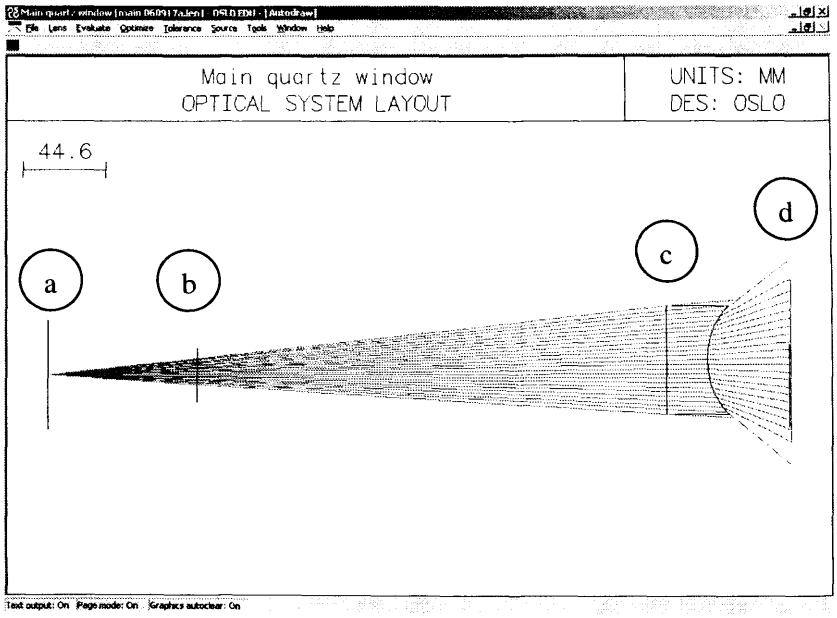

Figure D-2 Plan on optical system using OSLO software, fan of light rays

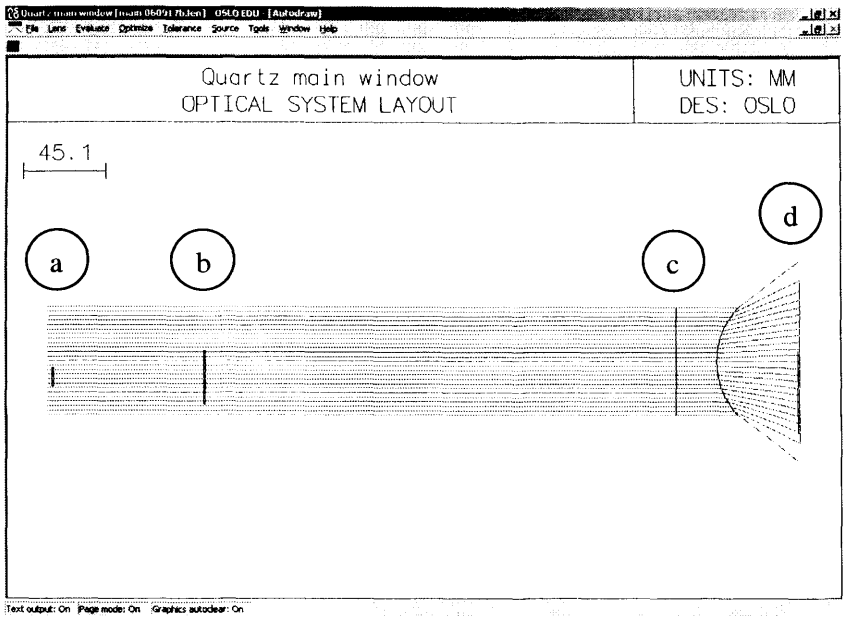

Figure D-3 Plan on optical system using OSLO software, parallel rays of light

Key to Figure D-1 and D-2

a: CCD chip

b: front surface of Nikon lens

c: back surface of main quartz window

d: area of interest in combustion chamber

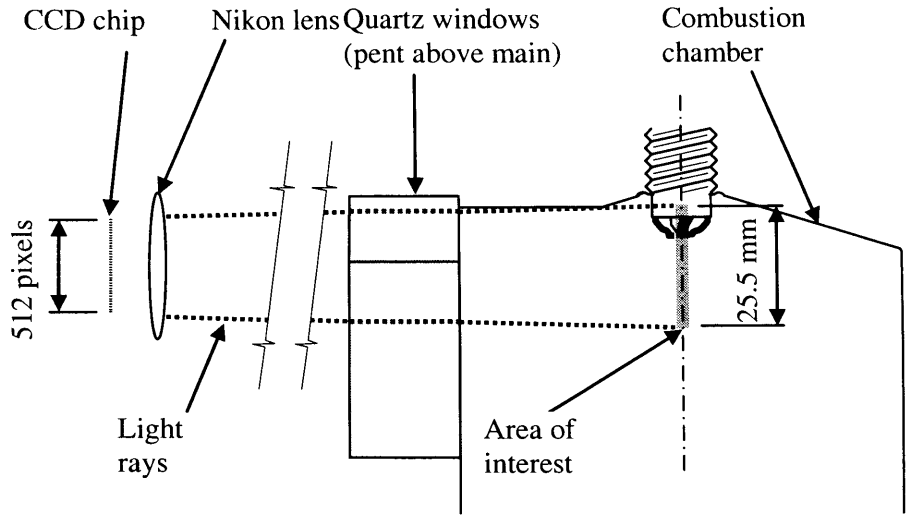

Figure D-4 Relationship between area of interest and pixels in vertical case

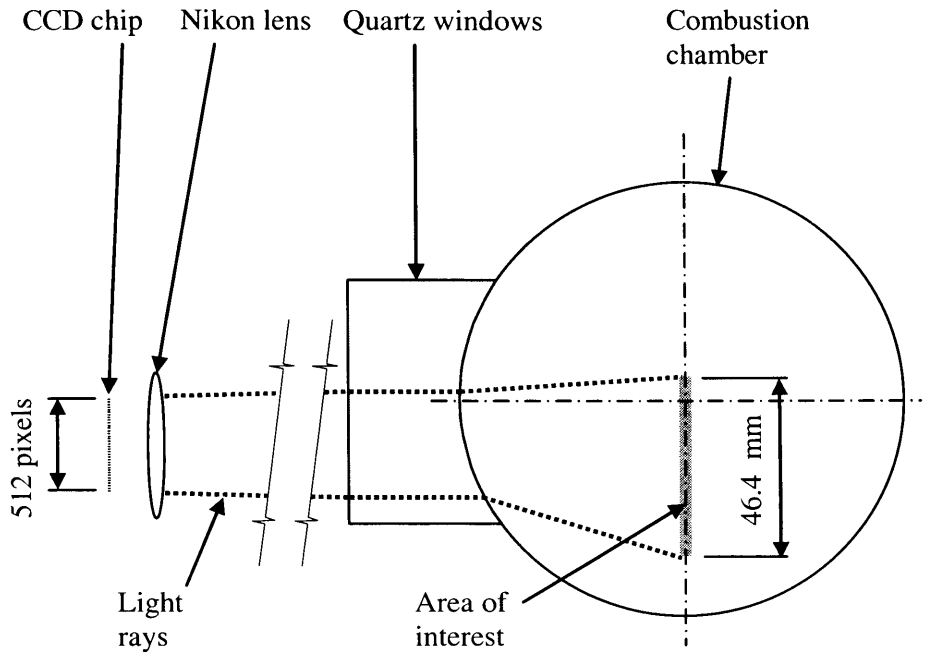

Figure D-5 Relationship between area of interest and pixels in horizontal case

remaining intervals which each had 34 pixels per "bin", apart from the last which again had 17 pixels. The entire 512 pixels in the columns of the IPP image now had a correction factor. The next step was to load the first two images, SOI 639 delta 05 CAD and delta 06 CAD, into Image Pro Plus. The x

and y pixel coordinates, relative to a fixed reference point of the pre-spray tip were noted.

The distance moved by the spray vertically, Y metres, was found from:

$$Y = \left| P_{v2} - P_{v1} \right| \times (F_{dv}) \qquad (D.1)$$

where P_{v2} was the vertical pixel coordinate in the later image, P_{v1} was the vertical pixel coordinate in the earlier image, F_{dv} was the vertical correction factor.

To find the distance moved by the spray horizontally, X metres, firstly the difference between the horizontal pixel coordinate of the later image and the earlier image was split into pixel "bins" (Figure D–6), according to the ray trace diagram (Figure D–3). Then the required distance was found from:

$$X = \sum\{(P_{h1} \times F_{dh1}) + (P_{h2} \times F_{dh2)} + \ldots\ldots \} \qquad (D.2)$$

where Ph_1 was the number of pixels in "bin 1" etc.,.F_{dh1} was the horizontal correction factor applicable to "bin 1" etc.. Next, Pythagoras's theorem was applied to the horizontal and vertical distances to arrive at the true distance, D $= \sqrt{(X^2 + Y^2)}$. Finally, the average velocity of the spray for the interval Δ05 CAD to Δ06 CAD was found from D/Δt, where Δt was the time difference between capturing the two images.

D.6 Results

The correction factors and corresponding number of pixels are shown in Table D-1.

D.7 Discussion

Only a small degree of distortion is evident around the centre of the window. However, there was considerable distortion at the edge which justified the extra effort taken with this approach.

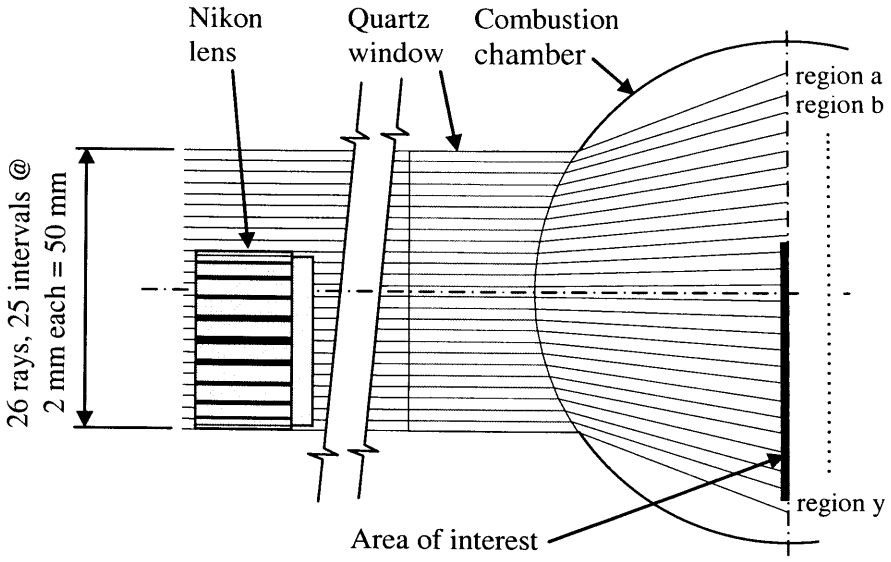

Figure D-6 Plan on elements illustrating calculation of correction factors for horizontal intervals on IPP images

region	separation of unrefracted rays	separation of refracted rays	factor for region	no pixels in region	factor for single pixel
a	2.000	2.976	1.488		
b	2.000	2.739	1.369		
c	2.000	2.562	1.281		
d	2.000	2.428	1.214		
e	2.000	2.318	1.159		
f	2.000	2.242	1.121		
g	2.000	2.176	1.088		
h	2.000	2.132	1.066		
i	2.000	2.101	1.051		
j	2.000	2.078	1.039	17	**0.053**
k	2.000	2.066	1.033	34	**0.053**
l	2.000	2.059	1.029	34	**0.053**
m	2.000	2.054	1.027	34	**0.053**
n	2.000	2.059	1.029	34	**0.053**
o	2.000	2.066	1.033	34	**0.053**
p	2.000	2.078	1.039	34	**0.053**
q	2.000	2.101	1.051	34	**0.054**
r	2.000	2.132	1.066	34	**0.054**
s	2.000	2.176	1.088	34	**0.055**
t	2.000	2.242	1.121	34	**0.056**
u	2.000	2.318	1.159	34	**0.057**
v	2.000	2.428	1.214	34	**0.059**
w	2.000	2.562	1.281	34	**0.062**
x	2.000	2.739	1.369	34	**0.065**
y	2.000	2.976	1.488	17	**0.069**

Table D -1 Conversion factors for horizontal intervals on IPP images

Appendix E

Current and future European emission standards

E1 Euro 4 standard

The Euro 4 standard superseded Euro 3 (Table 2-1, § 2.2.2) in 2005.

	Test: Euro 4, 2005.01	
	Diesel engine (g/km)	Gasoline engine (g/km)
CO	0.50	1.0
UHC	-	0.10
UHC+NO_x	0.30	-
NO_x	0.25	0.08
PM	0.025	-

Table E-1 Passenger vehicle emissions standards, Euro 4 [European Parliament, 2007]

E2 Proposed Euro 5 standard

The Euro 5 standard is due to come into force in 2009.

	Test: Euro 5, 2009.09	
	Diesel engine (g/km)	Gasoline engine (g/km)
CO	0.50	1.0
UHC	-	0.10
UHC+NO_x	0.23	-
NO_x	0.18	0.06
PM	0.005	0.005

Table E-2 Passenger vehicle emissions standards, Euro 5 [European Parliament, 2007]

REFERENCES

Alexander, P; Begg, S; Heikal, M; Li, G; Gold, M [2005] Airflow and fuel spray interaction in a gasoline DI engine. SAE 2005-01-2104.

Alfuso, S; Auriemma, M; Police, G; Praati, M [1993] The effect of Methyl-Ester of rapeseed oil on combustion and emissions of DI Diesel-engines. SAE 932801.

Amann, C. A. [1999a] Past experiences with automotive external combustion engines. Journal of Engineering for Gas Turbines and Power, Transactions of the ASME, Vol. 121, No. 3, p 546-550.

Amann, C. A. [1999b] Evaluating alternative internal combustion engines: 1950-1975. Journal of Engineering for Gas Turbines and Power, Transactions of the ASME, Vol. 121, No. 3, p 540-545.

Aradi, A; Imoehl, B; Avery, N; Wells, P; Grossar, R [1999] The effect of fuel composition and engine operating parameters on injector deposits in a high-pressure direct injection gasoline (DIG) research engine. SAE 1999-01-3690.

Ashley, S [2001] Fuel cells start to look real, Automotive Engineering International, Vol.109, No.3 March 2001.

Baumgarten, H; Bozelle, P; Gelger, J; Wolters, P [2001] Vehicle application of a 4-cylinder tumble DISI engine. SAE 2001-01-0735.

Befrui, B; Kneer, R; Breuer, S; Reckers, W; Robart, D; Wanlin, H; Weiten, C [2002] Investigation of a DISI fuel injector for a close-arranged spray-guided combustion system. SAE Technical paper, 2002-01-1133.

Borman, G; Ragland, K [1998] Combustion engineering, McGraw Hill. ISBN 0071159789.

Bosch [1996] Automotive Handbook (4th Edition). ISBN 1560919183.

Bucknall, R; Nightingale, C; Sulaimi, A [1998] City bus network based on distributed charging stations and on-board energy storage. Proceedings of 31st International Symposium on Automotive Technology and Automation, Düsseldorf, Germany, Paper 98EL036.

Bunting, A [1998] Powers that will be, Automotive Engineer (London), Vol. 23, No. 8, September 1998.

Castagné, M; Chevé, E; Dumas, J; Henriot, S [2000] Advanced tools for analysis of gasoline direct injection engines. SAE 2000-01-1903.

Cathcart, G; Zavier, A [2000] Fundamental characteristics of an air-assisted direct injection combustion system as applied to 4 stroke automotive gasoline engines. SAE 2000-01-0256.

Cengel, Y; Boles, M [1994] Thermodynamics, an Engineering approach. McGraw Hill, Second Edition. ISBN 0071141019.

Challen, B; Baransecu, R (editors) [1999] Diesel engine reference book, Butterworth Heinemann, Second edition. ISBN 0750621761.

Charlton, S [1998] Combustion-related emissions in CI engines, Handbook of air pollution from internal combustion engines – pollutant formation and control, Ed. Sher, E, Academic press, p358-419, Ch.11, 1998. ISBN 0126398550.

Chen, X [2005] Personal email correspondence. 30th June by email.

Choi, K; Park, J; Lee, N; Yu, C; Noh, S [1999] A research on fuel spray and air flow fields for spark-ignited direct injection using laser measurement technology. SAE 1999-01-0503.

Christensen, C [1997] The innovator's dilemma: when new technologies cause great firms to fail. Harvard Business School Press, Boston, Mass. ISBN 0875845851.

Christensen, M; Johansson, B; Einewall, P [1997] Homogeneous charge compression ignition (HCCI) using iso-octane, ethanol, and natural gas, a comparison with spark ignition operation. SAE 972874.

Comar Instruments [2004] Catalogue.

Davy, M; [2000] Two-Phase Fuel Visualisation in a Direct-Injection Gasoline Engine, PhD. Thesis, Department of Mechanical Engineering, University College London.

Davy, M; Williams, P; Anderson, R [1998] Effects of injection timing on liquid-phase fuel distributions in a centrally-injected four-valve direct-injection spark-ignition engine. SAE 982699.

Davy, M; Williams, P; Anderson, R [2000] Effects of fuel composition on mixture formation in a firing direct-injection spark-ignition (DISI) engine: an experimental study using Mie-scattering and planar laser-induced fluorescence (PLIF) techniques. SAE 2000-01-1904.

Degler, H [1938] Internal-combustion engines. John Wiley & Sons.

Delphi [2007] Multec injector http://delphi.com/manufacturers/auto/powertrain/gas/injsys/homogeneous/ (downloaded 17/5/07).

Department for Transport [2002] Emissions for road vehicles. http://www.transtatt.dft.gov.uk/tables/tsgb02/2/download/20602.xls (downloaded 20/12/02).

Department of the Environment, Transport and the Regions [2001a] http://www.transtat.detr.gov.uk/tables/tsgb00/1/10100.htm (downloaded 31/1/01).

Department of the Environment, Transport and the Regions [2001b] http://www.transtat.detr.gov.uk/tables/tsgb00/4/41500.htm (downloaded 6/2/01).

Dixson-Decleve, S [2002] Directive 98/70/EC quick overview of next steps. International fuel quality center. Paris Policy and Technology Briefing, 21/11/02.

Dryer, F [1976] Water addition to practical combustion systems – concepts and applications. Power systems, p279-295.

Duoba, M; Ng, K; Larsen, R [2001] Characterization and Comparison of Two Hybrid Electric Vehicles (Hevs)--Honda Insight and Toyota Prius. SAE 2001-01-1335.

Eckbreth, A.C [1996] Laser Diagnostics For Combustion Temperature And Species, Gordon and Breach Publishers, ISBN 9056995324.

European Parliament [2003] Directive 98/69/EC of the European Parliament http://europa.eu.int/eur-lex/pri/en/oj/dat/1998/l_350/l_35019981228en00010056.pdf (downloaded 14/03/03).

Fenton, J [1998] Handbook of automotive powertrains and chassis designs. Professional Engineering Publishing. ISBN 1860580750.

Financial Times [1997] "Comment and analysis" [10/6/97].

Financial Times [1998] "Inside track" [11/6/98].

Financial Times [1999a] "Outdoors/Motoring" [16/1/99].

Financial Times [1999b] "Personal finance" [3/4/99].

Financial Times [1999c] "Comment and analysis" [25/6/99].

Financial Times [1999d] "Comment and analysis" [16/8/99]

Financial Times [1999e] "National news" [8/9/99].

Financial Times [1999f] "Outdoors/Motoring" [16/1/99].

Financial Times [2000a] "Companies and finance" [23/3/00].

Financial Times [2000b] "National news" [23/9/00].

Flierl, R; Klüting, M [2000] The third generation of valvetrains – new fully variable valvetrains for throttle-free load control. SAE 2000-01-1227.

Frank, H., and Althoen, S. C. [1994] Statistics: Concepts and applications. Cambridge University Press. ISBN: 052144554X.

Fry, M. [1994] Optimization of mixture preparation in an S.I engine, PhD Thesis, Department of Mechanical Engineering, University College London.

Gäfvert, M; Årzén, K; Bernhardsson, B; Pedersen, L [2000] Simple feedback control and mode switching strategies for GDI engines. SAE 2000-01-0263.

Garrett, T; Newton, K; Steeds,W [2001] The Motor Vehicle, SAE International, 13th Edition. ISBN 0768006392.

Geiger, J; Grigo, M; Lang, O; Wolters, P; Hupperich, P [1999] Direct injection gasoline engines – combustion and design. SAE 1999-01-0170.

Georjon, T; Bourguignon, E; Duverger, T; Delhaye, B; Voisard, P [2000] Characteristics of mixture formation and combustion in a spray-guided concept gasoline direct injection engine: an experimental and numerical approach. SAE 2000-01-0534.

Graf, N., Gronki, J., Schulz, C., Baritaud, T., Cherel, J., Duret, P., Lavy, J [2001] In-cylinder combustion visualization in an auto-igniting gasoline engine using fuel tracer- and Formaldehyde-LIF imaging. SAE 2001-01-1924.

Graybeal, J.D [1988] Molecular spectroscopy, McGraw-Hill International, ISBN 0071004491.

Greig, A; Boyes, M [2002] Fuel cells and how they will impact on warship design. Proc I.Mar.E.S.T. 6th Intl. Naval Engineering Conf. (INEC), p217-227. Glasgow, 23- 25 April, 2002.

Guerrier, M. [1999] The development and evaluation of Phosphorescent Particle Tracking, PhD. Thesis, Department of Mechanical Engineering, University College London.

Guthrie, P [2001] A review of fuel, intake and combustion system deposit issues relevant to 4-stroke gasoline direct fuel injection engines. SAE 2001-01-1202

Han, D., Steeper, R. [2002] Examination of Iso-Octane/Ketone mixtures for quantitative LIF measurements in a DISI engine. SAE 2002-01-0837.

Han, Z; Reitz, R; Claybaker, P; Rutland, C; Yang, J; Anderson, R [1996] Modelling effects of intake flow structures on fuel/air mixing in a direct-injected spark-ignition engine. SAE 961192.

Hatano, K; Lida, K; Higashi, H; Murata, S [1993] Development of a new multi-mode variable valve timing engine. SAE 930878.

Hawley, J; Brace , C; Wallace, F; Horrocks , R [1998] Combustion-related emissions in CI engines, Handbook of air pollution from internal combustion engines – pollutant formation and control, Ed. Sher, E, Academic press, p118-170, Ch.10, 1998. ISBN 0126398550.

Heisler, H [1995] Advanced Engine Technology, Arnold, ISBN 0340568334.

Heywood, J [1998a] Internal combustion engine fundamentals. McGraw Hill, ISBN 0071004998.

Heywood, J [1998b] Motor vehicle emissions control: past achievements, future prospects. Handbook of air pollution from internal combustion engines – pollutant formation and control, Ed. Sher, E, Academic press, pp1-25, Ch.1, 1998. ISDN 0126398550.

Hochgreb, S [1998] "Combustion-related emissions in SI engines", Handbook of air pollution from internal combustion engines – pollutant formation and control, Ed. Sher, E, Academic press, pp118-170, Ch.6, 1998. ISBN 0126398550.

Horrocks, R [1992] Light duty diesels - the emissions challenge. Proceedings of the Institute of Mechanical Engineers, Vol.206.

Hotta, Y; Nakakita, K; Fuyoto, T; Inayoshi, M; Fujiwara, K; Sakata, I [2002] Cause of exhaust smoke and its reduction methods in an Hsdi diesel engine under high-speed and high-load conditions. SAE 2002-01-1160.

Institution of Mechanical Engineers [2002] Return of the rotary, Professional Engineering magazine [13/11/02].

Ipp, W; Egermann, J; Schmitz, I; Wagner, V; Leipertz, A; Hartmann, M; Schenk, M [2001] 2D mapping and quantification of the in-cylinder air/fuel-ratio in a GDI engine by means of LIF and comparison to simultaneous results from 1D Raman measurements. SAE Technical paper, 2001-01-1977.

Ipp, W; Wagner, V ; Krämer, H; Wensing, M; Leipertz, A; Arndt, S; Jain, A [1999] Spray formation of high pressure swirl gasoline injectors investigated by two-dimensional Mie and LIEF techniques. SAE 1999-01-0498.

Ismailov, M [1973] Instantaneous fuel flow rates measured in high pressure pipeline of gasoline direct injection engine. SAE Technical paper, 2001-01-1973.

Jackson, N; Stokes, J; Lake, T; Sapsford, S; Heikal, M; Denbratt, I [1996] Understanding the CCVS stratified EGR combustion system. SAE Technical paper, 960837.

Jackson, S [1997] Mixture preparation process in SI engines with particular reference to an air-assisted fuel vaporiser. PhD Thesis, 1997, Department of Mechanical Engineering, University College London.

Japanese Ministry of the Environment [2003] Motor vehicle exhaust emission standards http://www.env.go.jp/en/lar/regulation/mv.html (downloaded 7/03/03).

Jenkins, F.A and White, H.E [1981] Fundamentals of optics (4th edition), McGraw-Hill International, ISBN 0070853460.

Jost, K [1995] Reducing cold start emissions. Automotive Engineer, p22, December, 1995.

Kakoi, K; Tsutsui, Y; Ono, N; Umezawa, K; Kondo, N [1998] Emission reduction technologies applied to high-speed direct injection diesel engine. SAE 980173.

Kakuhou, A; Urishihara, T; Itoh, T; Takagi, Y [1999] Characteristics of mixture formation in a direct injection SI engine with optimized in-cylinder swirl air motion. SAE 1999-01-0505.

Kempton, W; Kubo, T [2000] Electric-drive vehicles for peak power in Japan. Energy Policy, Vol. 28, No. 1, (2000), p 9-18.

Kinoshita, M; Saito, A; Matsushita, S; Shibata, H; Niwa, Y [1999] A method for suppressing formation of deposits on fuel injector for direct injection gasoline engine. SAE 1999-01-3656.

Kubo, M; Sakakida, A; Liyama, A [2001] Technique for analyzing swirl injectors of direct-injection gasoline engines. SAE 2001-01-0964.

Lailler, P; Sarrau, J-F; Sarrazin, C [2001] Comparative study for `36 V' vehicle applications: Advantages of lead-acid batteries, Journal of Power Sources, Vol. 95, No. 1-2, Mar, p 58-67.

Lave, L; MacLean, H; Hendrickson, C; Lankey, R [2000] Life cycle analysis of alternative automobile fuel/propulsion technologies, Environmental Science Technology , Vol. 34, No. 17, (Sep 2000), p 3598-3605.

LaVision [2004] Products, high-speed intensifier camera, HighSpeedStar 5. http\\:www.lavision.de (downloaded 14/6/04).

Lin, M., Sick, V. [2002] Mixture evaporative characteristics prediction for LIF measurements using PSRK (predictive Soave-Redlich-Kwong) equation of state. SAE 2002-01-2750.

Loustalan P., [2005] Experimental investigation of near-nozzle characteristics of gasoline sprays from pressure-swirl atomisers, PhD. Thesis, Department of Mechanical Engineering, University College London.

Lozano, A., [1992] PhD thesis, Stanford University.

Lumley, J [1999] Engines: An Introduction, Cambridge University Press. ISDN 0521644895.

McTague, J [1990] The customer, the environment and the gasoline powered vehicle. Aust. Academy of Tech. Sci. and Eng. Symp., Melbourne, p129-145, October, 1990.

Media Cybernetics, [1994] Image-pro plus reference guide for windows. MANIPPRGw 970101.

Melton, L.A. and Verdieck, J.F [1984] Vapour/liquid visualisation in fuel sprays. 20th Symposium (International) on Combustion, The Combustion Institute.

Miller, M., [1992] Mixture preparation in automotive spark-ignition engines with particular reference to multipoint fuel systems, PhD. Thesis, Department of Mechanical Engineering, University College London.

Milton, B [1998] Control technologies in spark-ignition engines. Handbook of air pollution from internal combustion engines – pollutant formation and control, Ed. Sher, E, Academic press, p189-258, Ch.8, 1998. ISBN 0126398550.

Min, K; Cheng, W; Heywood, J [1994] The effects of crevices on the engine-out hydrocarbon emissions in SI engines. SAE paper 940306.

Miyajima, A; Okamoto, Y; Kadomukai, Y; Togashi, S; Kashiwaya, M [2000] A study on fuel spray pattern control of fuel injector of gasoline direct injection engines. SAE 2000-01-1045.

Moriya, Y; Watanabe, A; Uda, H; Kawamura, H; Yoshioka, M; Adachi, M [1996] A newly developed intelligent variable valve timing system – continuously controlled cam phasing as applied to a new 3 liter inline 6 engine. SAE 960579.

Murayama, T; Fujiwara, Y; Noto, T [2000] Evaluating waste vegetable oils as a diesel fuel. Proceedings of the Institution of Mechanical Engineers, Part D: Journal of Automobile Engineering, Vol. 214, No. 2, p 141-148.

National Statistics [2001a] "The UK in figures – social and welfare", http://www.statistics.gov.uk/ukin_figs/Dat_social.asp (downloaded 31/1/01).

National Statistics [2001b] "The UK in figures – Labour market", http://www.statistics.gov.uk/ukin_figs/Dat_labour.asp (downloaded 31/1/01).

Nitu, B; Singh, I; Zhong, L; Badreshany, K; Henien, N; Bryzik, W [2002] Effect of EGR on autoignition, combustion, regulated emissions and aldehydes in DI engines. SAE paper 2002-01-1153.

O'Donoghue, S., [2002] A study of fuel spray structure and its relationship to emissions and performance of a gasoline direct injection engine, PhD. Thesis, Department of Mechanical Engineering, University College London.

Ortmann, R; Arndt, S; Raimann, J; Grzeszik, R; Würfel, G [2001] Methods and analysis of fuel injection, mixture preparation and charge stratification in different direct injected SI engines. SAE 2001-01-0970.

Owen, K; Coley,T [1995] Automotive fuels reference book, SAE, 2nd edition. ISBN 1560915897.

Park, J; Xie, X; Im, K; Kim, H; Lai, M; Yang, J; Han, Z; Anderson, R [1999] Characteristics of direct injection gasoline spray wall impingement at elevated temperature conditions. SAE 1999-01-3662.

Photonic Science [2004] Cameras, fast dynamic self-illuminated applications, ISIS 4/1000. http\\:www.photonic-science.co.uk (downloaded 14/6/04).

Pontopiddan, M; Gaviani, G; Bella, G; Schilardi, M; Rocco, V [2000] Enhanced mixture preparation approach for lean stratified SI-combustion by a combined use of GDI and electronically controlled valve-timing. SAE 2000-01-0532.

Postma, N; Van Giessel, R; Reinink, F [1973] The Stirling engine for passenger car application, SAE 730648.

Preussner, C; Döring, C; Fehler, S; Kampmann S [1998] GDI: Interaction between mixture preparation, combustion system and injector performance. SAE 980498.

Queenan, K. [1998] Observation and measurement of fuel distribution within a spark-ignition engine, PhD. Thesis, Department of Mechanical Engineering, University College London.

Richardson, D [1997] European legislation for passenger car exhaust emissions. UNICEG meeting, University of Birmingham, 18/09/97.

Ryan,T; Callahan, T [1996] Homogeneous charge compression ignition of diesel fuel. SAE 961160.

Saito, A; Kawabata, M: Koga, K: Motomochi, M: Kaneko, Y [1978] Relationships among engine variable, exhaust gas emissions and fuel economy in gasoline engines. Mitsubishi Heavy Industries, Technical review, pp.54-61, February 1978.

Sandquist, H; Denbratt, I; Ingemarsson, A; Olsson, J [1998] Influence of fuel volatility on emissions and combustion in a direct injection spark ignition engine. SAE 982701.

Sandquist, H; Lindgren R; Denbratt, I [2000] Sources of hydrocarbon emissions from a direct injection stratified charge spark ignition engine. SAE 2000-01-1906.

Shepheard, B, Williams, P, Hale, T, Evans, R [2002] Development and evaluation of a novel optical interface for spark ignition engine research. SAE 2002-01-0742.

Sinclair Optics Incorporated [2001] OSLO light edition, rev 6.1. Ray-tracing software. (Downloaded from www.sinopt.com, 26/11/01).

Smedler, G; Ahlstrom, G; Fredholm, S; Frost, J; Loof, P; Marsh, P; Walker, A; Winterbone, D [1995] High performance diesel catalysts for Europe beyond 1996. SAE 950750.

Smith, J., Sick, V., [2005] Crank-angle resolved imaging of fuel distribution, ignition and combustion in a direct-injection spark-ignition engine. SAE 2005-01-3753.

Spear, P; Penny, N [1964] The development of the Rover-B.R.M. SAE 795b.

Spicher, U. and Velji, A [1984] Measurements of spatial flame propagation and flow velocities in a spark ignition engine. 20th Symposium (International) on Combustion, The Combustion Institute.

Stan, C; Lebrun, M [2000] Concept of interactive development of a GDI system with high-pressure modulation. SAE 2000-01-1042.

Stanglmaier, R; Li, J; Matthews, R [1999] The effect of in-cylinder wall wetting location on the HC emissions from SI engines. SAE 1999-01-0502.

Stanglmaier, R; Roberts, C [1999] Homogeneous charge compression ignition (HCCI): benefits, compromises and future engine applications. SAE 1999-01-3682.

Stevens, E; Steeper, R [2001] Piston wetting in an optical DISI engine: fuel films, pool fires, and soot generation. SAE 2001-01-1203.

Stiglitz, J. E [1997] Economics (2nd edition), W.W.Norton, New York.

Stone, R [1999] Introduction to Internal Combustion Engines. Third edition. Palgrave Macmillan. ISBN: 0333740130.

Structural Dynamics Research Corporation [2001] I-DEAS version 9. Computer aided draughting software (Installed 2001).

Styron, J., Kelly-Zion, P., Lee, C., Peters, J. and Lucht, R. [2000] Multicomponent liquid and vapour fuel distribution measurements in the cylinder of a port-injected, spark ignition engine. SAE 2000-01-0243.

Suh, E; Rutland, C [1999] Numerical study of fuel/air mixture preparation in a GDI engine. SAE 1999-01-3657.

Suzuki, M; Nishida, K; Hiroyasu, H [1993] Simultaneous concentration measurement of vapour and liquid in an evaporating diesel spray. SAE Technical paper, 930863.

Takeda, K; Sugimoto, T; Tsuchiya, T; Ogawa, M; Ueda, S; Yoneshige, K [2000] Slit nozzle injector for a new concept of direct injection SI gasoline engine. SAE 2000-01-1902.

Taylor, C [1985] The internal combustion engine in theory and practice. MIT press. Vol.I, 2nd Ed. ISBN 0262200511.

The Economist [1997] "An engine made of water" [5/4/97].

The Economist [1998] "Ripped off" [14/11/98].

The Economist [1999a] "Barbarians at the Bavarians' gates" [11/02/99].

The Economist [1999b] "Europe after communism" [6/11/99].

The Economist [2000a] "Wheels and wires" [8/01/00].

The Economist [2000b] "Finance and economics" [11/3/00].

The Economist [2000c] "Britain: Bus pass" [10/6/00].

The Economist [2000d] "Britain: Prescott's prize" [22/7/00].

The Economist [2000e] "Leader: Is oil poised to strike?" [9/09/00].

The Society of Motor Manufacturers and Traders Ltd. [2001] The UK motor industry overview http://www.smmt.co.uk/information/industryoverview.asp (downloaded 31/1/01).

Thring, R [1989] Homogeneous charge compression ignition (HCCI). SAE 892068.

Trinker, F; Cheng, J; Davis, G [1993] A feedgas HC emission model for SI engines including partial burn effects. SAE 932705.

United Nations [2001] Charting the progress of populations, www.undp.org/popin/wdtrends/chart/3.pdf (downloaded 5/2/01).

United States Environmental Protection Agency [2003] Federal and California exhaust and evaporative emission standards for light-duty vehicles and light-duty trucks, http://www.epa.gov/otaq/cert/veh-cert/b00001.pdf (downloaded 7/3/03).

Urieli, I, Berchowitz, D [1984] Stirling cycle analysis. Adam Hilger Ltd.. ISBN 0852744358.

Van der Wege, B; Hochgreb, S [2000a] Effects of fuel volatility and operating conditions on fuel sprays in DISI engines: (1) imaging investigation. SAE 2000-01-0535.

Van der Wege, B; Hochgreb, S [2000b] Effects of fuel volatility and operating conditions on fuel sprays in DISI engines: (2) PDPA investigation. SAE 2000-01-0536.

Vogel, O; Roussopoulos, K; Guzzella, L [1997] Variable valve timing implemented with a secondary valve on a four cylinder SI engine. SAE 970335.

Wagner, V., Ipp, W., Wensing, M., Leipertz, A [1999] Fuel distribution and mixture formation inside a direct injection SI engine investigated by 2D Mie and LIEF techniques. SAE 1999-01-3659.

Weaver, C., Wooldridge, S., Johnson, S., Sick, V., Lavoie, G. [2003] PLIF measurements of fuel distribution in a PFI engine under cold start conditions. SAE 2003-01-3236.

Webster, R [1999] Can the electricity distribution network cope with an influx of electric vehicles? Journal of Power Sources, Vol. 80, No. 1, p 217-225.

Wermuth, N., Sick, V. [2005] Absorption and fluorescence data of acetone, 3-pentanone, biacetyl, and toluene at engine-specific combinations of temperature and pressure. SAE 2005-01-2090.

White, D [1996] On the road to zero emissions, The Chemical Engineer, p34-41, July 1996.

Williams, P; O'Donoghue, S; Anderson, R; Richardson, S [2001] An experimental study of the spray characteristics of pressure-swirl atomizers for DISI combustion systems. SAE 2001-01-1974.

Witze, P. and Bopp, S [1991] Investigation of in-cylinder fluid motion using a head gasket instrumented with ionisation probes. SAE Technical paper, 910719.

Witze, P; Hall, M; Wallace, J [1988] Fibre-optic instrumented spark plug for measuring early flame development in spark ignition engines. SAE Technical paper, 881638.

Zhao, F; Harrington, D; Lai, M; [2002] Automotive Gasoline Direct-Injection Gasoline Engines. SAE International. ISBN 0768008824.

Zhao, F; Lai, M; Harrington, D [1997] A review of mixture preparation and combustion control strategies for spark-ignited direct-injection gasoline engines. SAE 970627.

Zhao, H. and Ladommatos, N [2001] Engine Combustion Instrumentation and Diagnostics, SAE International, ISBN 0768006651.